Plasma Physics Reports, Vol. 31, No. 6, 2005, pp. 439–451. Translated from Fizika Plazmy, Vol. 31, No. 6, 2005, pp. 483–495.

TOKAMAKS

Recombination Kinetics of Impurities during a Major Disruption in Tokamak Plasmas

V. A. Shurygin, N. N. Brevnov, and Yu. V. Gott

Nuclear Fusion Institute, Russian Research Centre Kurchatov Institute, pl. Kurchatova 1, Moscow, 123182 Russia

Received April 1, 2004; in final form, June 17, 2004

Abstract—The investigations of major disruptions in the TVD and DAMAVAND tokamaks showed that, in the rapid phase of disruption, accelerated (~1 keV) ions and charge-exchange neutrals are generated near the rational magnetic surfaces; this is accompanied by the bursts of line emission from light impurities (C, O). In the present paper, an analysis is made of the bursts of the CV triplet emission (2271–2278 Å) observed over all of the viewing chords in high-current discharges and also of a decrease in the spectral line emission below its initial (predisruption) level both in the plasma core and at the plasma edge in low-current discharges. The data from measurements of the spatial and temporal parameters of the CV line emission from the central and peripheral plasma regions in the rapid phase of disruption in the DAMAVAND tokamak are compared to the results from model calculations of the kinetics of the charge-state distribution of carbon impurity ions (during the disruption, their kinetics is governed by the increase in the effective recombination rate). A key result of the kinetic model is an increase in the effective rate of charge exchange of impurity ions by two orders of magnitude. Numerical simulations show that the dispersion of the charge-state distribution increases substantially; this is attributed to the rapid phase of disruption being dominated by the recombination of impurity ions through charge exchange with neutrals rather than by the anomalous transport. In this case, carbon impurities in the plasma are transported to the region of increased radiative losses on a time scale of 50 μs. © *2005 Pleiades Publishing, Inc.*

1. INTRODUCTION

Because of major disruption, almost one-half of all stored plasma energy is lost through radiation from impurities. A burst of radiation and rapid plasma cooling are observed in the rapid phase of a disruption, which is often called the energy quench phase. As the energy is released during the disruption in, e.g., the JET tokamak, the radiative loss power increases to about 1 GW over a time of about 100 μs, during which the plasma electron temperature T_e decreases from a few kiloelectronvolts to 10–100 eV [1].

Radiative power losses and plasma cooling observed during disruption are most often considered to be a consequence of the anomalously rapid transfer of cold impurities into the plasma core. At first glance, such considerations agree with the data from measurements of the time evolution of the emission from impurities in the rapid phase of disruption, in particular, with observations of the erosion of the radial profile of the soft X-ray intensity in the plasma [2]. In this way, the behavior of the impurity is interpreted in terms of its *dynamics* (transport), i.e., the possible processes of its transfer over the plasma (see, e.g., [1, 3, 4]). In what follows, the models based on such an interpretation will be referred to as *dynamic* models.

However, an analysis of the measurement data on emission from impurities (in particular, during a major disruption) should not be reduced to the interpretation of the ion dynamics alone, because it is also necessary to take into account the ion *kinetics*, i.e., the temporal evolution of the charge-state and/or excited-state distributions of the ions due to their ionization and recombination. To do this, it is necessary to determine, by one means or another, the time scales of the atomic processes occurring during the disruption. In fact, the interpretation of the measurement results and of the impurity transport derived from them can be justified only by knowing the quantitative relationships between the dynamic and kinetic processes (and, accordingly, their relative impact on the emission from impurities in the plasma).

Let us, for example, consider how to analyze impurity transport in the steady stage of a tokamak discharge by using the measured profiles of the line intensity. Such an analysis is usually based on the implicit assumption [5] that the rates of atomic processes are known almost exactly, which provides quantitative relationships between the dynamics of the impurity ions and their kinetics. The assumption that the kinetics of impurities can be described exactly makes it possible to introduce such empirical transport coefficients as the diffusion coefficient D_A and convection coefficient V_A and then to determine them. Nevertheless, the applicability of every such transport model is limited by its sensitivity to the D_A and V_A values, which in turn depends on the uncertainties in the rates of atomic pro-

1063-780X/05/3106-0439$26.00 © 2005 Pleiades Publishing, Inc.

cesses. The more exact the description of the impurity kinetics in the plasma, the more sensitive the model and, in particular, the closer the transport coefficients D_A and V_A are to their neoclassical values. However, even for steady-state plasma conditions in a tokamak, the empirical transport coefficients are often determined by uncertainties in the rates of atomic processes [6–8] (i.e., in the impurity kinetics) rather than the dynamics of impurity ions. This is why the description of transport in terms of the formally introduced coefficients D_A and V_A does not provide a correct interpretation of the measurement data (see [8] for details).

The same considerations apply even better to the observational data on the emission from impurities during a disruption, e.g., to the above data from measurements of the erosion of the radial profiles of the X-ray intensity [2]. Of course, these considerations alone (i.e., without kinetic analysis) do not give a definite answer to the question about the relationship between the dynamics and kinetics of ions and, in our opinion, do not yield any correct conclusions about the transport of impurities across the magnetic field.

In fact, the main plasma parameters and, accordingly, the rates of atomic processes change strongly over a very short time even at the very beginning of the rapid phase of disruption. In this case, the greatest uncertainties in the kinetics of the charge-state distributions during a disruption arise from the generation of charge-exchange neutral fluxes in its rapid phase [9] and thereby from the processes of charge exchange of the intrinsic plasma impurity with the neutrals of these fluxes. The data from numerous relevant fragmentary observations made on many tokamaks are now available in the literature (for a review of these data, see [9]).

Thus, in investigating disruptions in the TVD [9] and DAMAVAND [10] tokamaks, the charge-exchange neutral fluxes during the rapid phase were observed to increase rapidly (on a time scale of about 20 μs) by a factor of 10–200 over a wide energy range (from 50 to 1500 eV). In the DAMAVAND tokamak [10, 11], it was found that the relative growth in the neutral flux was greatest for energies of about 700 eV; in this case, the spectrum-averaged energy at different radii increased by a factor of about 2 to 4. In the rapid phase of disruption, the fluxes of accelerated ions and of charge-exchange neutrals are presumably generated near the rational magnetic surfaces (with $q = 1, 2$); this is accompanied by spatiotemporal variations in the emission from light plasma impurities [10]. In the case in question, the $q = 2$ rational magnetic surface occurs very near the plasma boundary: its radius is about 6–7 cm, the minor plasma radius being 7–8 cm.

Note that, in similar experiments on internal reconnection events in the TST-2 spherical tokamak, the profiles of line emission from CV, CIII, OV, and OIII ions were also observed to be subject to a rapid (over a time of about 50 μs) and substantial (by a factor of almost 6) Doppler broadening [12].

Hence, the available experimental data show that, in the rapid phase of disruption, not only the main plasma ions, but also the impurity ions are heated and accelerated in a transverse direction.

The effect of neutral fluxes generated during the rapid phase of disruption on the emission from impurities was considered in [13] when analyzing the time evolution of the X-ray spectra during a disruption in the TVD tokamak. It was shown that, in terms of the high effective rates of the charge exchange of impurity ions with neutrals produced during the disruption, it is possible to model the temporal behavior of the X-ray spectra observed over a broad energy range. Below, the models in which the analysis of the ionization–recombination kinetics of impurities is used to interpret the data from observations of the emission from impurities during a disruption will be referred to as *kinetic* models.

In the dynamic model of disruption, the charge-state kinetics of ions is usually excluded from consideration and the actual changes of the rates of atomic processes is taken into account by introducing large transport coefficients. For instance, the emission from impurities during a disruption is described in terms of the anomalous diffusion coefficient $D_A \sim 100$ m^2/s [14–16]. We believe that such a large value of D_A points, first of all, to the large uncertainty in the description of the kinetic processes that occur during the disruption and is unlikely to reflect the actual rate of ion diffusion in the disruption. In particular, if the charge-state kinetics of impurities during the disruption were described by such coefficient of diffusion over charge states [17] that is determined by the rates of ionization and recombination of the most abundant impurity ion species, then the D_A value required for the description could be reduced accordingly.

During the rapid phase of disruption, each of the impurity ion species that reradiate plasma energy turns into a state in which the total radiative power losses increase substantially due primarily to a change in the ion charge-state distribution. Under steady-state conditions, the range of the plasma parameters in which the radiative losses are greatest (see [18]) is sometimes called the radiation barrier [19]. The transition of the emitting impurity to the radiation barrier region depends on the value of its average charge. For light impurities (such as carbon and oxygen) in a steady-state plasma, the radiation barrier in terms of the electron temperature T_e lies below 40 eV, whereas for an iron impurity, it extends up to 1 keV. In this case, the average charge m in the carbon ion charge-state distribution is $m < 4$, which corresponds to ions with an unfilled L shell.

It may be asserted that, during a disruption, the impurity somehow makes a transition to a sort of radiation barrier. In dynamic models, the transition of the impurity atoms to a radiation barrier is possible due to their ionization after the impurity has come from the plasma edge to the plasma core. In a kinetic model (see,

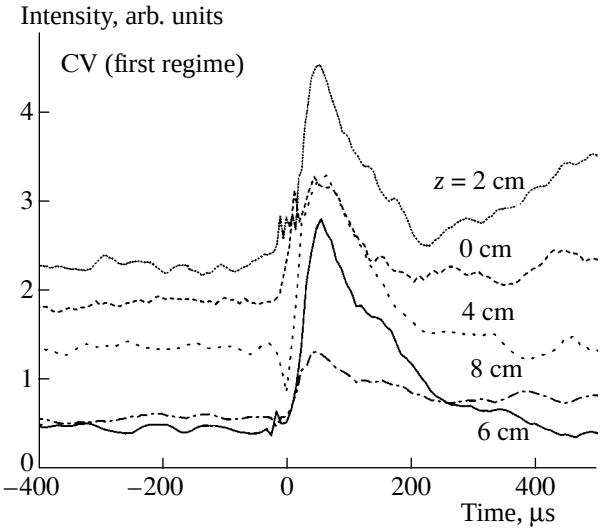

Fig. 1. Time evolution of the CV line intensity observed along different viewing chords (z = 0–8 cm) during the major disruption in the first regime.

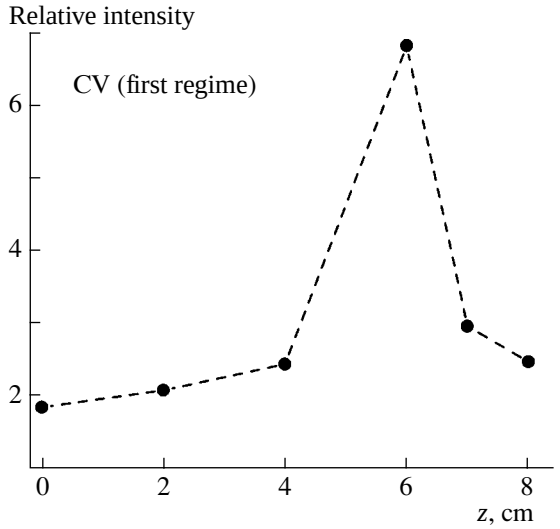

Fig. 2. Radial profile of the ratio of the maximum CV line intensities immediately after and before the disruption according to the data from Fig. 1.

e.g., [8, 13, 17]), this transition can occur as a result of recombination of the impurity ions that are already present in the plasma. A similar transition can also occur due to the charge exchange of the intrinsic plasma impurity with a neutral impurity that comes into the bulk plasma from the wall or from the plasma periphery. In this case, the ionization of the impurity coming into the plasma is accompanied by the recombination of the intrinsic plasma impurity.

Thus, the investigation of the charge-state kinetics of impurities during a disruption (in particular, the average charge of impurity in the radiation barrier, the time evolution of the distribution over charge states, as well as the possible transitions to these states) is of considerable interest for interpreting the behavior of impurities during a disruption. In the present paper, the kinetic model developed in [8] is used to interpret the time evolution of the line emission from CV ions from the plasma core and plasma periphery in the rapid phase of disruption in the DAMAVAND tokamak.

2. EXPERIMENTAL OBSERVATIONS OF THE EMISSION FROM LIGHT IMPURITIES DURING A DISRUPTION

The main parameters of the DAMAVAND tokamak are as follows [10, 11]: the plasma major radius is R = 36 cm, the plasma minor radius is a = 7 cm, the elongation of the cross section of the plasma column is k = 1.2, the toroidal magnetic field is $B_T \le 1$ T, the plasma current is $I_p \le 40$ kA, the electron density is $n_e \approx 10^{13}$ cm^{-3}, the electron temperature is $T_e \sim$ 200–300 eV, the ion temperature is $T_i \sim$ 100–150 eV, and the discharge duration is 15 ms. The value of the elongation k was chosen so as to avoid the rapid development of the vertical instability. MHD-driven disruptions of the plasma current were initiated by connecting an additional capacitor bank to the inductor 8 ms after the beginning of the discharge. As a result, the discharge current increased by 10–20% and became disrupted. The working gas was deuterium.

The two regimes with MHD-driven disruptions that will be considered below were chosen from the experimental database [9–11]. In the first regime, the plasma current was I_p = 32 kA, and in the second regime, it was I_p = 21 kA. The toroidal magnetic field was chosen so as to keep the safety factor at the plasma boundary nearly the same (q_a = 2.3) when the plasma current was varied. In chord measurements, the spatial resolution of the diagnostics was about 10 mm, the time resolution being about 5 μs. A more detailed description of the experimental conditions in discharges with disruptions and of the diagnostic systems is given in [9–11].

Figure 1 shows the behavior of the intensity of the CV spectral line (i.e., of the emission from the three essentially equiprobable $2p^3P$–$2s^3S_1$ transitions [20] at wavelengths of 2271–2278 Å in C^{4+} ions with an ionization energy of 392 eV) measured during a disruption in the first regime. The measurements were made along several chords viewing the plasma column at the distances of z = 0, 2, 4, 6, and 8 along the tokamak equatorial plane. The initial time (t = 0) was chosen to be that of the largest negative voltage spike over the major circumference of the torus. Figure 2 shows the radial profile of the ratio of the maximum CV line intensities immediately (t = 50 μs) after and before the disruption; the profile was reconstructed from the data presented in Fig. 1. From Figs. 1 and 2, we see that, in the rapid phase of disruption (just after the instant t = 0) in the first regime, a very intense burst of emission occurs

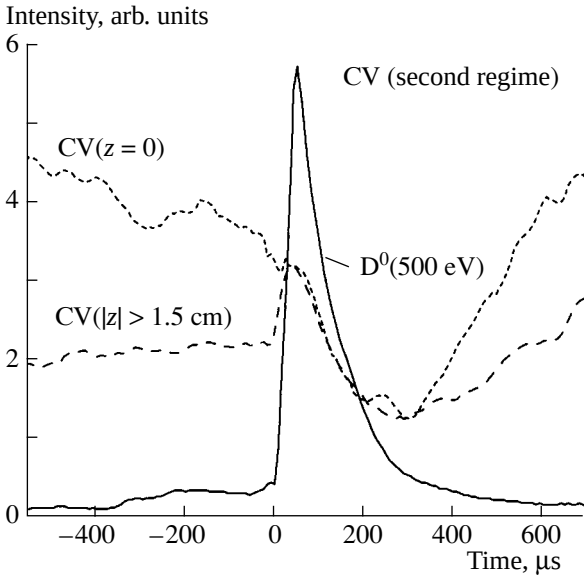

Fig. 3. Time evolution of the CV line intensity in the plasma center ($z = 0$) and at the plasma periphery ($|z| > 1.5$ cm) and of the flux of charge-exchange neutral atoms (D^0) with an energy of 500 eV in the rapid phase of disruption in the second regime.

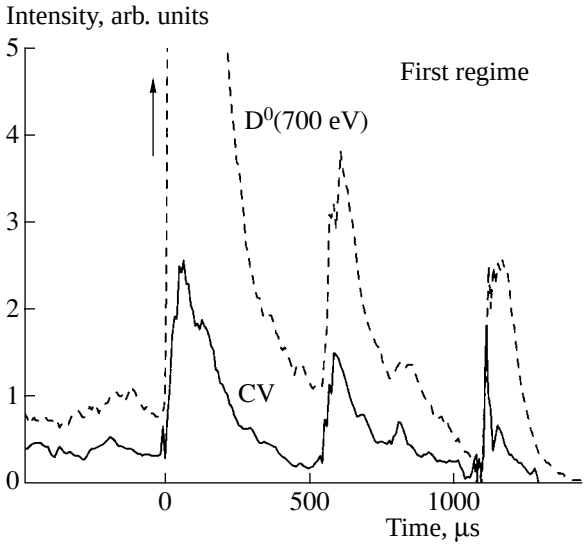

Fig. 4. Time evolution of the CV line intensity from the z= 6 cm viewing chord and of the flux of charge-exchange neutral atoms with an energy of 700 eV from the same chord in the rapid phase of disruption in the first regime.

along all of the viewing chords; the maximum relative increase in the intensity (by a factor of almost 7) is observed along the $z = 6$ cm chord, i.e., near the $q = 2$ rational magnetic surface.

In the second regime, the CV line intensity was measured in the central plasma region with a diameter of about 3 cm (roughly along the $z = 0$ chord) and at the plasma periphery ($|z| > 1.5$ cm), when the central plasma region was screened. The measurement results are presented in Fig. 3, which also shows the signal from the flux of charge-exchange neutrals with an energy of 500 eV. We can see that, even before the rapid phase of disruption (starting from a time of about $t \approx -300$ μs), the intensity of the CV line emission from the plasma core begins to decrease substantially; simultaneously, the charge-exchange particle flux starts increasing. At the beginning of the rapid phase of disruption (on time scales of about $t \approx 30$–50 μs), the CV emission continues to decrease but at a far slower rate; or, it almost stops decreasing. On a time scale of about $t \approx 300$ μs, the intensity again decreases. Thereafter, the signal intensity starts increasing. The intensity of the CV line emission from the plasma edge increases abruptly and then decreases to below its initial level. Measurements through a fully opened diagnostic window (in this case, the emission from the entire vertical cross section of the plasma was recorded) showed that the spectral line emission from the CV triplet state possessed approximately the same temporal behavior as that measured through a window with a closed center. Thus, we may assert that, during and after a disruption, the CV line emission comes predominantly from the periphery of the plasma column.

Thus, for $t > 0$ in the first regime, a burst of the CV line emission (with a rise time of about 50 μs) was observed in all z chords, including the central chord $z = 0$; in contrast, for $t > 0$ in the second regime, the emission was found to possess a qualitatively different behavior: it fell below the initial signal level both in the plasma core and at the plasma periphery.

At the same time, in the rapid phase of disruption, the emission from ions in low charge states (such as CIV, CIII, OV, etc.) increased in all tokamak operating regimes. Nevertheless, an analysis of the relevant series of measurements carried out in different regimes [8] allows us to conclude that, before and during a disruption, there is a correlation between the line emissions from D_β, OV, CV, CIV, and CIII ions and the charge-exchange neutral flux. As an example, Fig. 4 shows the time evolution of the CV line intensity and of the flux of charge-exchange neutrals, both measured along the $z = 6$ chord in the first regime. The series of peaks in CV emission corresponds to the peaks in the flux of neutral atoms with an energy of 700 eV. From the peak in Fig. 4 that corresponds to the time $t \approx 600$ μs, it can be inferred that the CV emission signal grows faster and reaches its maximum earlier than the flux of neutrals. The same characteristic feature can readily be derived from a comparison of the OV emission and the neutral flux that are shown in Fig. 10 from [8].

It is also seen that, before and after the beginning of the rapid phase of the major disruption, there are several subsequent small disruptions of different intensities, which are accompanied by the bursts of neutral fluxes. Figures 5–7 show the bursts of the D_β, OV, and

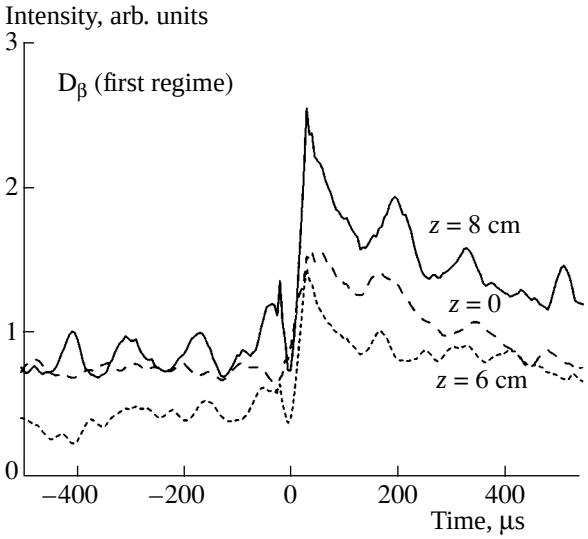

Fig. 5. Time evolution of the D_β line intensity along the central chord ($z = 0$) and peripheral ($z = 6$, 8 cm) chords in the rapid phase of disruption in the first regime.

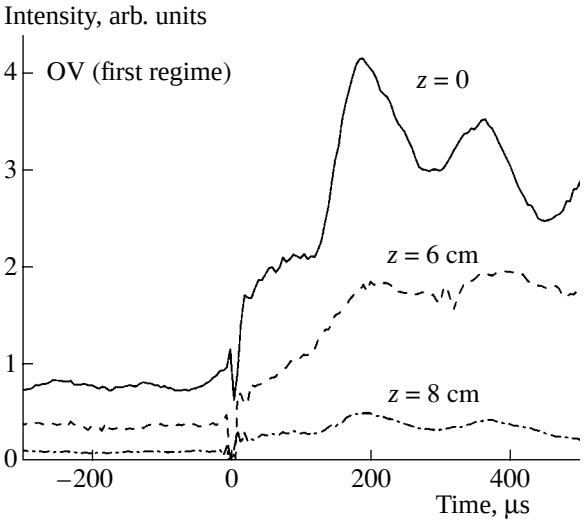

Fig. 6. Time evolution of the OV line intensity along the central chord ($z = 0$) and peripheral ($z = 6$ and 8 cm) chords in the rapid phase of disruption in the first regime.

CIV emission lines that correspond to these busts of neutral fluxes and that were measured along several z chords. Each curve in these figures was obtained by averaging over a series of three to five reproducible discharges and by adjusting the signals to the same reference time $t = 0$.

3. DYNAMICS AND KINETICS OF CV IONS

The ^3P levels of a CV (C^{4+}) ion can be populated in the two main ways: through electron impact excitation from the ground state and through charge exchange of a CIV (C^{5+}) ion with the capture of an electron into an excited state. The kinetic calculations of the emission from ions with different degrees of ionization are usually carried out using a collisional radiative model that also takes into account cascade processes. In the case under consideration, the population of the ^3P levels through charge exchange with neutrals is unlikely to have any significant effect on the observed emission from CV ions. This conclusion follows from the decrease in the CV emission (see Fig. 3) in the second regime at a time when the neutral influx into the plasma increases substantially. Consequently, the charge-exchange population mechanism in the second regime (and probably in the first regime too) can be excluded from consideration. This is why, in order to interpret the measurement data, we will restrict ourselves to analyzing the charge-state kinetics of the CV ions alone, assuming that their ^3P levels are populated primarily through the electron-impact excitation from the ground state. It should be emphasized, however, that, although the charge-exchange mechanism for populating the ^3P levels is eliminated from consideration, it should be taken into account in the analysis of charge-state kinetic processes, in which, on the contrary, it plays a dominant role. In our study, we will not analyze the kinetics of the ionized and excited states of the ions of other species (note that such an analysis implies the use of a collisional radiative model).

The line emission from light impurities during a disruption was investigated in the TFR [21] and TEXTOR [22] tokamaks. The line radiation that was observed just at the beginning of the major disruption in the TEXTOR tokamak [22] might well be emitted by the CV and OIV ions from the plasma edge; the intensity was then found to decrease below its initial level. This

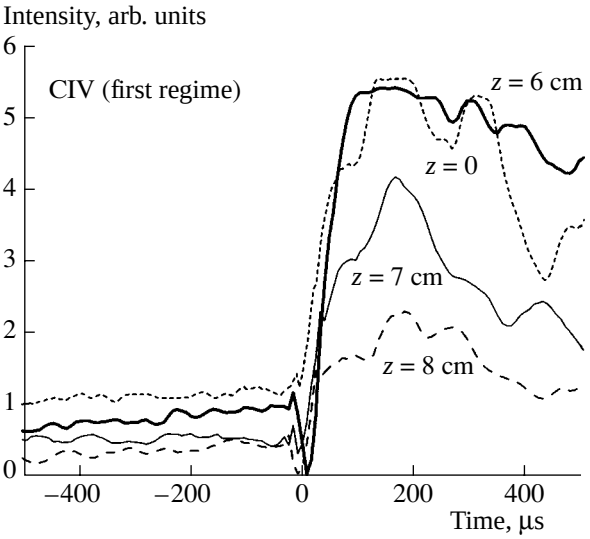

Fig. 7. Time evolution of the CIV line intensity along the viewing chords $z = 0$, 6, 7, and 8 cm in the rapid phase of disruption in the first regime.

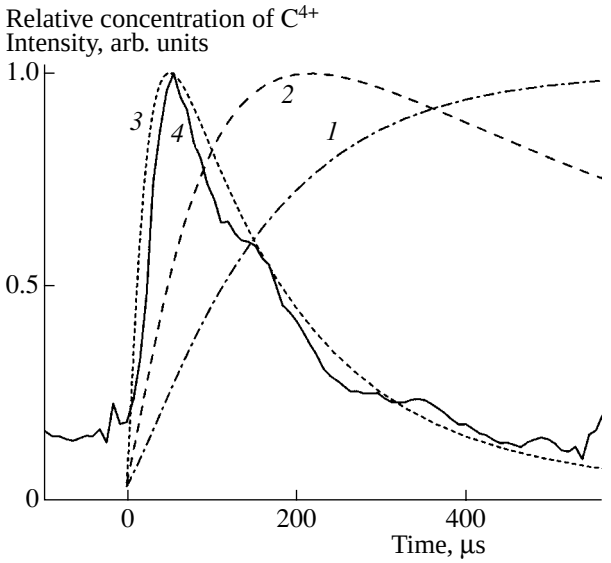

Fig. 8. Comparison of the time evolution of the CV line intensity measured along the z = 6 cm chord in the first regime (curve *4*) to the calculated time evolution of the relative concentration of the CV (C^{4+}) ions produced during the ionization of neutral carbon atoms for different plasma parameters: (*1*) T_e = 100 eV and $n_e = 3.5 \times 10^{12}$ cm^{-3}, (*2*) T_e = 1 keV and $n_e = 3.5 \times 10^{12}$ cm^{-3}, and (*3*) T_e = 3 keV and $n_e = 1.5 \times 10^{13}$ cm^{-3}.

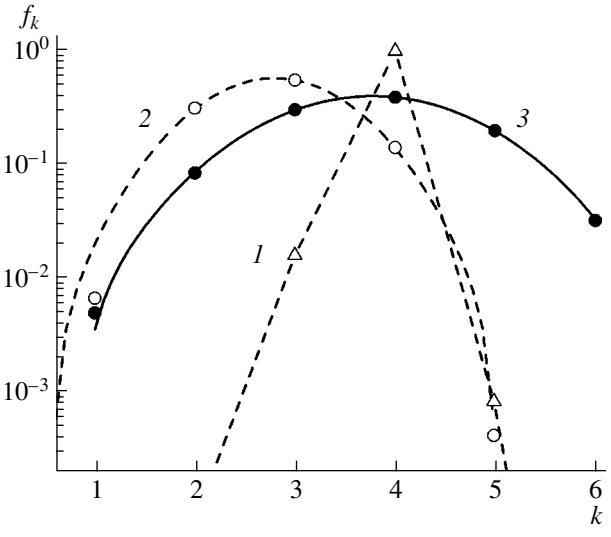

Fig. 9. Numerically calculated charge-state distributions of carbon ions (see text for explanation).

agrees with our observations of the CV line emission in the second regime. The behavior of the OIV line emission (1032 Å) in the TFR tokamak [19] during the major disruption is similar to that of the CV emission in the first regime. The bursts of emission from light impurities in the TFR tokamak were explained using the results of simulations with a transport code for impurities and by taking the anomalous values of transport coefficients. In this case, the diffusion coefficient D_A in the rapid phase of disruption should be increased from 4×10^3 to 10^5 cm^2 s^{-1} and the rate of convection toward the plasma core, V_A, from 400 to 2×10^3 cm s^{-1}.

From the standpoint of such dynamic models, the results we have obtained for the first regime (at a high plasma current; see Fig. 1) can be explained in the same manner as those in the TFR tokamak, i.e., in terms of the transfer of neutral carbon impurity atoms over the entire cross section of the plasma column and their subsequent ionization. However, the rise time of the signals from all the viewing chords in the first regime turns out to be abnormally short (less than 50 μs), which is inconsistent with the widely held opinion that the observed variations in the CV line emission are dominated by the ionization of a neutral impurity. The abnormal effect is also that this time is essentially the same for all z chords. The duration of the burst of the CV line emission from the plasma edge in the second regime is even shorter. It is, however, not such short rise times that are most difficult to explain in terms of the models involving transfer of impurities over the entire plasma, but rather the revealed decrease in the intensity of the line emission from helium-like carbon ions in the plasma core and also a decrease in this line intensity at the plasma periphery below its initial level (see Fig. 3) in the rapid phase of disruption in the second regime.

In order to explain these effects in terms of dynamic models, it would be necessary to assume the anomalously rapid transfer and ionization of the impurities that have come into the discharge and an equally rapid escape of carbon atoms that have been ionized to a helium-like state from almost the entire plasma column rather than from the plasma core alone. Note that such assumptions have to be made only if the possible kinetic processes are completely ignored. In contrast, a detailed analysis of the kinetics of impurities opens promising new ways for a description of the impurity dynamics.

It should be stressed, first of all, that, from the standpoint of the charge-state kinetics of impurities during a disruption, the CV line emission in the two regimes with disruptions seems to behave in an unusual fashion, too. The reason for this is as follows: The coronal equilibrium model implies that, in the quasisteady phase of the discharge, the relative concentration of the helium-like CV ions (which are most representative of the impurities) is nearly constant (~0.6–0.9) over a broad range of the plasma parameters, in particular, over the electron temperature range T_e = 10–150 eV typical of the plasma in the DAMAVAND tokamak. Consequently, an increase in the intensity or its severalfold decrease can be associated with anomalously rapid and very large variations not only in T_e but also in other parameters that govern the intensity of the CV spectral lines.

Following a dynamic model, we assume that neutral carbon atoms that come from the chamber wall instantly penetrate into the plasma column and are ionized during a disruption. Let us estimate what the plasma parameters are that govern the observed rise time of the line intensity of CV ions, on the one hand, and the observed rapid decrease in the intensity, on the other. Figure 8 compares the calculated time variations in the relative concentration of the CV ions after the ionization of neutral carbon atoms with the temporal behavior of the CV line intensity measured along the $z = 6$ cm viewing chord in the first regime. We can see that, for the plasma parameters typical of the disruption conditions under consideration ($T_e < 100$ eV, $n_e < 10^{13}$ cm^{-3}), the ionization of carbon atoms from their neutral states is capable of providing neither the short rise time of the signal nor its subsequent rapid decrease (especially in the edge plasma). Adjustment of the plasma parameters to the required values (see Fig. 8) yields the electron density n_e and electron temperature T_e that considerably exceed their actual values during a disruption, especially at the plasma edge. An important point is that, during a disruption, the electron temperature T_e decreases appreciably (rather than increases).

Hence, in order to explain the observed time evolution of the CV line emission (in particular, in the first regime) due to the ionization of neutral carbon atoms that have come into the discharge plasma, it would be necessary to assume an abrupt increase in the effective ionization rate due to an increase in the electron density and temperature over the entire cross section of the plasma column. We believe that, for any more or less realistic values of the plasma parameters, the rapid increase in the CV emission signal, as well as the subsequent rapid decrease in the signal intensity, cannot be explained as being due to ionization.

Some insight into the cause of the observed variations in the CV line emission can be gained from the behavior of the flux of fast charge-exchange neutral particles during a disruption in both regimes (see Fig. 3). In fact, the high generation rate of such a flux cannot be ignored in the analysis. The short rise time (20–50 μs) of the charge-exchange neutral flux generated in the rapid phase of disruption and a relative increase in the flux intensity by more than two orders of magnitude can be regarded as additional evidence for the significant increase in the effective rates of charge exchange of both the main ion plasma component and the impurities. As a result, the ion recombination kinetics should predominate over the other processes that affect the emission from impurities.

Since, in this case, the problem about the relationship between the dynamic and the kinetic processes remains unresolved, it is worth noting that our observations can in principle be explained by reference to the anomalous dynamic impurity transport processes during a disruption. Nonetheless, the possible interpretations should yield equivalent descriptions of the observed behavior of the impurity charge-state distribution. Thus, one of the versions of such a description can involve the recombination of the intrinsic multicharged plasma impurity ions as a consequence of their charge exchange with the impurity atoms and ions that come from the wall and are transferred into the plasma core by the anomalous transport processes considered in dynamic models [1–3]. These transport processes lead to a further increase in the effective rates of impurity recombination. As a result, the impurity recombination rates can become comparable to the rates of electron-impact excitation of impurities and can become important when the relative amount of impurities in the plasma increases [23].

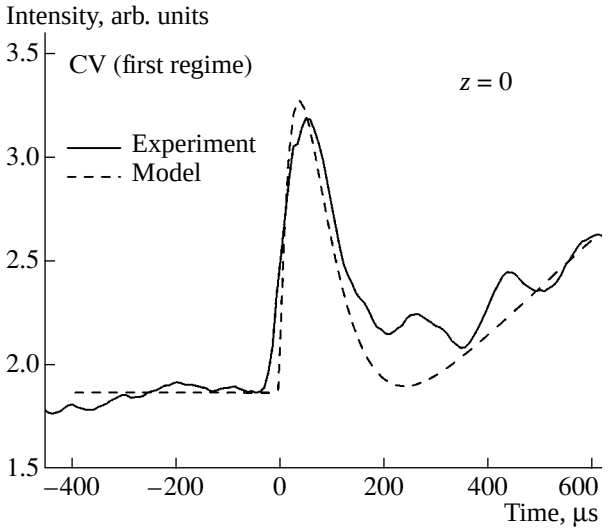

Fig. 10. Comparison of the model to the experiment: the calculated and measured time evolution of the CV line intensity at the plasma center ($z = 0$) during a disruption in the first regime.

4. KINETIC MODEL

The set of charge-state kinetic equations for the local values of the relative concentrations of the ions in each charge state has the form

$$\frac{df_k}{dt} = R_{k+1}f_{k+1} - (R_k + S_k)f_k + S_{k-1}f_{k-1}, \qquad (1)$$

where

$$f_k(t) = n_k(t)/n_i(t), \qquad (2)$$

and $n_i(t) = \sum n_k(t)$ is the total density of the impurity atoms of a given sort ($k = 0, 1, 2, \ldots, Z$). The quantities R_k and S_k are the total (summed over all processes) recombination and ionization rates, respectively. These rates are expressed in s^{-1} (because they contain as a factor the electron density n_e) and satisfy the relationships $R_0 = S_{-1} = R_{Z+1} = S_Z = 0$. Equations (1) were supple-

mented with the initial conditions $f_k(0) \geq 0$. Moreover, we have

$$\sum_{k=0}^{Z} f_k(t) = 1. \quad (3)$$

In our kinetic model, the initial (predisruption) state of the impurity was specified in terms of the parameters n_e, T_e, T_i, and $\xi_n = n_n/n_e$ (the relative concentration of neutral particles), whose values were taken to be consistent with the known plasma parameters in the DAMAVAND tokamak. Series of small disruptions (see Figs. 4–7) were described by representing the relative variations in the rates of charge-exchange recombination in the rapid phase of disruption in the form of an effective pulse with an amplitude A_{cx} and an exponential decay time τ_{cx}. In addition, measurements of X-ray spectra from the plasma periphery in the TVD tokamak (which is of the scale of the DAMAVAND tokamak) showed [24] that the edge plasma was dominated by accelerated electrons with an energy of about 1 keV; this circumstance was taken into account by introducing a certain effective electron temperature T_e at the plasma periphery.

The charge-state distributions of the carbon impurity were computed using the data for calculating the rates of atomic processes from [25]; in this case, the impurity ionization rate was described by the Lotz formula [26]. The photorecombination and dielectronic recombination rates were computed using the data from [22].

The charge-exchange recombination rate was calculated from the formula

$$R_k = n_e\xi_n(1+\beta)\langle\sigma_1^{cx}(k)v\rangle, \quad (4)$$

where the factor β accounts for the contribution of the excited states of the neutral atoms to the charge-exchange processes [27] (whose cross sections increase sharply with the principal quantum number n of the corresponding levels, $\sigma_n^{cx} \sim n^4$), $\sigma_1^{cx}(k)$ is the charge-exchange cross section for hydrogen atoms in the ground state, and v is the velocity of neutral particles. The cross section for charge exchange of hydrogen atoms in the ground state with impurities is about 10^{-15} cm^2. However, for the $n = 3, 4$ levels of hydrogen atoms, this cross section is as large as about 10^{-13} cm^2. Consequently, the excitation of 1% ($\beta \cong 1$) of neutral particles to the $n = 3, 4$ levels doubles the effective charge-exchange rate, the excitation of 2% ($\beta \cong 2$) of neutrals triples this rate, and so on.

A solution to Eqs. (1) with allowance for a given kinetic process will be called a translation of an impurity charge-state distribution (see also [8]). In the case of disruption due to the generation of an impurity flux, the recombination rates are far more higher than the rates of ionization processes [11]. In this case, the solution to Eqs. (1) will be called a dominant recombination translation. A more detailed description of other types of impurity charge-state translations is given in [8, 28].

The charge-state kinetics of impurities can conveniently be described in terms of the lowest moments of the distribution function, such as the average charge m and dispersion D:

$$m = \sum_{k=0}^{Z} k f_k, \quad (5)$$

$$D = \sum_{k=0}^{Z} k^2 f_k - m^2. \quad (6)$$

Moments (5) and (6) are appropriate quantitative parameters describing the position of the distribution center (m) and its shape (D). The initial values of the moments m and D can be estimated from the coronal equilibrium condition, i.e., from the condition of a steady-state balance between ionization and recombination, provided that the dynamic (transport) processes are ignored. It is clear that, when nonstationary processes are taken into account, the moments m and D can deviate markedly from their values in the coronal equilibrium. During a disruption, these deviations can be associated with both the dynamics and kinetics of impurity ions in the plasma.

It was found [8, 27] that a typical property of a nonstationary recombining plasma is a systematic broadening of the charge-state distributions of impurities. In contrast, a property typical of a nonstationary ionizing plasma is a decrease in the dispersion of the charge-state distributions in comparison with that in a steady-state plasma. However, in a number of limiting cases of charge-state kinetics, such as, e.g., the ionization of neutral atoms that penetrate instantly into the plasma column, the dispersion of their charge-state distributions is, as a rule, appreciably higher than that in a steady state and the distributions themselves are nearly Gaussian. Such kinetic properties of the variations in the charge-state distributions should be distinguished from the equally important effect of the ion dynamic (transport) processes.

Figure 9 shows charge-state distributions of carbon calculated for the following three cases: (*1*) a steady-state distribution corresponding to $m = 4$ (for $T_e \approx 40$ eV), (*2*) a distribution formed during the electron-impact ionization of carbon impurity atoms from the ground state 50 μs after they have instantly penetrated into the plasma with the parameters typical of the first regime, and (*3*) a distribution of carbon ions formed 50 μs after the rate of recombination from the ground state (governed by the plasma parameters typical of the first regime) has increased instantaneously by two orders of magnitude. The curves drawn through the points of distributions *2* and *3* are Gaussian distributions.

Steady-state distribution *1* in Fig. 9 has an interesting feature: its dispersion (width) is the lowest among the steady-state (coronal) distributions with $3 < m < 5$. Distribution *2* evolves to an analogous distribution at subsequent times ($t > 50$ μs); moreover, the distribution center is displaced toward larger values of m. However, distribution *3*, for which $m \approx 4$ and which arises in the case of a dominant recombination translation, is of maximum width. In principle, this purely kinetic widening of charge-state distribution *3* can be modeled by increasing the values of the empirical transport coefficients. Such an approach is often used to interpret the results of observations of the emission from impurities during a disruption, whereas the problem of whether the dynamic and kinetic processes have an equally important effect on the impurity charge-state distributions has not been considered at all.

We thus arrive at the following two conclusions. First, regardless of the actual relationship between the dynamic and kinetic processes, the model can be adjusted to fit the experimental data in a simpler way, namely, by modifying the rates of atomic processes (see, e.g., [11, 15, 25]) without using the transport coefficients D_A and V_A. Second, both these approaches turn out to be equivalent in the sense that they yield the same model charge-state distributions. Hence, the kinetic model, as well as the dynamic model, makes it possible to interpret observational data on the time evolution of the impurity charge-state distribution during a disruption.

5. SIMULATION RESULTS

The assumption that the rate of charge-exchange recombination of impurities increases by two orders of magnitude during a disruption plays the key role in the model proposed here. The effective rate of charge-exchange recombination of impurities in the rapid phase of disruption can increase due to the following three factors: first, due to the growth of the flux of neutral atoms (in particular, the product $n_e\xi_n$); second, at the expense of the factor β (the growth of the population of the excited states); and third, because of the charge exchange of multicharged ions with neutral impurity atoms that can penetrate into the plasma and with the main neutral component of the plasma. The model also takes into account variations in the mean energy over the spectrum of the main ion plasma component; these variations, however, are of minor importance.

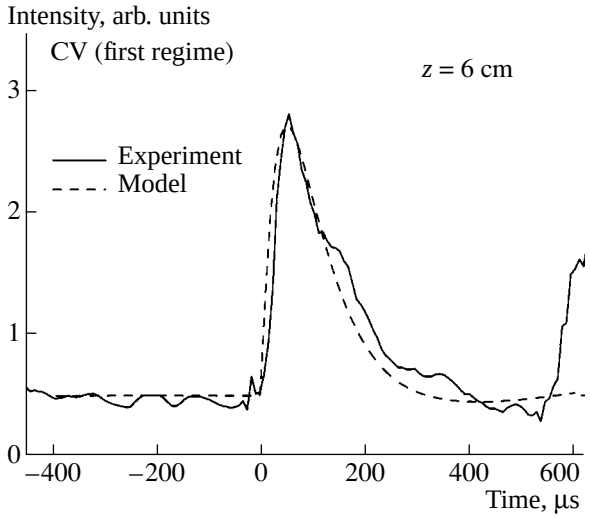

Fig. 11. Comparison of the model to the experiment: the calculated and measured time evolution of the CV line intensity at the plasma edge ($z = 6$ cm) during a disruption in the first regime.

A comparison of the numerical results obtained for the first regime with the experimental data is illustrated in Fig. 10 (for $z = 0$) and Fig. 11 (for $z = 6$ cm). The parameters of the model, as well as their variations at the time $t = 0$ that satisfactorily describe the behavior of the CV line emission in the first regime, are presented in Table 1.

From measurements of the time evolution of the line emission from charge-exchange neutrals during a disruption, it is known that the ion temperature $T_i(t)$ in the rapid phase increases by a factor of 2 at the plasma center ($z = 0$) and by a factor of 4 to 5 at the plasma periphery ($z = 6$ cm) (see above). Such variations in the ion temperature $T_i(t)$ were also taken into account in our simulations. It was assumed that the electron temperature T_e remains constant after it has decreased in the rapid phase of disruption; for example, in the first regime, we have $T_e\ (t > 0) \approx 35$ eV. From the behavior of most of the observed emission lines, it is seen, however, that, after the time $t = 250$ μs, the plasma parameters begin to be restored and the electron temperature T_e increases slightly, ending usually with a new disruption (Fig. 4). In our simulations, these variations in $T_e\ (t > 0)$ and the related series of small disruptions were modeled by choosing the time constant τ_{cx} to be sufficiently large for its effect on the signal shape was equivalent to that of the electron temperature T_e. This allowed us to

Table 1. Model parameters for the first regime

z, cm	n_e, cm^{-3}	ξ_n	$T_e(t)$ before/after disruption	$T_i(t)$ before/after disruption	A_{cx}	τ_{cx}, μs
0	10^{13}	3×10^{-4}	210 eV/35 eV	150 eV/300 eV	80	900
6	3.5×10^{12}	5.6×10^{-4}	1.5 keV/33 eV	25 eV/100 eV	300	700

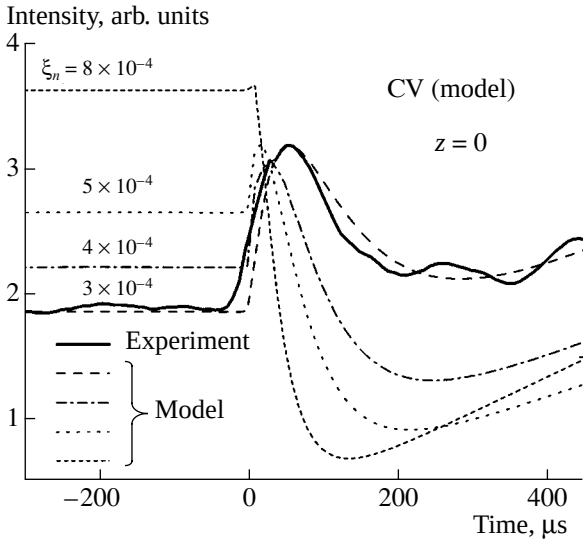

Fig. 12. Simulation of the time evolution of the CV line intensity during a disruption as a function of the relative neutral concentration ξ_n: transition from the evolution in the first regime to the evolution in the second regime and comparison to the data for the first regime ($z = 0$).

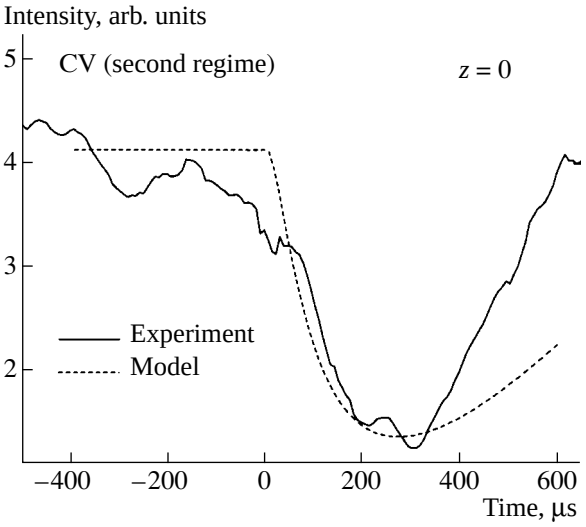

Fig. 13. Comparison of the model to the experiment: the calculated and measured time evolution of the CV line intensity at the plasma center ($z = 0$) during a disruption in the second regime.

substantially simplify the simulations of the signal observed at the end of the rapid phase of disruption ($t \approx 400$ μs). Another parameter that influences the behavior of the emission at these times is the electron density n_e; it is obvious that an increase in the electron density leads to a more rapid decrease in the signal intensity, and vice versa.

Although the simulation results agree well with observations, the main importance of the kinetic model lies not in the quantitative adjustment of the parameters but in its capability of providing a self-consistent description of the behavior of the CV line emission in the first regime, a corresponding description for the second regime, and a description of the CV line emission from the plasma core and plasma edge in both regimes.

From this point of view, the key model parameter that distinguishes between the first and second regimes is the relative concentration ξ_n of the neutral component before the disruption. Figure 12 shows how the CV line emission from the central plasma region evolves when the concentration ξ_n varies from the values typical of the first regime to the values with which the behavior of the CV line emission in the second regime (see Fig. 3) can be reproduced. The general result of the model is a decrease in the CV line emission from the central and/or peripheral plasma regions below its initial level, which is determined by the ξ_n value. From Fig. 12 we can see that the decrease in the intensity below its initial level in the second regime can be reproduced in the model by setting $\xi_n > (4–5) \times 10^{-4}$.

A comparison of the experimental data to the numerical results obtained for the second regime is illustrated in Fig. 13 (for $z = 0$) and Fig. 14 (for $|z| > 1.5$ cm). The parameters of the model, as well as their variations at the time $t = 0$ that satisfactorily describe the behavior of the CV line emission in the second regime, are given in Table 2.

From Tables 1 and 2 we can see that the suprathermal electrons plays an important role in the CV line emission from the plasma edge. In the model, the relevant parameter describes the effective temperature of the suprathermal component of the electron energy distribution function. We also see that the effective electron temperature T_e increases from the plasma center toward the plasma periphery (the relative amount of suprathermal electrons increases accordingly). In the model description of the edge plasma, the effective increase in the initial electron temperature T_e is equivalent to a decrease in the concentration ξ_n; this reduces the initial intensity and leads to a very short rise time of the model signal, followed by a decrease in the signal

Table 2. Model parameters for the second regime

z, cm	n_e, cm^{-3}	ξ_n	$T_e(t)$ before/after disruption	$T_i(t)$ before/after disruption	A_{cx}	τ_{cx}, μs
0	3.3×10^{12}	9×10^{-4}	210 eV/35 eV	140 eV/280 eV	80	600
>1.5	3.2×10^{12}	10^{-3}	1.5 keV/35 eV	100 eV/200 eV	90	600

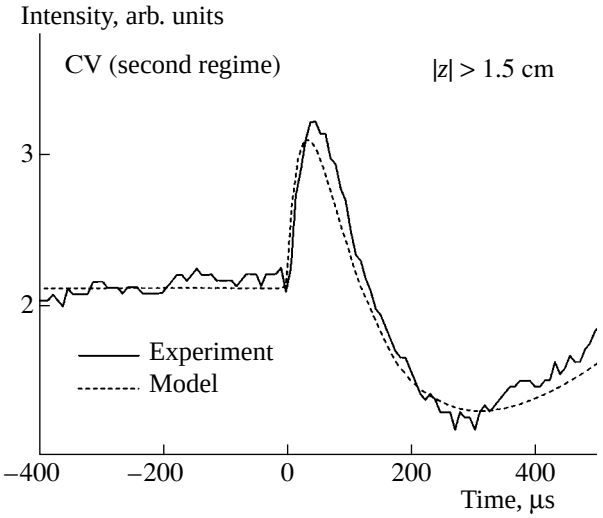

Fig. 14. Comparison of the model to the experiment: the calculated and measured time evolution of the CV line intensity at the plasma periphery ($|z| > 1.5$ cm) during a disruption in the second regime.

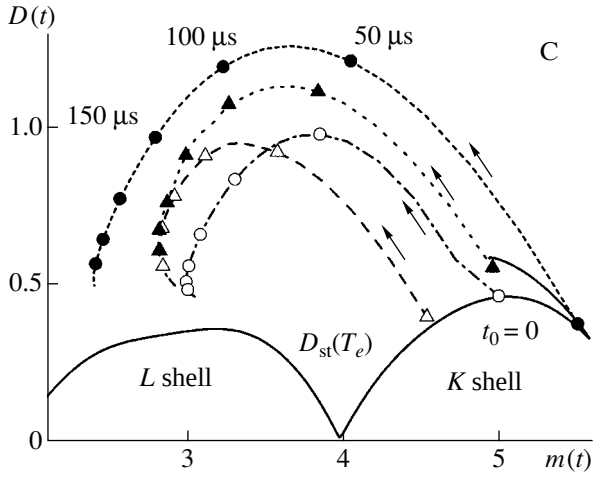

Fig. 15. Time evolution of the dispersion and the average charge of the charge-state distribution of carbon impurity ions (recombination translations) according to the results from simulations of the CV line emission: the open circles (dashed-and-dotted curve) are for the emission from the plasma center ($z = 0$) in the first regime, the closed circles (short dashes) are for the emission from the plasma edge ($z = 6$ cm) in the first regime, the open triangles (dashed curve) are for the emission from the plasma center ($z = 0$) in the second regime, and the closed triangles (dotted curve) are for the emission from the plasma periphery ($|z| > 1.5$ cm) in the second regime. The symbols along every curve show the values of the moments after each 50 μs. For comparison, the solid line shows how the moment $D_{st}(m)$ in coronal equilibrium for $\xi_n = 3 \times 10^{-4}$ varies along the curve of the moments as the electron temperature T_e changes.

intensity below its initial level. At the time at which the intensity of the CV line emission from the plasma periphery is the highest, the ion charge averaged over the charge-state distribution is $m \approx 4$. Note that, by this time ($t \sim 20$ μs), the growing flux of fast neutrals has yet not reach its maximum intensity.

The results of simulations make it possible to describe the temporal evolution of the carbon charge-state distribution during a disruption. The most convenient and illustrative description can be given in terms of the dependence $D(m)$. Each value of this function corresponds to a certain time t and an instantaneous carbon charge-state distribution in the plasma. In this way, the time evolutions $D(t)$ and $m(t)$ can conveniently be compared to their kinetic (or coronal) values or to the corresponding function $D_{st}(m)$.

Figure 15 shows the time evolution of the moments $D(m)$ of the carbon charge-state distribution function that were obtained in numerical simulations of the behavior of the CV line emission from the plasma center ($z = 0$) and from the plasma periphery ($z = 6$ cm and $|z| > 1.5$ cm) during a disruption in both of the regimes under investigation. For comparison, Fig. 15 also shows the calculated steady-state curve $D_{st}(m)$. Each point in this curve corresponds to a certain value of the electron temperature T_e rather than to a certain time, as in the case of curves $D(m)$. The curve $D_{st}(m)$ was computed for $\xi_n = 3 \times 10^{-4}$. When the effect of charge-exchange recombination on the steady-state dispersion is taken into account, the function $D_{st}(m)$ acquires a recombination branch (see [8] for details) and thereby becomes two-valued. The distributions that describe the interaction of suprathermal plasma electrons (having a high effective temperature, which, in the case at hand, is $T_e \sim 1.5$ eV) with impurities lie on this recombination branch of the function $D_{st}(m)$. The symbols along every curve $D(m)$ show the positions of the center of the charge-state distribution after each 50 μs. The closed and open symbols illustrate the time evolution of the charge-state distributions at the plasma edge and in the plasma core, respectively. Since the CV line emission at the periphery is dominated by suprathermal electrons, the initial values of m there are larger than those in the plasma core.

From Fig. 15 we see that the dispersion $D(m)$ of the charge-state distribution function increases substantially and very rapidly (over a time of about 50 μs) and the distribution center shifts rapidly toward the radiation barrier region ($m < 4$). This indicates that the radiative energy losses over the entire cross section of the plasma column become very great (see above).

6. CONCLUSIONS

In the DAMAVAND tokamak, chord measurements of the CV line emission in the rapid phase of disruption were carried out in two regimes. In the first regime (with a high plasma current), a burst of CV line emission was detected along all the viewing chords. In the second regime, the intensity of emission from the plasma core and plasma periphery was observed to decrease below its initial (predisruption) level. The

observed burst of CV line emission and the subsequent decrease of its intensity can only be attributed to very abrupt variations in the parameters describing the emission from impurities in the rapid phase of disruption.

An analysis of the ionization kinetics of a neutral carbon that could instantly penetrate from the chamber wall into the plasma column has showed that, for any more or less realistic values of the plasma parameters, the fairly rapid increase in the CV emission signal in both regimes, as well as the subsequent rapid decrease in the signal intensity below its initial level, cannot be explained in terms of a dynamic model. On this basis, we have concluded that the behavior of impurities during a disruption is, on the whole, dominated by recombination (rather than ionization) processes.

In order to interpret the observations, we have developed a kinetic model of the evolution of the carbon charge-state distributions during a disruption. The results of calculating temporal variations in the carbon charge-state distributions due to an increase in the effective recombination rate have been compared to the data from measurements of the CV line emission during a disruption. The model description of the time evolution of the CV line emission in the rapid phase of the major disruption in both regimes agrees well with experimental observations.

A key result of the proposed model is a relative increase in the effective rate of charge exchange of impurity ions by two orders of magnitude. The parameter that makes it possible to distinguish between the two regimes under consideration in describing the CV line emission during a disruption is the initial relative concentration of neutral particles: $\xi_n = 3 \times 10^{-4}$ in the first regime with a high plasma current, and $\xi_n > 5 \times 10^{-4}$ in the second regime with a low plasma current. In order to describe variations in the CV line emission from the plasma edge, it is also necessary to take into account the behavior of the suprathermal component of the electron energy distribution function. The predictions of the kinetic model proposed here agree qualitatively with the measurements and interpretations of the temporal behavior of the X-ray spectra from the plasma in the rapid phase of disruption in the TVD tokamak [13].

An experimental evidence for the substantial variations in the rates of charge exchange of both the main plasma component and the impurities is provided by a short rise time (20–50 μs) of the neutral flux that grows in the rapid phase of disruption and by an increase in its intensity by more than two orders of magnitude.

A consequence of the above processes of charge-state kinetics of plasma impurities in the rapid phase of disruption is the considerable increase in the dispersion of the carbon charge-state distribution and the transition of all of the carbon impurity in the plasma to the radiation barrier region over a time of about 50 μs; in this case, the center of the charge-state distribution (i.e., the average charge m of the carbon impurity) shifts from the range $m \geq 4$ into the range $m < 4$. Hence, the rapid phase of disruption is dominated by recombination processes, specifically, by the dominant recombination translation of the charge-state distribution of the carbon ions into the radiation barrier region. In order to investigate such a translation, it is very important to thoroughly examine the emission from helium-like states of light impurity ions.

ACKNOWLEDGMENTS

We are grateful to V.E. Zhogolev for providing us with subroutines for calculating the rates of atomic processes.

REFERENCES

1. D. J. Ward and J. A. Wesson, Nucl. Fusion **32**, 1117 (1992).
2. E. D. Fredrickson, K. M. McGuire, M. G. Bell, *et al.*, Nucl. Fusion **33**, 141 (1993).
3. R. G. Kleva and J. F. Drake, Phys. Fluids B **3**, 372 (1991).
4. S. V. Mirnov, A. M. Belov, D. Yu. Prokhorov, *et al.*, Preprint No. 0081-A, Troitsk Institute for Innovation and Fusion Research (TsNIIatominform, Troitsk, 2001).
5. C. Breton, A. Compant la Fontaine, and C. D. Michelis, J. Phys. B **16**, 2627 (1983).
6. O. Demokan, F. Waelbroek, and N. Demokan, Nucl. Fusion **22**, 921 (1982).
7. A. N. Zinov'ev and V. V. Afrosimov, in *Plasma Diagnostics*, Ed. by M. I. Pergament (Énergoatomizdat, Moscow, 1990), p. 56.
8. V. A. Shurygin, Fiz. Plazmy **30**, 483 (2004) [Plasma Phys. Rep. **30**, 443 (2004)].
9. A. V. Bortnikov, N. N. Brevnov, Yu. V. Gott, *et al.*, Fiz. Plazmy **21**, 672 (1995) [Plasma Phys. Rep. **21**, 634 (1995)].
10. E. Farshi, N. N. Brevnov, A. V. Bortnikov, *et al.*, Phys. Plasmas **8**, 3587 (2001).
11. R. Amrollakhi, I. Farshi, N. N. Brevnov, *et al.*, Fiz. Plazmy **28**, 579 (2002) [Plasma Phys. Rep. **28**, 535 (2002)].
12. A. Ejiri, S. Shiraiwa, Y. Takase, *et al.*, Nucl. Fusion **43**, 547 (2003).
13. V. A. Shurygin, Fiz. Plazmy **22**, 1075 (1996) [Plasma Phys. Rep. **22**, 975 (1996)].
14. TFR Group, Nucl. Fusion **25**, 981 (1985).
15. D. Pasini, M. Mattioli, A. W. Edwards, *et al.*, Nucl. Fusion **30**, 2049 (1990).
16. D. S. Gray, E. M. Hollmann, D. G. Whyte, *et al.*, in *Proceedings of the 30th EPS Conference on Controlled Fusion and Plasma Physics, St. Petersburg, 2003*, ECA **27A**, Paper P-4.91.
17. V. A. Shurygin, Plasma Phys. Controlled Fusion **41**, 355 (1999).
18. V. I. Gervids, A. G. Zhidkov, V. S. Marchenko, and S. I. Yakovlenko, in *Reviews of Plasma Physics*, Ed. by B. B. Kadomtsev (Énergoatomizdat, Moscow, 1982; Consultants Bureau, New York, 1987), Vol. 12.

19. V. A. Abramov and G. I. Krotova, Fiz. Plazmy **10**, 684 (1984) [Sov. J. Plasma Phys. **10**, 395 (1984)].
20. L. A. Vaĭnshteĭn and V. P. Shevel'ko, in *Structure and Properties of Ions in a Hot Plasma* (Nauka, Moscow, 1986) [in Russian].
21. TFR Group, Nucl. Fusion **25**, 919 (1985).
22. G. Waidmann and Kuang Guangli, Nucl. Fusion **32**, 645 (1992).
23. V. A. Bazylev and M. I. Chibisov, Fiz. Plazmy **5**, 584 (1979) [Sov. J. Plasma Phys. **5**, 327 (1979)].
24. Yu. V. Gott and V. A. Shurygin, Preprint No. IAE-5404/7 (Kurchatov Inst. of Atomic Energy, Moscow, 1991).
25. D. E. Post and R. V. Jensen, At. Data Nucl. Data Tables **20**, 397 (1977).
26. W. Lotz, Z. Physik **216**, 241 (1968).
27. V. A. Abramov, V. S. Lisitsa, and A. Yu. Pigarov, Pis'ma Zh. Éksp. Teor. Fiz. **42**, 288 (1985) [JETP Lett. **42**, 356 (1985)].
28. V. A. Shurygin, in *Proceedings of the 30th EPS Conference on Controlled Fusion and Plasma Physics, St. Petersburg, 2003*, ECA **27A**, Paper P-3.156.

Translated by G.V. Shepekina

Plasma Physics Reports, Vol. 31, No. 6, 2005, pp. 452–461. Translated from Fizika Plazmy, Vol. 31, No. 6, 2005, pp. 496–505.

STELLARATORS

Effect of Vacuum Chamber Boronization on the Plasma Parameters in the L-2M Stellarator

A. I. Meshcheryakov*, D. K. Akulina*, G. M. Batanov*, M. S. Berezhetskiĭ*, G. S. Voronov*, G. A. Gladkov*, S. E. Grebenshchikov*, V. A. Grinchuk*, I. A. Grishina*, L. V. Kolik*, N. F. Larionova*, A. A. Letunov*, V. P. Logvinenko*, A. E. Petrov*, A. A. Pshenichnikov*, G. A. Ryabenko*, K. A. Sarksyan*, N. N. Skvortsova*, O. I. Fedyanin*, N. K. Kharchev*, Yu. V. Khol'nov*, and V. M. Sharapov**

**Prokhorov Institute of General Physics, Russian Academy of Sciences, ul Vavilova 38, Moscow, 119991 Russia*

***Institute of Physical Chemistry, Russian Academy of Sciences, Leninskiĭ pr. 31, Moscow, 117071 Russia*

Received July 19, 2004; in final form, November 18, 2004

Abstract—After boronization of the vacuum chamber of the L-2M stellarator, radiative losses from ohmically and ECR heated plasmas were reduced by a factor of 3–4. Under these conditions, radiative losses in the ECRH regime comprise only 10–15% of the input microwave power. Some effects have been detected that were not observed previously: a substantial increase in the gradient of the electron temperature near the separatrix, a preferentially outward-directed radial turbulent particle flux (both throughout the discharge phase and from shot to shot), and a longer (by a factor of 2–3) duration of the plasma cooling phase. © *2005 Pleiades Publishing, Inc.*

1. INTRODUCTION

Experiments on the production and electron cyclotron resonance heating (ECRH) of plasmas in the L-2M stellarator have been carried out over a fairly long time [1]. A characteristic feature of these experiments is an unsurpassed specific heating power [2]. Under these conditions, the energy flux onto the wall of the vacuum chamber increases substantially; moreover, this flux is distributed nonuniformly over the wall surface, being concentrated mainly near the separatrix corners. It is well known that recycling leads to the generation of a neutral flux from the chamber wall. This flux consists of atoms and molecules of both the working gas (usually, hydrogen) and impurities (carbon, oxygen, etc.). The increase in the impurity concentration in the plasma leads to an increase in radiative losses and a decrease in the electron temperature [3]. In some L-2M experiments carried out at a high ECRH power ($P_{\mathrm{ECRH}} >$ 300 kW), a substantial increase in radiative losses could eventually lead to radiative collapse. For this reason, it was necessary to reduce the impurity flux into the plasma in those experiments.

Conventional conditioning of the stellarator chamber wall is performed by means of inductive and glow discharges. In the former case, a hydrogen plasma with a temperature of T_e = 0.1–1 eV is produced in a weak magnetic field B = 0.03 T with the help of an ohmic-heating transformer. Glow discharges in noble gases (helium or argon) are excited with the help of an anode inserted into the chamber and maintained at a potential of U = 400 V. In both cases, the chamber wall is heated up to 150–200°C. These methods were usually employed sequentially; this allowed us to improve the wall conditions in the stellarator chamber and to reduce the impurity flux from the wall. Nevertheless, radiative losses remained substantial and the plasma density increased during the discharge.

Deposition of boronized carbon films in glow discharges was first successfully employed in the TEXTOR tokamak [4]. A similar boronization procedure was applied to the W7-AS stellarator; As a result, the line intensities of low-Z impurities (C, O) decreased by one order of magnitude [5]. Real-time boronization was investigated in the CHS stellarator and was found to be a promising method for conditioning the chamber wall in the LHD stellarator [6].

The first boronization experiments in the TEXTOR tokamak were carried out with B_2H_6, which is a very toxic and flammable gas. Further, less toxic agents (such as $B(CH_3)_3$ and $B(C_2H_5)_3$) were used. However, these agents too are dangerous because they form explosive mixtures with air [7]. Later, specialists from the Institute of Physical Chemistry of the Russian Academy of Sciences proposed that carborane ($C_2B_{10}H_{12}$) be used for boronization [8]. Carborane is a nontoxic and nonexplosive powder that is readily evaporated at a temperature of 60–80°C. A simple and safe procedure of boronization with carborane was then successively used in T-11M, T-3M, T-10, and Tuman-3

1063-780X/05/3106-0452$26.00 © 2005 Pleiades Publishing, Inc.

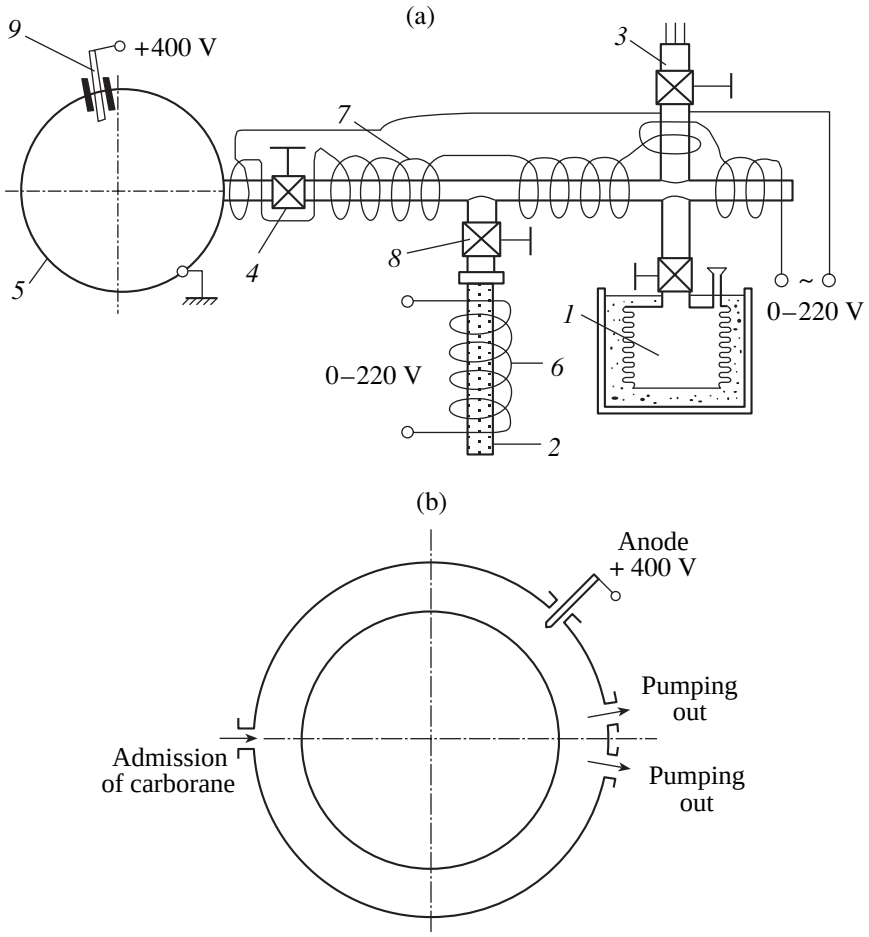

Fig. 1. (a) Schematic of the boronization chamber for the admission of carborane vapor into the L-2M stellarator: (*1*) silica gel pump, (*2*) cell with carborane, (*3*) thermocouple pressure gauge, (*4*) valve separating the boronization chamber from the stellarator, (*5*) stellarator chamber, (*6*, *7*) heating spirals; (*8*) valve controlling the carborane flux; and (*9*) glow discharge anode; (b) the arrangement of the pump-out flanges, the carborane admission system, and the glow discharge anode in the vacuum chamber of the stellarator (top view).

tokamaks [9]. A similar procedure is now regularly used in the L-2M stellarator.

2. BORONIZATION PROCEDURE

We designed and mounted an auxiliary (boronization) chamber that ensured continuous admission of carborane vapor during the boronization of the stellarator vacuum chamber (Fig. 1a). The boronization chamber consists of silica gel pump *1*; glass cell *2*, filled with carborane powder; and thermocouple pressure gauge *3*. Valve *4* separates the boronization chamber from stellarator chamber *5*. The boronization chamber was preevacuated to a pressure of $p = 2 \times 10^{-2}$ torr. Cell *2* was then heated by spiral *6* to a temperature of 60–80°C, and the carborane vapor pressure increased to $p = 1.5$ torr. The flux of carborane vapor into the stellarator chamber was controlled by valve *8*. The concentration of carborane vapor inside the stellarator chamber was monitored with the help of a thermocouple pressure gauge. To avoid the condensation of carborane vapor onto the wall of the boronization chamber, it was heated by spiral *7* to a temperature of 110–120°C.

A glow discharge in the stellarator chamber filled with a mixture of carborane vapor with helium was produced by applying a voltage of $U_a = +400$ V to anode *9*. The discharge current was $I_a = 1$ A, the pressure in the stellarator chamber was maintained at a level of $p_0 = 2 \times 10^{-3}$ torr, and the chamber was heated to a temperature of 150–190°C. During the glow discharge, the camber wall became coated with a borocarbon film. The process usually lasted for 0.5–1 h. Figure 1b shows the arrangement of the carborane admission system, the glow discharge anode, and the flanges for evacuating the stellarator vacuum chamber.

Since there was no lock chamber for taking a coated sample, we were unable to study the composition and thickness of the deposited borocarbon film. Neverthe-

Table 1

Atomic/molecular mass, amu	Resonance frequency, MHz	Composition of the residual gas	Relative peak intensity in the mass spectrum, arb. units	
			before boronization	after boronization
2	2295	H_2	1.0	0.9
4	1148	He	0.2	0.2
14	333	N	1.4	1.3
16	290	O	0.4	0.2
17	279	HO	0.6	0.0
18	256	H_2O	2.1	0.1
20	230	Ne	0.1	0.1
28	165	N_2	6.2	5.2
32	145	O_2	1.2	0.6
40	119	Ar	0.3	0.3
44	110	CO_2	0.2	0.1
54–56	82	?	0.0	0.1
70–72	65	?	0.0	0.3
136	35	$C_2B_{10}H_{12}$	0.0	0.4

less, the quality of boronization can be judged from the parameters of the plasma produced. Boronization (if successful) led to a significant (severalfold) decrease in the intensities of impurity lines and, accordingly, radiative losses.

An appreciable improvement of the discharge parameters was observed after five to six shots following the boronization procedure. The operating conditions remained stable and discharges were well reproducible over 150–180 shots (three to five workdays); after this period, the borocarbon coating gradually deteriorated.

The composition of the residual gas in the stellarator chamber changed substantially after boronization. This composition was quantitatively analyzed with the help of an IPDO-2 omegatron, measuring the partial gas pressure. The mass spectra of the residual gas before and after boronization are given in Table 1.

Boronization most strongly affected the content of water vapor and oxygen. After successful boronization, water vapor was almost absent in the spectrum, and the oxygen content halved. The mass spectrum showed the peaks of carborane vapor $C_2B_{10}H_{12}$ (136 amu) and gases with masses of 54–56 amu and 70–72 amu, which were presumably the disintegration products of carborane. The peaks related to the presence of carborane in the chamber were usually observed over three to six days after boronization and then gradually disappeared.

When choosing the optimum boronization conditions, the basic criterion was a considerable (severalfold) decrease in the intensities of oxygen and carbon lines and in the total radiative loss in stellarator shots. It was found that, when the carborane content in the glow discharge was lower than 20%, the quality of the deposited film was insufficient to significantly improve the plasma parameters, even when the boronization time was increased to 60 min. In this case, radiative losses from the ohmically heated plasma decreased insignificantly (by 30–40%) in comparison to discharges without preliminary boronization. When the carborane content in the gas mixture exceeded 25%, radiative losses decreased to the required level; in this case, the boronization time was reducable to 30 min. The optimum boronization conditions in L-2M were achieved at an initial carborane vapor concentration of 40%, a gas pressure of 2×10^{-3} torr, a glow-discharge current of 0.7–0.8 A, and a boronization time of 30–40 min.

3. EXPERIMENTS IN OHMIC-HEATING DISCHARGES

The parameters of the ohmically heated plasma changed substantially after boronization. Table 2 presents the main discharge and plasma parameters before and after boronization. Note that boronization most strongly affects the intensities of impurity lines and the total radiative loss. The decrease in the intensity of oxy-

Table 2. Plasma parameters in ohmic-heating discharges before and after boronization

Parameter	Before boronization	After boronization
Plasma current I_p, kA	17–19	17–19
Loop voltage U_1, V	4–4.5	2–2.5
Radiative power loss P_{rad}, kV	40–50	8–12
Intensity of oxygen lines I_O, arb. units	4–5	1
Intensity of carbon lines I_C, arb. units	3–4	1
Average plasma density n_e, 10^{19} m^{-3}	0.8–1.4	0.9–1.1
Central electron temperature T_e, eV	280	310

gen lines by a factor of 4–5 and in the intensity of carbon lines by a factor of 3–4 indicates a considerable decrease in the impurity concentration in the plasma. As a result, the radiation power measured by a bolometer decreased to ~10 kW. At the same plasma current, the loop voltage almost halved. The decrease in the loop voltage after boronization is explained by the low impurity concentration in the plasma and, accordingly, the low values of the effective ion charge number Z_{eff}.

It should be noted that boronization also affects the time evolution of the plasma density, plasma radiation, and loop voltage. The working gas (hydrogen) was fed into to the stellarator 40 ms before the beginning of ohmic heating. The initial plasma density is determined by gas puffing, whereas the time evolution of the plasma density is governed by the relation between the neutral flux from the chamber wall and the flux of plasma particles onto the wall. Without boronization, the plasma density steadily increased, radiative losses increased, the plasma current decreased, and the loop voltage increased during a discharge. Boronization allowed us to achieve a quasi-steady discharge with a time-independent plasma density, plasma current, and radiative losses at a somewhat decreasing loop voltage. The low loop voltage made it possible to save volt–seconds of the transformer (its resource is 0.18 V s) and to increase the duration of the plasma current pulse from 25 to 50 ms.

In spite of the threefold decrease in radiative losses after boronization, the central electron temperature increased insignificantly. This can be attributed to the lower heating power (P_{OH} = 35–45 kW) in comparison to discharges without boronization (P_{OH} = 65–80 kW).

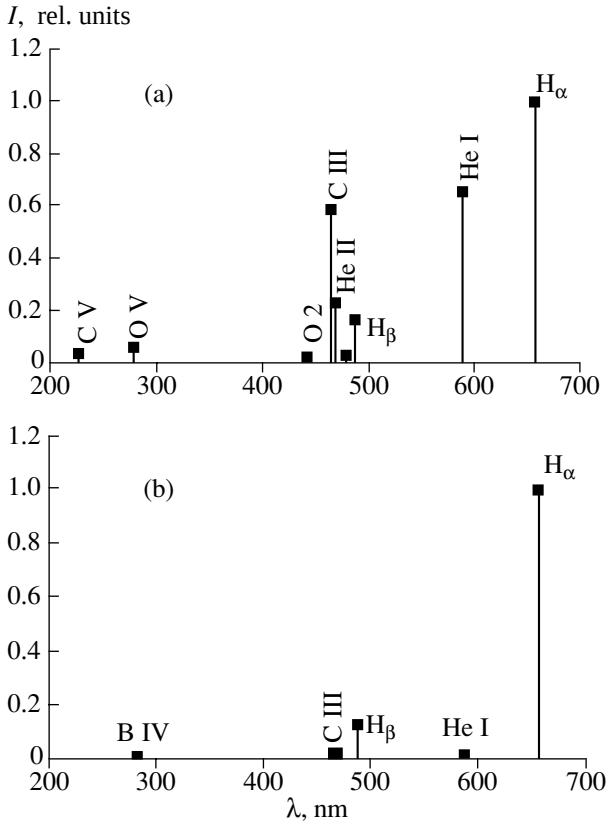

Fig. 2. Plasma radiation spectra in the wavelength range of 200–700 nm: (a) before and (b) after boronization.

4. EXPERIMENTS WITH ECRH DISCHARGES

The currentless plasma was produced and heated by microwave radiation at the second harmonic of the electron gyrofrequency. The duration of the heating pulse was 10 ms, and the microwave power was varied in the range 100–250 kW.

In ECRH discharges (like in ohmic-heating discharges), the intensities of impurity lines substantially decreased after boronization. Figure 2 compares the plasma radiation spectra observed in the wavelength range of 200–700 nm in ECRH discharges without (Fig. 2a) and with (Fig. 2b) boronization. It can be seen that the oxygen lines disappear and the carbon lines are reduced substantially. After boronization, the spectrum consists essentially of the spectral lines of the working gas (hydrogen).

As was noted above, the initial plasma density is determined by gas puffing, whereas the time evolution of the plasma density is governed by the neutral flux from the chamber wall; i.e., it depends on the plasma–wall interaction. Without boronization, the plasma density always increased during the microwave pulse (Fig. 3a) and the spectrum was dominated by the oxygen and carbon lines (Fig. 3b), whose intensities increased steadily in the active phase of the discharge. Radiative losses also increased and, in some shots, reached 50–70% of the heating power (Fig. 3c).

After boronization, the intensities of oxygen lines decreased by a factor of 4–5 and the intensities of carbon lines decreased by a factor of 3–4 (Fig. 4b). The total radiative losses were reduced by a factor of 3–4 (Fig. 4c) and comprised no more than 10–15% of the heating power. The intensity of the soft X-ray (SXR) continuum with photon energies in the range of 1.2–8 keV (measured by a KEVEX X-ray spectrometer) also decreased by a factor of 3–5.

Boronization substantially affected the time evolution of the plasma density. At a relatively low microwave heating power (P_{ECRH} = 100–200 kW), the line-averaged plasma density varied only slightly during the microwave pulse and over 8–10 ms after it, while the plasma energy was sufficient to ionize neutrals arriving from the chamber wall (Fig. 4a). In discharges with a higher heating power (P_{ECRH} = 200–350 kW), the line-averaged density somewhat decreased during the microwave pulse and slightly increased after it; in this case too, the plasma began to decay 8–10 ms after the microwave pulse. Multichord interferometric measure-

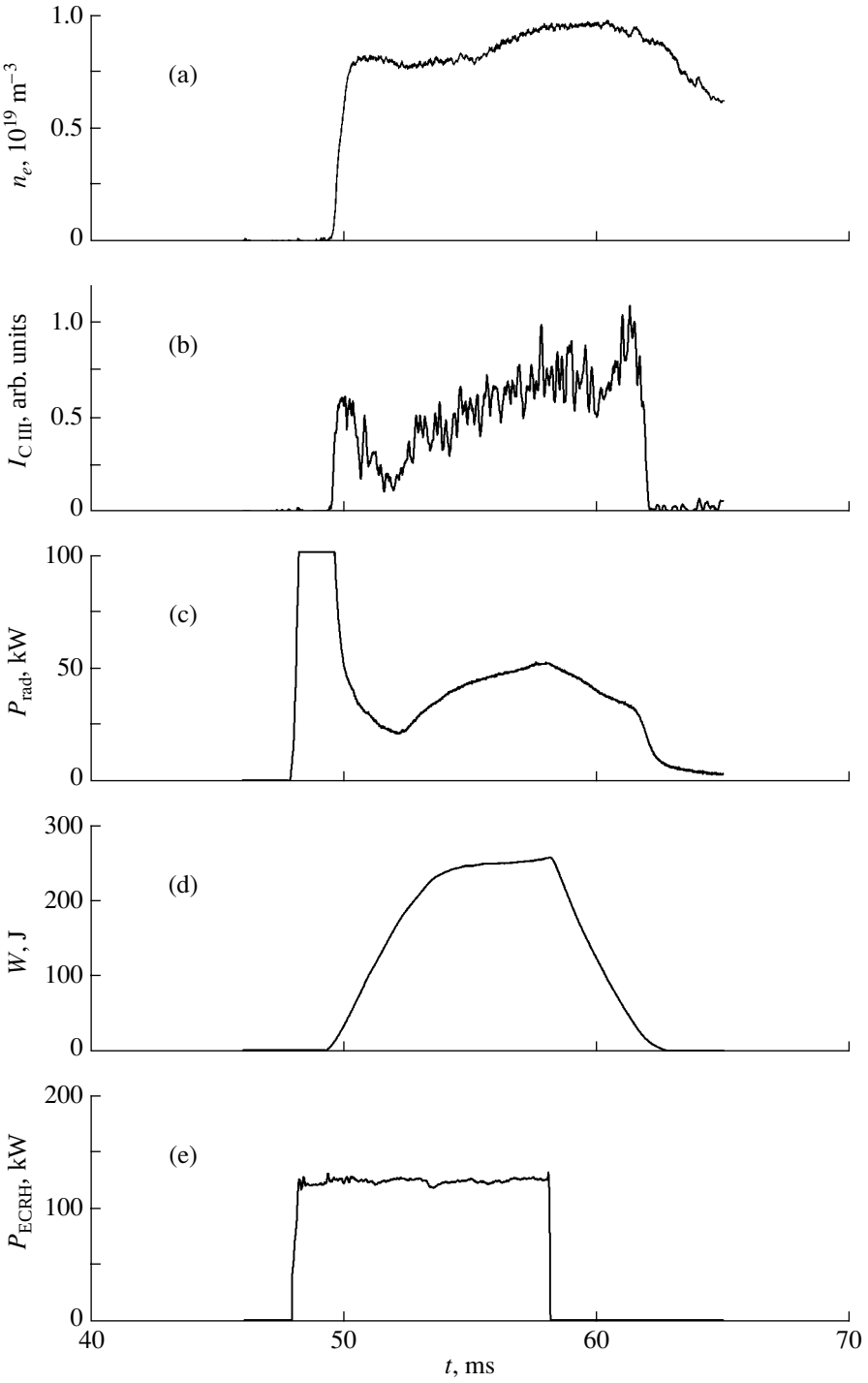

Fig. 3. Discharge parameters before boronization (shot no. 47734): (a) line-averaged plasma density, (b) intensity of the C III line, (c) radiation power, (d) plasma energy, and (e) microwave power.

ments showed that such behavior of the line-averaged plasma density before the decay phase was related to the rearrangement of the radial density profile, while the total number of the plasma particles did not change. The plasma density in the quasi-steady phase of the discharge could be controlled over a wide range ($n_e = (0.3–3.0) \times 10^{19}$ m^{-3}) with the help of a pulsed valve.

The radial profile of the electron temperature in L-2M was measured using four diagnostics: SXR spectrometry with the use of foils, measurements of the

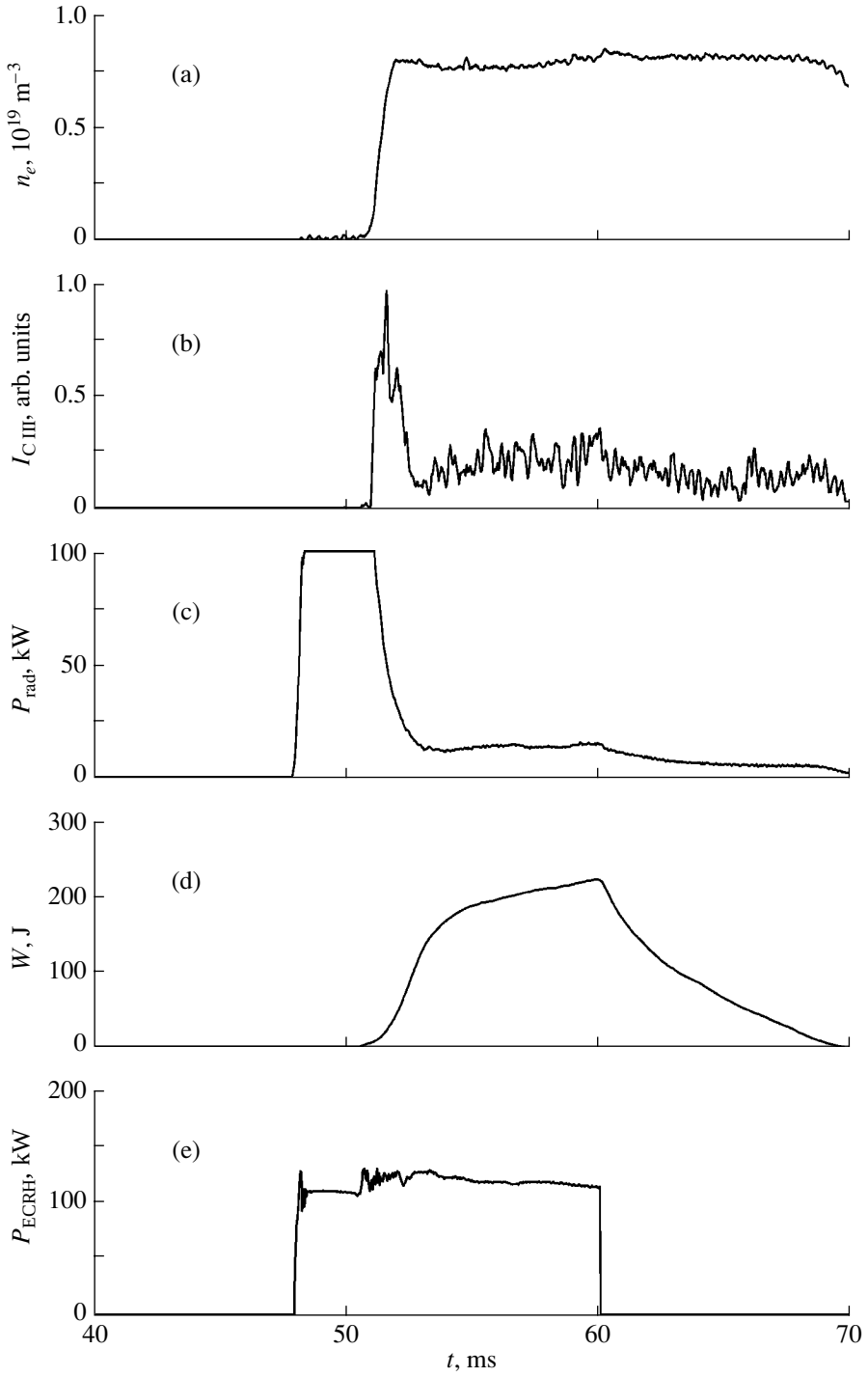

Fig. 4. Discharge parameters after boronization (shot no. 53292): (a) line-averaged plasma density, (b) intensity of the C III line, (c) radiation power, (d) plasma energy, and (e) microwave power.

electron cyclotron emission (ECE) at the second harmonic of the electron gyrofrequency, optical spectroscopy, and Langmuir probes. Each of these diagnostics measured a certain segment of the radial profile: the ECE and SXR diagnostics measured the plasma density in the plasma core ($0 < r/a < 0.6$, where r is the average radius of the elliptical magnetic surface and $a = 11.5$ cm is the average radius of the last closed magnetic surface); the optical spectroscopy covered the outer region of the plasma column ($0.5 < r/a < 0.95$); and Langmuir

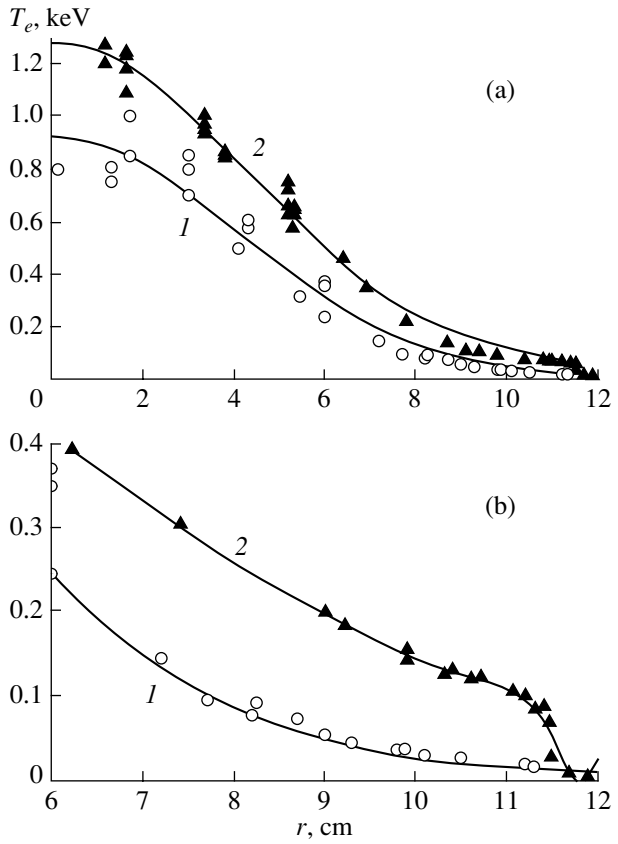

Fig. 5. Radial profiles of the electron temperature (a) over the entire plasma column and (b) at the plasma periphery (*1*) before and (*2*) after boronization.

probes measured the plasma temperature near the plasma boundary, where $T_e < 30$ eV. The entire profiles of the electron temperature in discharges with and without boronization are shown in Fig. 5a. It can be seen that, after boronization, the central electron temperature increased from 950 to 1250 eV, i.e., by nearly 30%. The relative increase in T_e was maximal near the plasma boundary (at $r = 11.5$ cm), where the electron temperature increased from 10–20 eV to ~100 eV (Fig. 5b). Before boronization, the main impurities were carbon and oxygen. Radiative cooling caused by emission from carbon and oxygen ions made the dominant contribution to the heat transport near the plasma boundary. In this case, the electron temperature at the plasma periphery was stabilized at a level of $T_e \sim 10$–20 eV, at which the radiation intensity of carbon and oxygen ions was maximal.

After boronization, the flux of carbon and oxygen from the chamber wall decreased severalfold; accordingly, radiative losses also decreased. As a result, the electron temperature at the plasma periphery increased to ~100 eV and a jump in T_e formed near the separatrix (at radii of $r = 11.5 \pm 0.2$ cm); i.e., a narrow ($\Delta r/a < 0.05$) layer with a very large temperature gradient occurred in the separatrix region. In discharges with preliminary boronization, such a layer was always present over a wide range of the microwave power and plasma density. The magnitude of the temperature jump was 100–150 eV. Previous probe measurements showed that the plasma density changed abruptly in the separatrix region by two orders of magnitude [10].

Local turbulent fluxes were measured using three single probes.[1] The probes measured plasma density fluctuations (in the regime of ion saturation current) and fluctuations of the floating potential. From these measurements, we calculated the turbulent radial particle flux. The sampling rate of probe signals was 1–5 MHz, and the length of the data arrays was 128 kB. Figures 6a and 6b show the results of measurements of the local turbulent flux before and after boronization, respectively. It can be seen that, before boronization, the flux is not unidirectional (positive and negative values in the figure correspond to an outward and an inward flux, respectively). The prevailing direction of the flux can be deduced from the sign of its asymmetry coefficient[2] calculated over reasonable time intervals (~1 ms). The asymmetry coefficient of the flux presented in Fig. 6a changes its sign during a discharge. After boronization, the probability density function of the local flux was found to be highly asymmetric: the asymmetry coefficient was positive and did not change its sign during a discharge. This corresponds to a turbulent flux directed predominantly toward the chamber wall. In this case, the probability density function of the flux magnitudes differed substantially from a normal (Gaussian) distribution throughout the entire discharge (Fig. 7).

Boronization had a substantial impact on the plasma cooling phase. Here, by the cooling phase we mean the discharge phase that begins after the ECRH pulse and continues to the total plasma cooling (which corresponds to the zero diamagnetic signal). The plasma density in the cooling phase (60–70 ms) changed insignificantly (see Fig. 4a), whereas the electron temperature measured from the ECE intensity steadily decreased. Note that the nested structure of the magnetic surfaces in the stellarator is created by external conductors only and is retained after the heating pulse is switched off. A comparison between Figs. 3 and 4 shows that, after boronization, the duration of the plasma cooling phase increases by a factor of 2–3 (from 3–4 to 8–10 ms). Evidently, the longer cooling time is due to a decrease in the radiation power and, accordingly, in the total power loss from the plasma.

[1] The local particle flux is defined as $\Gamma = (\delta n_e \delta v_r)$, where δn_e is a plasma density fluctuation and δv_r is a radial velocity fluctuation.

[2] Here, we are dealing just with the sign of the normalized asymmetry coefficient rather than with the difference between the local inward and outward fluxes, $M_3 = \frac{1}{N}\sum_{j=1}^{N}\left[\frac{\Gamma_j - \bar{\Gamma}}{\sigma}\right]^3$ (notation is standard).

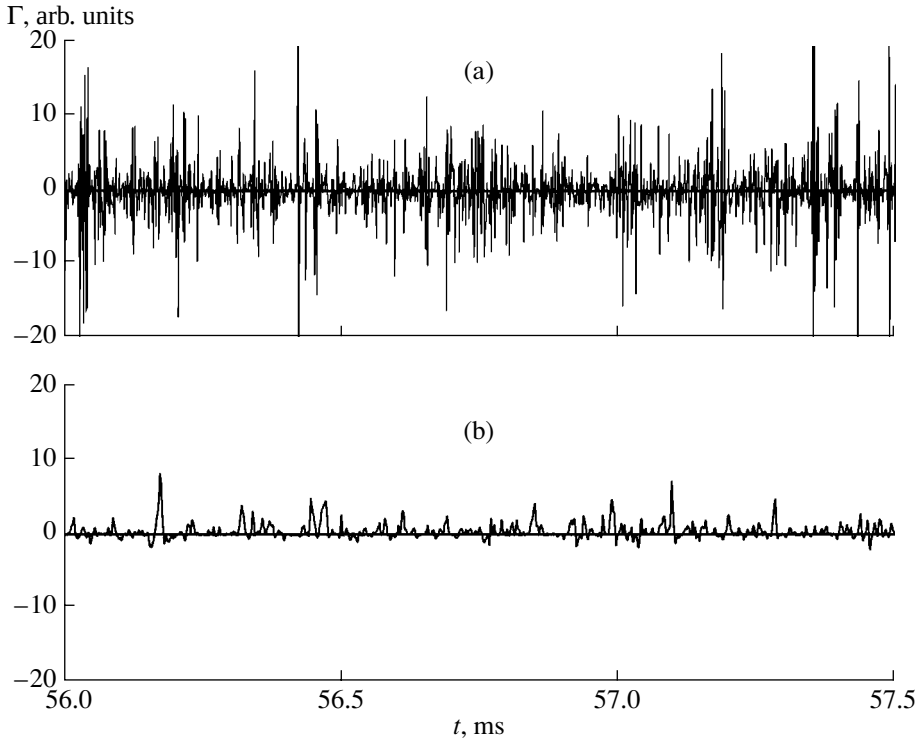

Fig. 6. Time evolution of the turbulent flux in the quasi-steady phase of the discharge (a) before boronization (shot no. 44487) and (b) after boronization (shot no. 53168).

The total power loss P_{loss} from the plasma can be derived from the global plasma energy balance equation

$$dW/dt = P_{ECRH} - P_{loss}. \quad (1)$$

After the microwave pulse is switched off ($P_{ECRH} = 0$), the energy balance equation takes the form

$$P_{loss} = -dW/dt. \quad (2)$$

Figure 8 shows the total power loss P_{loss} calculated by formula (2) from the diamagnetic signal (curve *1*) and the radiation power measured by a bolometer (curve *2*) in the cooling phase of discharges without (Fig. 8a) and with (Fig. 8b) preliminary boronization. It should be noted that, in the early cooling phase (over 0.5 ms after the heating pulse is switched off), the diamagnetic signal dW/dt is somewhat distorted because the eddy currents induced in the chamber wall contribute to the diamagnetic signal measured by a loop located outside the chamber. It can be seen that, 0.5 ms after the heating pulse is switched off, the total power loss is nearly the same in both discharges and amounts to 70–80 kW, whereas radiative losses are substantially different. In discharges without boronization, radiative losses comprise about 2/3 of the total power loss, whereas in discharges with boronization, this ratio is as low as 1/5. Hence, after boronization, radiative losses comprise only a small fraction of the total losses not only in the active phase, but also over 2–3 ms in the early cooling phase.

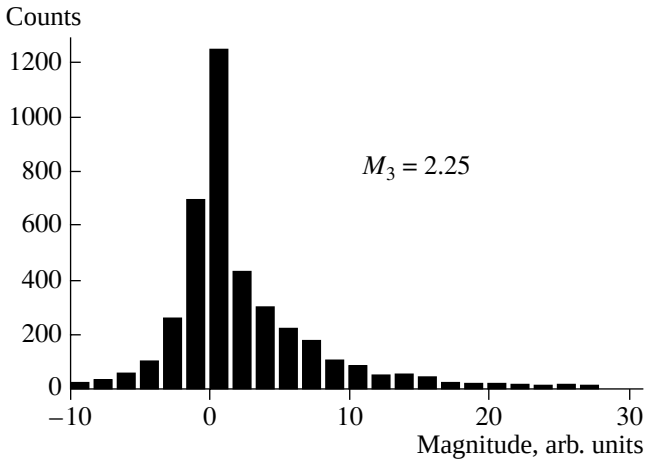

Fig. 7. Probability density function of the magnitudes of the local particle flux after boronization.

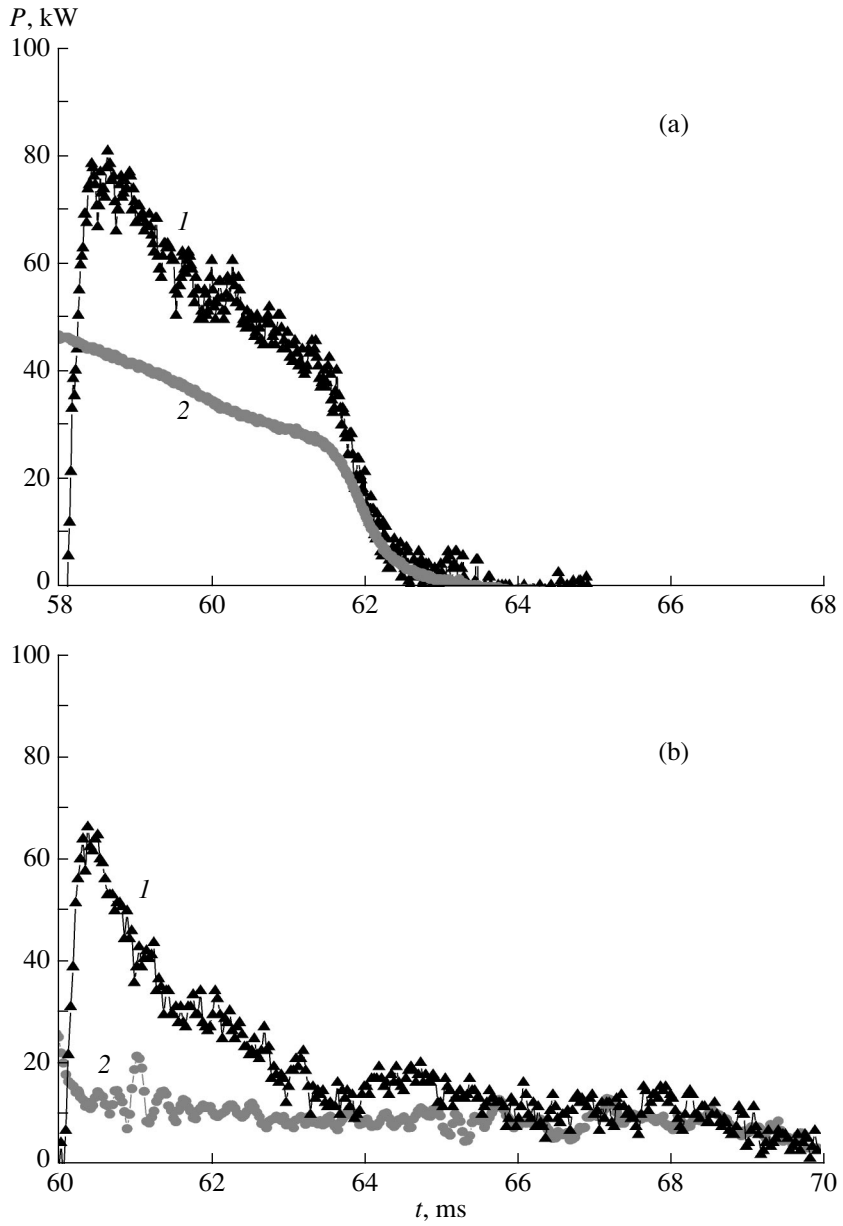

Fig. 8. Time evolution of the (*1*) total power loss and (*2*) radiative power loss in the cooling phase (a) before boronization (shot no. 47734) and (b) after boronization (shot no. 53292).

5. CONCLUSIONS

Boronization of the L-2M vacuum chamber has made it possible to substantially reduce radiative losses in both ohmically and ECR heated plasmas. Radiative losses in ECRH experiments do not exceed 10–15% of the input power. Note that, by the end of the ECRH pulse, radiative losses in discharges without boronization reach 50–70% of the heating power.

Boronization of the stellarator chamber wall allowed us to extend the operating density range to $n_e = (0.3–2.8) \times 10^{19}$ m^{-3} in ECRH experiments with an input power of $P_{\mathrm{ECRH}} = 300$ kW. Moreover, boronization made it possible to maintain the plasma density at a constant level during the heating pulse and also ensured the high reproducibility of discharges.

A substantial decrease in radiative losses has led to new effects. In our opinion, of great importance is that heat transport in the edge plasma changes its character: a large gradient of the electron temperature appears near the separatrix, where the temperature increases by 100–150 eV. Another new effect is that, after boronization, the radial turbulent particle flux near the plasma boundary is predominantly directed outward.

It should also be noted that, after boronization, the duration of the plasma cooling phase increases substantially due to a decrease in radiative losses.

ACKNOWLEDGMENTS

This work was supported in part by the RF Presidential program for Support of Leading Scientific Schools (grant no. NSh-1965.2003.2) and the Russian Foundation for Basic Research (project no. 04-02-16571).

REFERENCES

1. S. Grebenshchikov, D. Akulina, G. M. Batanov, *et al.*, J. Plasma Fusion Res. SERIES **1**, 41 (1998).
2. V. V. Abrakov, D. K. Akulina, E. D. Andryukhina, *et al.*, Nucl. Fusion **37**, 233 (1997).
3. V. V. Abrakov, D. K. Akulina, E. D. Andryukhina, *et al.*, in *Proceedings of the 10th Conference on Stellarators, Madrid, 1995*, p. 10.
4. J. Winter, H. H. Esser, L. Koenen, *et al.*, J. Nucl. Mater. **162–164**, 713 (1989).
5. R. Brakel, R. Burhenn, A. Elsner, *et al.*, in *Proceedings of the 8th Stellarator Workshop, Kharkov, 1991*, p. 349.
6. A. Sagara, Y. Hasegawa, H. Tsuzuki, *et al.*, Research Report No. NIFS-468 (NIFS, Toki, 1996).
7. J. Winter and H. J. Esser, J. Nucl. Mater. **176–177**, 486 (1990).
8. A. I. Kanaev, V. M. Sharapov, A. P. Zakharov, *et al.*, Dokl. Akad. Nauk SSSR **318**, 342 (1991) [Sov. Phys. Dokl. **36**, 404 (1991)].
9. V. M. Sharapov, S. V. Mirnov, S. A. Grashin, *et al.*, J. Nucl. Mater. **220–222**, 730 (1995).
10. M. S. Berezhetskii, V. P. Budaev, R. S. Ivanov, *et al.*, J. Nucl. Mater. **162–164**, 831 (1989).

Translated by N.F. Larionova

Plasma Physics Reports, Vol. 31, No. 6, 2005, pp. 462–475. Translated from Fizika Plazmy, Vol. 31, No. 6, 2005, pp. 506–520.

MAGNETIC CONFINEMENT SYSTEMS

Study of the Mechanism for Fast Ion Heating in the GOL-3 Multimirror Magnetic Confinement System

A. V. Arzhannikov, V. T. Astrelin, A. V. Burdakov, I. A. Ivanov, V. S. Koĭdan, S. A. Kuznetsov, K. I. Mekler, S. V. Polosatkin, V. V. Postupaev, A. F. Rovenskikh, S. L. Sinitskii, Yu. S. Sulyaev, and A. A. Shoshin

Budker Institute of Nuclear Physics, Siberian Division, Russian Academy of Sciences, pr. Akademika Lavrent'eva 11, Novosibirsk, 630090 Russia

Received July 1, 2003; in final form, August 4, 2004

Abstract—Results are presented from experimental studies of ion heating in the GOL-3 device. The experiments were carried out in a multimirror configuration with a local magnetic well. It was found that, during the injection of a relativistic electron beam, a decrease in the local density of the beam in a magnetic well, which is proportional to the decrease in the strength of the longitudinal magnetic field, results in the formation of a short plasma region with a low electron temperature. The measured longitudinal gradient of the plasma pressure corresponds to an electron temperature gradient of ~2–3 keV/m. Axially nonuniform heating of the plasma electrons gives rise to the macroscopic motion of the plasma along the magnetic field in each cell of the multimirror confinement system. The mixing of the counterpropagating plasma flows inside each cell leads to fast ion heating. Under the given experimental conditions, the efficiency of this heating mechanism is higher than that due to binary electron–ion collisions. The collision and mixing of the counterpropagating plasma flows is accompanied by a neutron and γ-ray burst. The measured ratio of the plasma pressure to the vacuum magnetic field pressure in these experiments reaches 0.2. © *2005 Pleiades Publishing, Inc.*

1. INTRODUCTION

Open confinement systems (linear magnetic mirror traps) were proposed and developed as devices for basic plasma physics research and also as candidates for nuclear fusion applications (see [1, 2]). At present, research on magnetic mirror systems is being carried out in several scientific centers [3–8] with various versions of the system. In particular, the GOL-3 device [9] is classed among multimirror open confinement systems [10, 11]. The plasma density in a multimirror trap is substantially higher than that in other magnetic confinement systems. The improved longitudinal plasma confinement in a multimirror system (as compared to the classical mirror trap) is achieved due to a frictional force that arises when a high-density plasma flows along a corrugated magnetic field.

A high-density plasma in GOL-3 is heated by a high-power relativistic electron beam generated by the U-2 accelerator [12]. When the beam is injected into the plasma, collective beam–plasma interactions lead to the excitation of Langmuir turbulence (see, e.g., [13, 14]). As a result, the energy of the relativistic electron beam is transferred primarily to the plasma electrons through Langmuir oscillations. The electron temperature rapidly reaches 2–3 keV at a density of $\sim 10^{21}$ m^{-3} (see [15]). To achieve such intense electron heating, it is necessary to suppress longitudinal electron heat conduction toward the system ends, at least, during the heating phase. There are now methods for reducing the longitudinal electron energy loss in open magnetic mirror systems; these methods allow one to reach and maintain a relatively high electron temperature in a device [5, 16, 17]. In particular, in the GOL-3 device, the longitudinal electron thermal conductivity is suppressed due to an abnormally high electron collision frequency during the collective relaxation of the relativistic electron beam in the plasma [18, 19]. This phenomenon gives rise to high longitudinal gradients of the electron temperature during the axially nonuniform plasma heating by a high-current relativistic electron beam [17].

In the first stage of GOL-3 experiments, the magnetic field of a solenoid was uniform throughout its entire length (except for the end mirrors). During electron heating, the plasma ions remained relatively cold because the duration of the experiment was insufficient for the electron and ion temperatures to be equalized by classical (binary) collisions.

When part of the solenoid was modified to operate with a corrugated magnetic field, the physics of the plasma processes changed substantially. First, the energy confinement time increased considerably (see, e.g., [3]). This effect was predicted theoretically and, in essence, motivated experiments with a multimirror confinement system. Second, the data from all available ion diagnostics (the analysis of charge-exchange neutrals, high-resolution spectroscopy, and the detection of neutrons from D–D reactions (see, e.g. [3])) showed that, after modification, the ion temperature in the multimirror configuration increased by more than one order

1063-780X/05/3106-0462$26.00 © 2005 Pleiades Publishing, Inc.

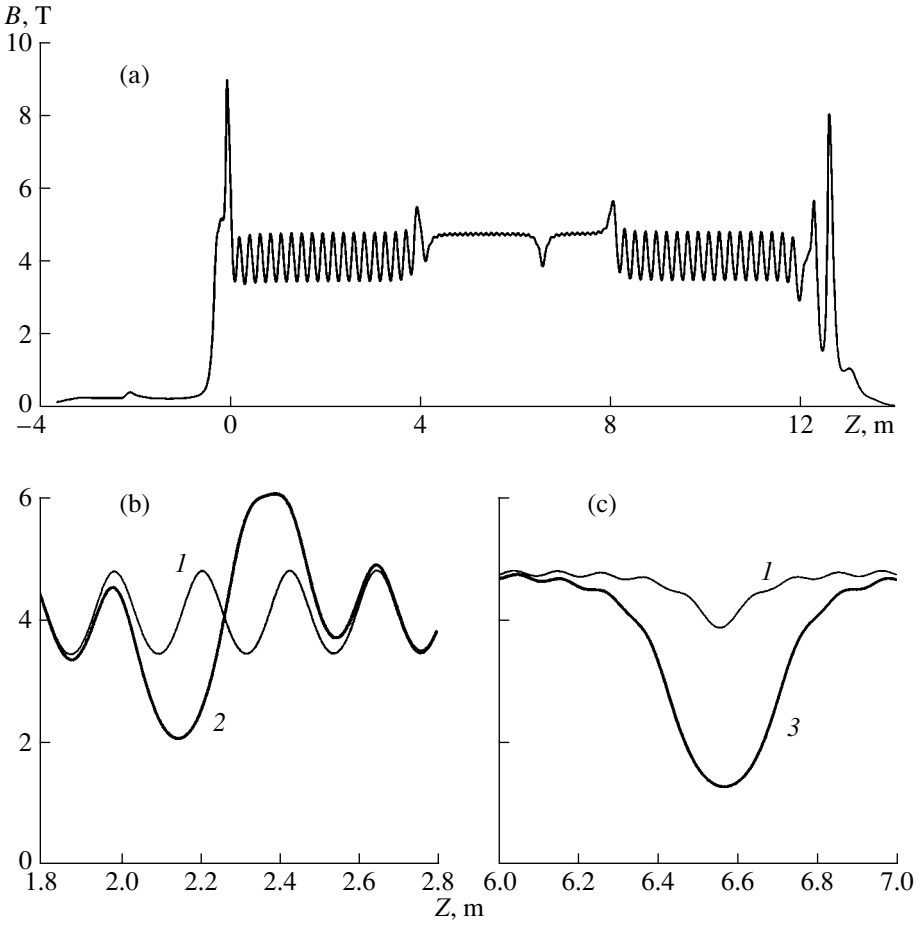

Fig. 1. Configuration of the magnetic field in the GOL-3 device: (a) the entire configuration with two end sections with a corrugated field and (b, c) the magnetic field distributions in configurations with a magnetic well: (*1*) basic configuration, (*2*) magnetic well in a section with a corrugated field, and (*3*) magnetic well in a section with a uniform field.

of magnitude (from 50–100 eV to 1–2 keV). This effect was unexpected, because ion heating lasted only a few microseconds. At a plasma density on order of 10^{21} m^{-3}, binary electron–ion collisions are certainly insufficient to provide the observed increase in the temperature over such a short time interval.

To explain such fast ion heating, we proposed another mechanism: the collective mechanism for energy transfer from the heating electron beam to ions due to the presence of a periodically nonuniform (corrugated) magnetic field in the device. In such a magnetic configuration, the beam current density increases at each maximum of the magnetic field and causes a more intense electron heating there. The electron temperature remains nonuniform along the magnetic field over a fairly long time because of an abnormally high collision frequency. As a result, maxima of the plasma pressure arise that cause the plasma to accelerate toward the minima of the magnetic field. The collision and mixing of the counterpropagating plasma flows lead to the heating of the plasma ions [20, 21]. In our opinion, this heating mechanism provides an explanation for the recent experimental results obtained in GOL-3. After optimizing the experimental parameters, it can serve as a basis for achieving fusion temperatures in our multimirror confinement system.

In this paper, we report on the results of experiments intended to clarify the mechanism of fast ion heating in a multimirror confinement system. We also present a numerical model describing the observed effects in a hydrodynamic approximation and discuss its consistency with the experiment.

2. EXPERIMENT AND DIAGNOSTICS

The design of the GOL-3 device is described in [3, 9]. The solenoid of the device consists of 110 coils with independent power supplies. The total length of the solenoid is about 12 m. The magnetic configuration can be varied depending on the goal of a specific experiment. In the basic configuration (see Fig. 1a), the solenoid was composed of three sections (it is this configuration to which we will compare all the modifications of the magnetic field geometry in each particular experi-

ment). The uniform magnetic field in the central 4-m-long section was 4.8 T. On both sides of the central section, there were sections with a corrugated magnetic field. Each of these sections contained 20 corrugation cells with a period of 22 cm. The maximum and minimum values of the magnetic induction over one period were 5.2 and 3.2 T, respectively. At the ends of the solenoid, single magnetic mirrors with a magnetic induction of 9 T were installed.

The required distribution of the hydrogen or deuterium density along the 10-cm-diameter vacuum chamber placed inside the solenoid was produced with the help of several pulsed valves. Experiments were usually carried out with a quasi-uniform gas puffing; in this case, the gas density in the central part of the chamber was nearly three times higher than that at the chamber ends (see [3]). The target plasma with a line-averaged density of $\sim 10^{21}$ m^{-3} and a temperature of ~2 eV was produced using a special linear discharge. A relativistic electron beam with an electron energy of ~0.9 MeV, a current of ~25 kA, a full duration of ~8 μs, and a total energy of ~120 kJ was then injected into the target plasma. The beam diameter in the section with a uniform field was about 6 cm.

To study the mechanism for fast ion heating in the GOL-3 device, we carried out two separate experiments in which a short region with a reduced field (a magnetic well) was created in the solenoid. These two experiments differed in the position of the magnetic well: in the first case, it was located at the center of the solenoid and, in the second case, at the center of the first section with a corrugated field. The magnetic induction and the shape of the magnetic field lines in the magnetic-well region depended on how the solenoid coils were connected to the power supply. Thus, the magnetic field geometry corresponded to either the basic magnetic configuration or a configuration with a magnetic well (without intermediate configurations). The corresponding longitudinal profiles of the magnetic induction are shown in Figs. 1b and 1c.

The plasma parameters were measured using standard diagnostics (see [22]). In addition, special diagnostics were designed to measure the plasma parameters in the magnetic-well region (see below). The set of diagnostics was different in the experiments with the above two modifications of the magnetic configuration (the diagnostics employed will be briefly described in the corresponding sections).

One of the basic diagnostics was a multifunction spectral system consisting of several instruments. The system measured the plasma emission spectra with a spatial resolution along the transverse coordinate (chord) and a spectral resolution of 0.03 nm. In each frame, the π- and σ-polarized emission components were recorded separately. Precise measurements of the contours of the spectral lines allowed us to separate different effects that lead to he broadening and/or splitting of these contours. The spectrum was usually recorded by five (of the available six) specialized units operating simultaneously. The system of spectral diagnostics is described in more detail in [23].

An important new diagnostics was a system for measuring the products of fusion reactions and the accompanying hard γ radiation. This system consisted of several scintillation detectors (stilbene, polystyrene, and NaI(Tl)) located at different distances from the plasma (including those placed on a mobile platform) and also an activation silver detector. The neutron and γ-ray diagnostics of the GOL-3 device, including the equipment and the digital technique for discriminating neutrons and the accompanying γ photons by analyzing the shape of a pulse, were discussed in more detail in [24].

3. EXPERIMENT WITH A MAGNETIC WELL IN THE CENTRAL SECTION OF THE SOLENOID

The first series of experiments was carried out with a magnetic well situated in the central section of the solenoid. At the center of this section, a special cell with a reduced magnetic field was formed. The center of the cell was located at $Z = 659$ cm. Around this cell, the diameter of the vacuum chamber was increased to 15 cm over a length of 42 cm, and the distance between the neighboring coils of the solenoid was increased by 4 cm. The coils adjacent to the point $Z = 659$ cm were powered separately and could be switched off in particular experiments. The magnetic induction at this point was 3.8 T when the neighboring coils were switched on, and it was 1.3 T when these coils were switched off (see Fig. 1c). In the latter case, the resulting magnetic configuration was a local magnetic well about 30 cm in length.

The time behavior of the plasma pressure inside and near the cell was measured with the help of several diamagnetic probes. In addition, the plasma in the cell was studied by spectroscopic methods. Neutron and γ-ray detectors were positioned near the cell.

Let us consider the data from diamagnetic measurements. Figures 2 and 3 show typical longitudinal profiles and waveforms of the plasma pressure derived from diamagnetic measurements. The initial plasma density in this case was 10^{21} m^{-3}. Far from the cell (at $Z = 524$ and 701 cm), the signals from diamagnetic detectors are identical in shape to those observed in experiments without a magnetic well and, in the central part of the solenoid, vary only slightly along the Z coordinate. The maximum pressure is $D = n_e T_e + n_i T_i \sim 10^{21}$ keV/m^3 (where n and T are the density and temperature and the subscripts e and i stand for electrons and ions, respectively). For comparison, the figure shows a hard bremsstrahlung signal from a detector located behind the beam collector (this signal provides the most adequate information about the time behavior of the power of the beam passed through the plasma). In the

configuration with a magnetic well, a substantial change in the plasma behavior was observed in the diamagnetic signal measured at the bottom of the magnetic well (the signal measured at $Z = 659$ cm in Fig. 3). In the course of plasma heating by the electron beam, the plasma pressure (which is determined in this stage by the electron temperature) in the magnetic well is 5–10 times lower than the pressure measured by detectors located a distance of ~40 cm, where the field is uniform.

As was found in our previous experiments, the plasma pressure during beam injection is primarily determined by the temperature of the electron component (and this component may actually be characterized by a local temperature). Thus, the observed large gradient of the plasma pressure along the magnetic field during the heating stage can be explained by the existence of a large (up to ~2.5 keV/m) longitudinal gradient of the electron temperature. This indicates directly that the electron thermal conductivity during beam injection is suppressed by several orders of magnitude in comparison to its classical value (see [25]). After the end of beam injection, the effects related to collective beam–plasma interactions disappear and the temperature begins to equalize along the plasma column. In this stage, we observed a sharp increase in the plasma pressure in the magnetic well (while the plasma pressure beyond the well decreases).The value of β in the magnetic well reached 15–20%.

The nonuniform electron pressure should produce a longitudinal ambipolar electric field, which accelerates the plasma on both sides of the magnetic well toward the central plane of the cell, where the counterpropagating plasma flows collide. The kinetic energy of the accelerated plasma ions should depend on the magnetic field configuration, the drop in the total pressure, and the profile of the electron temperature along the cell. The mean free path of the accelerated ions in these experiments is comparable to the cell length or is even longer. This means that the accelerated ion flows arriving from regions with a high magnetic field on both sides of the cell should mix in its central plane because of binary ion–ion collisions and/or because of the onset of turbulence in counterpropagating flows. The kinetic energy of the directed ion motion is, therefore, thermalized. This mechanism of collective energy transfer from the high-temperature electron component to ions seems to be rather efficient.

To verify the proposed mechanism for heating the plasma ions to a high temperature in a nonuniform magnetic field during beam injection, we performed numerical simulations and carried out special experiments in which a neutron and γ-ray burst was detected when the counterpropagating plasma flows collided in the central plane of the magnetic well. The plasma parameters were also studied by analyzing the behavior of the magnetic and electric fields measured by spectroscopic methods.

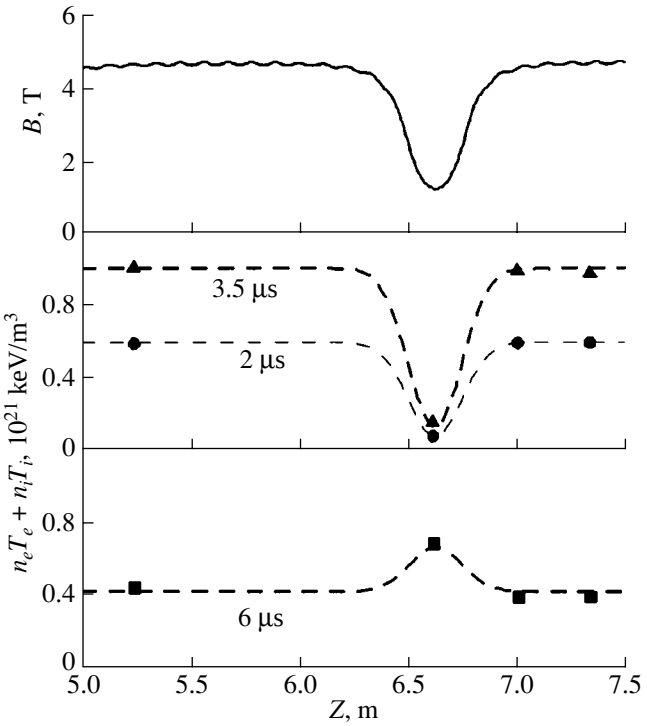

Fig. 2. Longitudinal profiles of the magnetic field (solid line) and the plasma pressure (dashed lines) for three different instants. The magnetic well is at $Z = 659$ cm.

4. STUDY OF THE PLASMA IN THE CENTRAL MAGNETIC WELL BY SPECTROSCOPIC METHODS

The spectroscopic system described above allowed us to measure the shapes of spectral lines with an accuracy that was high enough to separate different effects forming the line profile (thermal broadening, Zeeman splitting, Stark broadening, and isotopic shift). The structure of both hydrogen and impurity lines was measured.

One of the problems to be solved using spectroscopic diagnostics was to determine the topology of the magnetic field in the well at high values of β. To measure the magnetic field outside the high-temperature plasma region, it is convenient to use bright spectral transitions of impurity atoms and ions that are contained in the low-temperature peripheral plasma. One such line is the well-known sodium doublet (588.99 and 589.59 nm), which is mainly emitted from a relatively narrow annular region at the plasma periphery and is almost absent in the high-temperature plasma region. Sodium (along with some other elements) comes into the plasma from Zerodur limiters situated along the plasma column. Figure 4 shows the spectra of the σ- and π-polarized radiation recorded simultaneously in the 2-nm wavelength interval with the help of a CCD-equipped image converter. Solid lines at the centers of the frames depict the contours of the observed spectral lines calculated under the given

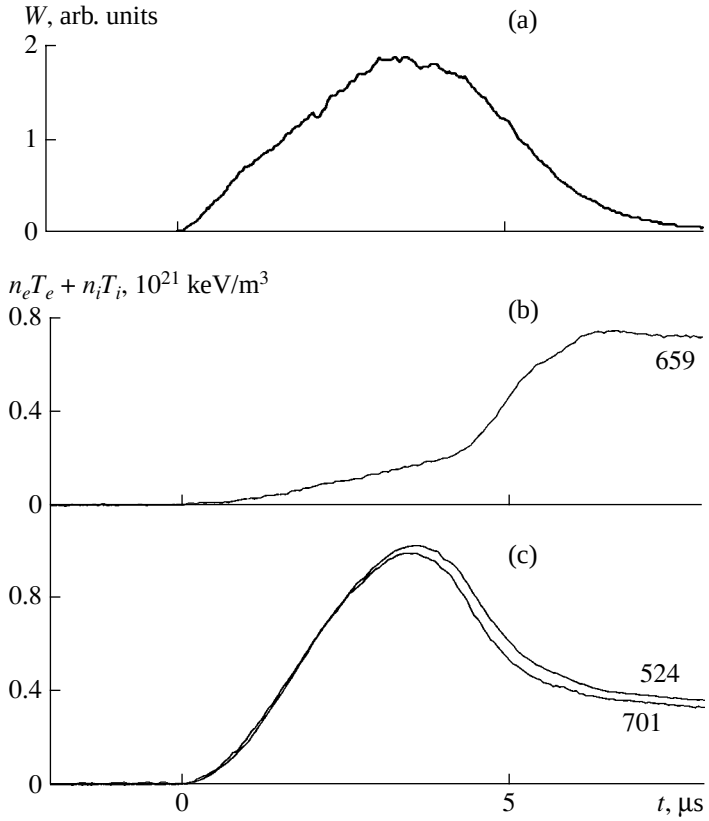

Fig. 3. Typical signal of bremsstrahlung measured behind the beam collector (a) and the waveforms of the plasma pressure in the central plane of the magnetic well (b) and at two points where the magnetic field is uniform (c). The numerals by the curves indicate the longitudinal coordinate *Z*.

experimental conditions. In the case of a high field, all of ten emission components are well resolved in the CCD frames.

For comparison, Figs. 4c and 4d show the contours of the H_α line in a high and a low magnetic field. The error in determining the magnetic field in these measurements was 0.3 T. Measurements of the σ component of the H_α line with the help of a multichannel fiber collector and an FEU-84 photomultiplier allowed us to trace the dynamics of splitting of this line in the magnetic well (see Fig. 5; the zero time coincides with the start of beam injection).

Similar measurements were performed for the σcomponents of the Na I (589.0 nm) line. The measurements showed that these components split by $\Delta\lambda = \pm 0.025$ nm relative to the π component and this broadening is independent of time. As was expected, the positions of the σ components for this line correspond to the splitting in the magnetic field.

The measurements showed that the splitting of the H_α hydrogen line after the propagation of the electron beam was larger than would be expected for the given magnetic field, whereas no additional splitting was observed in the sodium line. This indicates that these atoms were affected not only by the magnetic field, but also by a directed electric field, because the spectral transitions under discussion undergo different Stark broadening. The Stark broadening of the hydrogen line is a linear function of the electric field, whereas the Stark broadening of the sodium line is quadratic in the field strength. Let us estimate the electric field that would explain the observed additional broadening of the hydrogen line. When an electron passes from the n' excited state to the n state, the wavelength shift of a photon emitted by the electron is proportional to the electric field E:

$$\Delta\lambda = \frac{3}{4\pi}\frac{\hbar\lambda_0^2}{mec}[n'(n_1' - n_2') - n(n_1 - n_2)]E,$$

where n' and n are the principal quantum numbers and $n = n_1 + n_2 + |m| + 1$ in the case of a parabolic quantization (here, n_1 and n_2 are the parabolic quantum numbers and m is the magnetic quantum number; see [26]). Therefore, the H_α line splits into several components with $\Delta\lambda_N[\text{nm}] = 2.756 \times 10^{-3} NE$ [kV/cm], where N is a number from –4 to +4. (Depending on the direction of the electric field relative to the magnetic field and on the orientation of the polarizer, only some of these components are measured in the experiment.) The splitting of the spectral line in the electric field causes an additional

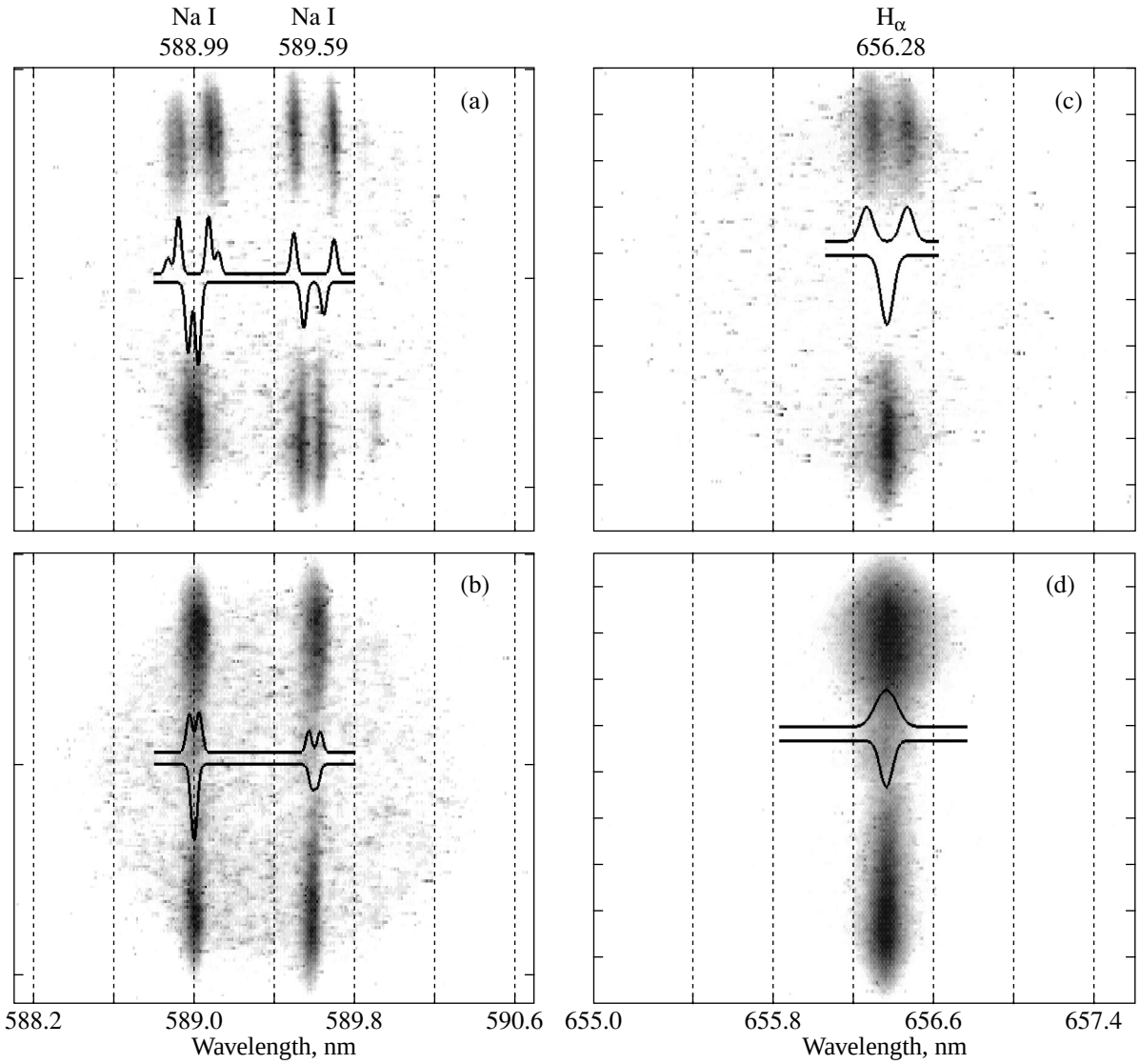

Fig. 4. Zeeman splitting of spectral lines in the magnetic field: (a, b) Na I doublet and (c, d) H_α line of hydrogen. The measurements are performed (a, c) in a magnetic field of 4.3 T and (b, d) in a 1.3-T magnetic well. The upper and lower parts of the frames corresponds to the σ-and π-polarization, respectively. The curves show the line profiles calculated for the corresponding magnetic fields and polarizations.

broadening of the measured contour of the hydrogen line. From the measured width of the H_α line, we infer that the electric field is on the order of 10 kV/cm. The presence of such an electric field in plasma may be related to different mechanisms. In beam–plasma experiments, high electric fields are usually excited due to intense collective relaxation of the beam and are related to the high level of Langmuir and ion-sound turbulence (see, e.g., [4]). In our case, such electric fields are also observed for some time after the end of beam injection. This indicates that the observed electric fields are related to the proposed mechanism for ion heating in the low-field cell of the multimirror system.

5. DETECTION OF NEUTRON AND γ-RAY BURSTS

It follows from our previous experiments that the heating of the plasma electrons at the edges of the magnetic well causes the plasma acceleration toward the center of the well. The characteristic velocity of the plasma flow is on the order of the ion-sound velocity (see Section 7). This means that the energy of the relative ion motion in the counterpropagating plasma flows can exceed 1 keV. Under the GOL-3 experimental conditions, this may manifest itself in the generation of neutron and γ-ray bursts.

Figures 6a–6c compare the neutron signal from a polystyrene scintillator detector positioned near the

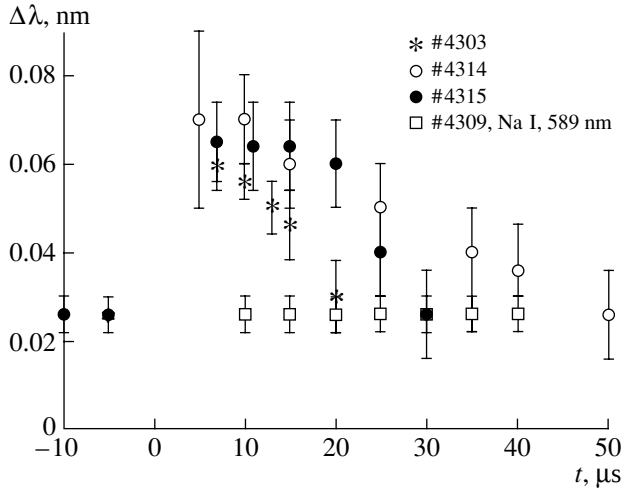

Fig. 5. Splitting of the σ component of the H_α line in a magnetic well for different instants. The data were obtained from several shots using a detector with a multichannel fiber collector. The beam injection into a cold dense plasma starts at the instant 0 μs. For comparison, the figure also shows the splitting of the Na I line (unlike hydrogen lines, this line is less sensitive to the electric field).

central magnetic well to the electron-beam bremsstrahlung signal measured behind the beam collector and to the plasma-pressure signal measured by a diamagnetic coil in the central plane of the magnetic well. Each plot presents two successive shots made under identical conditions (the signals differ in the line thickness). The neutron detector has a longitudinal spatial resolution of ~30 cm (which is equal to the distance from the plasma axis to the detector); i.e., it receives radiation directly from the region where the plasma flows collide. The start of beam injection corresponds to $t = 0$. It can be seen that, immediately after the beginning of beam injection, the detector signal is almost zero. A sharp radiation burst appears 4–5 μs later. This instant corresponds to a sharp growth of the transverse plasma pressure, which is measured by a diamagnetic coil. We recall that, in the proposed model of ion heating, such an increase in the pressure is a natural consequence of the collision and thermalization of two counterpropagating plasma flows arriving from the two slopes of the magnetic well.

Comparing the signals measured in two successive shots, we see that the shape of the neutron peak varies from shot to shot (in particular, after the first maxi-

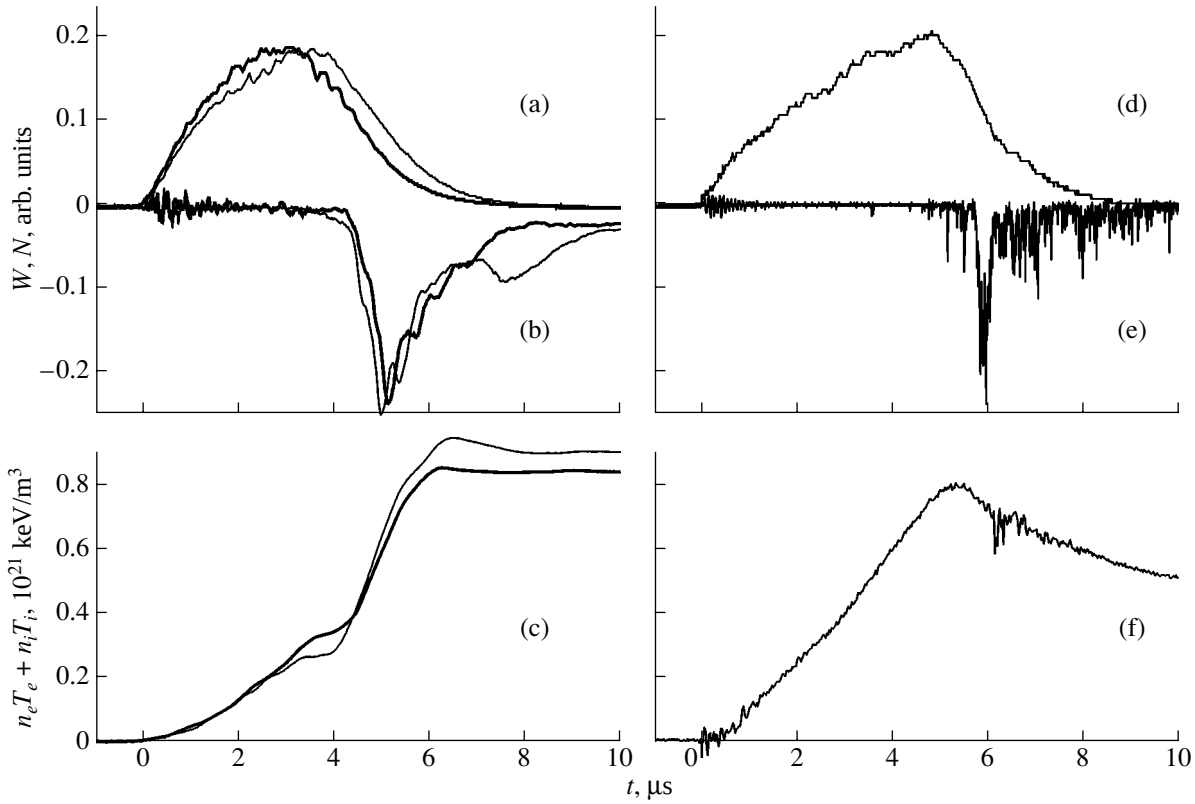

Fig. 6. Time delay of the neutron signal in a system with a nonuniform magnetic field: (a, d) bremsstrahlung power *W* measured behind the beam collector, (b, e) signals *N* from the photomultipliers of the neutron detectors ($Z = 5.7$ and 4 m, respectively), and (c, f) signals from diamagnetic coils ($Z = 5.69$ and 3.73 m, respectively). Plots (a)–(c) correspond to measurements in a configuration with a central magnetic well (in two successive shots) and plots (d)–(f) correspond to measurements in a regular multimirror system.

mum), although the shape of the diamagnetic signal varies only slightly. The sensitivity of the shape of the neutron signal to small variations in the initial parameters is also an indirect argument in favor of the proposed ion-heating mechanism.

The simultaneous processing of the neutron and diamagnetic signals allows us to verify the predictions of our ion-heating model in experiments with magnetic wells of different shape. In test experiments, we switched on magnetic coils located near the center of the well; as a result, the mirror ratio (the depth of the magnetic well) decreased from 3.7 to 1.2. In this case, the acceleration and motion of the counterpropagating plasma flows should change. In the case of a shallow magnetic well, the electrons at the center of the well are significantly heated by the electron beam. Consequently, both the local electron temperature at the center of the well and the temperature averaged over the well should be higher. In this case, it may be expected that the accelerated ions will earlier arrive at the center of the well, whereas the increase in the density there will be less pronounced and the final ion temperature will be some lower (the earlier appearance of neutrons in this case is explained by the shorter distance from the region with a high electron temperature to the region where the counterpropagating flows collide and thermalize). The experiment showed that, as was expected, the detector signals appeared as soon as the beam injection started, had substantially smaller amplitudes, and had no sharp peaks. The signals from the radiation detectors correlated with the signal from a diamagnetic coil located at the center of the magnetic well, and the pressure peak associated with the collision of the plasma flows was also less pronounced.

It is also interesting to consider the results from similar measurements performed in the section with a corrugated field. Figures 6d–6f compare the neutron signal from a stilbene scintillator detector located near the region with a corrugated magnetic field to the electron-beam bremsstrahlung signal and to the plasma-pressure signal measured near the position of the neutron detector. The neutron signal is almost zero up to ~6 μs (i.e., until the maximum of the diamagnetic signal, which is primarily determined by the electron component at this instant). In the stage where the transverse plasma pressure decreases, we observed a short intense neutron and γ-ray burst, which then transformed into a slowly decreasing signal (every short peak of duration ~30 ns in the signal from this detector corresponded to one fast particle that fell into the scintillator). The full duration of the neutron signal was 1–1.5 ms and depended on the experimental conditions. At the end of the first neutron burst, some of the diamagnetic coils located near the region of maximum neutron emission showed the presence of high-frequency MHD activity (see Fig. 6f), which may be regarded as an indication of the mixing of the counterpropagating plasma flows.

Thus, the appearance of a sharp neutron and γ-ray burst is consistent with the expected shape of the signal in the case of ion acceleration toward the center of the magnetic well.

6. EXPERIMENT WITH A MAGNETIC WELL IN THE MULTIMIRROR SECTION

In this experiment, the magnetic well was located nearly at the center of the entrance section with a corrugated field. The center of the magnetic well was at Z = 213 cm. The magnetic configuration for this case is shown in Fig. 1b. The specific features of this configuration (as compared to the previous case, where the magnetic well was located in the section with a uniform magnetic field) were as follows: (i) the plasma in this section had a higher temperature and lower density (for this reason, we might expect somewhat different plasma dynamics) and (ii) the corrugations adjacent to the magnetic well could influence the character of expansion of the high-temperature plasma in comparison to the plasma dynamics in the uniform section of the solenoid. The minimum axial magnetic field at the center of the magnetic well in this case was 2.1 T. The vacuum chamber in this region was standard (10 cm in diameter with 8-cm-diameter annular limiters). To prevent the beam from falling onto the wall of the vacuum chamber and the limiters in the magnetic-well region, we decreased the magnetic field in the region of the final compression of the beam by a factor of ~1.3. In this case, the peripheral part of the electron beam was cutoff by a special graphite limiter; as a result, the diameter of the beam transported through the plasma was smaller and, accordingly, the energy of the beam injected into the plasma was lower.

Figure 7 shows typical signals from diamagnetic coils located at different distances from the entrance mirror (Z = 0). The detectors nearest to the minimum of the magnetic field were located at Z = 208 and 209 cm, where the field was ~2.7 T (i.e., at the slope of the magnetic well). As in the previous case with a well at the center of the solenoid, signals from detectors located far from the well almost coincided with those measured in the basic magnetic configuration (without a magnetic well). At the same time, the time evolution of the plasma pressure measured by the detectors located at 208 and 209 cm was similar to the evolution discussed above: first, a slow (in comparison to the surrounding plasma) growth in the plasma pressure in the heating stage; then, a more rapid growth when the plasma flowed into the magnetic well from both sides; and finally, an abrupt jump in the pressure at the end of beam injection, when the classical electron heat conductivity was restored. The leading edges of these diamagnetic signals had specific shapes that could be identified as a result of several passages of the compression wave through the magnetic well with a subsequent partial reflection from the region with a strong magnetic field. We note three aspects in which this experiment

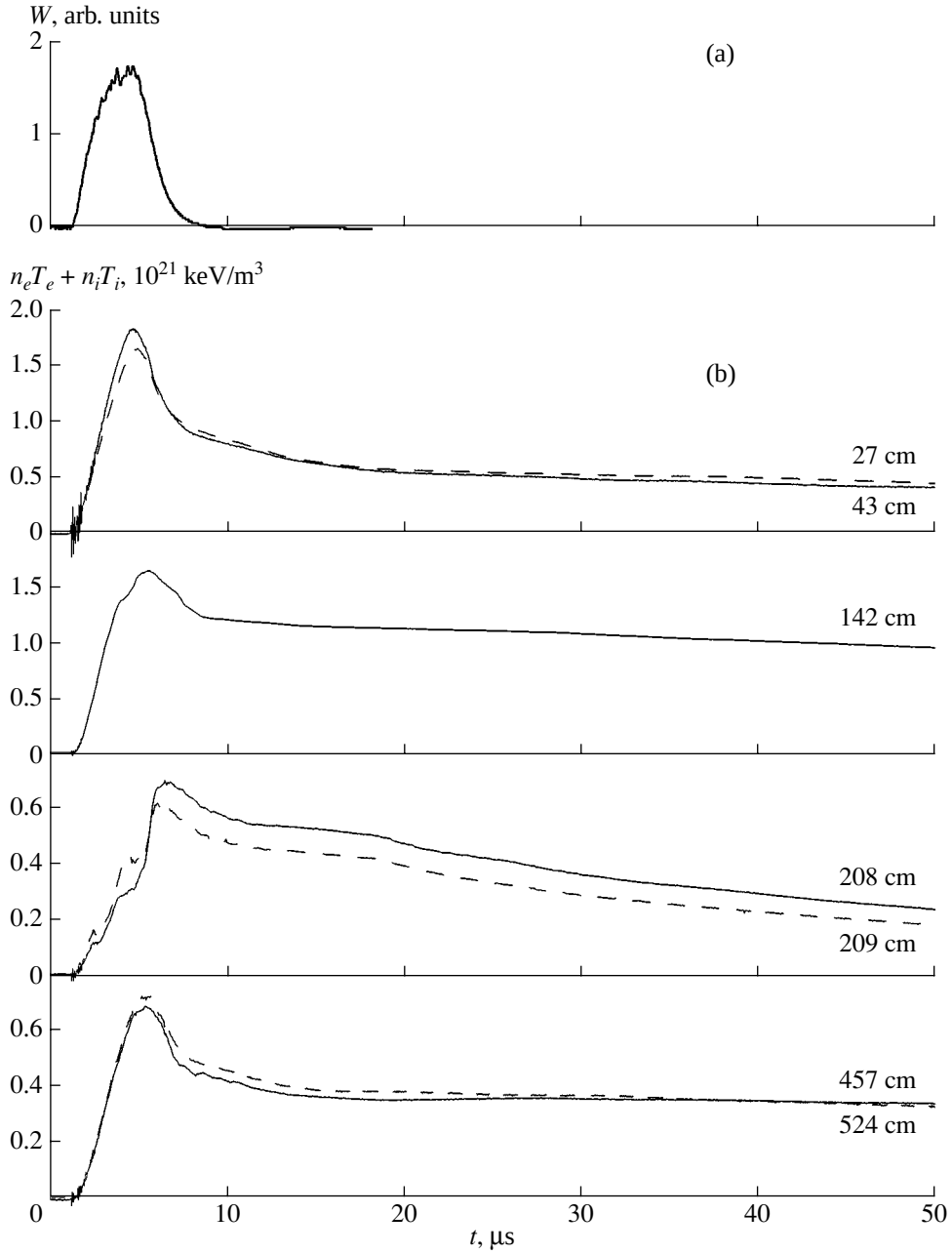

Fig. 7. (a) Bremsstrahlung power W measured behind the beam collector and (b) typical signals from diamagnetic coils. The numerals by the curves indicate the detector position Z. The center of the magnetic well is located at $Z = 213$ cm.

differed from the previous experiment with a well located at the center of the uniform section. First, there was a large gradient of the efficiency of plasma heating by the beam in the initial stage of its propagation through the plasma (because the growth rate of the beam instability decreased as the phase volume of the beam gradually increased). The heating gradient is easy to trace by comparing how the amplitudes of the diamagnetic signals change with distance from the entrance mirror (see Fig. 7). Second, each cell of the multimirror magnetic system can be regarded as a local magnetic well with a mirror ratio of 1.5; consequently, we might expect that the above processes of energy transfer from the heated electrons to the thermal energy of ions will occur within each cell. This must somewhat change the rate of energy transfer by electrons to the magnetic well from the far plasma regions in comparison to the case where the magnetic well was located in the section with a uniform magnetic field. Third, because of the construction of the solenoid and the coil

power supply, the magnetic well was asymmetric about the plane with a minimum field. In combination with the electron temperature gradient in the heating state, this prevented the counterpropagating plasma flows from a symmetric collision at the center of the magnetic well (in contrast to the case of a magnetic well at the center of the solenoid).

One of the goals of this experiment was to determine the value of β by spectroscopic methods. To do this, we used the fact that, on the time scale comparable to the characteristic time of energy exchange in the magnetic well, we can assume that the vacuum chamber of the device is perfectly conducting, i.e., that the magnetic flux within it is conserved. For this reason, the value of β can be determined by measuring the increase in the magnetic field in the annular gap between the high-temperature plasma and the chamber wall. To determine how the magnetic field increases in the plasma–wall gap, we measured the splitting of a neon spectral line excited by a cold gas discharge insulated from the hot plasma. For this purpose, a neon lamp was inserted into the gap between the plasma and the vacuum chamber and a cold gas discharge was excited there. The splitting of the Ne I (640.23 nm) line was then observed with the help of the spectral system.

The results from measurements of the magnetic field from the Zeeman splitting of the neon line are shown in Fig. 8 for different instants relative to the start of beam injection. Experimental points were averaged over three shots. The figure also shows the results of measurements performed with a cold preliminary plasma; these results correspond to the vacuum magnetic field. During beam injection, which started at $t = 0$, the spectral width of the neon line substantially increased over the time interval of 20–25 μs. The line width then returned approximately to the value corresponding to the vacuum magnetic field. After the passage of the electron beam, the magnetic field at the plasma periphery increased on average by $\Delta B = 0.13 \pm 0.05$ T relative to the vacuum magnetic field. A comparison of the data from spectroscopic and diamagnetic measurements showed that, over the time interval from 0 to 25 μs, the magnetic field measured from the splitting of the neon line near the vacuum chamber wall corresponded to that given by diamagnetic measurements. Thus, taking into account the geometry of our experiment (the plasma occupied almost the entire cross section of the vacuum chamber), we find $\beta = 12 \pm 5\%$.

We also measured the H_α profile. Figure 9 shows the measured contours of the H_α line. The contours of the π- and σ-components were obtained in different shots, the exposure time being from 8 to 14 μs from the start of beam injection. The measurements showed that this radiation was emitted from the region occupied by the peripheral plasma. As in experiments with a central magnetic well, the observed broadening of the line profile was larger than that expected for the Zeeman effect. Most likely, the additional broadening was due to the generation of electric fields in the plasma.

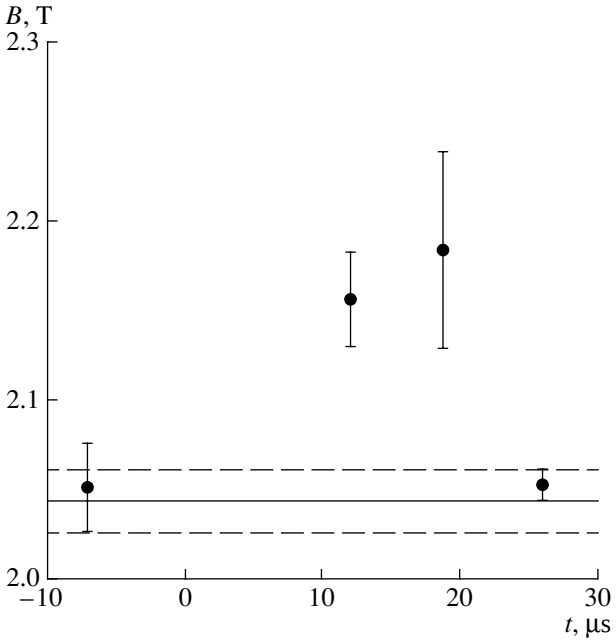

Fig. 8. Measurements of the magnetic field in the gap between the plasma and the wall by the Zeeman splitting of the neon line. The solid line shows the data for the case of a cold preliminary plasma (the vacuum field). The dashed lines show the spread in the measured values over a series of shots. The points correspond to experiments with the injection of the heating beam.

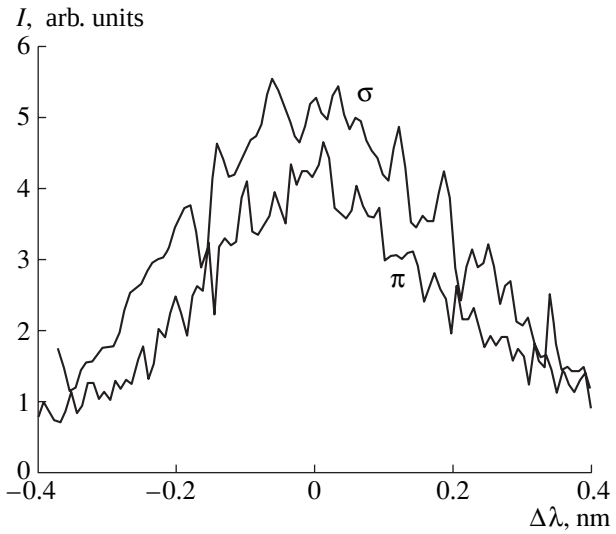

Fig. 9. Contour of the H_α line measured 11 μs after the beginning of electron beam injection (π and σ are the components relative to the magnetic field). The full width at half maximum of the contour exceeds the expected value of Zeeman splitting.

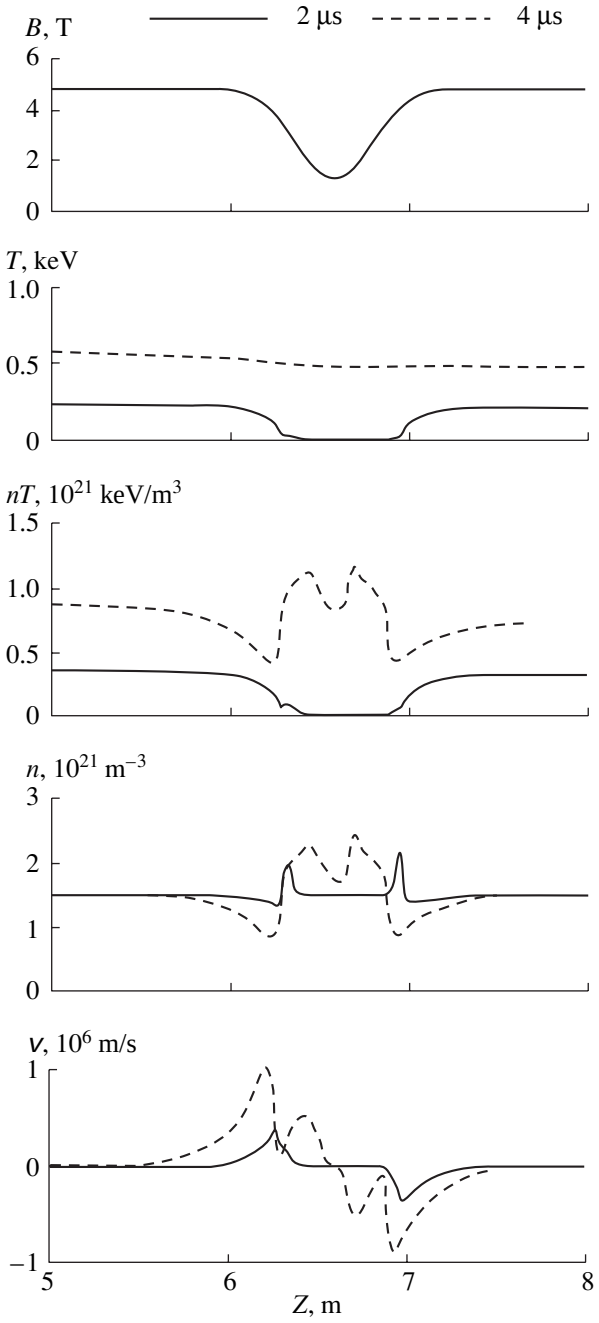

Fig. 10. Modeling of a magnetic cell: the profiles of the magnetic field and the plasma parameters at $t = 2$ and 4 μs.

7. RESULTS OF NUMERICAL SIMULATIONS

The excitation of large-amplitude ion-sound waves in a plasma with a uniform density and the nonuniform plasma heating by an electron beam were also studied by numerical simulations. The numerical model used is briefly described in the Appendix. Let us consider the results of simulations for the case of a central magnetic well. The hydrodynamic approximation used to describe the ion dynamics is valid only in the initial stage of plasma acceleration, when ion-sound perturbations are excited. This approximation is then inapplicable because the ion mean free path becomes comparable to the length of the magnetic well. The simulations were performed for the entire plasma system with the actual longitudinal profile of the magnetic field. Below, we only discuss the time behavior of the plasma for the case of a central magnetic well with $B_{max}/B_{min} \sim 3.7$.

Figure 10 shows the longitudinal profiles of the magnetic field and the temperature, pressure, density, and velocity of the plasma at an intermediate instant ($t = 2$ μs) and just before the collision of the plasma flows ($t = 4$ μs). Since in the initial state ($t = 0$, $T = 0$, $nT = 0$, $n = 1.5 \times 10^{21}$ m^{-3}, and $v = 0$), the plasma is uniform, whereas the beam density n_b is proportional to the local value of the magnetic field, plasma heating at the bottom of the magnetic well is insignificant because the ratio n_b/n at this point at $t \le 2$ μs is lower than the threshold value. One can see that, under the action of the pressure gradient the perturbation of the plasma velocity arises and the plasma begins to move toward the bottom of the magnetic well. Direct electron exchange between the main plasma and the plasma at the bottom of the well (the so-called replacement wave [27]) is suppressed by the abnormally intense scattering of electrons in a strongly turbulent plasma.

This is confirmed by the time behavior of the diamagnetic signal, which shows that the plasma pressure varies much more slowly than it might be expected from the rate of replacement of cold electrons with hot ones. The pressure wave continues to develop even in the stage where the electron thermal conductivity becomes classical (proportional to $T^{5/2}$). The heating of the cold plasma is accompanied by the redistribution of the temperature along the system axis ($t = 4$ μs). As a result, counterpropagating plasma flows with ion velocities on the order of $\tilde{V} \sim (\tilde{n}/n)\sqrt{T_e/M}$ arise. These flows give rise to density perturbations with an amplitude of $\tilde{n}/n \sim 0.5$. The maximum ion velocity in the wave (see Fig. 10) corresponds to a kinetic energy of $\varepsilon_i \sim 100$ eV, which far exceeds the increase in the ion energy due to binary electron–ion collisions over this time interval.

The simulated evolution of the excited ion-sound perturbation qualitatively agrees with the experimentally observed longitudinal profile and time behavior of the plasma pressure. The main simplifications of the model are the use of a gas-dynamic approximation in describing plasma flows (in this case, the interpenetration of the flows cannot be described correctly) and the introduction of an artificial viscosity (this can lead to an underestimation of the maximum ion flow velocity). The model also ignores a further acceleration of the ion flows after they intersect the central plane of the well (Fig. 10). Note that, at ion velocities calculated in our model, the ion mean free path is longer than the magnetic well. This means that the transit ions whose veloc-

ities fall within the loss cone of the confinement system will give up their energy and become thermalized on a spatial scale that is longer than the magnetic well. The energy of the trapped ions will be redistributed inside the well.

In the experiment in which the magnetic well is located in the section with a corrugated magnetic field, the counterpropagating ion flows arise in each cell of the multimirror confinement system. The energy is then redistributed over the entire length of the device. It is important that the fast ion flows form under the action of electron temperature gradients over a short time interval and are then thermalized over a time on the order of the ion–ion collision time (or even more rapidly in the presence of collective scattering). This ensures energy transfer from the plasma electrons to the ions over a time that is much shorter than the electron–ion energy exchange time due to binary collisions.

8. DISCUSSION OF RESULTS AND CONCLUSIONS

We carried out experimental studies of the plasma behavior in the cells of the GOL-3 multimirror device. The experiments were aimed primarily at clarifying the mechanism for fast ion heating to temperatures on the order of 1 keV in the multimirror confinement system. For this purpose, relatively short magnetic wells with a magnetic field reduced to 2.1 and 1.3 T were created at distances of 213 and 659 cm from the entrance mirror, respectively.

It was found that, during the injection of a relativistic electron beam, a decrease in the local density of the beam in a local magnetic well, which is proportional to the decrease in the strength of the longitudinal magnetic field, results in the formation of a short plasma region with a low electron temperature (several times lower than the temperature in the adjacent regions of the plasma column). The measured longitudinal gradient of the plasma pressure corresponds to an electron temperature gradient of ~2–3 keV/m. This experiment demonstrates directly the effect of strong (by several orders of magnitude) suppression of the longitudinal electron thermal conductivity due to collective plasma–beam interaction in the plasma heating stage. After the end of beam injection, this effect disappears, the plasma pressure in the region with a reduced magnetic field increases, and the plasma in the remaining part of the device cools.

Our experiments and numerical simulations showed that axially nonuniform heating of the plasma electrons gives rise to a macroscopic motion of the plasma along the magnetic field in each cell of the multimirror confinement system. The mixing of the counterpropagating plasma flows inside each cell leads to fast ion heating. Under our experimental conditions, the efficiency of this heating mechanism is higher than that due to binary electron–ion collisions.

The mechanism for fast ion heating considered here should lead to the excitation of large-amplitude waves of the plasma density. At present, a special experiment in which such density waves will be measured directly is under way. For this purpose, we are modifying the existing Thomson scattering system at a wavelength of 1.06 μm.

It is found that the collision and mixing of counterpropagating plasma flows are accompanied by a neutron and γ-ray burst.

The recorded profiles of the spectral lines emitted from the regions with reduced magnetic field indicate that the interaction of the plasma flows is also accompanied by the generation of strong electric fields. Spectral and magnetic probe measurements show that, in our experiments, the ratio of the plasma pressure to the vacuum magnetic field pressure is 0.1–0.2.

ACKNOWLEDGMENTS

We are grateful to R.Yu. Akent'ev, É.R. Zubairov, V.G. Ivanenko, M.V. Ivantsivskiĭ, V.V. Konyukhov, A.G. Makarov, V.S. Nikolaev, and V.D. Stepanov for their assistance in performing experiments in the GOL-3 Device. This work was supported in part by the Russian Academy of Science; the RF Ministry of Industry, Science, and Technologies; and the Russian Foundation for Basic Research (project nos. 00-02-17649 and 03-02-16271).

APPENDIX

Numerical Model

The excitation of large-amplitude ion-acoustic waves in a uniform plasma and the nonuniform plasma heating by an electron beam were simulated using the modified ISW two-fluid hydrodynamic code. In the initial heating stage, the ion temperature of the plasma produced by a linear discharge in deuterium is low (on the order of several electronvolts) and the ion mean free path is much sorter than the cell length. For this reason, simulations were performed in a gas-dynamic approximation. The plasma dynamics is described by the continuity equation and the equation of motion [28]:

$$\frac{\partial n}{\partial t} + B\frac{\partial}{\partial z}\left(\frac{nV}{B}\right) = 0, \tag{1}$$

$$\begin{aligned}&\frac{\partial V}{\partial t} + BV\frac{\partial}{\partial z}\left(\frac{V}{B}\right) + \frac{V^2}{B}\frac{\partial B}{\partial z}\\ &+ \frac{1}{Mn}\frac{\partial(nT+\mu)}{\partial z} + \frac{1}{MB}(T_e + T_i)\frac{\partial B}{\partial z} = 0,\end{aligned} \tag{2}$$

where n and V are the plasma density and velocity, t is time, B is the magnetic induction, z is the longitudinal coordinate, M is the ion mass, $T = T_e + T_i$, and $\mu =$

$-\lambda_0^2 nM\frac{\partial V}{\partial z}\left|\frac{\partial V}{\partial z}\right|$ is the artificial viscosity introduced in order to prevent the breaking of nonlinear and shock waves (here, $\lambda_0 \sim 3$–10 cm is the characteristic wavelength at which viscosity begins to play an important role).

The distributions of the electron and ion temperatures, T_e and T_i, are described by the heat balance equations for electrons and ions [28], which in our case take the form

$$\frac{3}{2}\frac{\partial nT_e}{\partial t} + B\frac{\partial}{\partial z}\left(\frac{3}{2}\frac{nT_eV}{B}\right) + nT_eB\frac{\partial}{\partial z}\left(\frac{V}{B}\right) = \frac{\partial}{\partial z}\left(\kappa_e\frac{\partial T_e}{\partial z}\right) + Q_e, \quad (3a)$$

$$\frac{3}{2}\frac{\partial nT_i}{\partial t} + B\frac{\partial}{\partial z}\left(\frac{3}{2}\frac{nT_iV}{B}\right) + nT_iB\frac{\partial}{\partial z}\left(\frac{V}{B}\right) = \frac{\partial}{\partial z}\left(\kappa_i\frac{\partial T_i}{\partial z}\right) + Q_i, \quad (3b)$$

where the longitudinal thermal conductivities are defined by the formulas

$$\kappa_e = F_e(Z_{\text{eff}})\frac{nT_e\tau_e/\zeta}{m}, \quad (4)$$

$$\kappa_i = F_i(Z_{\text{eff}})\frac{nT_i\tau_i}{M}. \quad (5)$$

Here, τ_e and τ_i are the electron and ion collision times, m is the electron mass, Z_{eff} is the effective ion charge number in the presence of impurities, the factors in expressions (4) and (5) are equal to $F_e \sim 3.5$ and $F_i \sim 3.9$ [28], ζ is the coefficient of suppression of the longitudinal electron thermal conductivity (this coefficient depends on the level of plasma turbulence during beam–plasma interaction; to take into account its dependence on the beam parameters, we introduce the approximating function in the form $\zeta = 1 + (\zeta_{\max} - 1)(P(t)/P_{\max})^2 R(n_b/n)$, where the value of $\zeta_{\max} \sim 10^2$–10^3 is determined experimentally; see [19]), $P(t)$ is the beam power, $P_{\max}$ is the maximum beam power, and $R(n_b/n)$ is the measured dependence of the beam energy loss on the ratio of the beam electron density to the plasma density [21]. When the growth rate of the beam instability is lower than the electron collision frequency, the beam energy loss is assumed to be zero. When the mean free path of the plasma particles is on the order of or longer than the scale length of the pressure inhomogeneities, the thermal conductivity is limited by the value $\kappa = \kappa_{\max}(\exp(-\kappa/\kappa_{\max}) - 1)$, where $\kappa_{\max} = q_{\max}/|dT/dz|$, $q_{\max} = 3/(2\sqrt{\pi})(nTV_T)$ is the maximum possible thermal flux of the plasma particles, and V_T is their thermal velocity. The sources $Q_{e,i}$ on the right-hand side of Eqs. (3a) and (3b) describe variations in the energies of the plasma components:

$$Q_e = Q_0 + \partial E/\partial t - \partial(E_{\text{ion}} - E_0)/\partial t + n\nu_\varepsilon^{e/i}(T_i - T_e), \quad (6)$$

$$Q_i = n\nu_\varepsilon^{i/e}(T_e - T_i) - \partial\mu/\partial z, \quad (7)$$

where $\nu_\varepsilon^{e/i} = \nu_\varepsilon^{i/e}$ is the electron–ion collision frequency; $E_0 = \frac{3}{2}n(T_{e0} + T_{i0})$ is the initial plasma energy; $T_{e0} = T_{i0} = T_0$; and $E_{\text{ion}}(n, T)$ is the cost of ionization, which depends on the plasma parameters. The term Q_0 in expression (6) describes plasma heating by the electron beam, and the function $\partial E/\partial t$ in expression (6) describes plasma heating due to the relaxation of the high-energy tail of the plasma electrons:

$$\frac{\partial E(\xi, T_h, t)}{\partial t} = \frac{P(t)\eta_h}{T_hS(\xi)}\int_{\varepsilon'_{\min}}^{\infty}\psi(\xi, T_h, \varepsilon')\exp(-\varepsilon')d\varepsilon'. \quad (8)$$

Here, $\varepsilon' = \varepsilon/T_h$ is the energy of fast electrons normalized to their average energy T_h, $\varepsilon'_{\min}$ is the energy at which the mean free path $R_0 = 2.5\varepsilon/(\Lambda/10)$ is equal to $\langle nl\rangle = \int n(l)dl$, $\xi = \langle nl\rangle/R_0$, and $\psi(\xi, \varepsilon)$ is the function describing electron energy absorption in the target.

The boundary conditions at the ends of the system correspond to cold dense plasma bunches that form in the course of an experiment at the ends of the plasma column. First, this is a nitrogen or krypton plasma bunch through which the current of the linear discharge is closed when the beam is injected into the plasma column and, second, this is the dense plasma near the exit electrodes forming the linear discharge (these electrodes are located downstream from the first exit magnetic mirror of the device).

The initial conditions are chosen such that the system is uniformly filled with deuterium, which is partially ionized by a linear axial discharge at a temperature $T_0(t = 0) \sim 1$ eV. Under our experimental conditions, the initial plasma density is uniform and equal to $n(z) = n_0 = 1.5 \times 10^{21}$ m^{-3}. The initial plasma velocity is equal to zero.

REFERENCES

1. G. I. Budker, in *Plasma Physics and the Problem of Controlled Thermonuclear Reactions*, Ed. by M. A. Leontovich (Izd. Akad. Nauk SSSR, Moscow, 1958; Pergamon, New York, 1959), Vol. 3.
2. A. S. Bishop, *Project Sherwood: the U.S. Program in Controlled Fusion* (Addison-Wesley, Reading, 1958; Gosatomizdat, Moscow, 1960); R. Post, Nucl. Fusion **27**, 10 (1987).
3. V. S. Koidan, R. Yu. Akentjev, A. V. Arzhannikov, *et al.*, Trans. Fusion Sci. Technol. **43** (1T), 30 (2003).

4. L. N. Vyacheslavov, V. S. Burmasov, I. V. Kandaurov, *et al.*, Pis'ma Zh. Éksp. Teor. Fiz. **75**, 44 (2002) [JETP Lett. **75**, 41 (2002)].
5. A. A. Ivanov, G. F. Abdrashitov, A. V. Anikeev, *et al.*, Trans. Fusion Sci. Technol. **43** (1T), 51 (2003).
6. K. Yatsu, T. Cho, M. Higaki, *et al.*, Trans. Fusion Sci. Technol. **43** (1T), 10 (2003).
7. T. D. Akhmetov, V. S. Belkin, I. O. Bespamyatnov, *et al.*, Trans. Fusion Sci. Technol. **43** (1T), 58 (2003).
8. M. Kwon, J. G. Bak, K. K. Choh, *et al.*, Trans. Fusion Sci. Technol. **43** (1T), 23 (2003).
9. M. A. Agafonov, A. V. Arzhannikov, V. T. Astrelin, *et al.*, Plasma Phys. Controlled Fusion **38** (12A), A93 (1996).
10. G. I. Budker, V. V. Mirnov, and D. D. Ryutov, Pis'ma Zh. Éksp. Teor. Fiz. **14**, 320 (1971) [JETP Lett. **14**, 212 (1971)].
11. A. J. Lichtenberg and V. V. Mirnov, in *Reviews of Plasma Physics*, Ed. by B. B. Kadomtsev (Consultants Bureau, New York, 1996), Vol. 19, p. 53.
12. A. V. Arzhannikov, V. B. Bobylev, V. S. Nikolaev, *et al.*, in *Proceedings of the 10th International Conference on High-Power Particle Beams, San Diego, 1994*, Vol. 1, p. 136.
13. B. N. Breizman and D. D. Ryutov, Nucl. Fusion **14**, 873 (1974).
14. B. N. Breizman, in *Reviews of Plasma Physics*, Ed. by B. B. Kadomtsev (Énergoatomizdat, Moscow, 1985; Consultants Bureau, New York, 1987), Vol. 15.
15. A. V. Arzhannikov, V. T. Astrelin, A. V. Burdakov, *et al.*, Trans. Fusion Technol. **39** (1T), 17 (2001).
16. N. I. Arkhipov, A. M. Zhitlukhin, V. M. Safronov, and Yu. V. Skvortsov, Fiz. Plazmy **20**, 868 (1994) [Plasma Phys. Rep. **20**, 782 (1994)].
17. A. V. Burdakov, S. G. Voropaev, V. S. Koĭdan, *et al.*, Zh. Éksp. Teor. Fiz. **109**, 2078 (1996) [JETP **82**, 1120 (1996)].
18. A. V. Burdakov and V. V. Postupaev, Preprint No. 92-9 (Budker Inst. of Nuclear Physics, Siberian Division, Russian Acad. Sci., Novosibirsk, 1992).
19. V. T. Astrelin, A. V. Burdakov, and V. V. Postupaev, Fiz. Plazmy **24**, 450 (1998) [Plasma Phys. Rep. **24**, 414 (1998)].
20. R. Yu. Akentjev, A. V. Arzhannikov, V. T. Astrelin, *et al.*, in *Proceedings of the 29th EPS Conference on Plasma Physics and Controlled Fusion, Montreux, 2002*, Paper P-5.057.
21. A. V. Arzhannikov, V. T. Astrelin, A. V. Burdakov, *et al.*, Trans. Fusion Sci. Technol. **43** (1), 172 (2003).
22. A. V. Burdakov, S. G. Voropaev, V. S. Koĭdan, *et al.*, Fiz. Plazmy **20**, 223 (1994) [Plasma Phys. Rep. **20**, 206 (1994)].
23. R. Yu. Akent'ev, A. V. Burdakov, I. A. Ivanov, *et al.*, Prib. Tekh. Éksp., No. 2, 71 (2004) [Instrum. Exp. Tech. **47**, 224 (2004)].
24. A. V. Burdakov, V. V. Postupaev, A. F. Rovenskikh, and Yu. S. Sulyaev, *X All-Russia Conference on the Diagnostics of High-Temperature Plasmas, Troitsk, 2003*, Abstracts of Papers, p. 42.
25. A. V. Arzhannikov, V. T. Astrelin, A. V. Burdakov, *et al.*, Pis'ma Zh. Éksp. Teor. Fiz. **77**, 426 (2003) [JETP Lett. **77**, 358 (2003)].
26. L. D. Landau and E. M. Lifshitz, *Quantum Mechanics: Non-Relativistic Theory* (Nauka, Moscow, 1989; Pergamon, Oxford, 1977).
27. A. A. Ivanov, L. L. Kozorovitskiĭ, and V. D. Rusanov, Dokl. Akad. Nauk SSSR **184**, 811 (1969) [Sov. Phys. Dokl. **14**, 126 (1969)].
28. S. I. Braginskii, in *Reviews of Plasma Physics*, Ed. by M. A. Leontovich (Gosatomizdat, Moscow, 1963; Consultants Bureau, New York, 1965), Vol. 1.

Translated by N.F. Larionova

Plasma Physics Reports, Vol. 31, No. 6, 2005, pp. 476–483. Translated from Fizika Plazmy, Vol. 31, No. 6, 2005, pp. 521–529.

PLASMA OSCILLATIONS AND WAVES

Experiments on Cross-Polarization Scattering in the Upper Hybrid Resonance Region

A. D. Gurchenko, E. Z. Gusakov, M. M. Larionov, K. M. Novik, V. L. Selenin, and A. Yu. Stepanov

Ioffe Physicotechnical Institute, Russian Academy of Sciences, Politekhnicheskaya ul. 26, St. Petersburg, 194021 Russia

Received May 26, 2004

Abstract—In experiments on the FT-1 tokamak, the effect is observed of the cross-polarization scattering of microwave radiation by low-frequency plasma microturbulence in the upper hybrid resonance region. The radar diagnostics based on this effect was used to measure the frequencies and wavenumbers of the fluctuations that cause cross-polarization scattering. © *2005 Pleiades Publishing, Inc.*

1. INTRODUCTION

The development of the methods for diagnosing the magnetic component of plasma microturbulence in tokamaks is of importance in view of the problem of anomalous electron transport [1]. Magnetic fluctuations are traditionally measured by probes, which can, however, be used only at the plasma periphery [2]. The level of magnetic turbulence in hot plasmas is usually estimated from the lifetime of runaway electrons. This method provides data averaged over the duration and cross section of the discharge and over the fluctuation spectrum [3]. Diagnostics based on the collective scattering of electromagnetic waves are difficult to apply to magnetic fluctuations because of their low amplitude: $\delta B/B \approx (10^{-5}$–$10^{-4})$, which is two orders of magnitude lower than the amplitude of density fluctuations measured by conventional scattering diagnostics. There is yet, however, a possibility to diagnose magnetic fluctuations using the effect of cross-polarization scattering (CPS). In this method, the probing and scattered waves propagate normally to the external magnetic field [4–6]. Since, in this case, plasma density fluctuations do not cause depolarizing scattering, the CPS method makes it possible to detect lower amplitude magnetic fluctuations.

The CPS diagnostics of magnetic fluctuations was employed in the Tore Supra tokamak [7]. It provided the first direct measurements of magnetic fluctuations and their correlation with electron heat transport. In these pioneering studies, a receiving antenna with a high mode selectivity was protected from a direct fall of the extraordinarily polarized probing radiation by the cutoff surface. Nevertheless, the parasitic signal from the small-angle scattering of the extraordinary wave by density fluctuations still could reach the receiving antenna after multiple depolarizing reflections from the cutoff surface and chamber wall. Another drawback of the experimental technique used in [7] was a questionable estimate of the localization of the CPS region by the position of the cutoff surface for the probing wave and, accordingly, an unreliable estimate of the fluctuation wave vector (see [8, 9]).

An alternative scheme of CPS diagnostics based on the scattering in the upper hybrid resonance (UHR) region was proposed in [8, 9]. In this scheme, the extraordinary probing wave is launched in the equatorial plane from the high-field side. As the wave propagates across the magnetic field, it traverses the region of the electron-cyclotron resonance (ECR), where it undergoes slight damping [10] (for moderate-scale machines with an electron temperature of $T_e < 4$ keV). The UHR position in the equatorial plane, R_{UH}, is determined by the equality

$$\omega_i^2 = \omega_{ce}^2(R_{UH}) + \omega_{pe}^2(R_{UH}), \qquad (1)$$

where ω_i is the probing frequency, ω_{ce} is the electron cyclotron frequency, and ω_{pe} is the plasma frequency. In the vicinity of the UHR, the projections of the wave vector of the probing wave k_i and the wave electric field on the gradient of the permittivity $\varepsilon = 1 - \omega_{pe}^2/(\omega_i^2 - \omega_{ce}^2)$ (for equatorial probing, this gradient is directed along R) increase sharply. In this region, the CPS of the probing wave by the small-scale fluctuations [8, 9] with a broad spectrum of radial wavenumbers $\omega_{ce}/c < q_R \leq \rho_{ce}^{-1}$ can occur (here, ρ_{ce} is the electron cyclotron radius and c is the speed of light). The ordinarily polarized CPS signal is received from the low-field side by an antenna that is also situated in the equatorial plane. The opaque region, whose thickness is much larger than the wavelength of the probing wave, protects the receiving antenna from a direct fall of the extraordinary wave. With this one-dimensional probing scheme, resolution

1063-780X/05/3106-0476$26.00 © 2005 Pleiades Publishing, Inc.

in wavenumbers can be achieved using the time-of-flight [11] or correlation [12] techniques.

The theory of CPS in the UHR region [9] predicts that, contrary to the commonly accepted view [4–6], the nonlinear ponderomotive force (which is proportional to $(\mathbf{v}_\Omega \cdot \nabla) \cdot \mathbf{v}_i + (\mathbf{v}_i \cdot \nabla) \cdot \mathbf{v}_\Omega$) is not negligibly small as compared to the Lorentz force (which is proportional to $\mathbf{v}_i \times \mathbf{B}_\Omega$) in the electron-cyclotron frequency range (here, $\mathbf{v}_\Omega$ is the low-frequency component of the electron flow velocity, $\mathbf{v}_i$ is the velocity perturbation in the field of the probing wave, and $\mathbf{B}_\Omega$ is a low-frequency fluctuation of the magnetic field). Moreover, in the UHR region, the nonlinear ponderomotive force dominates. The CPS effect, in this case, is caused by fluctuations of the longitudinal electron current, which are related to magnetic field fluctuations via Ampére's law. Simulations performed in a one-dimensional planar model under the assumption that the directional patterns of the probing and receiving antennas are narrow show that the efficiency of CPS in the UHR region is proportional to the squared radial wavenumber of fluctuations, $(q_R c/\omega_{ce}(R_{UH}))^2$. A one-dimensional analysis performed for the case of oblique propagation also shows that, in conventional tokamaks, the parasitic CPS signal caused by density fluctuations in the UHR region is substantially suppressed due to the presence of the small factor $(\omega_{pe}^8/\omega_{ce}^6\omega_i^2)_{UH}$. An important advantage of the proposed diagnostic scheme is that the scattering by small-scale fluctuations in the UHR region is highly localized.

The first experimental results on CPS in the UHR region were reported in [13] and were also mentioned [11], which was devoted to the application problems of radar techniques. This study presents a detailed description of the experiments on CPS by low-frequency small-scale fluctuations in the UHR region in the FT-1 tokamak with the use of the time-of-flight scheme. The experimental setup is described in Section 2, and the experimental results are described and discussed in Section 3. In Section 4, the amplitude of magnetic fluctuations in the FT-1 tokamak is estimated using the results of CPS measurements.

2. EXPERIMENTAL SETUP

The experiments on CPS in the UHR region were carried out in the FT-1 tokamak [14] with the large radius $R_0 = 62.5$ cm and limiter radius $a = 15$ cm. The measurements were performed in the quasi-steady phase of the discharge at a plasma current of $I_P \approx 30$ kA, an electron density of $n_e(R_0) \approx 10^{13}$ cm^{-3}, and an electron temperature of $T_e(R_0) \approx 400$ eV. The toroidal magnetic field B_T at the chamber axis could be varied from 0.69 to 1.2 T. This allowed us to operate in regimes in which the UHR surface was either accessible or inaccessible for the probing wave, as well as to vary the spatial position of this surface.

The probing wave was launched and the scattered signal was received by two horn antennas installed in front of one another in the equatorial plane of the torus. The antenna emitting extraordinary (X) waves with a <1% admixture of an ordinary (O) wave was set on the high-field side. The beamwidth of this antenna at a level of –3 dB was 16° (±8° with respect to the equatorial plane). The round-horn receiving antenna with an aperture of $D = 3.6$ cm was installed on the low-field side. The O- or X-polarized scattered signal was selected using a rotatable transition to a rectangular waveguide operating at the fundamental mode (at a probing frequency of 28 GHz). The UHR surface was always in the Fresnel zone of this antenna. Calibration experiments showed that the mode selectivity of this antenna was better than 5%. Various probing and receiving schemes were used: X ⟶ O with launching the probing wave from the high-field side, O ⟶ X with launching the probing wave from the low-field side, and X ⟶ X with launching the probing wave from the high-field side.

Resolution in the radial wavenumbers of the scattering fluctuations was achieved using the time-of-flight technique based on the effect of the slowing down of extraordinary waves in the UHR region. The delay time of the signal scattered from the UHR region (in particular, the X ⟶ O CPS signal) is related to the wavenumber $q_R = k_i(R_s)$ of the fluctuations that cause forward scattering [15] via the following simple formula:

$$t_d = \int_{R_a}^{R_s(q_R)} dx/V_g + t_w, \qquad (2)$$

where R_s is the radial position of the scattering point, R_a is the position of the probing antenna, V_g is the projection of the wave group velocity on the major radius (in Fig. 1b, curve *3* shows the group velocity of an extraordinary wave propagating toward the UHR and curve *4* shows the group velocity of a Bernstein wave propagating away from the UHR), and t_w is the time delay related to the propagation of microwave radiation in waveguides. The time during which the scattered ordinary wave propagates from the UHR region to the receiving antenna (<0.07 ns) can be ignored compared to the total delay in the plasma, $t_d - t_w > 10$ ns. In what follows, by the delay time t_d we mean the delay in plasma, $t_d - t_w$, since the waveguide delay t_w can be eliminated when calibrating the system. Curve *1* in Fig. 1a shows the delay time as a function of the fluctuation wavenumber (see formula (2)) for $B_T = 1$ T. The curve $t_d(q_R)$ deviates from the linear dependence predicted in [15] under the assumption that scattering point lies near the UHR (Fig. 1a, curve *2*) only after the probing wave is linearly converted into a strongly slowed-down ($V_g \approx 10^8$ cm/s) electron Bernstein wave.

The delay time of the scattered signal with respect to the probing pulse (and, accordingly, the radial wave-

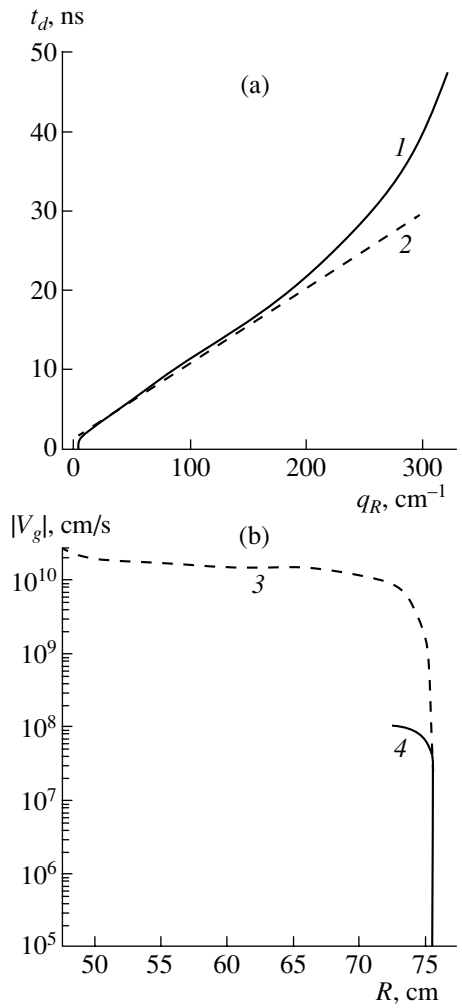

Fig. 1. (a) Delay time of the signal scattered forward from the UHR region as a function the radial wavenumber of scattering fluctuations in a warm plasma: (*1*) calculation by formula (2) and (*2*) analytical estimate from [15]. (b) Group velocity of an extraordinary wave (curve *3*) and a Bernstein wave (curve *4*) vs. major radius.

number q_R of the scattering fluctuations) was measured using the radar probing technique [11]. The probing wave at a frequency of 28 GHz was modulated in amplitude by a sequence of short pulses with a full width at half-maximum of τ = 3.5 ns and repetition period of T = 70 ns and then was launched into the plasma through the horn antenna. Without modulation, the antenna output power was no higher than 20 W. The scattered radiation was received by the antenna placed on the opposite side of the plasma column. Gating the received radiation by the same sequence of pulses allowed us to separate from the scattered signal the component corresponding to a given delay time. The delay time was determined from the shift between the modulating and gating pulses. When calibrating the system, this shift was set at zero in order to eliminate the waveguide delay t_w. The calibration was performed with an empty chamber (without plasma). The X-polarized probing radiation was received by the opposite antenna tuned to the same polarization (X ⟶ X). After superheterodyne reception and amplification, the frequency spectra $p_s(f_s - f_i)$ (where f_i and f_s are the frequencies of the probing and scattered radiation, respectively) of the signal fraction cut out by the strobe gate were analyzed using a spectrum analyzer with a 2-ms time resolution. In calibrating, the spectrum displayed only a narrow line at $f_s - f_i = 0$, corresponding to the probing frequency, whereas in the presence of plasma, the spectrum was broadened due to the scattering by low-frequency fluctuations.

3. OBSERVATIONS OF CPS IN THE UHR REGION

The $X \longrightarrow O$ CPS spectra of the radiation scattered forward from the UHR region at B_T = 1 T ($x_{UH} = R_{UH} - R_0 \approx 13$ cm) are shown in Fig. 2a. Curve *1* shows the spectrum measured without gating (continuous reception). This spectrum has broad wings spreading from 0.3 to 2 MHz. Within this interval, the spectral density of the scattered signal decreases by more than 20 dB and reaches the noise level (determined by the suprathermal electron cyclotron radiation) at $f_s - f_i$ = 2 MHz. With gating, the sensitivity of the method does not decrease because both the signal and the noise decrease by a factor of 20, in proportion to the off-duty factor of the probing pulses. The spectra obtained for delay times of t_d = 5, 15, and 40 ns are shown in Fig. 2a by curves *2*, *3*, and *4*, respectively. Similarly to spectrum *1*, these spectra have broad and fairly slowly decaying (quasi-Lorentzian) wings spreading to $f_s - f_i$ = 2 MHz. The maximum amplitude of the spectrum decreases monotonically with delay time to a saturation level, which is reached at t_d = 30 ns. The saturation level is determined by the scattering of the residual continuous probing wave passing through the modulator and attenuated by 20 dB. In contrast to the maximum amplitude, the behavior of the spectral wings is nonmonotonic. For frequencies shifted from the probing one by more than 0.3 MHz, the scattered signal first increases and then decreases with increasing delay time. This is illustrated in Fig. 2b for four different spectral components of the signal with frequencies of (*1*) 0.33, (*2*) 0.6, (*3*) 1.0, and (*4*) 1.5 MHz. The curves were plotted using the experimental points taken from the spectra obtained at different delay times. By using curve *1* in Fig. 1a, we calculated the corresponding dependences of the power of the same spectral components on the radial wavenumber of the scattering fluctuations (Fig. 2c). It can be seen from Fig. 2a that the spectrum width increases with delay time. The spectrum width was determined at a certain power level (e.g., –3 dB or –10 dB) with respect to the maximum of the spectrum.

The CPS effect was also observed when probing from the low-field side by the O ⟶ X scheme. The spectra recorded at a magnetic field of 1 T (Fig. 3a,

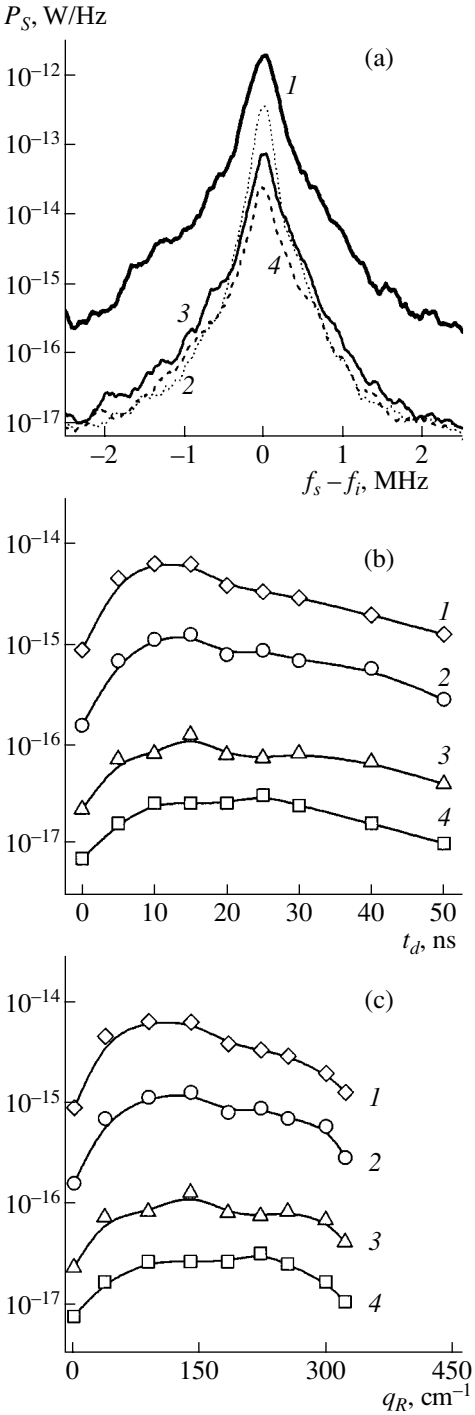

Fig. 2. (a) CPS spectra (X ⟶ O) for $B_T = 1$ T: curve *1* corresponds to continuous reception, and curves *2*, *3*, and *4* correspond to delay times of 5, 15, and 40 ns, respectively. The power of the CPS signal at frequencies of (*1*) 0.33, (*2*) 0.6, (*3*) 1.0, and (*4*) 1.5 MHz as a function of (b) the delay time and (c) the radial wavenumber of fluctuations.

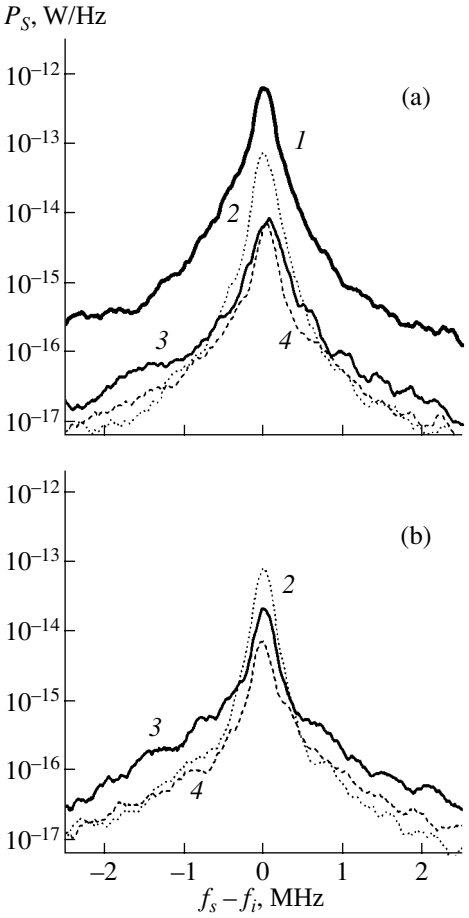

Fig. 3. CPS spectra (O ⟶ X) for B_T = (a) 1.0 and (b) 1.1 T: curve *1* corresponds to continuous reception, and curves *2*, *3*, and *4* correspond to delay times of 5, 15, and 40 ns, respectively.

$x_{UH} \approx 13$ cm) resemble the spectra shown in Fig. 2a, whereas the spectra recorded at 1.1 T (Fig. 3b, $x_{UH} \approx 14$ cm) are appreciably wider (the spectral density remains substantial at frequency shifts of up to 2.5 MHz). In both cases, the spectra display the same features as those observed when probing from the high-field side. The spectral wings for a delay time of 15 ns (Fig. 3, curves *3*) are higher by 5–10 dB than those for a delay time of 5 ns (curves *2*) or 40 ns (curves *4*). The nonmonotonic dependence of the signal power on the delay time and, consequently, on the radial wavenumber of the scattering fluctuations is illustrated in Fig. 4 for four different frequencies: (*1*) 0.33, (*2*) 0.6, (*3*) 1.0, and (*4*) 1.5 MHz. These dependences were obtained for three different magnetic fields (and accordingly, to different UHR positions): $B_T = 1$ T (Fig. 4a, $x_{UH} \approx 13$ cm), 1.1 T (Fig. 4b, $x_{UH} \approx 14$ cm), and 0.85 T (Fig. 4c, $x_{UH} \approx 11.5$ cm). At the plasma periphery, the point at which the probing wave is linearly transformed into a Bernstein wave shifts toward larger wavenumbers due to the decrease in the electron temperature. This is why the dependences in Fig. 4b measured for delay times of up to 50 ns extend farther (up to 450 cm^{-1}) and reach the level of the nondelayed signal, which corresponds to small q_R. At a magnetic field of 1 T (Figs. 2c, 4a), a 50-ns time delay was insufficient to reach the initial sig-

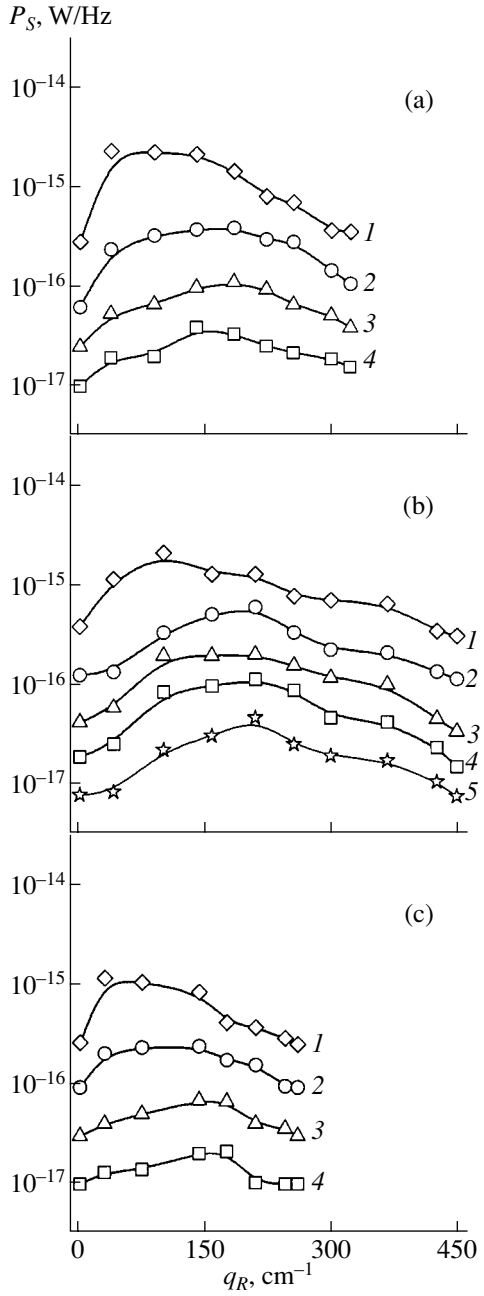

Fig. 4. Spectral power of the O ⟶ X CPS signal at frequencies of (*1*) 0.33, (*2*) 0.6, (*3*) 1.0, (*4*) 1.5, and (*5*) 2.5 MHz as a function of the radial wavenumber of fluctuations for B_T = (a) 1.0, (b) 1.1, and (c) 0.85 T.

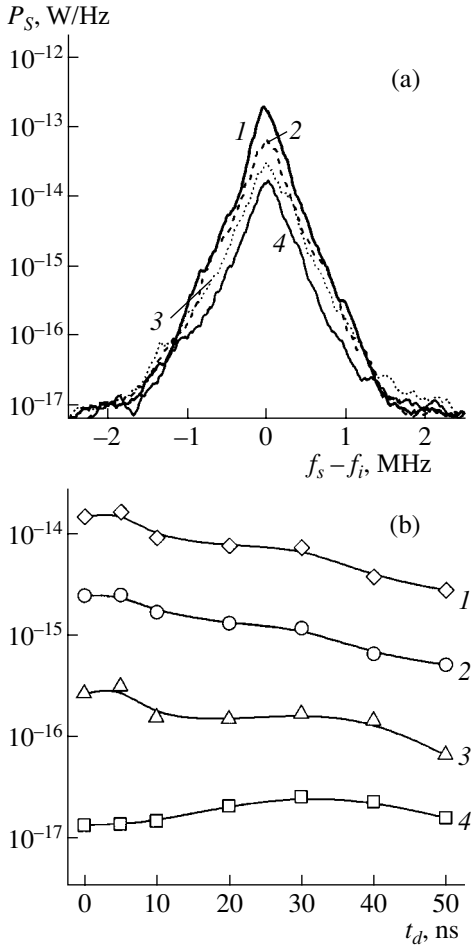

Fig. 5. (a) X ⟶ X spectra for B_T = 1 T and different delay times: t_d = (*1*) 5, (*2*) 10, (*3*) 30, and (*4*) 50 ns). (b) Spectral power of the X ⟶ X signal at frequencies (*1*) 0.33, (*2*) 0.6, (*3*) 1.0, and (*4*) 1.5 MHz vs. delay time.

nal level. For weaker magnetic fields, the frequency spectra were narrower and the spectral wings were lower by 3–7 dB; this is probably related to a decrease in the relative level of fluctuations in the plasma core. A significant feature of the above dependences is the shift of the maximum of the scattered signal toward larger radial wavenumbers and higher frequencies of turbulent fluctuations. This effect has the form of a dispersion curve: $\omega \sim V_R q_R$, where $V_R \approx 0.7$–0.9 km/s.

An unexpected result was that, when probing from the high-field side, we observed a substantial signal with an unchanged polarization from the low-field side (X ⟶ X). Figure 5a shows the spectra recorded at a magnetic field of 1 T for different delay times: (*1*) 5, (*2*) 10, (*3*) 30, and (*4*) 50 ns. The peak amplitudes of the spectra are comparable to those observed in the X ⟶ O and O ⟶ X schemes; however, the spectra in Fig. 5a, plotted on a log-linear scale, show a clear triangular shape. This is why the spectra for delay times lesser than 20 ns are wider than in the case of CPS. The signal power as a function of the delay time is shown in Fig. 5b for frequencies of 0.33 (*1*), 0.6 (*2*), 1.0 (*3*), and 1.5 MHz (*4*). In contrast to the case of CPS, the X ⟶ X signal at frequencies lower than 1.5 MHz decreases monotonically with delay time. At these frequencies, the X-mode signal is higher than the CPS signal by 2–10 dB at $t_d < 15$ ns and by 2–4 dB at $t_d > 20$ ns.

It should be noted that the wide X-mode spectra recorded from the low-field side at large delay times

cannot be caused by scattering in the UHR region. Since the thickness of the opaque region between the cutoff and UHR surfaces is $\Delta R \approx 1.2$ cm, which is by a factor of 20–30 larger than the wavelength of the probing radiation in the UHR region, the slowed-down forward-scattered extraordinary wave must be suppressed by eight to thirteen orders of magnitude. The most probable reason for the appearance of an intense X-mode signal is depolarizing wall reflections of the parasitic O-mode component of the probing wave. The spectral broadening of such a signal can be caused by the propagation of the nascent extraordinary wave through the turbulence zone between the wall and the cutoff surface. Similar spectra slowly decaying over time were observed in reflectometric measurements in [11], where the extraordinary wave turned out to be trapped in a high-Q cavity between the horn antenna and the cutoff surface.

At first glance, the presence of a high-power X-mode signal at the low-field side casts some doubt on the origin of the weaker O-mode signal due to CPS in the UHR region. However, the antenna selectivity at the low-field side enables the 95% suppression of the power of the extraordinary wave falling directly into the horn tuned to the ordinary wave. Since the intensity of the X-mode signal exceeds the CPS signal by no more than 2–10 dB, the high level of the CPS signal cannot be explained by a direct fall of the extraordinary wave into the receiving horn. A more complicated mechanism involving double reflection from the wall and single X ⟶ O depolarization is also of minor importance because of the significant suppression of the signal caused by the attenuation of the extraordinary wave as it penetrates through the opaque barrier and is then depolarized and by the subsequent double cyclotron absorption of the ordinary wave and its strong refraction in the plasma core, where plasma density is close to the critical one. At the same time, the most convincing argument in favor of the assumption that the CPS signal observed in the X ⟶ O experimental scheme comes from the UHR region is the nonmonotonic dependence of the signal on the delay time, as well as the shape of the spectrum, which is rather different from that in the X ⟶ X case. The delay of the main fraction of the CPS signal by 15–30 ns can be attributed only to the slowing down of the probing wave in the UHR region. It should be noted that the delay time of the CPS signal significantly exceeds that of the signal backscattered from the UHR region (about 10 ns [11]). Thus, the occurrence of the X ⟶ O signal cannot also be explained by depolarization reflections from the tokamak wall of the extraordinary wave backscattered from the UHR region.

To confirm the decisive role of the UHR in the onset of the CPS signal, we performed measurements at B_T = 0.69 T ($R_{UH} \approx -14.0$ cm). In this case, the cutoff surface encloses the UHR region ($R_c \approx -14.9$ cm) so that it is inaccessible for the probing wave. The corresponding

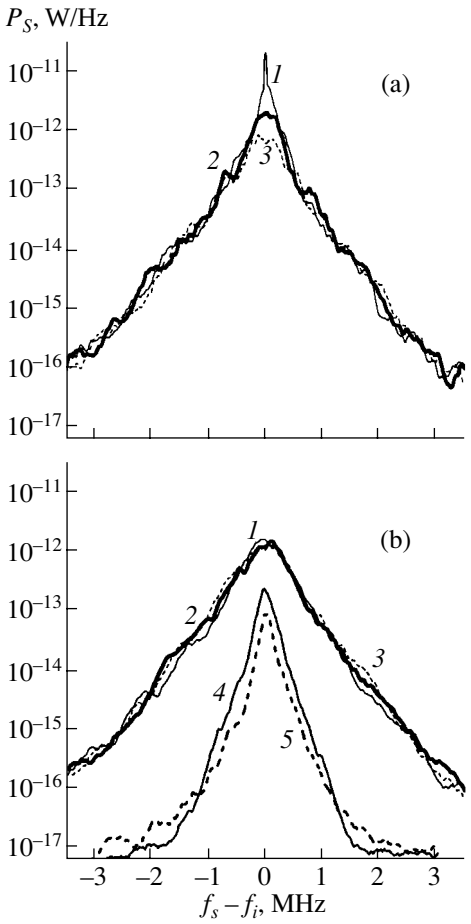

Fig. 6. (a) X ⟶ O and (b) *X* ⟶ *X* scattered spectra observed from the low-field side for (a) B_T = 0.69 T (the UHR surface is inaccessible for the probing wave) and (b) B_T = 1 T at t_d = (*1*) 2.5, (*2*) 5, and (*3*) 15 ns. Curves *4* and *5* show the *X* ⟶ *X* spectrum for a delay time of 5 ns and the X ⟶ O spectrum for a delay time of 15 ns, respectively.

X ⟶ O spectra observed from the high-field side are shown in Fig. 6a. For the signal delayed by 2.5 ns (curve *1*), we observed a broad triangular spectrum with a narrow line at the probing frequency, which disappeared at a delay time of 5 ns (curve *2*). This narrow short-lived line presumably corresponds to the parasitic O-mode component of the probing pulse. A further increase in the delay time to 15 ns (curve *3*) only decreases the spectrum amplitude and does not affect its width. The X ⟶ X spectra measured under the same conditions for the same delay times of (*1*) 2.5, (*2*) 5, and (*3*) 15 ns are shown in Fig. 6b. They resemble the above O-mode spectra but do not have a narrow peak at short delay times. The main feature of the spectra observed at a low magnetic field is an insignificant decrease in the amplitude of the scattered signal. This is probably related to the electron cyclotron resonance for the probing wave being absent in the plasma volume. For comparison, Fig. 6b also shows (on the same scale)

the above X ⟶ X (5 ns, curve *4*) and X ⟶ O (15 ns, curve 5) spectra measured at $B_T = 1$ T. It can be seen that not only the temporal behavior of the scattered spectra but also their width and shape change appreciably when the UHR surface is inaccessible for the probing wave.

4. ESTIMATE OF THE LEVEL OF MAGNETIC FLUCTUATIONS

In the previous section, it has been shown that, although the X ⟶ O signal is observed simultaneously with intense X-mode signals at both the high-field side (enhanced scattering signal) and the low-field side (X ⟶ X signal), the X ⟶ O signal is nevertheless caused by the CPS of the probing wave by small-scale fluctuations in the UHR region. Taking into account that the small-angle CPS by density fluctuations in the UHR region is significantly suppressed [9], we ascribe the observed CPS signal to the magnetic component of turbulence. To estimate the level of magnetic fluctuations, we used the wavenumber spectrum of fluctuations obtained by interpolating the frequency spectra (Figs. 2a and 3) measured with resolution in wavenumbers. The major contribution to magnetic turbulence comes from low-frequency fluctuations, which dominate in the CPS spectrum. The spectrum of low-frequency magnetic fluctuations was described by the approximating formula

$$\int \left|\frac{\delta B}{B_0}\right|^2_{\mathbf{q},\Omega} \frac{dq_z}{2\pi} = \frac{b^2\Omega_0^{2\alpha}\exp(-|\mathbf{q}_\perp|/q_0)}{(\Omega^2 + |\mathbf{q}_\perp|^2 V^2)^\alpha}, \qquad (3)$$

where $\Omega = 2\pi(f_s - f_i)$ is the fluctuation frequency and $\mathbf{q}_\perp$ is the transverse (with respect to the magnetic field) component of the fluctuation wave vector. The parameters V, α, and q_0 describe the shape of the spectrum, while the parameter $b^2\Omega_0^{2\alpha}$ describes its amplitude. These parameters were determined using the theoretical formula relating the spectral density of the CPS signal to the spectrum of magnetic fluctuations $S(q_R, \Omega)$ (see [9], formula (11)).

When deriving formula (3), we also used the expression for the power p_s^0 of the scattered signal at the central line ω_0 of the spectrum of the amplitude-modulated probing wave. Since, in spectral measurements, we used only one spectral line arising due to the modulation of the probing and scattered radiation, the signal power decreased in proportion to the off-duty factor T/τ. If we represent the waveform of the probing signal as a sequence of Gaussian pulses, $A_i(t) = A_0 \sum_{n=-\infty}^{n=\infty} \exp\left(-i\omega_0 t - \frac{(t-nT)^2}{\tau^2}\right)$, then the central line of scattered spectrum can be expressed as

$$p_s^0 = |A_0|^2 \pi \frac{\tau^2}{T^2} \int_0^\infty \frac{dq_R}{2\pi} S(q_R, \Omega) \exp\left(-\frac{\left(q_R \frac{\partial R_{UH}}{\partial \omega_i} + t_d\right)^2}{\tau^2}\right), \qquad (4)$$

where the maximum delay time t_d is shorter than the pulse repetition period T.

The mean values of the interpolation parameters at which expression (3) best fits the measured spectra are $\alpha \approx 1.5$, $V \approx 5 \times 10^3$ cm/s, and $q_0 \approx 90$ cm^{-1}.

In accordance with the one-dimensional planar model [9], the parameter $b^2\Omega_0^{2\alpha}$ was determined with account of the attenuation of the extraordinary wave due to refraction (about 6×10^{-2}) and the attenuation of the radar signal due to amplitude modulation (see formula (4)). The resulting value is $b^2\Omega_0^{2\alpha} \approx 70$.

Extrapolating formula (3) to long scales $q_R < \omega_{ce}/c$ and assuming that fluctuations are distributed uniformly across the magnetic field, the relative intensity of magnetic fluctuations can be written as

$$\left|\frac{\delta B}{B_0}\right|^2 = \int \frac{d^3\mathbf{q}\,d\Omega}{(2\pi)^4} \left|\frac{\delta B}{B_0}\right|^2_{\mathbf{q},\Omega} = \frac{b^2\Omega_0^3}{2\pi^2 V^2} \ln\frac{q_0}{q_{\min}}, \qquad (5)$$

where $q_{\min} = 3$ cm^{-1} corresponds to the maximum turbulence scale, which may be assumed to be equal to the distance between the UHR region and the diaphragm (about 2 cm). After substituting the above approximation parameters into formula (5), we obtain a rough estimate for the amplitude of magnetic field perturbations: $\delta B/B_0 \le 7 \times 10^{-4}$.

This value is higher than conventional estimates obtained from magnetic measurements in the edge plasma or from the analysis of the loss of runaway electrons. The discrepancy can be attributed to the imperfect extrapolation procedure or the incorrect interpretation of the CPS spectra. In particular, the assumption that the most intense central part of the CPS spectrum is associated with the scattering by magnetic fluctuations can lead to an overestimated level of magnetic turbulence. Indeed, the central line did not show a nonmonotonic dependence on the delay time, which is typical of the CPS signal. Hence, this part of the spectrum may be (at least partially) produced due to small-angle scattering of the parasitic O-mode that is present in the probing radiation and propagates in the cavity formed by metal wall of the tokamak.

5. CONCLUSIONS

The CPS of the probing microwave radiation by magnetic fluctuations in the UHR region has been observed experimentally. The experiments have shown

that, in accordance with theoretical predictions [4, 8, 9], the CPS of an extraordinary probing wave excited at the high-field side into an ordinary wave detected at the low-field side is almost identical to the CPS of an ordinary wave excited at the low-field side into an extraordinary wave detected at the high-field side. The time-of-flight technique based on the effect of the slowing down of extraordinary waves in the UHR region was employed for local CPS measurements of the spectra of the magnetic component of low-frequency (below 2 MHz) small-scale (0.14–11 mm) turbulence with resolution in radial wavenumbers. It is shown that the shape of the CPS spectrum and its dependence on the delay time differ substantially from those observed in the experiments in which the scattered radiation with an unchanged polarization was received from the low-field side.

ACKNOWLEDGMENTS

This study was supported by the Russian Foundation for Basic Research (project no. 05-02-16569), the RF Presidential Program on State Support of Leading Scientific Schools (grant no. NSh-2159.2003.2), INTAS (grant nos. YSF2002-104, 01-2056), and the Netherlands Organization for Scientific Research (NWO) in cooperation with the Russian Foundation for Basic Research (grant NWO–RFBR no. 047-016-015).

REFERENCES

1. A. B. Rechester and M. N. Rosenbluth, Phys. Rev. Lett. **40**, 58 (1978).
2. S. J. Zweben, C. R. Menyuk, and R. J. Taylor, Phys. Rev. Lett. **42**, 1270 (1979).
3. C. W. Barnes and J. D. Strachan, Phys. Fluids **26**, 2668 (1983).
4. T. Lehner, D. Gresillon, X. L. Zou, *et al.*, in *Proceedings of the 12th EPS Conference on Controlled Fusion and Plasma Physics, Budapest, 1985*, Vol. II, p. 644.
5. T. Lehner, J. M. Rax, and X. L. Zou, Europhys. Lett. **8**, 759 (1989).
6. L. Vahala, G. Vahala, and N. Bretz, Phys. Fluids B **4**, 619 (1992).
7. X. L. Zou, L. Colas, M. Paume, *et al.*, Phys. Rev. Lett. **75**, 1090 (1995).
8. E. Z. Gusakov, in *Proceedings of the 25th EPS Conference on Controlled Fusion and Plasma Physics, Prague, 1998*, ECA **22C**, 39 (1998).
9. E. Z. Gusakov, Fiz. Plazmy **28**, 627 (2002) [Plasma Phys. Rep. **28**, 580 (2002)].
10. Yu. F. Baranov and V. I. Fedorov, Fiz. Plazmy **9**, 677 (1983) [Sov. J. Plasma Phys. **9**, 391 (1983)].
11. D. G. Bulyiginskiy, A. D. Gurchenko, E. Z. Gusakov, *et al.*, Phys. Plasmas **8**, 2224 (2001).
12. A. D. Gurchenko, E. Z. Gusakov, M. M. Larionov, *et al.*, in *Proceedings of the 27th EPS Conference on Controlled Fusion and Plasma Physics, Budapest, 2000*, ECA **24B**, 416 (2000).
13. D. G. Bulyginskiy, A. D. Gurchenko, E. Z. Gusakov, *et al.*, in *Proceedings of the 25th EPS Conference on Controlled Fusion and Plasma Physics, Prague, 1998*, ECA **22C**, 1546 (1998).
14. I. P. Gladkovskiĭ, V. E. Golant, V. V. D'yachenko, *et al.*, Zh. Tekh. Fiz. **43**, 1632 (1973) [Sov. Phys. Tech. Phys. **18**, 1029 (1973)].
15. E. Z. Gusakov and A. D. Piliya, Pis'ma Zh. Tekh. Fiz. **18** (10), 63 (1992) [Sov. Tech. Phys. Lett. **18**, 325 (1992)].

Translated by N.N. Ustinovskiĭ

Plasma Physics Reports, Vol. 31, No. 6, 2005, pp. 484–492. Translated from Fizika Plazmy, Vol. 31, No. 6, 2005, pp. 530–538.

BEAMS IN PLASMA

Nonlinear Theory of the Low-Frequency Interaction of Ion Beams with the Virtual Cathode of a Relativistic Electron Beam

V. A. Balakirev, N. I. Onishchenko, and I. N. Onishchenko

National Science Center Kharkov Institute of Physics and Technology, ul. Akademicheskaya 1, Kharkov, 310108 Ukraine

Received March 15, 2004; in final form, June 3, 2004

Abstract—A study was made of the nonlinear low-frequency interaction of a longitudinal ion beam with a virtual cathode of a relativistic high-current electron beam injected into a cylindrical drift chamber. Cases are considered in which the electron and ion beams have the same radii and in which the radius an ion beam is greater than that of an electron beam. © *2005 Pleiades Publishing, Inc.*

1. INTRODUCTION

Low-frequency (LF) ion oscillations play an important role in the dynamics of high-current long-duration (about one microsecond or more) relativistic electron beams (REBs). LF ion processes manifest themselves most markedly in such devices and apparatuses as vircator microwave oscillators [1], pasotrons [2–4], and also collective ion accelerators [5–8]. In vircators with a plasma anode [1], intense ion beams form just inside the device. The excitation of LF ion oscillations in such systems can lead to the LF modulation of the generated microwave radiation and can give rise to fast ion beams. This is also true for pasotrons, in which long-duration electron beams are focused by means of a plasma.

In collective ion accelerators whose operation is based the double (spatial and temporal) modulation of an REB [5], the LF relaxation ion oscillations can affect the electron virtual cathode (VC) so as to produce a deep modulation of the REB current at low frequencies (on the order of several tens of megahertz) [8]. In the present paper, we report the results from investigations of the nonlinear interaction of ion beams with the VC of a high-current REB.

2. PHYSICAL MODEL AND BASIC EQUATIONS

We consider a drift chamber in the form of a semi-infinite metal tube whose end at $z = 0$ is a perfectly conducting diaphragm, through which two charged particle beams (an REB and a nonrelativistic ion beam) are injected. The system is placed in a uniform axial magnetic field. The electrons are assumed to be magnetized, and the effect of the magnetic field on the ion motion is ignored. Such a situation can easily be realized in experiments [8] because of the large difference in the masses of electrons and ions and, accordingly, in their gyroradii. The electron current is assumed to be higher than the vacuum limiting current. For a thin-walled annular REB in the absence of an ion beam, the vacuum limiting current is given by the expression [9]

$$I_{\lim} = I_A \frac{(\gamma_0^{2/3} - 1)^{3/2}}{2\ln(a/r_e)},$$

where $I_A = \dfrac{mc^3}{e} = 17$ kA, γ_0 is the relativistic factor, a is the radius of the drift chamber, and r_e is the REB radius. When the injected ions enter the VC region, they exert a neutralizing effect on the electron space charge. As a result, the electron VC will evolve in both space and time.

The nonlinear interaction of an ion beam with an electron VC is described by the following approach. The ions and electrons are both modeled as infinitely thin ring-shaped macroparticles. The laws of motion of macroparticles are treated in terms of the dependence of the radii of the rings, $r_{i,e} = r_{Li,e}(t, t_{0i,e})$, and the longitudinal coordinates of their centers, $z_{i,e} = z_{Li,e}(t, t_{0i,e})$, on time. Here, the subscripts i and e refer to the ions and electrons, respectively; t is the running time; and $t_{0i,e}$ is the time at which the corresponding macroparticle flies into the drift chamber.

The macroparticle density is given by the expression

$$dn_{e,i} = dN_{0e,i} \frac{\delta(r - r_{Le,i})}{2\pi r_{Le,i}} \delta(z - z_{Le,i}), \qquad (1)$$

where r and z are the radial and longitudinal coordinates and $dN_{0e,i}$ is the number of particles in the corresponding infinitely thin ring. The number of particles in

1063-780X/05/3106-0484$26.00

a ring is related to the injection current $I_{e,i}(t)$ by the relationship

$$dN_{0e,i} = \frac{1}{e} I_{e,i}(t_{0e,i}) dt_{0e,i}.$$

The electric potential Φ_G of a system of electron and ion ring macroparticles with density (1) satisfies the Laplace equation

$$\frac{1}{r}\frac{\partial}{\partial r} r \frac{\partial \Phi_G}{\partial r} + \frac{\partial^2 \Phi_G}{\partial z^2} = 2dN_{0e} e \frac{\delta(r - r_{0e})}{r_{0e}} \delta(z - z_{Le}) - 2dN_{0i} e \frac{\delta(r - r_{Li})}{r_{Li}} \delta(z - z_{Li}). \quad (2)$$

The boundary conditions for Eq. (2) imply that the potential vanishes at the drift chamber wall,

$$\Phi_G(r = a, z) = 0, \quad \infty > z \geq 0,$$
$$\Phi_G(r, z = 0) = 0, \quad a \geq r \geq 0. \quad (3)$$

The expression for the electric potential that satisfies these boundary conditions has the form

$$\Phi_G(r, z) = -\frac{2edN_{0i}}{a} \times \sum_{n=1}^{\infty} \frac{J_0\left(\lambda_n \frac{r_{Li}}{a}\right) J_0\left(\lambda_n \frac{r}{a}\right)}{\lambda_n J_1^2(\lambda_n)} \left[e^{-\frac{\lambda_n}{a}(z + z_{Li})} - e^{-\frac{\lambda_n}{a}|z - z_{Li}|} \right] + \frac{2edN_{0e}}{a} \sum_{n=1}^{\infty} \frac{J_0\left(\lambda_n \frac{r_{Le}}{a}\right) J_0\left(\lambda_n \frac{r}{a}\right)}{\lambda_n J_1^2(\lambda_n)} \times \left[e^{-\frac{\lambda_n}{a}(z + z_{Le})} - e^{-\frac{\lambda_n}{a}|z - z_{Le}|} \right], \quad (4)$$

where λ_n are the roots of the Bessel function, $J_0(\lambda_n) \equiv 0$.

The first terms in the brackets in the infinite sums describe the potential of the image charges induced in a perfectly conducting diaphragm and the second terms account for the potentials of the electron and ion macroparticles. The total potential of a system of an ion and an electron beam is obtained by summing the contributions of all macroparticles (i.e., by integrating over the injection times):

$$\Phi(r, z) = -\frac{2}{a} \sum_{n=1}^{\infty} \frac{J_0\left(\lambda_n \frac{r}{a}\right)}{\lambda_n J_1^2(\lambda_n)} \times \left\{ J_0\left(\lambda_n \frac{r_{0e}}{a}\right) \int_0^t I_e(t_{0e}) \left[e^{-\frac{\lambda_n}{a}(z + z_{Le})} - e^{-\frac{\lambda_n}{a}|z - z_{Le}|} \right] dt_{0e} - \int_0^t I_i(t_{0i}) J_0\left(\lambda_n \frac{r_{Li}}{a}\right) \left[e^{-\frac{\lambda_n}{a}(z + z_{Li})} - e^{-\frac{\lambda_n}{a}|z - z_{Li}|} \right] dt_{0i} \right\}. \quad (5)$$

The integration in this expression for the potential is carried out from the times at which the first electron and ion ring macroparticles enter the drift chamber ($t_{0e} = 0$ and $t_{0i} = 0$, respectively) to the running time $t_{0e,i} = t$. The annular beams of electrons and ions are described as having infinitely thin walls. Since the electrons are assumed to be magnetized (i.e., to execute one-dimensional motion), the radius of the annular electron beam remains unchanged, $r_{Le}(t, t_0) = r_{0e}$, where r_{0e} is the initial electron beam radius. At the same time, the radial coordinates of the ions, $r_{Li}(t, t_{0i})$ depend on time. Knowing the electric potential of a system of an ion and an electron beam, we can readily find the longitudinal and radial components of the electric field, which are determined by the positions of all the electrons and ions within the drift chamber at a given time:

$$E_r = -\frac{2}{a^2} \sum_{n=1}^{\infty} \frac{J_1\left(\lambda_n \frac{r}{a}\right)}{J_1^2(\lambda_n)} \times \left\{ J_0\left(\lambda_n \frac{r_{0e}}{a}\right) \int_0^t I_e(t_{0e}) \left[e^{-\frac{\lambda_n}{a}(z + z_{Le})} - e^{-\frac{\lambda_n}{a}|z - z_{Le}|} \right] dt_{0e} - \int_0^t I_i(t_{0i}) J_0\left(\lambda_n \frac{r_{Li}}{a}\right) \left[e^{-\frac{\lambda_n}{a}(z + z_{Li})} - e^{-\frac{\lambda_n}{a}|z - z_{Li}|} \right] dt_{0i} \right\},$$

$$E_z = -\frac{2}{a^2} \sum_{n=1}^{\infty} \frac{J_0\left(\lambda_n \frac{r}{a}\right)}{J_1^2(\lambda_n)} \left\{ J_0\left(\lambda_n \frac{r_{0e}}{a}\right) \times \int_0^t I_e(t_{0e}) \left[e^{-\frac{\lambda_n}{a}(z + z_{Le})} - \mathrm{sgn}(z - z_{Le}) e^{-\frac{\lambda_n}{a}|z - z_{Le}|} \right] dt_{0e} \right. \quad (6)$$

$$-\int_0^t I_i(t_{0i})J_0\left(\lambda_n\frac{r_{Li}}{a}\right)$$

$$\times\left[e^{-\frac{\lambda_n}{a}(z+z_{Li})}-\mathrm{sgn}(z-z_{Le})e^{-\frac{\lambda_n}{a}|z-z_{Li}|}\right]dt_{0i}\Bigg\}.$$

We then close the basic set of equations by substituting the expressions for the electric field components into the equations of motion for electrons and ions:

$$\frac{dp_{Le}}{dt}=-eE_z,\quad \frac{dz_{Le}}{dt}=c\frac{p_{Le}}{\sqrt{p_{Le}+m^2c^2}},$$
$$\frac{d^2z_{Li}}{dt^2}=\frac{e}{M}E_z,\quad \frac{d^2r_{Li}}{dt^2}=\frac{e}{M}E_r. \tag{7}$$

Here, p_{Le} is the longitudinal electron momentum and M and m are the masses of an ion and an electron, respectively. We introduce the dimensionless variables

$$P_{Le}=\frac{p_{Le}}{mc},\quad Z_{Le,i}=\frac{z_{Le,i}}{a},\quad T=\frac{tc}{a},$$
$$T_{0e,i}=\frac{t_{0e,i}c}{a},\quad R_{Li}=\frac{r_{Li}}{a},\quad R_{0e}=\frac{r_{0e}}{a},$$

where P_{Le} and Z_{Le} are the dimensionless momentum of an electron and its dimensionless longitudinal coordinate, T is the dimensionless running time, T_{0e} is the dimensionless injection time of an electron, R_{0e} is the dimensionless radius of the electron beam, and Z_{Li} and R_{Li} are the longitudinal and radial dimensionless coordinates of the ions. In terms of these variables, the equations of motion (7) take the form

$$\frac{dP_{Le}}{dT}=\frac{2I_e}{I_A}\sum_{n=1}^{\infty}\frac{J_0(\lambda_nR_{0e})}{J_1^2(\lambda_n)}\Bigg\{J_0(\lambda_nR_{0e})\int_0^t\Psi_e(T'_{0e})dT'_{0e}$$
$$\times[e^{-\lambda_n(Z_{Le}+Z'_{Le})}-\mathrm{sgn}(Z_{Le}-Z'_{Le})e^{-\lambda_n|Z_{Le}-Z'_{Le}|}]$$
$$-\alpha\int_0^t\Psi_i(T'_{0i})dT'_{0i}J_0(\lambda_nR'_{Li})$$
$$\times[e^{-\lambda_n(Z_{Le}+Z'_{Li})}-\mathrm{sgn}(Z_{Le}-Z'_{Li})e^{-\lambda_n|Z_{Le}-Z'_{Li}|}]\Bigg\},$$

$$\frac{dZ_{Le}}{dT}=\frac{P_{Le}}{\sqrt{1+P_{Le}^2}},$$

$$\frac{d^2Z_{Li}}{dT^2}=-\frac{2m}{M}\frac{I_e}{I_A}\sum_{n=1}^{\infty}\frac{J_0(\lambda_nR_{Li})}{J_1^2(\lambda_n)}$$
$$\times\Bigg\{J_0(\lambda_nR_{0e})\int_0^t\Psi_e(T'_{0e})dT'_{0e}$$
$$\times[e^{-\lambda_n(Z_{Li}+Z'_{Le})}-\mathrm{sgn}(Z_{Li}-Z'_{Le})e^{-\lambda_n|Z_{Li}-Z'_{Le}|}]$$
$$-\alpha\int_0^t\Psi_i(T'_{0i})dT'_{0i}J_0(\lambda_nR'_{Li})$$
$$\times[e^{-\lambda_n(Z_{Li}+Z'_{Li})}-\mathrm{sgn}(Z_{Li}-Z'_{Li})e^{-\lambda_n|Z_{Li}-Z'_{Li}|}]\Bigg\},$$

$$\frac{d^2R_{Li}}{dT^2}=-\frac{2m}{M}\frac{I_e}{I_A}\sum_{n=1}^{\infty}\frac{J_1(\lambda_nR_{Li})}{J_1^2(\lambda_n)}$$
$$\times\Bigg\{J_0(\lambda_nR_{0e})\int_0^t\Psi_e(T'_{0e})dT'_{0e}$$
$$\times[e^{-\lambda_n(Z_{Li}+Z'_{Le})}-e^{-\lambda_n|Z_{Li}-Z'_{Le}|}]$$
$$-\alpha\int_0^t\Psi_i(T'_{0i})dT'_{0i}J_0(\lambda_nR'_{Li})$$
$$\times[e^{-\lambda_n(Z_{Li}+Z'_{Li})}-e^{-\lambda_n|Z_{Li}-Z'_{Li}|}]\Bigg\}.$$

Here, for brevity, we introduce the following notation:

$$Z'_{Le}\equiv Z_{Le}(T,T'_{0e}),\quad Z'_{Li}\equiv Z_{Li}(T,T'_{0i}),$$
$$R'_{Li}\equiv R_{Li}(T,T'_{0i}),\quad \alpha=\frac{I_i}{I_e}.$$

The dependence of the currents of electrons and ions on the time at which they fly into the drift chamber, $I_e(t_{0e})$ and $I_i(t_{0i})$, was chosen to have the form $I_e(t_{0e}) = I_e\Psi_e(T_{0e})$ and $I_i(t_{0i}) = I_i\Psi_i(T_{0i})$, where the functions $\Psi_e(T_{0e})$ and $\Psi_i(T_{0i})$ describe the profiles of the electron and ion current pulses.

The case $\Psi_{e,i} = 1$ corresponds to the constant currents of the electrons and ions injected into the drift chamber. This is precisely the case we will be considering.

3. RESULTS OF NUMERICAL ANALYSIS

We begin with a brief description of the formation of a VC in the absence of ions. Figure 1 shows the phase portrait of an REB with the following parameters: the electron energy is E_e = 280 keV, the electron current is I_e = 5.6 kA, and the electron beam radius is 1.6 cm. The radius of the drift chamber is a = 2.5 cm. For these values of the parameters of the REB and of the drift cham-

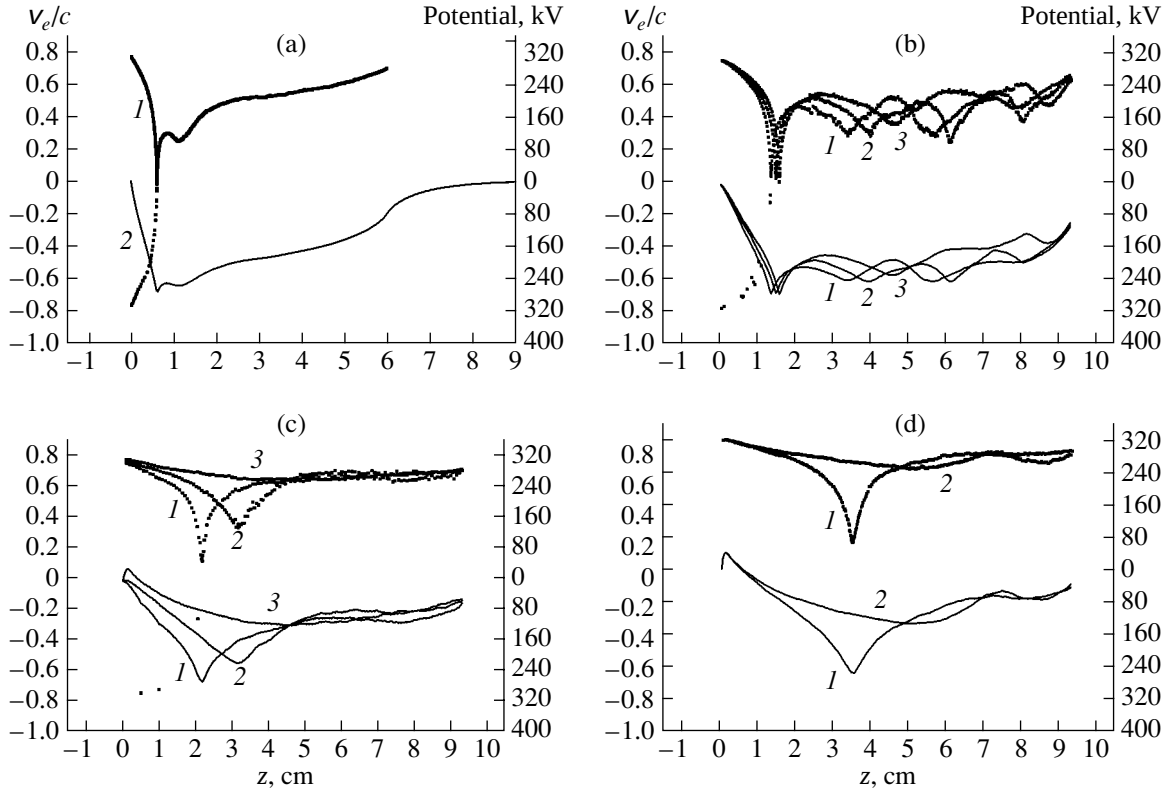

Fig. 1. Phase portraits of an electron beam and longitudinal profiles of the electric potential at different times for I_e = 5.6 kA, E_e = 280 keV, r_{0e} = 1.6 cm, E_i = 25 keV, and r_{0i} = 1.6 cm: (a) phase portrait of an electron beam (curve *1*) and longitudinal profile of the electric potential (curve *2*) for $I_i = 0$; (b) phase portraits of an electron beam and longitudinal profiles of the electric potential for N_i/N_e = 1.5 at the times t = (*1*) 1.6, (*2*) 2, and (*3*) 2.4 ns; (c) phase portraits of an electron beam and longitudinal profiles of the electric potential for N_i/N_e = 1.5 at the times t = (*1*) 4.6, (*2*) 6, and (*3*) 8 ns; and (d) phase portraits of an electron beam and longitudinal profiles of the electric potential for N_i/N_e = 4.5 at the times t = (*1*) 4.6 and (*2*) 6 ns.

ber, the limiting current is equal to I_{lim} = 3.8 kA, which is lower than the current of the injected electrons. The relevant series of numerical simulations was performed for 600 electron macroparticles and 1200 ion macroparticles. Curve *1* in Fig. 1a shows that an electron VC does indeed form in the drift chamber. We can readily see that there are both transmitted and reflected electrons. Within a region of radius $r = r_{0e}$, which is the region of the VC formed by the REB (Fig. 1a, curve *2*), the potential takes its minimum value close to the initial beam energy (in voltage units).

We now turn to an analysis of the effect of the ion beam on the formation of an electron VC in a situation in which the ion and electron beams are injected into the drift chamber simultaneously. We begin with a simple case in which the electron and ion beams have the same initial radius, $r_{0e} = r_{0i}$ = 1.6 cm. The ion current is 540 A, and the initial ion energy is E_i = 25 keV. To reduce the computation time, the model electron-to-ion mass ratio was set equal to m/M = 1/40. The ions were assumed to be singly charged. For the above parameters of the system, the ratio of the line densities (the number of particles per unit beam length) of the ion and electron beams is equal to N_i/N_e = 1.5, where $N_{e,i} = I_{e,i}/ev_{0e,i}$, with $v_{0e,i}$ being the electron and ion initial velocities.

Figures 1b and 1c display the phase portraits of the electrons and the longitudinal profile of the electric potential in the beam region $r = r_{0e}$ at different times. Figure 1b provides evidence for the formation of an electron VC in the drift chamber. We can clearly see that there are both transmitted and reflected electrons. In the VC region (see Fig. 1b, the lower curves *1–3*), the potential assumes its minimum value close to the initial beam energy (in voltage units). Within the time interval $t < 4.8$ ns, the ions neutralize the electron beam space charge; as a result, the VC is displaced deep into the chamber and disappears. The VC velocity increases from 2.3×10^8 cm/s at t = 1.4 ns to 4.25×10^8 cm/s at t = 4.8 ns. The velocity of the VC is substantially lower than that of the accelerated ions. For this reason, the ions are not involved in the process of continuous acceleration by the moving potential well of the VC. That the ions are not subject to self-synchronous acceleration may well be associated with the smallness of the model ion mass, $M = 40m$. The motion of the VC is accompa-

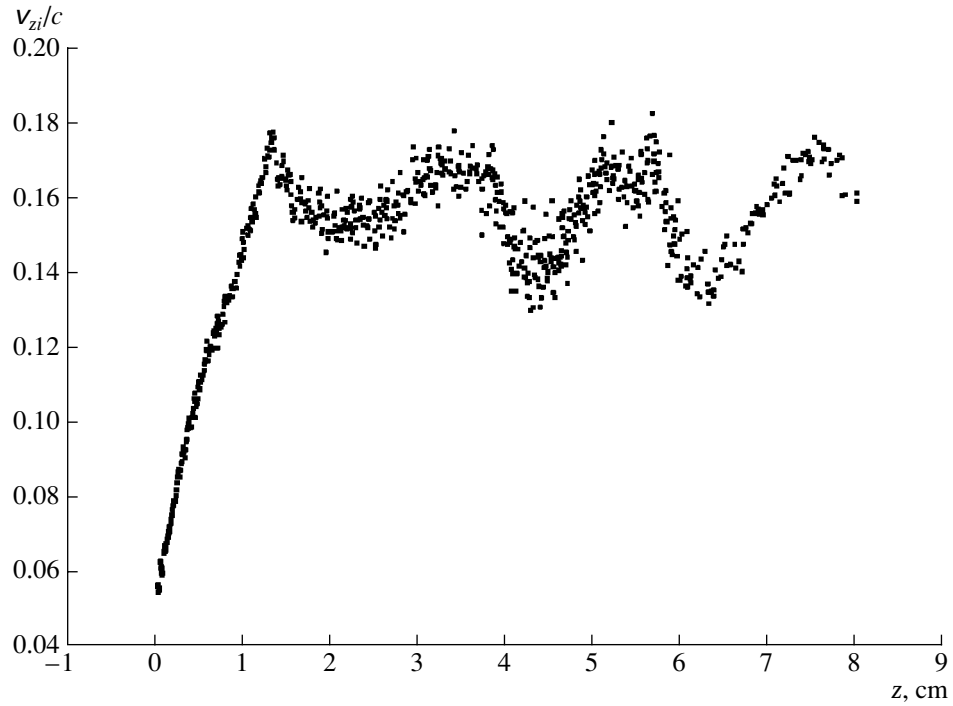

Fig. 2. Phase portrait of the ions at the time $t = 1.6$ ns for $r_{0e} = r_{0i} = 1.6$ cm and $N_i/N_e = 1.5$.

nied first by the formation of one additional minimum in the potential profile and then by the formation of a wave structure with a length of approximately 7 cm and with three spatial periods. From Fig. 1 we see that the potential wave propagates in the same direction as the VC. The excitation of the wave perturbation of the electric potential is seen in the phase portrait of the electrons. Within the REB, the LF space charge wave propagates. The phase velocity of the potential wave is much higher than the VC propagation velocity and is much lower than the mean ion velocity within the LF wave region. Figure 2 presents the phase portrait of the ions at the time $t = 1.6$ ns. The ions are seen to be accelerated in the space charge field of the REB. At the bottom of the potential well of the VC, the energy of the accelerated ions is approximately equal to the REB energy. Having passed through the minimum in the VC potential, the ions enter the potential wave structure. Accordingly, their velocity along the system changes in a wavelike manner. After time $t = 2.8$ ns, the potential wave structure begins to be damped and, by the time $t = 4$ ns, the potential profile becomes smooth. In the radial direction, the ions execute small oscillations because they are at the bottom of a radial potential well created by the space charge of the REB. The state with a VC and a smooth potential profile lasts up to the time $t = 4.6$ ns, after which the VC disappears (Fig. 1c). The ion acceleration process then terminates almost completely, resulting in the formation of an ion virtual anode (VA) in the injection region. The potential profile in Fig. 1c is seen to have a positive maximum, which is formed by the ion VA just near the injection plane.

Let us consider the LF dynamics of an electron VC for the case in which the ion beam current is three times higher than that in the previous case, specifically, $I_i = 1.62$ kA. For this ion current, we have $N_i/N_e = 4.5$, and, under the action of such an ion beam, the VC relaxes in qualitatively the same way as it does in the presence of a low-current ion beam. The increase in the ion beam current leads to the increase in the propagation velocity of the electron VC from 3×10^8 to 4.4×10^8 cm/s and the increase in the propagation velocity of the first minimum of the wave structure (the phase velocity) from 1.6×10^9 to 2.25×10^9 cm/s. A comparison between Fig. 1c and 1d shows that the higher the propagation velocity of the VC, the shorter the time during which it disappears.

Figure 3 depicts the phase portrait of the ions at $t = 2$ ns. We see that an ion VA forms near the injection plane ($z = 0$). Some of the ions are reflected from the VA, and the others are captured in the acceleration process. Just near the injection plane, the electric potential has a positive maximum, which is formed by the ion VA. Within the VA, the ions acquire a transverse momentum and thereby begin to oscillate in the radial direction. The intensity of these oscillations is low and they have no significant effect on the relaxation of the electron VC. Figure 4 demonstrates time evolutions of the minimum value of the electric potential in the VC region for ion-to-electron line density ratios of 4.5 and 1.5. Although the ion currents are very different, the electron VCs in these two cases exist for roughly the

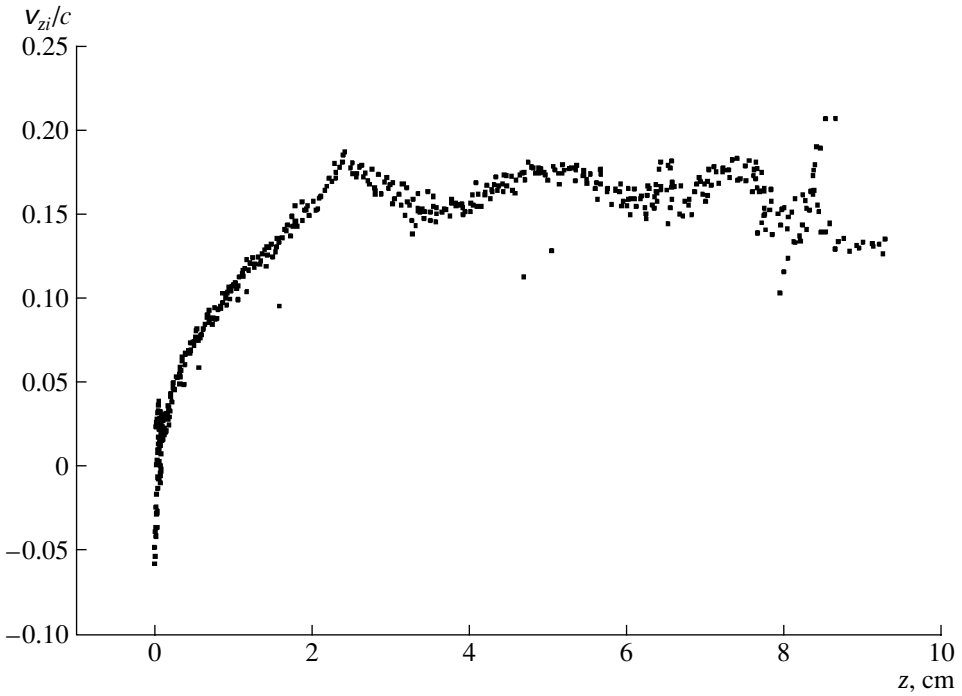

Fig. 3. Phase portrait of the ions at the time $t = 2$ ns for $r_{0e} = r_{0i} = 1.6$ cm and $N_i/N_e = 4.5$.

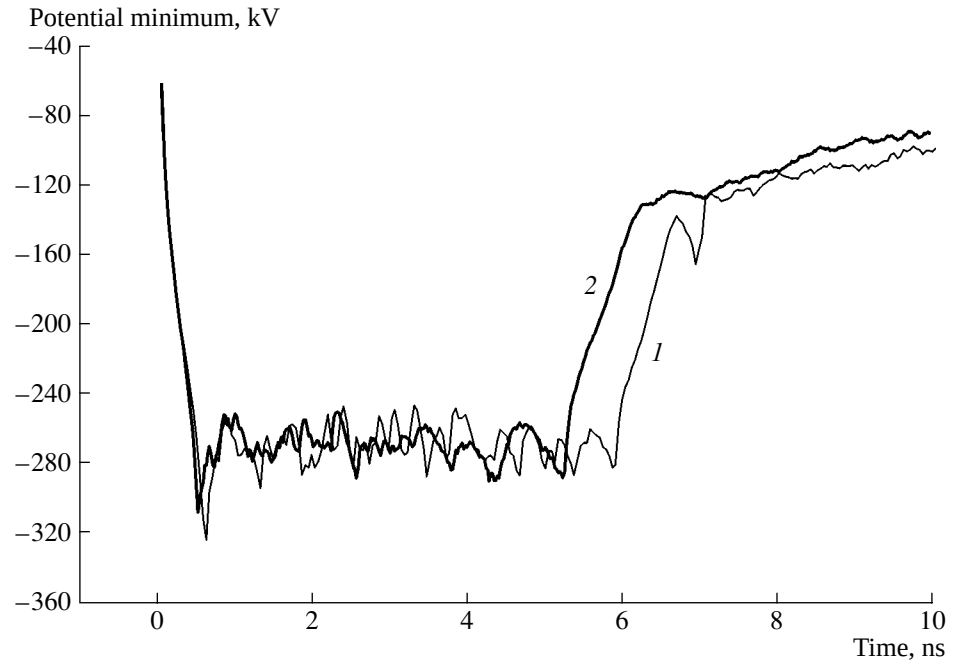

Fig. 4. Time evolutions of the minimum value of the electric potential for $r_{0e} = r_{0i} = 1.6$ cm and for $N_i/N_e =$ (*1*) 1.5 and (*2*) 4.5.

same time and the electric potentials are of about the same magnitude.

Hence, at high ion beam currents, both an electron VC and an ion VA can exist simultaneously in the system. The ion VA can be regarded as an ion emitter whose intensity is restricted by the space charge of the ion beam. This happens when the density of the plasma injected into the system is high [10]. This is why the transmitted ion current will be determined by both the potential drop across the electron VC and by the dis-

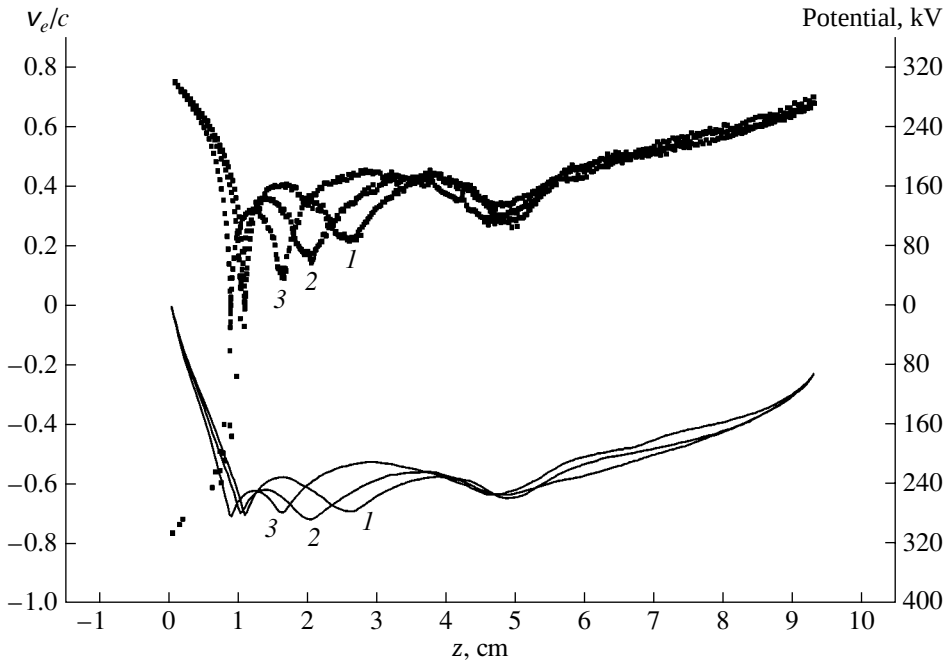

Fig. 5. Phase portraits of an electron beam and longitudinal profiles of the electric potential for r_{0e} = 1.6 cm, r_{0i} = 2.3 cm, and N_i/N_e = 1.5 at the times t = (*1*) 2.2, (*2*) 2.4, and (*3*) 2.6 ns.

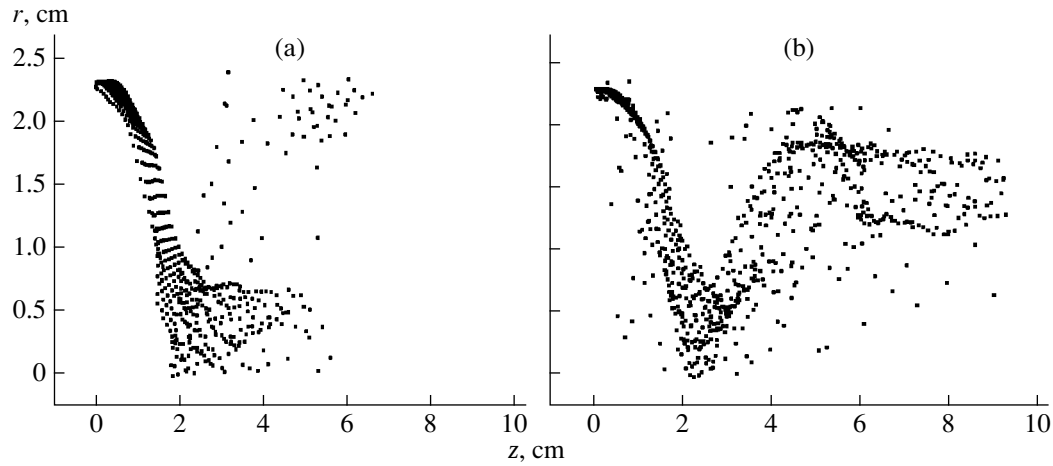

Fig. 6. Positions of the ions in the (r, z) plane for r_{0e} = 1.6 cm, r_{0i} = 2.3 cm, and N_i/N_e = 1.5 at the times t = (a) 1.6 and (b) 2.6 ns.

tance from the ion VA (i.e., from the injection plane) to the electron VC (the Child–Langmuir law).

Let us consider the LF dynamics of the VC of an REB when the initial radius of the injected ion beam is larger than that of the electron beam. In this case, the ions propagate in the two-dimensional potential well of the space charge of the electron VC and, along with translational motion, they execute radial oscillations. The relevant series of numerical simulations was carried our for the above parameters of the electron beam and for the following parameters of the ion beam: the beam current was I_i = 540 A (N_i/N_e = 1.5), the beam radius was r_{0i} = 2.3 cm, and the ion energy was E_i = 25 keV.

The phase portraits of the electrons and the electric potential profiles at different times are shown in Fig. 5. In the initial stage of the process (t < 2 ns), the VC is displaced from the injection plane deep into the chamber and then, within the time interval 2 ns < t < 3 ns, it is displaced in the opposite direction. After the time interval 3 ns < t < 6 ns, within which the electron VC again moves uniformly into the chamber, it begins to

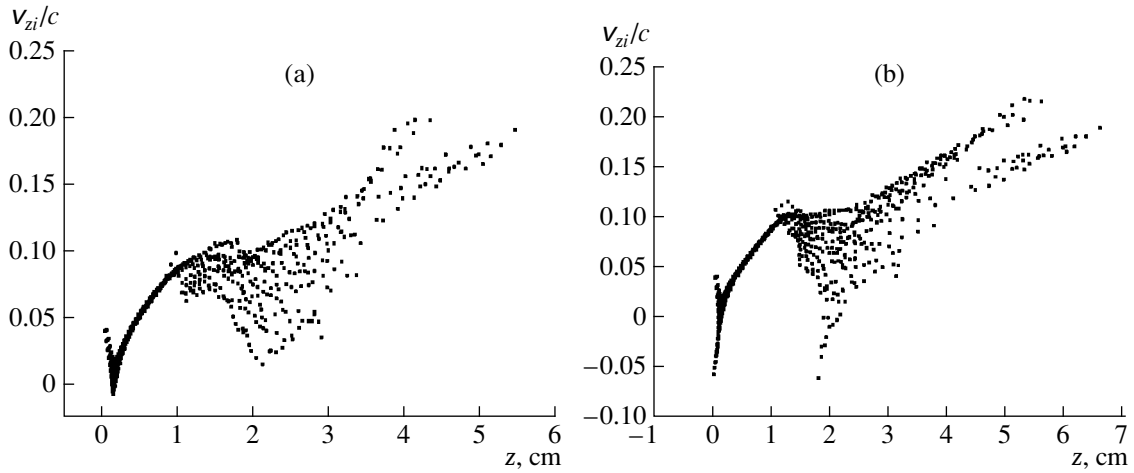

Fig. 7. Phase portraits of the ions for r_{0e} = 1.6 cm, r_{0i} = 2.3 cm, and N_i/N_e = 1.5 at the times t = (a) 1.4 and (b) 1.6 ns.

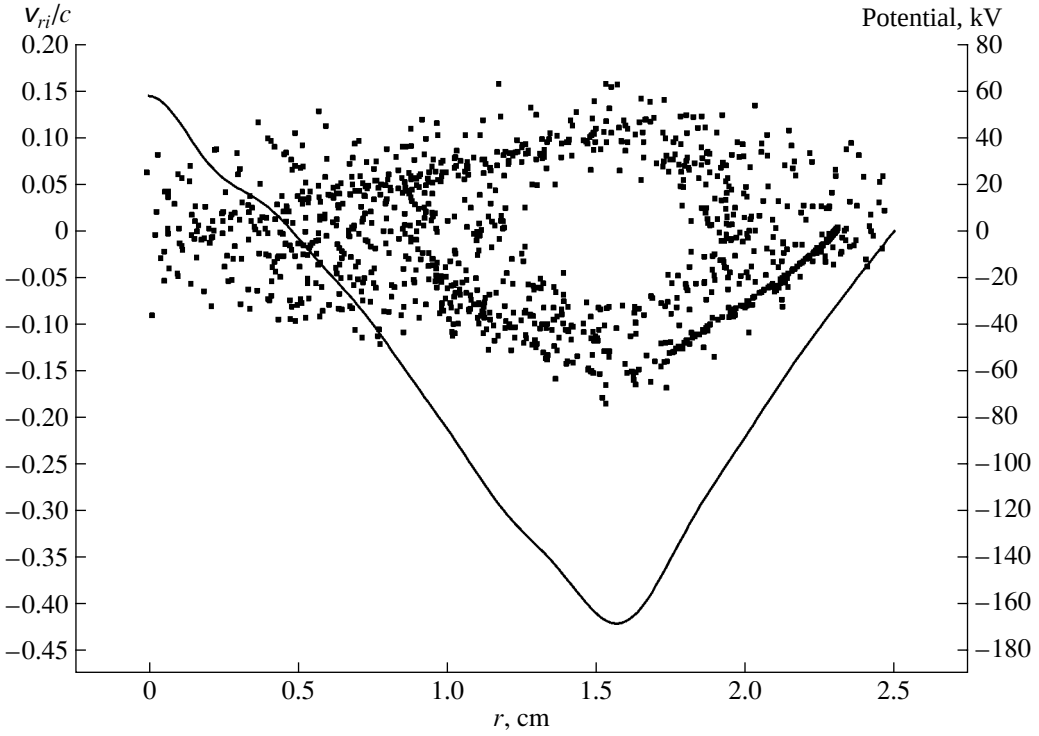

Fig. 8. Phase plane (v_r, r) of the ions and the radial profile of the electric potential in the cross section z = 0.9 cm of the drift chamber for r_{0e} = 1.6 cm, r_{0i} = 2.3 cm, and N_i/N_e = 1.5 at the time t = 11.6 ns.

execute steady-state oscillations about its mean position, whose longitudinal coordinate is approximately equal to z_{VC} = 1.8 cm. The first minimum in the potential of the wave structure executes large-amplitude oscillations in the longitudinal direction and, on the average, is displaced into the drift chamber.

Finally, we consider the ion dynamics. Figure 6 shows the radial distribution of the ions at different times, and Fig. 7 presents the phase plane (v_{zi}, z) of the ions. The ion VA is seen to oscillate in both longitudinal and radial directions. Because of the radial oscillations of the ion VA, the angle of injection of the transmitted ion beam into the drift chamber also varies periodically. As the ions move radially in the electric field of the space charge of the electron VC, they are focused toward the system axis. In the focal region ($z_{Fi} \approx 2$ cm), which is behind the electron VC, the positive potential increases considerably and a second ion VA arises

(Fig. 7). In this case, some of the ions at the leading edge of the ion beam are additionally accelerated in the field of the space charge of the forming ion VA. The energy of the accelerated ions at the leading edge of the ion beam is 500 keV. After the leading edge of the ion beam has passed through the drift chamber, the energy of the accelerated ions falls to approximately the energy of the REB electrons. In the radial direction, a radial potential well is formed, on one side, by the REB and, on the other, by the ions that have been accumulated in the axial region of the drift chamber. In this potential well, the ions execute radial oscillations (Fig. 8). Since the angle of injection of the transmitted ion beam varies periodically over time, the position of the ion focus oscillates in the longitudinal direction. As the ion focus is displaced toward the electron VC, it increases the electric potential there, so the VC disappears. As the ion focus is displaced deep into the drift chamber, the VC again arises. In simulations, this process was observed to repeat itself four times. As a result, the electron VC will eventually disappear because of the accumulation of ions in its region.

4. CONCLUSIONS

In this paper, we have investigated the interaction of an ion beam with the VC of a high-current REB injected into a cylindrical drift chamber. We have considered the cases in which the electron and ion beams have the same initial radius and in which the initial radius of the ion beam is greater than that of the electron beam. In the first case, the relaxation of the electron VC is accompanied by the formation of an LF wave structure. The wave perturbation is localized in the electron VC region and persists for a finite time. In the final stage, the LF oscillations are damped completely and the electron VC disappears. In the second case, the relaxation of the electron VC is largely affected by the transverse ion oscillations in the field of the space charge of the electron–ion system. It is shown that, in such a system, an electron VC and two ion VAs can exist simultaneously. One ion VA forms near the injection plane, and the other arises in the ion beam focus, which is behind the electron VC. The position of the ion VA in the injection region varies periodically in both longitudinal and radial directions. The ion beam, too, is focused periodically. As the ions approach the electron VC, they neutralize its space charge, so the VC disappears. As the ions move in the longitudinal direction away from the previously existing VC, a new VC arises and then, again, disappears because of the accumulation of ions in the system. As a result, a two-stream laminar flow forms in the drift chamber.

ACKNOWLEDGMENTS

This work was supported in part by the Science and Technology Center in Ukraine, project no. 1569.

REFERENCES

1. A. L. Babkin, A. E. Dubinov, and V. S. Zhdanov, Fiz. Plazmy **23**, 343 (1997) [Plasma Phys. Rep. **23**, 316 (1997)].
2. A. E. Dubinov, I. Yu. Kornilova, and V. D. Selemir, Usp. Fiz. Nauk **172**, 1225 (2002) [Phys. Usp. **45**, 1109 (2002)].
3. Yu. P. Bliokh, G. S. Nusinovich, J. Felsteiner, and V. L. Granatstein, Phys. Rev. E **66**, 056503 (2002).
4. Yu. P. Bliokh and G. S. Nusinovich, IEEE Trans. Plasma Sci. **29**, 951 (2001).
5. Yu. P. Bliokh, G. S. Nusinovich, and V. L. Granatstein, in *Proceedings of the International Workshop on High-Energy Density and High-Power RF, Snowbird, UT, 2001*, p. 45.
6. V. A. Balakirev, A. M. Gorban', I. I. Magda, *et al.*, Fiz. Plazmy **23**, 350 (1997) [Plasma Phys. Rep. **23**, 323 (1997)].
7. G. L. Olson, Phys. Fluids **18**, 585 (1975).
8. W. Peter, R. Faehl, C. Snell, and N. Yonas, IEEE Trans. Nucl. Sci. **32**, 350 (1985).
9. V. V. Belikov, A. G. Lymar, and N. A. Khizhnyak, Pis'ma Zh. Tekh. Fiz. **1**, 615 (1975) [Sov. Tech. Phys. Lett. **1**, 276 (1975)].
10. P. T. Chupikov, D. V. Medvedev, I. N. Onishchenko, *et al.*, Probl. At. Sci. Tecnol., Ser. Nucl. Phys. Invest., No. 1, 32 (2004).

Translated by I.A. Kalabalyk

Plasma Physics Reports, Vol. 31, No. 6, 2005, pp. 493–496. Translated from Fizika Plazmy, Vol. 31, No. 6, 2005, pp. 539–542.

PLASMA DYNAMICS

Self-Consistent Electron and Ion Flows in a Fast Z-Pinch

A. N. Dolgov

Moscow Engineering Physics Institute, Kashirskoe sh. 31, Moscow, 115409 Russia

Received February 25, 2004; in final form, April 12, 2004

Abstract—Results are presented from experimental studies of fast Z-pinches produced in plasmas of high-*Z* elements. An analysis of a plasma structure emitting X radiation and time-resolved measurements of the electron emission showed that a self-consistent regime of electron and ion motion is established in the plasma channel of the discharge. It was found that, in this regime, the electron component makes a negative contribution to the net current and an electrically neutral supersonic plasma flow propagates along the discharge axis in the direction of the net current. © *2005 Pleiades Publishing, Inc.*

In [1], self-consistent electron and ion flows in a high-current plasma channel were considered in a collisionless plasma model. It was shown that, at high plasma densities, a regime can be established in which the electron component makes a negative contribution to the net current, which concentrates within a thin surface layer. In the central part of the channel, the electrons and ions move with the same axial drift velocities to produce an electrically neutral plasma flow propagating along the axis in the direction of the net current.

In the present paper, it is shown experimentally that a similar regime can be established in fast Z-pinches produced in plasmas of high-*Z* elements.

Experiments were carried out with a low-inductance vacuum spark (Fig. 1). The working medium was anode erosion products (iron). Discharges were excited in a vacuum chamber at an initial vacuum no worse than 10^{-4} torr. As a current source, we used a bank of high-voltage low-inductance capacitors (C = 12 μF) connected to the discharge unit through a coaxial forming line. The maximum current was $I_{max} \approx 150$ kA, and the current rise time was $T/4 \approx 2$ μs. A typical oscillogram of the time derivative of the discharge current measured by a magnetic probe positioned between the central and return-current electrodes of the discharge unit is shown in Fig. 2. Near the first current maximum, we can see a so-called "peculiarity," which indicates the pinching of the discharge channel.

The structure of X-ray sources in the discharge plasma in the wavelength ranges of $\lambda \le 15$ Å and $\lambda \le 3$ Å was recorded by two pinhole cameras (Figs. 3, 4). In the range $\lambda \le 15$ Å, the radiation was dominated by the *L*-shell emission of Fe, whose intensity far exceeded the intensity of harder X-ray emission. In the range $\lambda \le 3$ Å, most energy was emitted in the *K*-lines of Fe. Radiation sources in the spectral range $\lambda \le 15$ Å were usually seen as a chain of plasma objects extended in the axial direction. The typical length of an object was ~1 mm, and the transverse size was 0.2–0.3 mm. In pinhole images, the objects frequently had the form of a pair of parallel or slightly diverging lines of thickness ≤0.1 mm that were extended along the discharge axis. This may be due to the hollow structure of the plasma channel. Radiation in the spectral range $\lambda \le 3$ Å was emitted from three sources: a plasma spot (micropinch) [2, 3], the surface of one of the electrodes, and the discharge plasma located between the micropinch and the electrode. Pinhole images showed that a directed flow of high-energy electrons formed in every discharge. The flow of electrons whose energy was sufficient to excite X-ray emission in the range $\lambda \le 3$ Å propagated from the micropinch region toward the anode (Fig. 4a) or toward the cathode (Figs. 4b, 4c). The propagation direction of the electron flow depended on the parameters of the discharge circuit. When a forming line of capacitance ~10^{-9} F was inserted between the discharge unit and the capacitor bank, the discharge conditions depended on the characteristic time τ during which the signal propagated through the forming line. For $\tau \le 10$ ns, the electron flow propagated toward the anode, whereas for $\tau \ge 30$ ns, it propagated toward the cathode. When the high-energy electrons propagated toward the cathode, they apparently moved in the axial supersonic plasma flow that was also directed toward the cathode. From the pattern of a standing shock wave that arose when the flow met with a needle installed on the cathode surface, we could determine the Mach number $M = 1/\sin\frac{\theta}{2}$, where θ is the angle of the cone formed by the standing shock wave. Knowing the plasma temperature in the discharge channel, we thus could determine the axial plasma velocity [4]. Pinhole images of the standing shock wave highlighted by the flow of high-energy electrons allowed us to conclude that the Mach number and the axial plasma velocity in the discharge reached $M \cong 3$–4 and $v_z \cong (3\text{–}4) \times 10^6$ m/s, respectively. No supersonic plasma flow of this kind was observed near the anode surface.

When the electron flow propagated toward the cathode, the plasma electrons were directly detected with

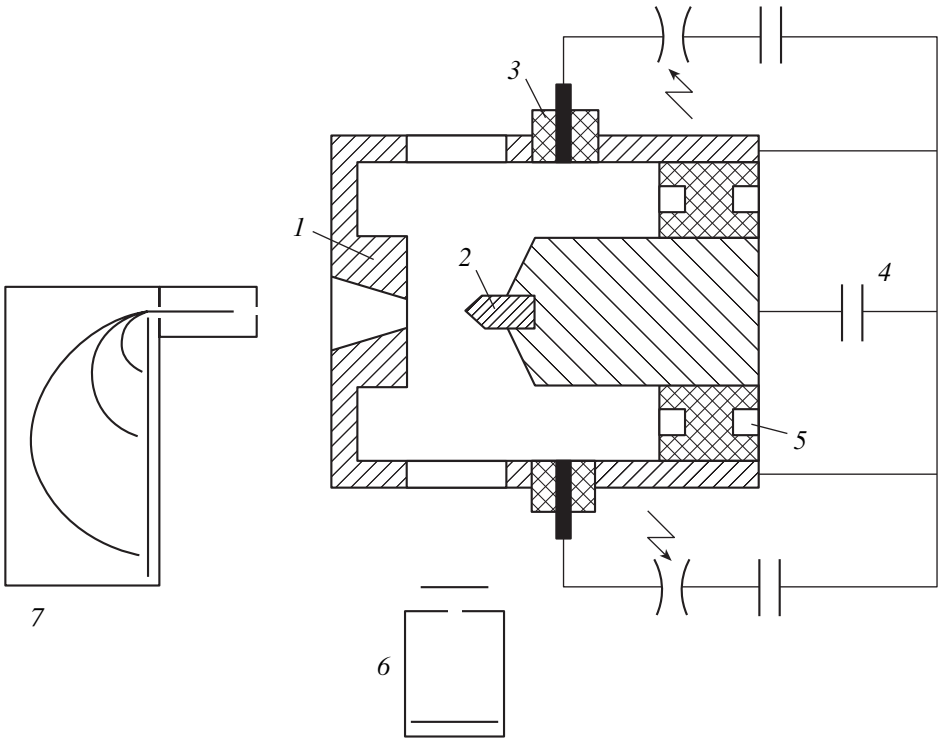

Fig. 1. Schematic of the experimental setup: (*1*) cathode of the discharge unit, (*2*) anode, (*3*) system for initiating a discharge, (*4*) high-voltage capacitor bank, (*5*) insulator, (*6*) pinhole camera, and (*7*) magnetic analyzer.

the help of a magnetic analyzer [5]. The analyzer was placed inside the vacuum chamber, at the discharge axis, a distance of ~0.5 m from the discharge unit. The electron beam was output from the interelectrode gap through a channel in the outer electrode. The electrons were preliminarily recorded with the help of a photoemulsion detector. The maximum of the electron spectrum was in the energy range of 40–60 keV. Time-resolved measurements of electrons with these energies were then performed with the help of a VEU-6 electron multiplier tube (EMT). For this purpose, a part of the analyzer housing was removed and the detector was attached directly to the analyzer.

Simultaneously with electron measurements, we performed time-resolved measurements of X radiation in the range $\lambda \leq 3$ Å with the help of a scintillation detector [6] consisting of an absorbing filter (beryllium), a plastic scintillator, and a photomultiplier. Figure 5 shows synchronized signals from the (a) X-ray detector and (b) electron detector. The first pulse from the electron detector appeared immediately after the first X-ray pulse and coincided with the first maximum

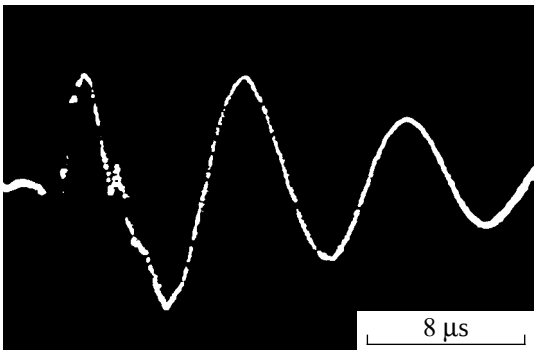

Fig. 2. Oscillogram of the time derivative of the discharge current measured by a magnetic probe.

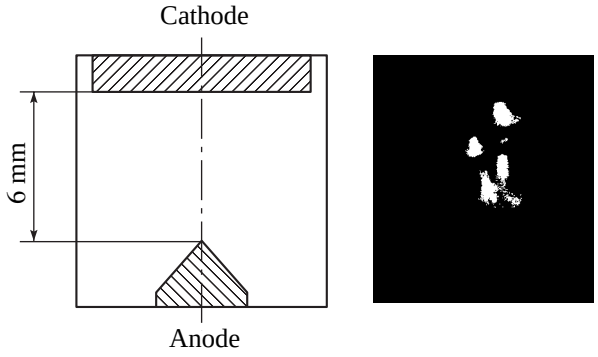

Fig. 3. X-ray pinhole image of the interelectrode space recorded in the range $\lambda \leq 15$ Å.

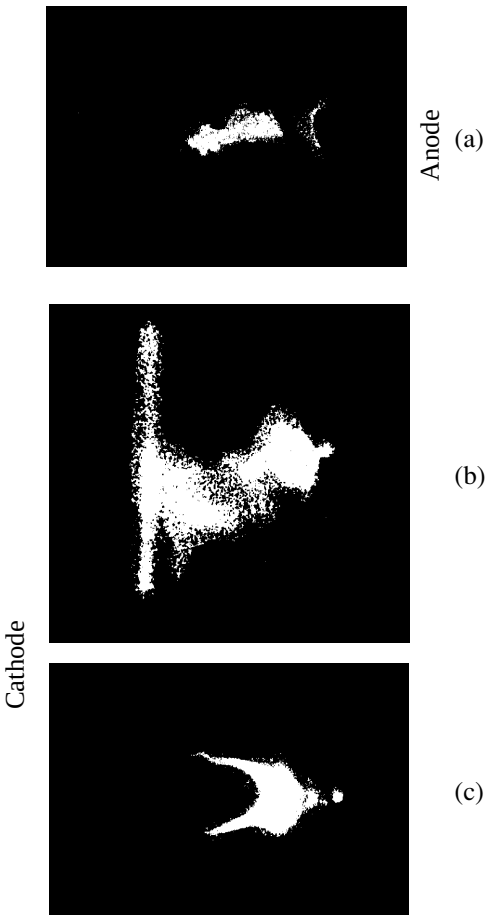

Fig. 4. X-ray pinhole images of the interelectrode space recorded in the range $\lambda \leq 3$Å for different configurations of the discharge unit.

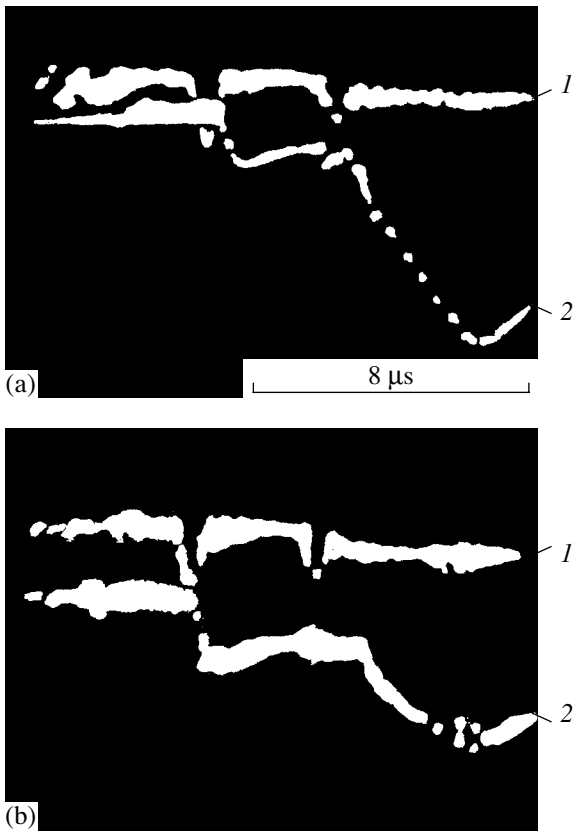

Fig. 5. Synchronized signals from the (*1*) X-ray detector and (*2*) electron detector.

of the discharge current. The high-energy electron flow propagated in the direction of the net current; i.e., it made a negative contribution to the net current. The generation of the high-energy electron flow may be attributed to the formation of a micropinch [7]. The second pulse from the electron detector (which appeared not in every discharge) nearly coincided with the accompanying X-ray pulse. The second electron pulse was observed at the instant when the current reached its second maximum after reversal of the electrode polarity. Accordingly, the electron flow in this case propagated in the direction opposite to the direction of the net current, and its generation was not related to the pinching process [8]. The last large-amplitude pulse in the EMT signal is associated with the flow of electrically neutral plasma penetrating into the analyzer from the discharge.

The above interpretation of the observed EMT signals is confirmed by the following: In X-ray films and nuclear emulsions used as electron detectors, there were no traces revealing the presence of radiation reflected from the components of the radiation analyzer, i.e., the radiation that might cause the appearance of parasitic EMT signals. This is also confirmed by the EMT signals recorded in the magnetic analyzer channel not coinciding with the photomultiplier signals recorded in the X-ray channel. At the same time, the spectra of high-energy electrons in the discharge under study were recorded many times with the help of the magnetic analyzer and different detectors [5, 8, 9]. The interpretation of the large-amplitude pulse in the EMT signal is based on the results of measurements of the spectrum of ions and neutrals emitted from the discharge in the axial direction [10–12]. Moreover, there is direct evidence in favor of our assumption concerning the nature of the large-amplitude pulse. When a magnetic barrier was introduced on the beam path outside the analyzer, the EMT signal showed the absence of electron pulses, but the large-amplitude pulse was always present.

High-resolution X-ray pinhole images of the micropinch region indicate the skinning of the discharge current in the so-called first compression stage, which lasts for 20–50 ns and during which the fast (~0.1 ns) local second compression occurs [2, 4]. The fast implosion of the plasma constriction to a micron size causes the generation of high-energy electrons, whereas the first compression may be associated with a

current regime in which the electron component makes a negative contribution to the net current. The role of the forming line in the discharge circuit is to provide the required current rise time in the micropinch decay stage and to restore the conductivity of the plasma channel [1].

The phenomenon observed can, however, be explained in another way. It is well known that there are current losses and reverse-current regions in Z-pinches [13–15]. It is usually assumed that these effects are caused by the formation of closed toroidal current structures in the discharge plasma [16]. It has recently been shown that the reverse current is not inevitably closed in the discharge plasma [17]. Hence, the observed electron motion can be interpreted (at least under certain conditions) as a reverse current flowing between the electrodes of the discharge unit.

REFERENCES

1. G. V. Karpov, Fiz. Plazmy **26**, 146 (2000) [Plasma Phys. Rep. **26**, 133 (2000)].
2. V. V. Vikhrev, V. V. Ivanov, K. N. Koshelev, and Yu. V. Sidel'nikov, Dokl. Akad. Nauk SSSR **282**, 1361 (1982) [Sov. Phys. Dokl. **27**, 153 (1982)].
3. M. A. Gulin, A. N. Dolgov, O. V. Nikolaev, and A. S. Savelov, Fiz. Plazmy **16**, 1015 (1990) [Sov. J. Plasma Phys. **16**, 590 (1990)].
4. V. V. Vikhrev, V. V. Ivanov, and K. N. Koshelev, Fiz. Plazmy **8**, 1211 (1982) [Sov. J. Plasma Phys. **8**, 688 (1982)].
5. A. A. Gorbunov, M. A. Gulin, A. N. Dolgov, *et al.*, Pis'ma Zh. Éksp. Teor. Fiz. **50**, 320 (1989) [JETP Lett. **50**, 355 (1989)].
6. V. V. Averkiev, A. N. Dolgov, V. A. Kaplin, *et al.*, Prib. Tekh. Éksp., No. 5, 158 (1992).
7. A. N. Dolgov, N. N. Kirichenko, V. K. Lyapidevskiĭ, *et al.*, Fiz. Plazmy **19**, 97 (1993) [Plasma Phys. Rep. **19**, 50 (1993)].
8. M. A. Gulin, A. N. Dolgov, N. N. Kirichenko, and A. S. Savelov, Zh. Éksp. Teor. Fiz. **108**, 1309 (1995) [JETP **81**, 719 (1995)].
9. A. A. Gorbunov, M. A. Gulin, A. N. Dolgov, *et al.*, Preprint No. 023 (Moscow Engineering Physics Inst., Moscow, 1998).
10. V. A. Veretennikov, M. A. Gureĭ, A. N. Dolgov, *et al.*, Pis'ma Zh. Tekh. Fiz. **21** (11), 78 (1995) [Tech. Phys. Lett. **21**, 940 (1995)].
11. A. N. Dolgov, Fiz. Plazmy **22**, 629 (1996) [Plasma Phys. Rep. **22**, 569 (1996)].
12. A. E. Gureĭ, A. N. Dolgov, D. E. Prokhorovich, *et al.*, Fiz. Plazmy **30**, 41 (2004) [Plasma Phys. Rep. **30**, 38 (2004)].
13. G. S. Sarkisov, B. Étlisher, S. Attelan, *et al.*, Pis'ma Zh. Éksp. Teor. Fiz. **62**, 775 (1995) [JETP Lett. **62**, 797 (1995)].
14. P. S. Antsiferov, K. N. Koshelev, V. I. Krauz, *et al.*, Fiz. Plazmy **16**, 1319 (1990) [Sov. J. Plasma Phys. **16**, 764 (1990)].
15. M. Scholz, R. Miklaszewski, V. A. Gribkov, and F. Mezzetti, Nukleonika **45**, 155 (2000).
16. R. B. Baksht and A. V. Fedunin, Plasma Phys. Controlled Fusion **43**, 849 (2001).
17. O. N. Krokhin, V. Ya. Nikulin, and S. P. Tsybenko, *XXXI Zvenigorod Conference on Plasma Physics and Controlled Nuclear Fusion, Zvenigorod, 2004*, Abstracts of Papers, p. 159.

Translated by N.F. Larionova

Plasma Physics Reports, Vol. 31, No. 6, 2005, pp. 497–511. Translated from Fizika Plazmy, Vol. 31, No. 6, 2005, pp. 543–559.

LOW-TEMPERATURE PLASMA

Determination of the Drag Coefficient of a Toroidal Plasma Vortex in Air

U. Yusupaliev

Moscow State University, Vorob'evy gory, Moscow, 119992 Russia

Received August 18, 2004; in final form, October 28, 2004

Abstract—Forces acting on toroidal vortices in an unbounded medium (plasma vortices in air and vortex rings in air and water) are investigated. A solution to the equations describing such votrices is obtained. It is shown that this solution satisfactorily agrees with experiment. Based on the experimental results and the solution obtained, the drag coefficient C_x of such vortices is found. For the same Reynolds numbers, the value of C_x may be much less than the drag coefficient of a drop-shaped axisymmetric body (0.045), which is known to be the best streamlined object. © *2005 Pleiades Publishing, Inc.*

1. INTRODUCTION

It is only recently (since the late 1970s) that plasma toroidal vortices (PTVs) in air have begun to be studied [1–3]. Further investigations in this field were reported in [4–13]. A PTV usually forms when an axisymmetric pulsed plasma flow is ejected into air from a specially designed plasmatron. Experiments [10] show that the PTV in air is most stable when the plasma flow is subsonic: $\Pi < \Pi_0$ and $\beta_B \le 1$, where $\Pi = p_\Pi/p_\infty$ and $\beta_B = \tau_B/\Delta t_u$ are dimensionless parameters characterizing the plasma flow, Π_0 is the critical value of the dimensionless parameter Π that separates subsonic and supersonic modes of plasma ejection, $p_\Pi = p_0 + bq(t)$ is the gas-kinetic plasma pressure in the plasmatron discharge chamber, p_0 is the initial gas pressure in the discharge chamber, p_∞ is the pressure of the ambient gas, q is the specific energy deposition in the discharge, b is the proportionality factor between q and p_Π, Δt_u is the time during which the plasma is ejected from the discharge chamber, and τ_B is the PTV formation time. At $\beta_B \le 1$, a mushroom-shaped plasma cloud (similar to that formed in nuclear or high-power conventional explosions) arises during a discharge in a subsonic ejection mode. In the late stage of ejection ($t > \Delta t_u$), the mushroom cap transforms into a PTV (a glowing plasma ring) and the accompanying plasma cloud that is not involved in vortex motion. As time elapses, the glowing ring separates from the plasma cloud. By a stable PTV, we mean a vortex whose lifetime τ_L is much longer that the plasma ejection time Δt_u (specifically, $\tau_L/\Delta t_u \ge 70$). Such a PTV in an unbounded medium (air) can be regarded as a long-lived currentless plasma object. In [1], the PTV was supposed to be one of the possible models of ball lightning. According to data from [8, 10], the initial Reynolds number $Re = V_0R_0/\nu$ of a stable PTV is 10^5–10^7, where V_0 is the initial propagation velocity of the vortex, R_0 is its initial radius, and ν is the kinematic viscosity of the air.

The distribution of the electron density $n_e(t)$ in a PTV at $t \ll \Delta t_u$ was measured in [5] using the laser scattering technique. At an initial working gas pressure of $p_0 = 0.7 \times 10^5$ Pa, an initial discharge voltage of 20 kV, and a discharge duration of $\Delta t_u \approx 200$ μs, the electron density in the PTV at the time $t = 48$ μs was found to be $n_e \approx 4 \times 10^{16}$ cm^{-3} and, at $t = 98$ μs, it was ~10^{16} cm^{-3}. The behavior of $n_e(t)$ in a PTV at $t > \Delta t_u$ has been studied very poorly because of the experimental difficulties.

One of the basic properties of the PTV is that, before decaying, it covers a fairly large distance in the medium (in comparison to the distance covered by a spherical plasma cloud of the same size). The PTV path length depends on the initial PTV parameters and can be as large as $x_{max} \approx (60–150)R_0$ [8]. We note that toroidal (ring) vortices in air [14–20] and water [21, 22] possess the same property. Moreover, an analysis of the experimental data [6–8, 14, 15, 17, 21, 22] has shown that PTVs and vortex rings in air and water possess some other identical properties. Thus, the radius $R(t)$ of the vortex increases and its translational velocity $V_x(t)$ decreases as the vortex propagates though the gas. It has been established experimentally that the radius $R(t)$ of both PTVs and vortex rings in air and water increases linearly with increasing distance $x(t)$ covered by the vortex:

$$R(t) = R_0 + \alpha x(t), \tag{1}$$

where α is the expansion angle of the vortex (the ratio of the increment in the vortex radius to the distance $x(t)$). It was found that $\alpha \approx$ const within measurement errors in the initial vortex parameters. We note that, for the PTV, formula (1) was verified only for the initial stage of the vortex propagation (up to a time of (10–20)Δt_u [6–8]).

It follows from the above that both PTVs and vortex rings in air and water have similar dynamic properties; hence, we may assume that their motion can be described by the same equations. As to the thermody-

namic properties of PTVs and vortex rings, they differ significantly. In this sense, vortex rings in air and water should be classed with low-temperature toroidal vortices, while PTVs in air should be classed with high-temperature vortices.

For many practical applications, it is of interest to determine the law of motion $x(t)$ of a toroidal vortex in an unbounded medium. The law of motion $x(t)$ of a vortex ring was found for the first time in [14] by solving a self-similar problem. To solve the problem, the authors of [14] introduced the turbulent viscosity coefficient $\nu_*(t) = \lambda V_x(t)R(t)$ (where λ is a certain constant, which is determined by comparing the theoretical and experimental results). Assuming that turbulent gas motion in a toroidal vortex obeys the Helmholtz equation, they derived a set of equations for the vorticity Ω and the stream function ψ. The equations obtained conserve the total momentum $\mathbf{P}_0$. A self-similar solution to these equations yields the following law of motion of a toroidal vortex:

$$x(t) = \frac{R_0}{\alpha}\left(\left(1 + \frac{4\alpha V_0 t}{R_0}\right)^{\frac{1}{4}} - 1\right). \qquad (2)$$

In [14], the results obtained in the self-similar model were compared to the experimental data. It was shown that the law of motion (2) of a vortex ring satisfactorily agrees with experiment at $4\alpha V_0 t/R_0 \le 4$ (i.e., in the initial stage of the vortex propagation). For $4\alpha V_0 t/R_0 > 4$, however, the theoretical dependence deviates from the experimental data. This was also pointed out in [21], in which vortex rings in water were studied experimentally.

In order to determine the maximal path length of a toroidal vortex, it is necessary to find the forces acting on the vortex. However, in the available papers on PTVs [1–13] and vortex rings [14–22], this problem was not investigated. This may be attributed to the experimental difficulties in measuring the forces (e.g., the drag force) acting on a toroidal vortex. Note that the problem of determining physical mechanisms responsible for the reduction of the drag coefficient of a toroidal vortex is of fundamental importance because the knowledge of these mechanisms may be useful not only in searching new methods for the reduction of the drag coefficient of a body propagating through a gas or liquid but also in studying the general features of self-organizing systems. The goal of the present paper was to investigate the forces acting on a PTV in air and to determine the drag coefficient of such a vortex.

In [10], the following characteristic feature of the PTV and the accompanying plasma cloud was pointed out: for an energy deposited in the discharge of 20–23 kJ and a discharge duration of $\Delta t_u \approx 200$–250 μs, the PTV emits IR radiation in the wavelength range of 3.2–4.2 μm during 0.9–1.0 s, whereas the plasma cloud emits only during 15–20 ms. Such an anomalously long duration of the PTV glow is still poorly understood. From general considerations, it may be supposed that the drag coefficient C_x of the PTV is related to its lifetime τ_L (or the maximal path length $x_{\max}$): the lesser C_x, the larger τ_L and $x_{\max}$. It follows from this that the knowledge of the drag coefficient of the PTV may shed light on the mechanism for its anomalously long glow.

The time evolution of the charged particle density, temperature, chemical composition, and other parameters of the accompanying plasma cloud were studied in [8, 23–25].

Another type of long-lived plasma objects is a spatially localized plasma object (LPO) produced with the help of a microwave discharge in air [26, 27]. In those papers, LPOs were investigated experimentally both in a quiet atmosphere and under conditions of forced convection. The presence of circular (vortex) plasma motion inside an LPO under conditions of forced convection was demonstrated by evaporating thin ceramic probes. Such a vortex was found to have the shape of a torus. It may be said that vortex plasma motion inside an LPO insulates it from the ambient medium [27]. The characteristic plasma velocity inside an LPO is 0.2 m/s. In [26, 27], the most interesting for our purposes is the behavior of LPOs after the microwave oscillator is switched off. Thus, the decay time of an LPO with a temperature of 2500 K, plasma density of 2×10^{12} cm^{-3}, and radius of 3 cm in the presence of plasma circulation after the pumping is switched off is longer than 0.15 s, whereas the decay time of an LPO with almost the same parameters but without circulation is shorter than 0.01 s. This confirms the previously observed experimental result [1, 4, 7–10]: when a PTV is present inside an LPO, its lifetime (0.1–1.0 s) is much longer than the lifetime of an LPO (plasma cloud) without vortex plasma motion (15–20 ms).

It follows from the above that the anomalously long lifetime and stability of both high-temperature PTVs and low-temperature vortex rings in air and water are related to the toroidal configuration of the vortex motion of the plasma, gas, or liquid.

In order to avoid terminological confusion, by a toroidal vortex we here mean a vortex propagating through an unbounded medium (in contrast to similar vortices that are generated in a liquid bounded by two rotating cylinders and that are usually referred to as Taylor vortices [28]).

2. EXPERIMENTAL SETUP AND DIAGNOSTIC TECHNIQUE

To produce a PTV in air at atmospheric pressure, we used two pulsed plasmatrons (Fig. 1) consisting of two metal disk electrodes *1*, dielectric discharge chamber *2*, and nozzle *3*. The design and operating principle of the plasmatrons were described in detail in [8, 10]. Each plasmatron was powered through its own discharge circuit with a capacitive energy storage. The main parameters of the discharge circuits and plasmatrons are given

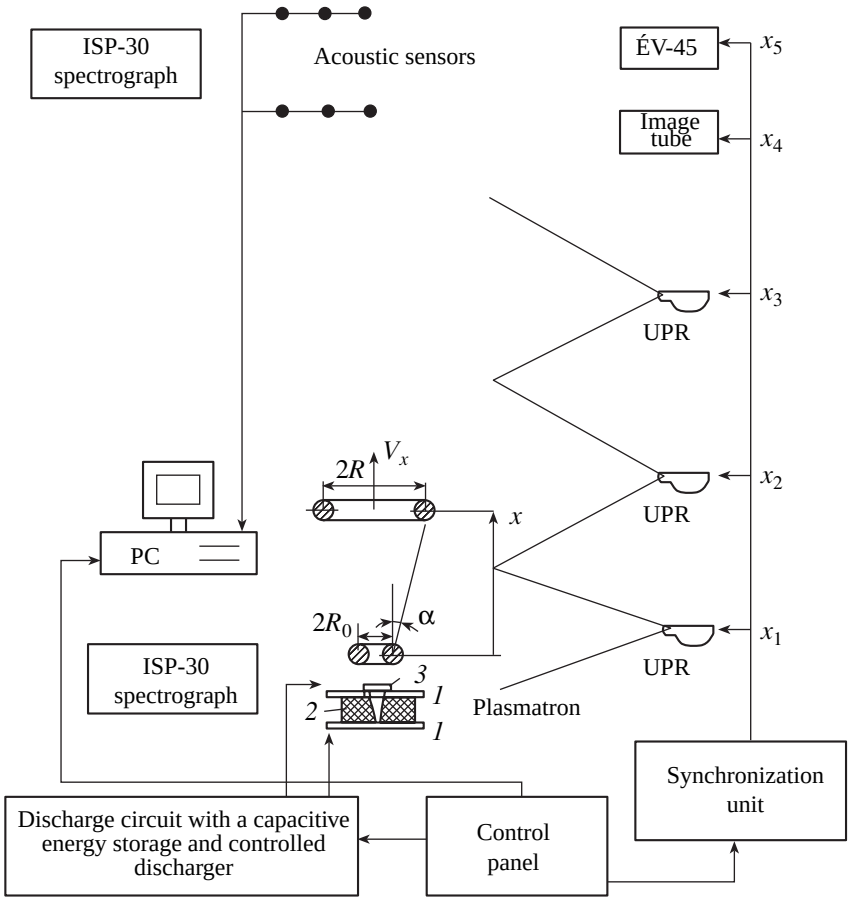

Fig. 1. Block-diagram of the experimental setup and diagnostic facility. In the experiments, the positions of the UPRs, image tube, and acoustic sensors were varied within the ranges x_1 = 0.3–1.0 m, x_2 = 2.0–3.5 m, x_3 = 4.0–6.5 m, x_4 = 8.0–12.0 m, and x_5 = 5.0–15.0 m,

in the table. Methods for measuring the main parameters of the high-current discharges of pulsed plasmatrons were described in detail in [29, 30].

The block diagram of the experimental setup used to study the time evolution of the shape and dimensions of the PTV and the accompanying radiating plasma cloud is shown in Fig. 1. The plasmatron discharge and three SFR-2M ultrafast photorecorders (UPRs) were synchronized by a specially designed electronic system. As a result, the PTV leaving the field of view of one photorecorder immediately entered the field of view of the next photorecorder. The positions of the photorecorders x_1, x_2, and x_3 (see Fig. 1), the delay times of their magnetic detectors, and the mirror rotation velocities were

Table

Parameters of the discharge circuits	Capacitance of the capacitor bank, μF	Operating voltage, kV	Maximum amplitude of the discharge current, kA	Damping decrement of the discharge current and voltage	Duration of energy deposition in the discharge, μs	Energy deposited in the plasmatron discharge, kJ	Volume of the plasmatron discharge chamber, cm^3	Diameter of the plasmatron nozzle, mm	Working gas pressure in the plasmatron discharge chamber, 10^5 Pa
First discharge circuit	C_1 = 30	U_1 = 5–25	50–55	0.84–0.87	180–200	0.2–3.0	3–12	5–12	0.5–2.0
Second discharge circuit	C_2 = 144, 288	U_2 = 8–35	420–470	0.84–0.87	200–250	1.0–55.0	100	8–65	0.5–1.0

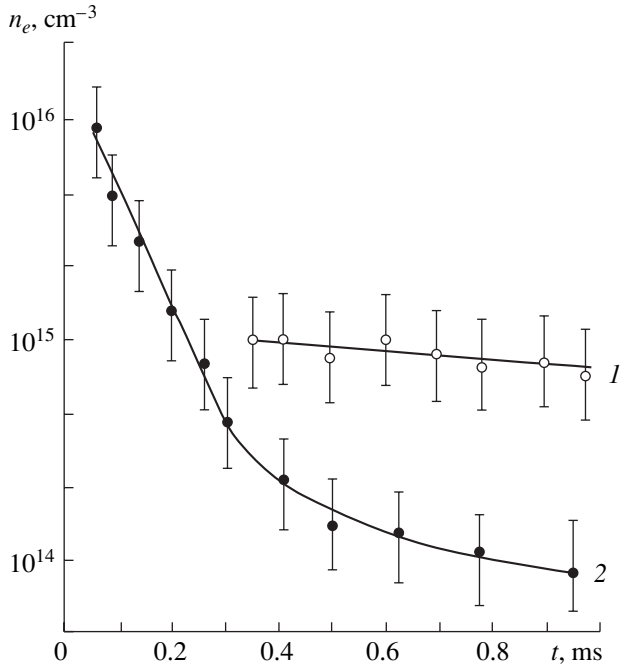

Fig. 2. Time evolution of the electron density n_e in (*1*) the PTV and (*2*) the plasma cloud in the initial stage of vortex motion.

adjusted for each particular operating mode of the plasmatron. The rotation velocity of the UPR mirrors was varied from 2000 to 60000 rpm. The relative error in determining the PTV coordinates by ultrafast recording was 5–7%. Another specific features of ultrafast photorecording as applied to the dynamics of the PTV and plasma cloud were described in detail in [8, 10].

In the late stage of PTV propagation, when it was impossible to take PTV images with the help of photodetectors, we used an image tube with a luminophor screen, which was installed at point x_4 (Fig. 1). The coefficient of electron multiplication of the microchannel plate of the image tube was 3×10^4. A cassette with a photofilm was attached immediately to the luminophor screen. The start-up of the image tube and its frame duration were controlled using a specially designed generator, which was synchronized with the operation of the entire experimental setup.

When it was impossible to take PTV images with the help of the image tube, the PTV coordinates were determined by small-size acoustic (pressure) detectors (Fig. 1). A similar method for determining the coordinates of a vortex ring in air was used in [31]. The signals from acoustic detectors were fed to a PC with a built-in LabCard board, the start-up of which was delayed by a time t_4 with respect to the beginning of the discharge.

The radial profile of the fluid velocity in a PTV was measured using shadowgraphy technique [32] in combination with ultrafast photorecording (in some respects, this method turned out to be more advantageous than thermal and laser Doppler animometry [33]). In shadowgraphs, nonuniformities of the plasma flow with a characteristic size of 2–3 mm were observed over the entire cross section of the torus. These nonuniformities were used to measure both the PTV translational velocity and the radial profile of the rotational velocity in the PTV frame of reference. The error in measuring the plasma velocity by this method was no larger than 7–10%. Shadowgraphs were obtained using two 300-mm-diameter Maksutov objectives and ultrafast photorecording [10]. An ÉV-45 high-intensity radiation source with a temperature 39 000 K was used for illumination.

The charged particle density in the PTV and in the accompanying plasma cloud was determined by measuring the relative intensities of the forbidden and allowed spectral lines of copper [34, 35]. This method is only slightly sensitive to the temperature; this makes it very attractive for diagnosing nonequilibrium plasmas. For this reason, the plasmatron electrodes were made of copper. For diagnostics, we used the forbidden spectral lines with wavelengths of 401.58, 405.58, and 365.2 nm. With these forbidden transitions of copper, it was possible to measure the electron density n_e in the range from 10^{14} to 10^{16} cm^{-3}. It is of interest to study the time evolution of the electron density $n_e(t)$ in both the PTV and the plasma cloud. For this purpose, their radiation spectra were measured simultaneously. The value of n_e obtained by this method is in fact the density averaged over the line of sight (along the diameter of the plasma cloud and along the major radius of the glowing core of the toroidal vortex) and over the observational time (40–60 μs).

The time behavior of the chemical composition in the PTV and the plasma cloud was determined from their emission and absorption spectra. At times $t_5 \gg \Delta t_u$ (when the PTV was glowing feebly), the vortex was illuminated by an ÉV-45 high-intensity reference source and the absorption spectrum of the vortex was recorded by an SP-30 spectrograph. The start-up time t_5 of the ÉV-45 reference source and the distance x_5 at which it was installed (Fig. 1) were adjusted for each particular experiment.

3. EXPERIMENTAL RESULTS

3.1. Figure 2 shows the results of processing the measured relative intensities of the forbidden and allowed spectral lines of copper for C_2 =144 μF, U_2 = 20 kV, $p_0 = 0.7 \times 10^5$ Pa, and $\Delta t_u \approx 250$ μs. The solid curves show the averaged electron density in the PTV (curve *1*) and the plasma cloud (curve *2*). It can be seen that, over a time period of ~750 μs (from 250 μs to 1 ms from the beginning of plasma ejection), the electron density in the plasma cloud decreases by almost one order of magnitude. Just after the termination of the discharge current ($t \geq 250$ μs), the electron density in the plasma cloud drops very rapidly. However, 200–260 μs

later, the decay rate of $n_e(t)$ decreases substantially and curve *2* reaches a nearly quasi-steady level of about 10^{14} cm^{-3}. If the decay of the plasma cloud were governed by recombination, the quantity $1/n_e(t)$ would depend linearly on time, the slope of this dependence being determined by the recombination coefficient α_r. From 90 to 450 μs after the beginning of the discharge, the decay of the plasma cloud is recombinational in character with a recombination coefficient of $\alpha_r \approx 4 \times 10^{-11}$ cm^3/s. At $t > 500$ μs, the decay of the plasma cloud substantially deviates from recombinational. In other words, the recombination of the plasma cloud in the late stage is substantially slowed; i.e., the lifetime of the plasma cloud significantly exceeds the recombination time $\tau_r = 1/(\alpha_r n_e) \approx 10$ μs. A possible reason for such time behavior of the electron density in the plasma cloud can be a change in the recombination mechanism. Indeed, spectral measurements showed the presence of molecular bands in the plasma cloud radiation at $t > 350$–500 μs. Naturally, in the presence of molecules, mechanisms for recombination and ionization differ substantially from those in an atomic gas (e.g., because dissociative recombination in the presence of molecules plays a dominant role) [36, 37].

A comparison of curves *1* and *2* in Fig. 2 shows that the recombination of the plasma in the PTV is slowed down even to a greater extent than in the plasma cloud. This is one of the main results of our study.

The correctness of the measurements of the relative intensities of the forbidden and allowed spectral lines of copper was verified as follows: According to [5], the electron density in a PTV at $t = 98$ μs was ~10^{16} cm^{-3}. To compare our results to those obtained in [5], we used the same plasmatron operating mode and determined n_e by the above optical method at $t = 98$–120 μs. The comparison showed that, within measurements errors, this method yielded the same value of n_e as in [5]. At $t \geq 1.3$ ms ($t > \Delta t_u$), the electron density n_e should decrease to ~10^{13} cm^{-3}. This value of n_e falls within the range of the critical electron densities n_{cr} for millimeter microwaves. For this reason, at $t \geq 1.3$ ms, n_e was determined from the cutoff of the probing microwave signal. It is known [29, 38] that, for a microwave signal in plasma to be cut off at $n_e > n_{cr}$, it is necessary that (i) the electron–neutral collision frequency ν_{en} be much lower than the frequency f of the probing microwave signal ($\nu_{en} \ll f$) and (ii) the characteristic dimensions of the plasma object be much larger than the wavelength λ of the probing microwave. For the given plasmatron operating mode, the effective collision frequency was $\nu_{en} \approx 5 \times 10^{10}$ s^{-1} and, according to the data from the UPRs, the characteristic size of the plasma cloud at $t \geq 1.3$ ms was 0.10–0.12 m. To satisfy the above requirements, we used probing microwaves with a wavelength of $\lambda = 8$ mm, for which $n_{cr} = 1.8 \times 10^{13}$ cm^{-3}. Under these conditions, the probing microwave was cut off at $t \approx 1.3$ ms.

The above allows us to suppose that one of the main reasons for the slower plasma recombination in the PTV and the longer PTV glow (as compared to those in a plasma cloud with the same initial temperature and electron density) is the rotational motion of the plasma in the ambient medium.

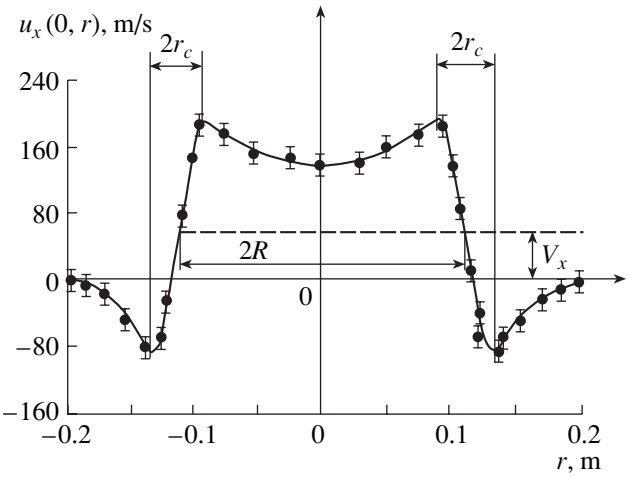

Fig. 3. Radial profile of the axial component of the particle velocity $u_x(0, r)$ in the PTV in the laboratory frame of reference at the end of vortex formation for a nozzle diameter of 65 mm, $C_2 = 144$ μF, and $U_2 = 17$ kV.

3.2. Let us introduce cylindrical coordinates (r, φ, x) with the x axis directed along the propagation direction of the PTV, the coordinate origin ($x = 0$, $r = 0$) being at the geometric center of the vortex. Since the PTV is nearly axisymmetric, its parameters are essentially independent of the azimuthal angle φ. Figure 3 shows a characteristic radial profile of the axial plasma velocity $u_x(0, r)$ in the laboratory frame of reference at $x = 0$. It can be seen that, within experimental errors, $u_x(0, r)$ in the core of the PTV depends linearly on the radius; i.e., the plasma in the PTV core rotates as a solid body. Beyond the core, the velocity $u_x(0, r)$ rapidly decreases and almost vanishes at a distance of $(2.0$–$2.5)r_c$ from the core boundary (here, r_c is the minor radius of the PTV core).

Our experiments show that the PTV motion begins to differ substantially from that of the accompanying plasma cloud only after a toroidal plasma core rotating as a solid body has formed in the PTV. We emphasize that this is one of the main results of our study: the PTV exists as a self-maintained hydrodynamic structure evolving according its own laws of motion only after a toroidal plasma core rotating as a solid body has formed in it. It is such toroidal vortices that are stable. Below, we will consider just such stable toroidal vortices.

In the course of its formation, the PTV accumulates rotational and translational kinetic energy. After the PTV has formed, it propagates as a self-maintained hydrodynamic structure at the expense of this accumulated energy. It follows from experimental results that the rotational kinetic energy of such a PTV is a factor of 2.5 to 3 higher than its translational energy.

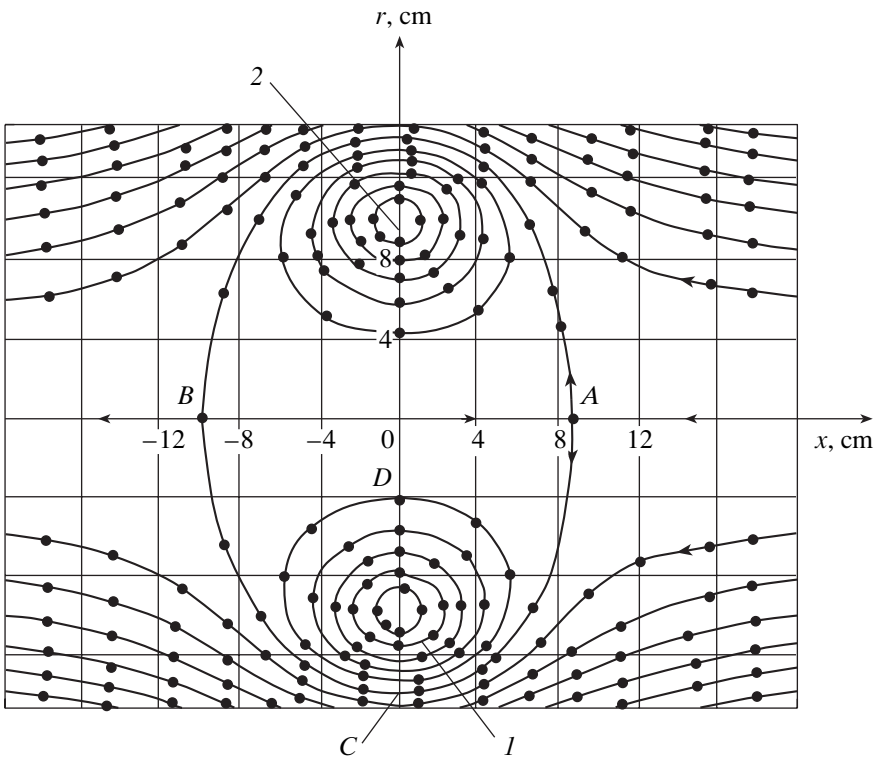

Fig. 4. Streamline pattern for a PTV in the comoving frame of reference at the time t = 1.5 ms after vortex formation for a nozzle diameter of 65 mm, C_2 = 144 μF, and U_2 = 20 kV.

3.3. Figure 4 shows a characteristic PTV streamline pattern in the comoving frame of reference. The pattern was constructed by the method described in [20, 39, 40]. The streamlines in Fig. 4 correspond to the contour lines of the stream function ψ with a step between contours of $\Delta\psi = 0.018$. The streamline pattern shown in Fig. 4 is essentially identical to that for a vortex ring in air (the latter was obtained for the first time with the help of thermal animometry in [39] and then in [41]). The PTV major radius R (the distance from the PTV center to the minor axis of the glowing toroidal core; see Fig. 1) was also measured using ultrafast photorecording. It was found that, within experimental errors, both methods yielded the same results. In our study, the PTV radius was usually measured by ultrafast photorecording because of its relative simplicity.

The streamline pattern consists of two regions: the closed inner region (the vortex atmosphere) and the outer region (the air flowing around the vortex). Inside the vortex atmosphere, the plasma moves along closed streamlines enveloping the toroidal core of the vortex. The vortex atmosphere has the shape of an ellipsoid of revolution and propagates as a single entity through the ambient air with a velocity directed along the small axis of the ellipsoid. This property of the toroidal vortex is confirmed by the time behavior of the emission and absorption PTV spectra: the plasma particles (ions, atoms, and molecules) involved in vortex motion are not lost as the PTV propagates through air.

It can be seen from Fig. 4 that the streamline pattern is slightly asymmetric about the $x = 0$ plane. The asymmetry is most pronounced at the boundary of the vortex atmosphere. The distance from the center of the vortex to this boundary in the positive direction along the x axis is less than that in the negative direction by 6–10%. The degree of asymmetry increases with increasing initial vortex propagation velocity V_0.

3.4. We investigated the relationship between the major PTV radius $R(t)$ and the distance $x(t)$ covered by the vortex in air. Figure 5 shows a series of frames illustrating the PTV dynamics. It can be seen that $R(t)$ increases with time, while the PTV glow intensity decreases. At the time $t \geq (300–500)\Delta t_u$ after the formation of the vortex (this time depends on the initial PTV parameters), the PTV core begins to oscillate in the radial and axial directions. In this case, it is hard to unambiguously determine the geometric parameters of the vortex. The amplitude of these oscillations increases with time, and the vortex eventually decays. The measurements of $R(t)$ and $x(t)$ have shown that formula (1) remains valid until the onset of PTV oscillations.

3.5. Figure 6 shows the measured normalized distance x/R_0 covered by a PTV in air as a function of the dimensionless time $4\alpha V_0 t/R_0$ (the law of motion) for the

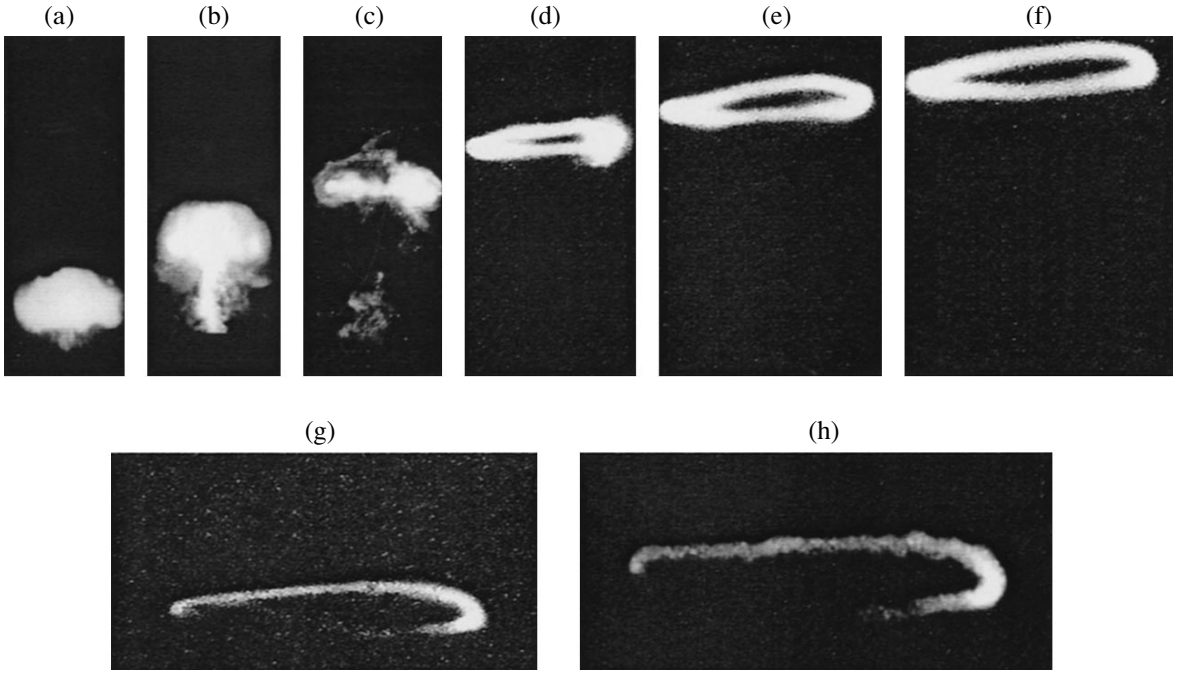

Fig. 5. Dynamics of the PTV in air for a nozzle diameter of 12 mm, $C_1 = 30$ μF, and $U_1 = 25$ kV at different times after the beginning of the plasmatron discharge: t = (a) 0.045, (b) 0.12, (c) 1.0, (d) 15, (e) 35, (f) 50, (g) 75, and (h) 120 ms. Photographs (a)–(c) were taken with the use of an NS8 neutral filter, while photograph (h) was obtained with the help of an image tube.

following initial PTV parameters: $\alpha = 8 \times 10^{-3}$, $V_0 = 120$ m/s, and $R_0 = 0.15$ m. The circles and crosses in Fig. 6 show the PTV coordinates measured using UPRs and acoustic detectors, respectively. For this initial parameters, the PTV becomes unstable and its core begins to oscillate in the radial and axial directions at $4\alpha V_0 t/R_0 \geq 14$–15.

Our experiments have shown that the maximal PTV path length x_{max} depends on the expansion angle α of the vortex: the less the angle α, the larger the path length x_{max}. This means that the expansion angle is related to the drag coefficient C_x of the vortex: the less the angle α, the less the drag coefficient C_x. This is also confirmed by the data from experimental studies of vortex rings in air [15, 17]. This effect is still poorly understood.

3.6. The chemical composition of the PTV was measured from its emission and absorption spectra. In the stage of PTV formation ($t \leq \Delta t_u$), the emission spectrum turned out to be rather complicated: the continuum was superimposed by the spectral lines of the ions and atoms of the working gas (Xe, Kr, N_2), the electrodes (Cu, Al, Fe), and the dielectric wall of the plasmatron discharge chamber (ε-caprolactam, whose molecule mainly consists of C, H, and N). At $t > \Delta t_u$, the intensity of the continuum and the ionic spectral lines decreased substantially as the PTV plasma cooled, whereas Xe and Kr continued to emit intense lines in the 800- to 1000-nm wavelength range and the bands of the CN, C_2, FeO, OH, AlO, and CuO diatomic molecules appeared in the emission spectrum. At $t \gg \Delta t_u$ (when the vortex was glowing feebly), the characteristic lines of Xe and Kr in the 800- to 1000-nm wavelength range and the absorption bands of the CO_2, H_2O, C_2N_2 triatomic molecules appeared in the PTV absorption spectrum.

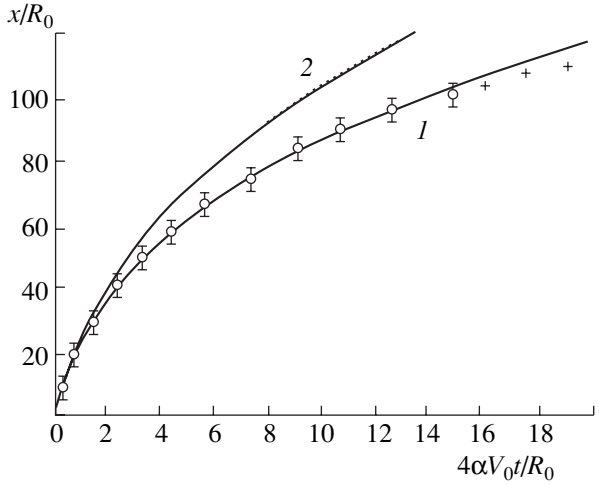

Fig. 6. Measured and calculated dependences of the normalized distance x/R_0 covered by a PTV in air as functions of the dimensionless time $4\alpha V_0 t/R_0$. The symbols show the experimental results, while curves *1* and *2* show the results of calculations.

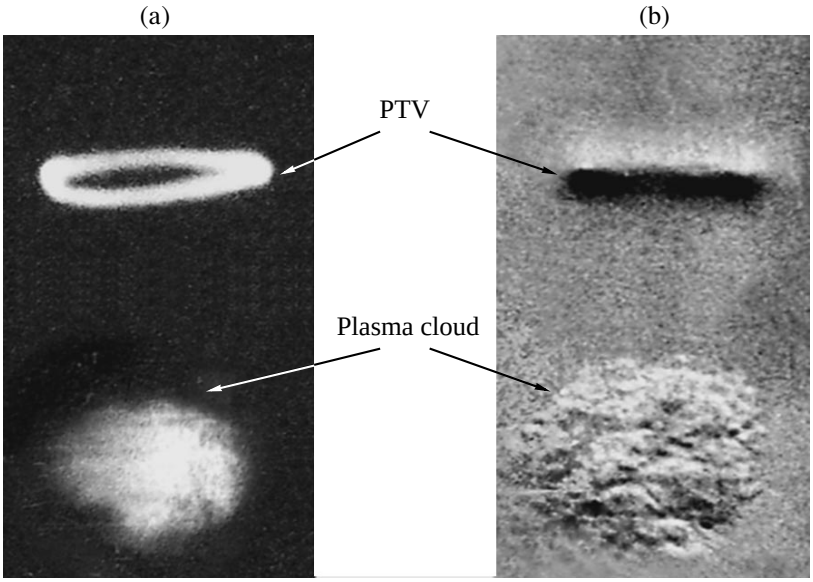

Fig. 7. Images of the PTV and the plasma cloud that is not involved in vortex motion at the time t = 5.4 ms after the beginning of the discharge for a nozzle diameter of 12 mm, C_1 = 30 μF, and U_1 = 20 kV. Photograph (a) was taken in spontaneous plasma emission, while shadowgraph (b) was obtained with the help of backlighting technique.

The results of spectral measurements allow us to conclude that the ions and atoms that were initially involved in vortex motion are not lost as the vortex propagates through air. The ions recombine with electrons and transform into atoms. These atoms, in turn, interact between one another, thereby giving rise to diatomic and then triatomic molecules. The atoms of the working gas are first detected in the emission spectrum. When their emission becomes too weak to be recorded, their presence in the vortex is confirmed by analyzing the absorption spectrum. The occurrence of oxygen atoms in the vortex indicates that the ambient air is involved in vortex motion in the stage of PTV formation, because oxygen is initially absent in the working gas, the electrodes, and the dielectric wall of the plasmatron discharge chamber. An analysis shows that the presence of atomic oxygen in the cooling PTV plasma leads to exothermic chemical reactions; as a result, an additional thermal energy is released. In this sense, the PTV is an open dynamic system into which the oxidant comes from the ambient medium in the stage of PTV formation. The additional thermal energy released in oxidizing reactions depends on the initial concentration of C, Fe, H, Al, and Cu and can be comparable to the energy deposited in the plasmatron discharge. This is confirmed by estimates obtained in [25] for a plasma cloud under the assumption that all the carbon and hydrogen atoms contained in the plasma jet are oxidized to the stable CO_2 and H_2O molecules.

It follows from the spectral measurements and Fig. 6 that the ions, atoms, and molecules involved in vortex motion are transferred by the PTV without significant loss over a fairly great distance, one much longer than that over which they are transferred by the irrotational plasma cloud. For the initial PTV parameters corresponding to Fig. 6, the plasma vortex covers a distance of 13–15 m over a time of 0.6–0.7 s, whereas the plasma cloud with the same initial parameters covers a distance of no larger than 1.2–1.5 m over a time of 15–20 ms and then decays. That the plasma cloud covers such as short distance is naturally explained by the strong turbulization of the plasma and the ambient medium (air) behind the cloud (see Fig. 7b).

4. QUANTITATIVE ANALYSIS OF THE VORTEX DYNAMICS AND THE DERIVATION OF ITS EQUATIONS OF MOTION

The mechanical momentum of the PTV was determined from the measurements of its propagation velocity $V_x(t)$, radial expansion velocity $V_r(t)$, and radius $R(t)$. The experiments have shown that the PTV momentum decreases with time, which contradicts to the basic assumption of the self-similar model of a toroidal (ring) vortex [14, 15]. According to Newton's second law, the momentum of such a vortex changes under the action of the forces arising in the interaction of the vortex with the ambient medium. Thus, to describe the propagation of a toroidal vortex, it is necessary to find the net force acting on it.

The forces acting on a toroidal vortex can be determined by considering the interaction between the vortex and the ambient medium, as well as between different parts of the vortex. Let us first consider the streamline pattern shown in Fig. 4. It can be seen that the streamline pattern of the air flow around the vortex atmosphere resembles that of a continuous gas flow around a solid body of the same shape. The streamlines

of the air flow are bent under the action of the force exerted by the vortex on the incident flow. In turn, according to Newton's third law, the incident air flow should exert the equal (but oppositely directed) drag force on the propagating toroidal vortex. It is the action of this drag force to which the experimentally observed asymmetry of the streamline pattern (Fig. 4) can be attributed.

By analogy with a solid body [28, 33, 42], we will assume that the total drag force F_C acting on a toroidal vortex propagating through a viscous medium (gas or liquid) is the sum the normal-stress force F_F, determined by the shape of the vortex, and the viscous friction force F_V, related to the shear stress near the vortex surface:

$$F_C = F_F + F_V = F_F + \eta\int_S((\nabla\times\mathbf{V})\times\mathbf{e}_n)_x dS. \qquad (3)$$

Here, dS is the element of the area of the vortex surface, $\mathbf{V}$ is the fluid velocity, η is the dynamic viscosity of the ambient medium, and $\mathbf{e}_n$ is the unit vector directed along the normal to the vortex surface. It can be seen from Fig. 4 that the fluid velocity at the boundary of the vortex atmosphere *ACB* varies only slightly along the normal to the vortex surface ($\nabla\times\mathbf{V}\approx 0$). As a result, the viscous friction force is absent in spite of the ellipsoid being poorly streamlined. However, the normal-stress force related to the shape of the vortex is nonzero.

To find the expression for the force F_F, we make use of the theory of similarity and dimensionality. An analysis of experimental data on PTVs and vortex rings [14–22] shows that the motion of the ambient medium around of the vortex is determined by the following four parameters: the propagation velocity V_x of the vortex, its maximum transverse cross section S_M, and the density ρ_∞ and dynamic viscosity η of the ambient medium. It follows from experimental data [1, 2, 7, 8, 10, 14, 17, 19–22] that the propagation velocity of a toroidal vortex is lower than the speed of sound; therefore, the compressibility of the medium can be ignored. From the above four parameters, only one dimensionless quantity can be composed: the Reynolds number of the vortex $Re = \dfrac{\rho_\infty V_x\sqrt{S_M}}{\eta}$. According to the theory of similarity and dimensionality [43], the dimensionless quantities characterizing the mechanical motion of the ambient medium around the vortex (in particular, the quantity $C_x = \dfrac{F_F}{(1/2)\rho_\infty V_x^2 S_M}$) are functions of Re. Therefore, the expression for the force F_F can be represented in the form

$$F_F = C_x(Re)\frac{\rho_\infty V_x^2}{2}S_M. \qquad (4)$$

By analogy with hydrodynamic flows, the dimensionless quantity C_x can be called the drag coefficient of the toroidal vortex.

That the drag coefficient C_x is a function of the Reynolds number has been confirmed experimentally (e.g., by vortex shadowgraphs). Figure 7a shows a typical photograph of the PTV and the accompanying plasma cloud that is not involved in vortex motion for an initial PTV propagation velocity of $V_0 < 140$ m/s, and Fig. 7b shows their shadowgraph. It can be seen that, at such velocities, the air flow behind the vortex is not turbulized, whereas the plasma cloud and the air flow behind it are highly turbulized. Shadowgraphs taken at higher initial propagation velocities ($V_0 \geq 140$–160 m/s) show that, in this case, the air flow behind the vortex is slightly turbulized. A turbulent air flow behind the vortex was also observed in [2]. The appearance of such a turbulent flow means that the gas flowing around the vortex acquires kinetic energy and rotational moment. The source of this kinetic energy is the rotational motion of the toroidal vortex, because its translational (drift) motion occurs mainly at the expense of its rotational energy. In other words, the increase in the initial PTV velocity to $V_0 \geq 140$–160 m/s (i.e., an increase in the Reynolds number) leads to an increase in the force exerted on the vortex by the air flow and, accordingly, an increase in the drag coefficient C_x.

Thus, the equation of motion for a toroidal vortex (treated as the single entity) along the x axis in an unbounded medium with allowance for the condition $\nabla\times\mathbf{V}\approx 0$ and formula (4) can be written in the form

$$\frac{d}{dt}(m_B V_x) = -C_x\frac{\rho_\infty V_x^2}{2}S_M, \qquad (5)$$

where $m_B = \rho_{av}(4\pi/3)R^3$ is the mass of the plasma (gas) involved in vortex motion and ρ_{av} is the average mass density of the plasma (gas) in the vortex. The mass m_B was evaluated using the mean-value theorem, because the measured radial profile of the plasma density inside the vortex was monotonic.

Let us now determine the forces acting on the toroidal vortex in the radial direction. For this purpose, we consider the interaction between two diametrically opposite vortex elements *1* and *2* (see Fig. 4) with equal (but oppositely directed) intensities (velocity circulations) $\pm\Gamma$. Element *2* with intensity Γ generates around itself a velocity field that acts on element *1*. According to Bernoulli's law, the pressure p_C at point C is higher than the pressure p_D at point D. Therefore, according to [33], unit-length element *1* undergoes the attraction force

$$f_A = \frac{\rho_\infty\Gamma^2}{4\pi R}, \qquad (6)$$

which is directed to the center of the toroidal vortex; i.e., element *2* attracts diametrically opposite element *1*. Under the action of this force, element *1* shifts along the

x axis, i.e., it drifts in the direction perpendicular to the attraction force f_A.

The mechanism for the origin of the drift motion of element *1* under the action of the attraction force f_A is similar to that of the drift motion of charged particles rotating around magnetic field lines under action of a force directed perpendicularly to the magnetic field [44].

On the other hand, as the vortex propagates in the axial direction, the air flowing around element *1* produces the pressure difference $p_D - p_C > 0$ between points D and C according to Bernoulli's law. Therefore, element *1* undergoes the radial force exerted by the air flow around the vortex. As a result, the toroidal vortex expands radially. According to [33], the expansion force per unit length of the toroidal vortex is equal

$$f_E = \rho_\infty V_x \Gamma. \quad (7)$$

For linear vortices, the forces f_A and f_E counterbalance one another. With allowance for this, in [33], the propagation velocity V_x of a linear vortex was found to be $\Gamma/4\pi R$. For toroidal vortices, these forces do not counterbalance one another. Indeed, experiments [4, 6–8, 15, 17–19, 21, 22] show that toroidal vortices expand with time. This means that the forces f_E and f_A are not counterbalanced; i.e., the vortex undergoes a nonzero net expansion force $F_E - F_A = 2\pi R(f_E - f_A)$. This force can be found from the radial component of the equation of motion:

$$\frac{d}{dt}(m_B V_r) = F_E - F_A. \quad (8)$$

To solve Eqs. (5) and (8), it is necessary to find the relationship between V_x and R. Such a relationship can be found from formula (1): $\frac{dR}{dt} = V_r = \alpha V_x$. Therefore, with allowance for Eq. (8), we obtain

$$\frac{d}{dt}(m_B V_r) = \alpha \frac{d}{dt}(m_B V_x) = -\alpha C_x \frac{\rho_\infty V_x^2}{2} S_M, \quad (9)$$

i.e., the net force is equal to

$$F_E - F_A = -\alpha C_x \frac{\rho_\infty V_x^2}{2} S_M. \quad (10)$$

Thus, to find the law of motion of a toroidal vortex, it is necessary to solve Eq. (5). Taking into account that the average mass density in the vortex varies with time more slowly than the vortex propagation velocity, Eq. (5) can be rewritten in the form

$$R\frac{dV_x}{dt} = -\left[\frac{3}{2} C_x \left(\frac{\rho_\infty}{\rho_{av}}\right) + 3\alpha\right] V_x^2 = -BV_x^2. \quad (11)$$

This equation is reduced to the following nonuniform nonlinear one-variable differential equation:

$$(R_0 + \alpha x)\frac{d^2x}{dt^2} = -B\left(\frac{dx}{dt}\right)^2 \quad (12)$$

with the initial conditions

$$x(0) = 0, \quad R(0) = R_0. \quad (13)$$

We integrate Eq. (12) over time and find the constant of integration from initial conditions (13) to obtain the law of motion of the toroidal vortex,

$$x(t) = \frac{R_0}{\alpha}\left\{\left\langle 1 + \left[\frac{3C_x}{2\alpha}\left(\frac{\rho_\infty}{\rho_{av}}\right) + 1\right]\frac{4\alpha V_0}{R_0} t\right\rangle^{\frac{1}{\frac{3C_x}{2\alpha}\left(\frac{\rho_\infty}{\rho_{av}}\right)+4}} - 1\right\} \quad (14)$$

and the formula describing the time evolution of the vortex propagation velocity,

$$V_x(t) = V_0\left\{1 + \left[\frac{3}{2}\frac{C_x}{\alpha}\left(\frac{\rho_\infty}{\rho_{av}}\right) + 1\right]\frac{4\alpha V_0}{R_0} t\right\}^{\frac{-\frac{3}{2}\frac{C_x}{\alpha}\left(\frac{\rho_\infty}{\rho_{av}}\right)-3}{\frac{3}{2}\frac{C_x}{\alpha}\left(\frac{\rho_\infty}{\rho_{av}}\right)+4}}. \quad (15)$$

With these formulas, we find the time evolution of the vortex radius:

$$R(t) = R_0\left\{1 + \left[\frac{3}{2}\frac{C_x}{\alpha}\left(\frac{\rho_\infty}{\rho_{av}}\right) + 1\right]\frac{4\alpha V_0}{R_0} t\right\}^{\frac{1}{\frac{3C_x}{2\alpha}\left(\frac{\rho_\infty}{\rho_{av}}\right)+4}}. \quad (16)$$

If we set $C_x = 0$ in formulas (14)–(16) (i.e., if we assume that the drag force is absent), these formulas will coincide with the formulas for $x(t)$ (see Eq. (1)), $V_x(t)$, and $R(t)$ obtained using the self-similar model of a turbulent vortex ring in air [14]:

$$V_x(t) = \frac{V_0}{\left(1 + \frac{4\alpha V_0}{R_0} t\right)^{\frac{3}{4}}}, \quad (17)$$

$$R(t) = R_0\left\{1 + 4\alpha\frac{V_0}{R_0} t\right\}^{\frac{1}{4}}. \quad (18)$$

In this sense, the self-similar model of a turbulent vortex ring is a particular case of our model.

An important point is that all the quantities in formulas (14)–(16) (except for the drag coefficient C_x) may be determined experimentally. This allows one to

calculate C_x from experimental data. Figure 6, besides the experimental data, shows the theoretical curves calculated by formula (14) (curve *1*) and by the self-similar model [14] (curve *2*) for the following initial PTV parameters: $\alpha = 8 \times 10^{-3}$, $\rho_\infty/\rho_{av} = 5$, $V_0 = 120$ m/s, and $R_0 = 0.15$ m. It is seen that the curve calculated by formula (14), satisfactorily agrees with experimental data at $C_x \approx 0.0012$ almost until the PTV begins to decay.

From the measured quantities $V_x(t)$, $R(t)$, α, and ρ_∞/ρ_{av} and from formulas (6), (7), and (10), we can determine one of the main parameters of the toroidal vortex—the velocity circulation Γ:

$$\Gamma(t) = 2\pi\left(\frac{\rho_\infty}{\rho_{av}}\right)V_x(t)R(t)\left[1 + \sqrt{1 + \left(\frac{4\alpha C_x}{\pi}\right)\left(\frac{\rho_\infty}{\rho_{av}}\right)}\right]. \quad (19)$$

If we set $C_x = 0$ and $\rho_\infty/\rho_{av} = 1$ (a vortex ring produced by a submerged pulsed jet) in this formula, it coincides with the formula

$$\Gamma = \Gamma_0\left\{1 + 4\alpha\frac{V_0}{R_0}t\right\}^{-\frac{1}{2}} = \Gamma_0\left(\frac{R_0}{R(t)}\right)^2, \quad (20)$$

obtained using the self-similar model of a turbulent vortex ring [15] (here, Γ_0 is the initial velocity circulation of the vortex).

5. VORTEX RINGS IN AIR AND WATER

5.1. Vortex Ring in Air

Let us now determine the drag coefficient C_x for a vortex ring in air. The most complete experimental information about the law of motion of a vortex ring in air at atmospheric pressure is given in [14, 17]. The circles in Fig. 8 shows the experimental data [14] for the following initial vortex parameters: $R_0 = 0.1$ m, $V_0 = 4.3$ m/s, and $\alpha = 6 \times 10^{-3}$ ($Re \approx 5 \times 10^4$). For these parameters, the average gas mass density in the vortex was equal to the mass density of the ambient gas: $\rho_B \approx \rho_\infty$. Curves *1* and *2* show the theoretical curves calculated for such a vortex by formulas (1) and (14), respectively. It can be seen from Fig. 8 that curve *2* satisfactorily agrees with experimental data at $C_x \approx 0.0042$; this is not the case, however, for curve *1*, calculated using the self-similar model [14].

Formula (14) predicts that the larger the vortex radius R_0, the longer the vortex path length x_{max}. Indeed, according to [16], in which toroidal vortices generated by explosions in air were investigated, a toroidal vortex with an initial radius of ~2 m, initial propagation velocity of ~100 m/s, and $\alpha \approx 6 \times 10^{-3}$ covers a distance about $x_{max} \approx 500$ m. According to formula (14), the vortex covers this distance over a time of 50–70 s at $C_x \approx 0.004$–0.0045.

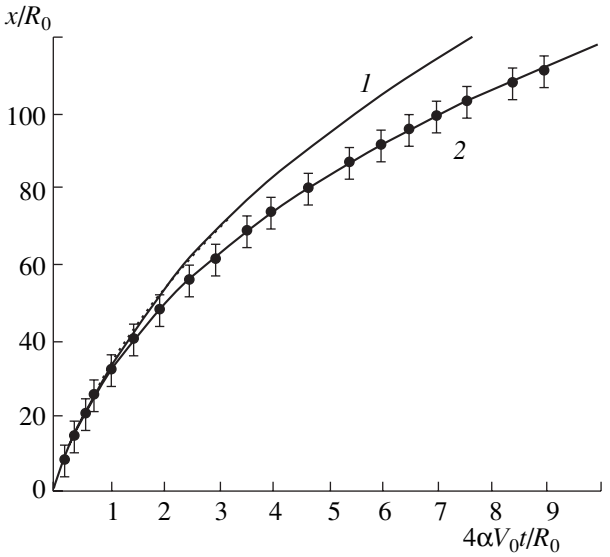

Fig. 8. Measured and calculated dependences of the normalized path x/R_0 covered by a vortex ring in air as functions of the dimensionless time $4\alpha V_0 t/R_0$. The circles show the experimental results [14], while curves *1* and *2* show the results of calculations.

5.2. Vortex Ring in Water

The drag coefficient C_x of a vortex ring in water was determined using the experimental data from [21], in which vortex rings propagating downward along the normal to the water surface and those propagating in the opposite direction (toward the water surface) were investigated. At $Re < 0.5 \times 10^4$, vortices propagating toward the water surface decelerated near this surface and decayed. At $Re = (0.5–1.0) \times 10^4$, the vortices were reflected from the water surface and then propagated in the opposite direction (downward). At the instant of reflection, a bowl containing the vortex (which was clearly seen in photographs) formed on the water surface. The measurements of the vortex propagation velocity showed that it did not change after reflection. This means that the vortex undergoes elastic reflection from the water surface; i.e., it behaves as a solid body (this property of the vortices was not known earlier). At $Re > 1.3 \times 10^4$, the vortices decayed after colliding with the water surface. If the vortex approached the water surface at a sufficiently high velocity, its decayed in an explosive manner and a portion of water was ejected upward.

The law of motion of a toroidal vortex in water was investigated at $Re = (0.5–1.0) \times 10^4$. The circles in Fig. 9 show the experimental data obtained in [21] for the following initial vortex parameters: $R_0 = 0.17$ m, $V_0 = 0.6$ m/s, and $\alpha = 10^{-2}$. The vortices were visualized by adding a small amount of dye to water. The average mass density of the colored water in the vortex was close to the average mass density of the ambient water: $\rho_B \approx \rho_\infty$. Figure 9 compares theoretical curves *1* and *2*,

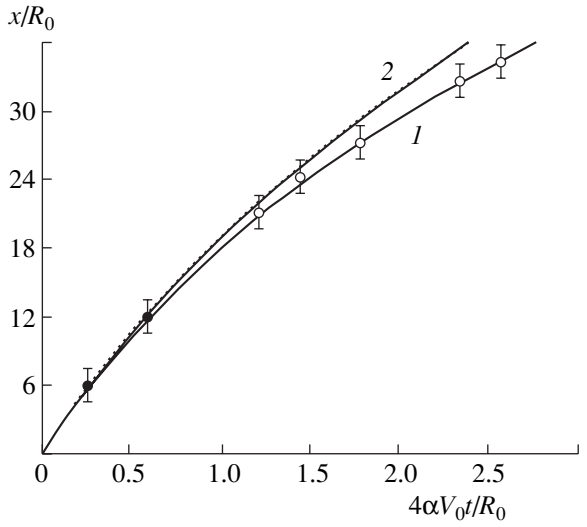

Fig. 9. Measured and calculated dependences of the normalized path x/R_0 covered by a vortex ring in water as functions of the dimensionless time $4\alpha V_0 t/R_0$. The circles show the experimental results [21], while curves *1* and *2* show the results of calculations.

calculated by formulas (14) and (1), respectively, against the experimental data obtained for the above vortex parameters. It can be seen that curve *1* (in contrast to curve *2*) agrees satisfactorily with the experimental data at $C_x = 0.008$.

5.3. Comparison to the PTV

A comparison of theoretical curve (14) to the experimental data on PTVs and vortex rings in air and water for another initial parameters shows that the quantity $\frac{3C_x}{2\alpha}\left(\frac{\rho_\infty}{\rho_{av}}\right)$ for PTVs is about 1.3–1.5, whereas for a vortex ring, it is about 1.0–1.2. From this, we obtain the following estimate for C_x:

$$C_x \approx A\frac{2}{3}\left(\frac{\rho_{av}}{\rho_\infty}\right)\alpha, \qquad (21)$$

where $A \approx 1.1$–1.5; i.e., the drag coefficient C_x of a toroidal vortex is directly proportional to the expansion angle of the vortex. This explains the experimentally observed relationship between C_x and α (see Section 3).

Thus, in spite of the shape of a toroidal vortex (an ellipsoid of revolution with a major axis perpendicular to the vortex propagation velocity; see Fig. 4) being poorly streamlined, its drag coefficient for the same Reynolds numbers turns out to be less than the drag coefficient of an axisymmetric teardrop-shaped body (0.045), which is known to be the best streamlined form [42].

6. THERMAL CHARACTERISTICS OF THE PTV

To measure the plasma temperature in localized plasma objects (such as the PTV and the accompanying plasma cloud) in which recombination dominates over ionization and plasmochemical reactions occur is a rather complicated problem [36], which deserves special consideration. To gain a better insight in this problem, it is expedient to analyze the relation between the thermal characteristics of a high-temperature PTV and the law of its motion. Let us consider the spatial distribution of the temperature of heavy plasma particles within the PTV and the plasma cloud. Figure 10 shows typical radial profiles of the rotational molecular temperature in (a) the PTV and (b) the plasma cloud, which radiate in the near UV and visible spectral regions. The method for measuring the spatial distribution of the rotational molecular temperature in plasma is described in detail in [29]. According to [29, 36, 45], the rotational–translational relaxation proceeds fairly rapidly; therefore, the rotational molecular temperature is close to the temperature of the heavy plasma particles. At $t \approx 250$ μs, i.e., just after the PTV and the plasma cloud has been formed from the mushroom cap (see Fig. 5b), the plasma temperatures in the PTV and the cloud are the same and are equal to 8000–8500 K.

It follows from Fig. 10 that the gradient of the plasma temperature at the boundary of the PTV glowing core is much larger than that at the periphery of the cloud. If the thermal conductivity of the plasma were the same in the PTV and the cloud, then the heat flux at the boundary of the PTV core would be much larger than that at the boundary of the plasma cloud because of the much larger temperature gradient at the PTV boundary. As a result, the PTV would cease to glow earlier than the plasma cloud. This, however, contradicts the experimental results: for the same initial conditions, the plasma cloud radiates in the visible region only during 15–20 ms, whereas the PTV continues glowing up to 100–700 ms, depending on the initial parameters. Taking into account that air at atmospheric pressure begins to radiate in the visible range at a temperature of about 2000 K, this means that the plasma temperature in the cloud decreases from 8000–8500 to 2000 K over 15–20 ms, whereas the PTV plasma cools much more slowly (over 100–700 ms). Such a slow cooling of the PTV plasma, whose the temperature gradient is very large, may be explained only by a substantial decrease in the heat flux from the rotating PTV plasma (i.e., a decrease in the effective thermal conductivity) as compared to that from the nonrotating plasma cloud. This is confirmed by the data from [46, 47], in which it was shown that the heat flux toward the tube wall from the hot gas flowing through was substantially reduced when the gas rotated along the tube axis. An analogy can also be drawn between the decrease in the effective thermal conductivity in the PTV and the reduction in the transverse transport coefficients in a magnetized

plasma [48]. Apparently, the difference between the transverse and longitudinal (with respect to the rotation axis) transport coefficients is a general feature of the rotating plasma (gas), irrespective of the means by which this rotation is produced.

The reduction in the heat flux from the PTV can be explained as follows: In rotating frame of reference, an elementary volume of the gas undergoes the equivalent gravity force (the centrifugal force) directed from the rotation axis. As is well known, the hotter gas in a gravitational field moves (convects) against gravity under the action of the buoyancy force. In our case, the hotter plasma and, in a later stage, the hotter gas also should move toward the rotation axis (the minor axis of the torus) under the action of the force that is an analog of the buoyancy force in the gravitational field. As a result, the hotter plasma (gas) is accumulated near the rotation axis and (according to the terminology of [27]) becomes to be insulated from the ambient medium. In case of a low-temperature vortex ring, the outer gas layers at the boundary of the vortex core, rotating as a solid body, lag behind the inner ones; this lead to the heating of the gas in the boundary layer due to the viscous dissipation of the rotational energy. The heated gas then convects toward the rotation axis, as in a high-temperature PTV. The reduction of the radial heat flux in a turbulent vortex ring was estimated quantitatively in [49].

In Section 4, we have considered the forces exerted on the PTV by the air flowing around the vortex and the interaction forces between different parts of the vortex. With regard to the forces acting inside the vortex (such as the Coriolis force, buoyancy force, and viscous force), they may lead to a partial conversion of the internal vortex energy (the thermal energy released due to electron–ion recombination, chemical reactions, and condensation of vapor) into rotational energy [50]. As the thermal energy is released, the local plasma density in the vortex decreases and the plasma with a reduced density undergoes the buoyancy force directed to the rotation axis. The plasma moving toward the rotation axis under the action of this force undergoes the Coriolis force, which acts to accelerate plasma rotation. Thus, under the action of the buoyancy and Coriolis forces, the thermal energy released in the vortex is partially converted into the rotational energy; i.e., the loss of the rotational energy is reduced. In case of a low-temperature vortex ring, thermal energy is released in the viscous layer at the boundary of the vortex core. If the released energy is larger than the total energy loss, then the vortex is enhanced; otherwise, it is self-maintained. From this point of view, the PTV in air can be regarded as a self-organized dynamic system. In other words, the lifetime of the vortex as a self-maintained hydrodynamic structure increases due to the forces arising in it.

The above forces can lead to the suppression of the fluid velocity fluctuations (especially low-frequency ones) in the direction perpendicular to the axis of gas rotation [51]. The stabilization of an arc discharge by the forced rotation of the gas in the discharge chamber may also be attributed to the action of these forces [52]. Therefore, the problem of the forces acting inside the PTV deserves special consideration.

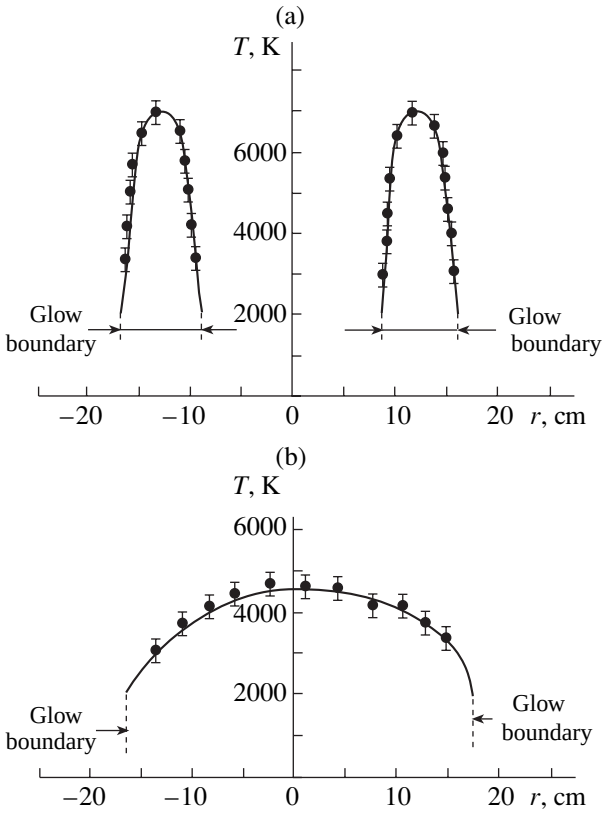

Fig. 10. Radial profiles of the rotational molecular temperature in (a) the PTV and (b) the plasma cloud at the time t = 0.6 ms for a nozzle diameter of 65 mm, C_2 = 144 μF, and U_2 = 23 kV. According to [45], the temperature at the visible boundaries of the glowing plasma objects is taken to be ≈2000 K.

7. CONCLUSIONS

The above analysis shows that the long distance covered by a PTV in air is related to the small value of its drag coefficient C_x, whereas its anomalously long glow is related to the suppression of both the heat flux from the vortex into the ambient medium and the fluid velocity fluctuations (especially low-frequency ones) in the direction perpendicular to the rotation axis. We have determined the power expended by a toroidal vortex on the penetration through the ambient viscous medium. The next problem to be addressed is determining the losses by radiation and heat conduction. In solving this problem, it is necessary to take into account the decrease in the heat flux from the vortex, which depends on the angular rotation velocity and the energy that is initially stored in the vortex (translational and rotational kinetic energy, plasma thermal energy,

energy of the excited plasma particles, chemical energy, etc.).

The similarity between high-temperature PTVs in air and low-temperature vortex rings in air and water allows one to describe their dynamics by the same equations.

ACKNOWLEDGMENTS

I thank A.F. Aleksandrov, A.A. Rukhadze, V.A. Chernikov, L.S. Kuz'menkov, and I.B. Timofeev (deceased) for supporting this work and for their helpful discussions. I wish to express my gratitude to A.I. Sokolov (deceased) for his help in constructing the experimental setups and performing the experiments. I am also grateful to my friends for their generous financial support in constructing the experimental setups in 1994–2000.

REFERENCES

1. A. M. Andrianov and V. I. Sinitsin, Zh. Tekh. Fiz. **47**, 2318 (1977) [Sov. Phys. Tech. Phys. **22**, 1342 (1977)].
2. A. I. Klimov, F. V. Shugaev, and M. A. Ibragim, Vestnik MGU, Ser. Fiz., Astron., No. 3, 24 (1978).
3. A. A. Luchnikov, A. M. Gozhakov, P. D. Sereda, and I. P. Sokolov, Prib. Tekh. Éksp., No. 2, 237 (1981).
4. A. F. Aleksandrov, I. B. Timofeev, V. A. Chernikov, and U. Yusupaliev, in *Kinetic and Gas-Dynamic Processes in Nonequlibrium Media* (Mosk. Gos. Univ., Moscow, 1986).
5. A. F. Aleksandrov, B. Azzedin, Yu. Bakhgat, *et al.*, Zh. Tekh. Fiz. **56**, 2392 (1986) [Sov. Phys. Tech. Phys. **31**, 1431 (1986)].
6. I. B. Timofeev, V. A. Chernikov, and U. Yusupaliev, *7th All-Union Conference on Low-Temperature Plasma, Tashkent, 1987*, Abstracts of Papers, Part 1, p. 267.
7. A. F. Aleksandrov, I. B. Timofeev, V. A. Chernikov, and U. Yusupaliev, in *Proceedings of the XVII International Conference on Phenomena in Ionized Gases, Suansu, 1987*, Part 2. p. 426.
8. U. Yusupaliev, Candidate's Dissertation in Mathematics and Physics (Mosk. Gos. Univ., Moscow, 1988).
9. A. F. Aleksandrov, I. B. Timofeev, V. A. Chernikov, and U. Yusupaliev, Teplofiz. Vys. Temp. **26**, 639 (1988).
10. U. Yusupaliev, Zh. Tekh. Fiz. **74** (7), 52 (2004) [Tech. Phys. **49**, 858 (2004)].
11. V. N. Kunin and L. V. Furov, Izv. Vyssh. Uchebn. Zaved., Fiz., No. 6, 119 (1990).
12. V. N. Kunin and L. V. Furov, in *Proceedings of the European Interdisciplinary Congress on Ball Lightning (Vizotum'93), Salzburg, 1993*, p. 50.
13. V. N. Kunin, V. S. Pleshivtsev, and L. V. Furov, Teplofiz. Vys. Temp. **35**, 866 (1997).
14. A. A. Lugovtsov, B. A. Lugovtsov, and V. F. Tarasov, in *Dynamics of Continuous Media* (Inst. Gidrodinamiki SO AN SSSR, Novosibirsk, 1969), Vol. 3, p. 50.
15. B. A. Lugovtsov, Extended Abstract of Doctoral Dissertation in Mathematics and Physics (Inst. Gidrodinamiki SO AN SSSR, Novosibirsk, 1973).
16. M. A. Lavrent'ev and B. V. Shabat, *Hydrodynamic Problems and Their Mathematical Models* (Nauka, Moscow, 1973).
17. V. F. Tarasov, Extended Abstract of Candidate's Dissertation in Mathematics and Physics (Inst. Gidrodinamiki SO AN SSSR, Novosibirsk, 1975).
18. T. Maxworthy, J. Fluid Mech. **81**, 465 (1977).
19. K. Shariff and M. Leonard, Ann. Rev. Fluid Mech. **24**, 235 (1992).
20. D. G. Akhmetov, Extended Abstract of Candidate's Dissertation in Mathematics and Physics (Inst. Gidrodinamiki SO RAN, Novosibirsk, 2002).
21. V. I. Boyarintsev, T. E. Boyarintseva, D. G. Korotaev, *et al.*, Mekh. Zhidk. Gaza, No. 3, 125 (1997).
22. L. S. Kokorev, B. N. Kostyunin, and D. A. Kurov, in *Problems of Thermal Physics of Nuclear Reactors* (Atomizdat, Moscow, 1976), Vol. 5, p. 5.
23. A. F. Aleksandrov, A. P. Ershov, K. Sh. Isaev, and I. B. Timofeev, in *Proceedings of the XVII International Conference on Phenomena in Ionized Gases, Suansu, 1987*, Part 2, p. 436.
24. A. Anders, A. P. Ershov, and K. Sh. Isaev, Contrib. Plasma Phys. **28**, 537 (1988).
25. K. Sh. Isaev, Candidate's Dissertation in Mathematics and Physics (Mosk. Gos. Univ., Moscow, 1990).
26. V. A. Zhil'tsov, Zh. F. Lyaĭtner, É. A. Manykin, *et al.*, Zh. Éksp. Teor. Fiz. **108**, 1966 (1995) [JETP **81**, 1072 (1995)].
27. A. A. Skovoroda, Zh. Éksp. Teor. Fiz. **112**, 877 (1997) [JETP **85**, 474 (1997)].
28. L. D. Landau and E. M. Lifshitz, *Fluid Mechanics* (Nauka, Moscow, 1986; Pergamon, Oxford, 1987).
29. *X-Ray Diagnostics of Plasmas*, Ed. by W. Lochte-Holtgreven (American Elsevier, New York, 1968; Mir, Moscow, 1971).
30. A. F. Aleksandrov and A. A. Rukhadze, *Physics of High-Current Electric-Discharge Light Sources* (Atomizdat, Moscow, 1976).
31. M. Yu. Zaĭtsev, V. F. Kop'ev, A. G. Munin, and A. A. Potokin, Dokl. Akad. Nauk SSSR **312**, 1080 (1990) [Sov. Phys. Dokl. **35**, 488 (1990)].
32. V. A. Vasil'ev, *Shadow Methods* (Nauka, Moscow, 1972).
33. T. E. Faber, *Fluid Dynamics for Physicists* (University Press, Cambridge, 2001).
34. L. I. Grechikhin, Teplofiz. Vys. Temp. **6**, 507 (1968).
35. G. I. Bakanovich and L. I. Grechikhin, Teplofiz. Vys. Temp. **7**, 338 (1969).
36. L. M. Biberman, V. S. Vorob'ev, and I. T. Yakubov, *Kinetics of Nonequilibrium Low-Temperature Plasmas* (Nauka, Moscow, 1982; Consultants Bureau, New York, 1987).
37. Yu. P. Raizer, *Gas Discharge Physics* (Nauka, Moscow, 1987; Springer-Verlag, Berlin, 1991).
38. V. E. Golant, *Microwave Methods for Investigating Plasmas* (Nauka, Moscow, 1968).
39. D. G. Akhmetov and O. P. Kisarov, Prikl. Matem. Tekh. Fiz. **7** (4), 120 (1966).
40. D. G. Akhmetov, Prikl. Matem. Tekh. Fiz. **42** (5), 70 (2001).

41. J. P. Sullivan, S. E. Windall, and S. Ezekiel, AIAA J. **11**, 1384 (1973).
42. A. G. Strelkov, *Mechanics* (Nauka, Moscow, 1975).
43. L. I. Sedov, *Similarity and Dimensional Methods in Mechanics* (Nauka, Moscow, 1965; Academic, New York, 1959).
44. D. A. Frank-Kamenetskii, *Course of Plasma Physics* (Atomizdat, Moscow, 1968).
45. Ya. B. Zel'dovich and Yu. P. Raizer, *Physics of Shock Waves and High-Temperature Hydrodynamic Phenomena* (Nauka, Moscow, 1966; Academic, New York, 1966, 1967), Vols. 1, 2.
46. A. Ibetson and D. J. Tritton, J. Fluid Mech. **68**, 639 (1975).
47. E. P. Sukhovich, in *Proceedings of the All-Union Conference on Heat and Mass Transfer, Minsk, 1976*, Vol. 1, Part 2, p. 172.
48. *Encyclopedia of Low-Temperature Plasma*, Ed. by V. E. Fortov (Nauka, Moscow, 2000), Vol. 1.
49. A. T. Onufriev, in *Physical Mechanics*, Vol. 4: *Dynamic Processes in Gases and Solids* (Leningr. Gos. Univ., Leningrad, 1980), p. 31.
50. U. Yusupaliev, A. K. Maslov, and S. A. Shuteev, Prikl. Fiz., No. 1, 3 (2000).
51. A. I. Borisenko, O. N. Kostikov, and V. I. Chumachenko, in *Proceedings of the 1st Scientific and Technological Conference on Vortex Phenomena and Their Application in Industry, Kuibyshev, 1974*, p. 268.
52. M. F. Zhukov, Izv. Sib. Otd. Akad. Nauk SSSR, Ser. Tekh. Nauki, No. 8, 3 (1975).

Translated by A.S. Sakharov

Plasma Physics Reports, Vol. 31, No. 6, 2005, pp. 512–518. Translated from Fizika Plazmy, Vol. 31, No. 6, 2005, pp. 560–566.

LOW-TEMPERATURE PLASMA

Macroscopic Separation of Charges in a Pulsed Electric Discharge

G. D. Shabanov and B. Yu. Sokolovskiĭ

Konstantinov Institute of Nuclear Physics, Russian Academy of Sciences, Gatchina, St. Petersburg, 188350 Russia

Received December 11, 2003; in final form, April 22, 2004

Abstract—The possibility of separating charges in an ordinary electric discharge was demonstrated. The luminous object formed after the end of the discharge was found to exist over a few hundred milliseconds, or six orders of magnitude longer than the lifetime of an ideal plasma of the same volume. It is shown that the luminous object has a negative electric charge and has no free charged particles of opposite sign. *© 2005 Pleiades Publishing, Inc.*

1. INTRODUCTION

A new type of electric discharge excited in air over a water surface was discovered at the Konstantinov Institute of Nuclear Physics (Gatchina) [1–3]. In such a discharge, two phases can be distinguished: a discharge that is initially produced around a negative electrode (a jet ejected from the water) and a long-lived autonomous luminous object (LO) into which the discharge transforms thereafter. The LO exists over a few hundred milliseconds without external energy supply. In [2], it was supposed that the LO had an unneutralized electric charge localized in the thin LO shell. Studies of the electric characteristics of such discharges [4–6] confirmed the presence of an unneutralized electric charge in the LO. It was also hypothesized that the LO was a one-component plasma consisting of only negative charged particles [5]. An anomalously strong response of this unneutralized system (both the jet and the LO) to a weak harmonic action (laser radiation with a power as low as 10^{-3} W) allowed the authors of [4] to suggest that the leader of a streak lightning could be controlled by a low-power laser. The problem of controlling lightnings by lasers was investigated in [7–9]. Two basic methods of laser control are usually considered: (i) the generation of a laser spark at the top of a lightning rod (in this case, the spark serves as an extension of the rod) and (ii) the generation of a laser spark at a large altitude, in the region where the thundercloud field is maximum. Moreover, in [9], the interesting hypothesis was put forward that "a cloud of charged aerosol is a self-organizing system."

2. EXPERIMENT

The results obtained in this paper, which continues the studies [1–6], may be of interest in developing new methods for the laser control of lightning. For this purpose, it is necessary to gain a better insight into the structure of LOs and the nature of electric charge carriers in them. We believe that the leader of streak lightning is best modeled by the discharge investigated in our study. When performing probe measurements, it is necessary to have a certain, even if rough, model of the object under study. Among the LO models considered in [2, 3], the most preferable is that proposed in [2]. In that model, the LO was treated as a shell structure formed of a highly nonideal plasma.

The concept of a device for generating LOs is outlined in [1, 2], and its design is described in [3, 4]. The basic component of the device is a 0.6-mF capacitor bank, which is charged to 5.5–6.0 kV. A discharge is excited by switching the capacitor bank to a 6-mm-diameter graphite electrode (cathode), which projects over 2–3 mm from the water surface. The side surface of the electrode is insulated from the water by a quartz tube. The annular positive electrode (anode) is immersed in water at a depth of 15 cm. After the high voltage is applied to the discharge gap, a slipping discharge propagates over the water surface and a water jet is ejected upward from the negative electrode. After 80 ms, the capacitor bank is disconnected (the residual voltage being 3 kV) and the jet separates from the electrode to form a LO. The LO evolution is described in [3]. At 60–100 ms, the LO usually appears as a jellylike body (see Fig. 1); sometimes the LO is shaped as a perfect sphere. If the discharge is interrupted at early times (<80 ms), the second LO appears near the switching rod (Fig. 2). Figure 2 shows a photograph of the first (greater) LO, which forms near the graphite electrode, and the second LO, which is located near the copper rod. The emission intensities and colors of both LOs are almost the same. The LO formed near the graphite electrode exists over a longer time, and the LO colors in the decay stage are somewhat different. This indicates that, in essence, water plays the role of a variable resistance. We positioned detectors near the LO, at a height of 25–45 cm above the electrode. The minimum height of the

1063-780X/05/3106-0512$26.00 © 2005 Pleiades Publishing, Inc.

Fig. 1. Photograph of an LO. The inset at the top left of the figure shows a slipping discharge that preceded the appearance of a jet and its subsequent transformation into the LO.

detector was chosen with account of the time during which the LO propagates to the detector: about 100 ms after the end of the discharge. The LO rises at a velocity of about 1 m/s, approaches the detector at 100 ms, and leaves it at about 200 ms. When investigating the LO, we used a Langmuir probe, a double probe, a dipole antenna, and their various combinations.

The signals of the current of negative charge carriers to an unbiased Langmuir probe and to a probe biased by +300 V are shown in Figs. 3a and 3b, respectively. In the probe signals, peaks of the probe current are clearly seen when the leading and trailing edges of the LO cross the probe (Fig. 3a). In Fig. 3b, the signal from the trailing edge is less pronounced, but there is a sharp spike of opposite (positive) polarity. Starting from a bias of +600 V, this peak somewhat broadens, but the shape of the signal generally remains the same. The probe theory does not suggest the appearance of the current of positive ions to the probe as the positive bias increases. Estimates show that, at a bias of +300 V, the electric field at the probe amounts to 14 kV/cm. The observed behavior of the probe current may be attributed to electron emission; this is also evidenced by the probe glow that is seen with the naked eye [10]. The results obtained in [11] and probe measurements with a

Fig. 2. Generation of two LOs in the same discharge. The second LO (on the right) is located near the copper rod.

negative bias down to –600 V allow us to conclude that there are no positive ions in the LO.

Figure 4 shows a signal from a high-resistance double probe electrically insulated from the measurement facility. The shape of this signal shows the presence of an electric field inside the LO; this means that the LO interior is spatially charged. Figure 4 does not demonstrate the presence of a shell; however, as the input resistance of the probe is decreased, the probe signal shows sharp jumps in the electric field [11], which indicate the presence of a shell.[1] In an ordinary plasma, a double probe introduces minimal perturbations. In our case, however, the double probe with a low input resistance destroyed the LO when it contacted the shell. The data presented in Fig. 4 were not processed with a computer. Since probe measurements are hard to interpret, we also used a dipole antenna, which interacts only slightly with the LO.

The dipole antenna and its measurement circuit were specially designed by S.I. Stepanov, E.A. Drobchenko, G.D. Shabanov, and A.I. Egorov for studying LOs. Structurally, the dipole antenna is a double probe with an electrode distance of 3 mm; however, in contrast to an ordinary double probe, the electrodes of the dipole antenna are insulated from one another. We used two versions of the dipole antenna: with and without a reference electrode. In some measurements, the refer-

[1] These measurements confirmed the presence of a nonluminous layer between the shell and the interior of the LO. The nonluminous layer is free of charged particles. A similar layer with a thickness of 0.1–0.2 mm was also detected in Avramenko's jet. Such a layer arises due to Coulomb repulsion between like charges that are present in the shell and the interior of the object [2]. In the LO, this layer is 2–3 mm thick in its upper part and ~20 mm thick in its lower part. For the lower part of the LO, this can be seen from the probe signal shown in Fig. 3a. In the upper part of the LO, the probe did not show the presence of this layer because the probe size was too large. We could not use a smaller probe because the probe conductors were melted when interacting with the LO, no matter whether the conductor was grounded or not.

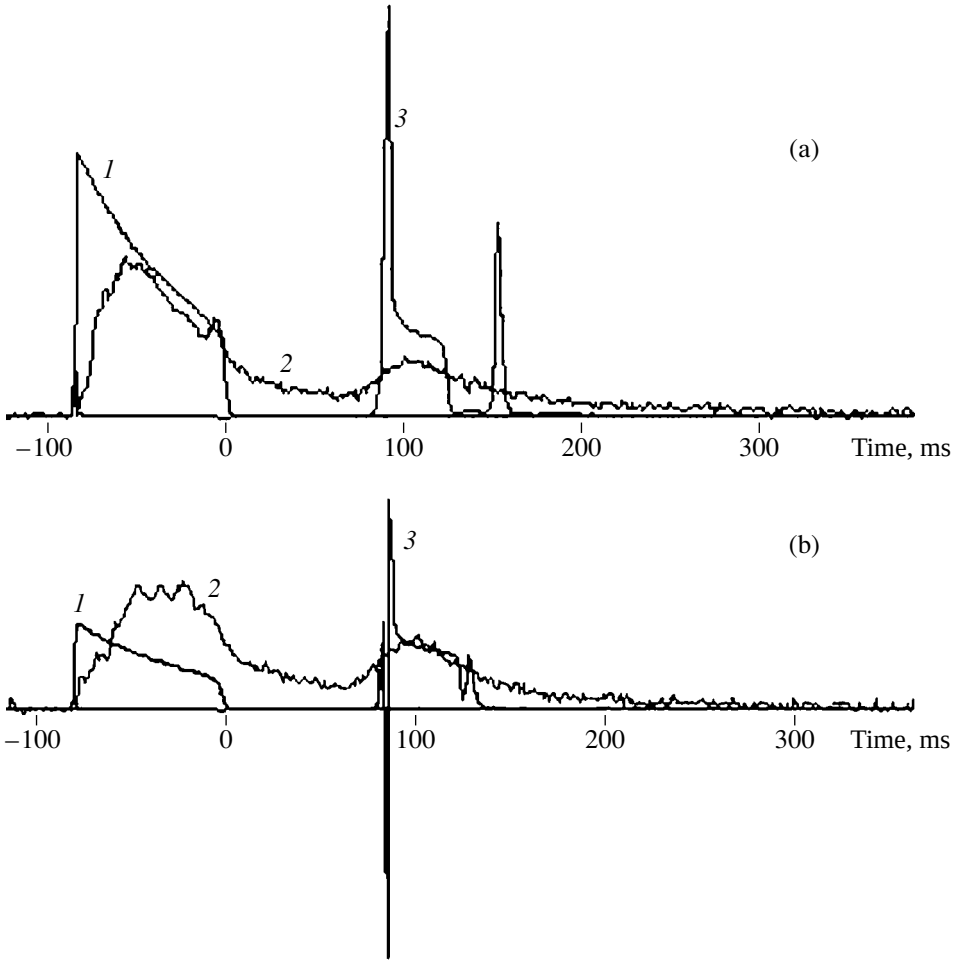

Fig. 3. Experiment with (a) a 0.45-mm-diameter unbiased Langmuir probe and (b) a probe biased by +300 V: the time evolution of (*1*) the voltage across the discharge gap (the maximum voltage is 5.5 kV), (*2*) the LO intensity (arb. units), and (*3*) the current of negatively charged particles to the probe. The peaks of the probe current correspond to the leading (5 μA) and trailing edges of the LO.

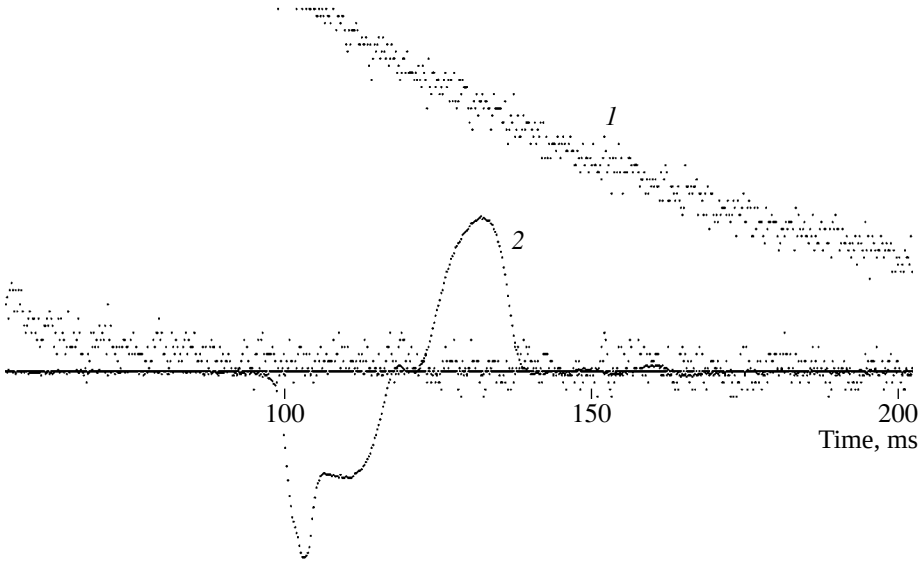

Fig. 4. Experiment with a double probe: (*1*) the time evolution of the LO intensity (arb. units) and (*2*) the double-probe signal.

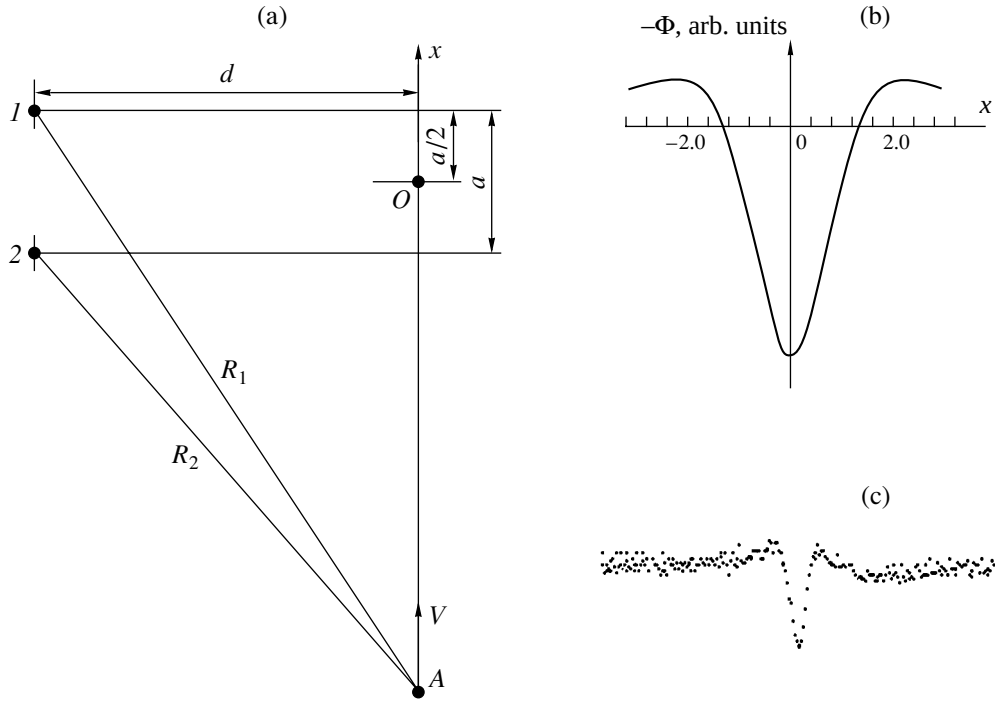

Fig. 5. (a) Scheme of calibrating the dipole antenna: the tips of the dipole antenna are at points *1* and *2*, *A* is a point source, and *d* is the minimal distance between the source and the dipole antenna; (b) dipole-antenna signal calculated by formula (2); and (c) dipole-antenna signal measured during the passage of a 2-cm-diameter source, to which a potential of 5.5 kV was applied.

ence electrode was used as a Langmuir probe. The dipole antenna was calibrated in a uniform capacitor field (in various media) and under conditions similar to our experimental conditions. Figure 5a shows the scheme of calibrating the dipole antenna by point source *A* (the tips of the dipole antenna are at points *1* and *2*). The 2-cm-diameter source, to which a voltage of 5.5 kV was applied, was carried near the dipole antenna along the *x* axis, the minimal distance *d* between the source and the dipole antenna being 1 cm.

Let us derive the expressions for the potential difference between the tips of the dipole antenna $\varphi_1 - \varphi_2$ and for the observed signal $\Phi(x) = \dfrac{d(\varphi_1 - \varphi_2)}{dt}$. The distances from the source to the antenna tips are

$$R_1^2 = d^2 + \left(x + \frac{a}{2}\right)^2, \quad R_2^2 = d^2 + \left(x - \frac{a}{2}\right)^2.$$

From this, we obtain

$$\varphi_1 - \varphi_2 = Q\left(\frac{1}{R_1} - \frac{1}{R_2}\right)$$

$$= Q\left(\frac{1}{\left(d^2 + x^2 + ax + \dfrac{a^2}{4}\right)^{\frac{1}{2}}} - \frac{1}{\left(d^2 + x^2 - ax + \dfrac{a^2}{4}\right)^{\frac{1}{2}}}\right).$$

For $a \ll d$, we can ignore the term $\dfrac{a^2}{4}$ in the radicand and to factor $\dfrac{Q}{(d^2 + x^2)^{\frac{1}{2}}}$ out. We then find

$$\varphi_1 - \varphi_2 = -aQ\frac{x}{(d^2 + x^2)^{\frac{3}{2}}} \tag{1}$$

and

$$\Phi(x) = \frac{d(\varphi_1 - \varphi_2)}{dt} = \frac{d(\varphi_1 - \varphi_2)}{dx}\frac{dx}{dt}$$

$$= -aVQ\left[\frac{1}{(x^2 + d^2)^{\frac{3}{2}}} - \frac{3x^2}{(x^2 + d^2)^{\frac{5}{2}}}\right]$$

or

$$\Phi(x) = A\frac{d^2 - 2x^2}{(x^2 + d^2)^{\frac{5}{2}}}, \tag{2}$$

where $A = -aVQ$ and $V = \dfrac{dx}{dt}$ is the velocity of the source.

The curve in Fig. 5b corresponds to expression (2) at $d = 2$ cm. Figure 5c shows an experimental curve obtained for the above parameters of the antenna and

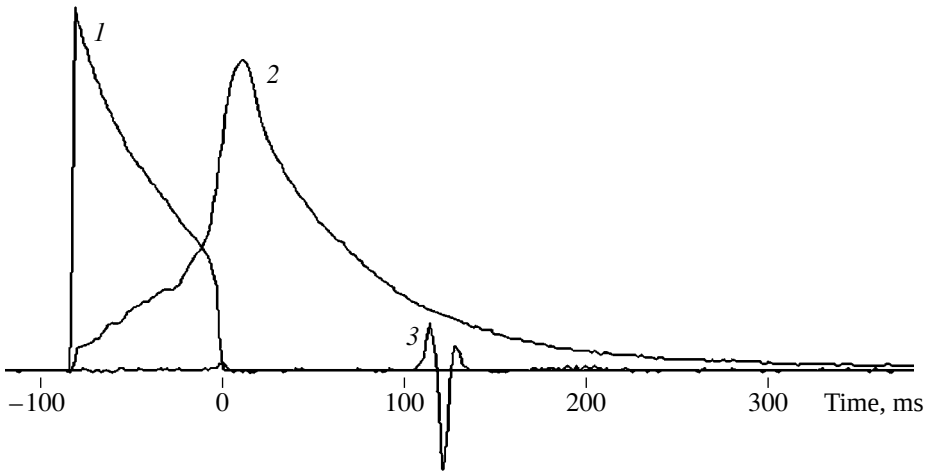

Fig. 6. Experiment on the propagation of a LO near the dipole antenna: the time evolution of (*1*) the voltage across the discharge gap, (*2*) the LO intensity (arb. units), and (*3*) the dipole-antenna signal.

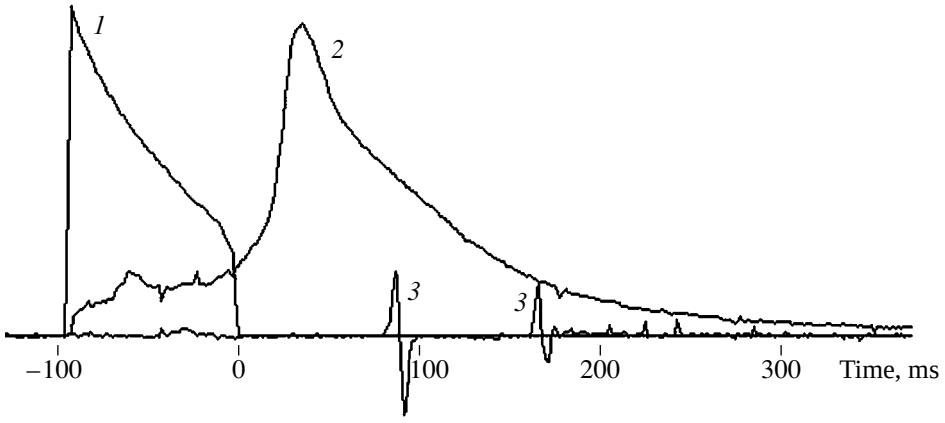

Fig. 7. Passage of the dipole antenna through the center of the LO: the time evolution of (*1*) the voltage across the discharge gap, (*2*) the LO intensity (arb. units), and (*3*) the dipole-antenna signal.

the source and for a source velocity of higher than 2 m/s. The curve corresponding to expression (1) is obtained by integrating the curve in Fig. 5b. An analysis of expression (2) shows that the dipole-antenna signal depends crucially on the parameter d; this agrees with the experimental results.

Figure 6 shows the antenna signal for an experiment in which a compact LO about 8 cm in diameter passed by the dipole antenna with a velocity of higher than 2 m/s, the minimal distance between the LO surface and the antenna being 2 cm. When the antenna fell into the LO interior, the signal corresponded to the passage of the detector through a charged plane (Fig. 7). In Fig. 7, this corresponds to curve *3* with two oscillations, which appear when the detector passed through the front and rear walls of the LO shell.

3. DISCUSSION

In the electric discharge under study [1–3], the macroscopic separation of charges results in the generation of a negatively charged LO. From the measurement results, it is rather difficult to determine the absolute values of the electric charge, field, and temperature of the LO, even though we calibrated the detectors and modeled different regimes of interaction between the LO and detectors. Thus, according to calibration in air, the shell field in some experiments was found to be 7 kV/cm, whereas the calibration in a conducting medium (e.g., in a liquid) gave a field lower by a factor of 2 to 3. It follows from probe measurements that the LO has a thin shell in which the electric parameters change by a jump and that the shell consists of negatively charged particles with a high density or high

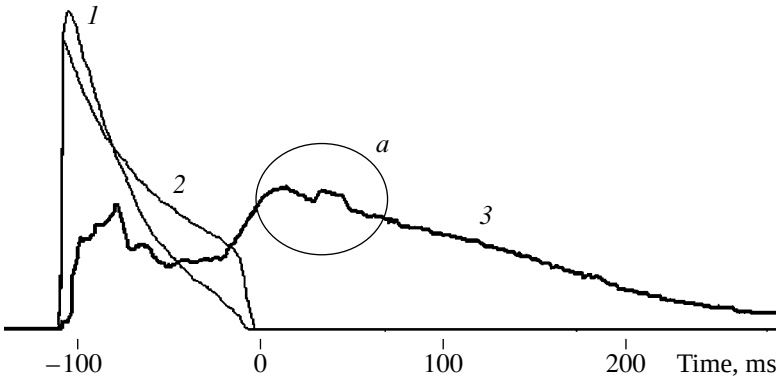

Fig. 8. Experiment on the interaction of a propagating LO with a 0.08-mm wire: the time evolution of (*1*) the discharge current (the maximum current is 52 A); (*2*) the voltage across the discharge gap, and (*3*) the LO intensity (arb. units). The plateau with an enhanced intensity in region *a* corresponds to the interaction between the wire and the LO. In the course of interaction, the end of the wire was melted to form a sphere 0.2 mm in diameter.

mobility. Signals from the dipole antenna show that an unneutralized electric charge is mainly localized in the shell (Fig. 7). From the experimental results presented in Fig. 6, it follows (with allowance for the modeling and calibration measurements) that the LO electric charge is greater than -10^{-7} C. In [11], the authors refined the model of the LO shell proposed in [2], where it was assumed that the unneutralized electric charge was concentrated in the shell and the charge carriers had short-range order. This is possible if the potential energy of Coulomb interaction between particles exceeds their thermal kinetic energy. Shell and stratified charged particle systems with both short- and long-range orders were studied experimentally in [12, 13]. In this context, data on the interaction of lightning with copper rods [14] may be interpreted as the appearance of concentric circular layers spaced by 4 μm in the fine structure of lightning. Using results of measurements with Langmuir probes biased from –600 to +600 V, we may suppose that there are several closely spaced layers of likely charged particles in the LO shell [11].

Strong Coulomb interaction between particles in nonideal systems causes gas–liquid–solid phase transitions. This can be enough for the system to be displaced as a whole in response to a weak external action [15]. Taking this into account, the authors of [4, 5] proposed that streak lightning be controlled with the help of a low-power laser. In [9], a system of charged particles was considered as being self-regulating. According to our estimates, the coupling parameter Γ of the system considered in [9] with parameters reported in [16] is larger than unity; i.e., the system is nonideal. It follows from this that the potential energy of the system is larger than its kinetic energy; therefore, the cloud could be self-regulating.[2]

[2] Many examples of the self-regulation of LOs were given in [2, 11], in particular, the recovery of the LO shell after its damage (see Fig. 8).

As was noted in [9], a laser spark extending a grounded electrode is unable to initiate lightning when the thundercloud electric field is too low; this is a serious disadvantage of this method of lightning protection. This method is efficient only when the electric field is strong enough to initiate an upward leader even in the absence of a laser spark [9]. The same disadvantage is peculiar to the method proposed in [4, 5], where it was suggested that the leader be subject to an exter-

Fig. 9. Interaction between the jet and the laser beam. The laser beam propagates from right to left perpendicular to the discharge axis at a height of 22 cm above the electrode. The formation of the LO begins after the jet has traversed a distance of 8.5 cm across the laser beam.

nal action in the final (rather than initial) stage of its formation.

Therefore, the most promising method of lightning protection is to initiate lightning at a high altitude, where the field is sufficiently strong [7, 8]. This allows thunderclouds to be discharged in sparsely populated regions [7], far from the protected objects. To guide the leader formed to a desired point, the method proposed in [4, 5] can be used. The results of investigations of the action of a low-intensity laser with a power lower than 10^{-3} W (see Fig. 9) on a nonideal Coulomb system of charged particles (as well as other relevant effects [2, 11, 15]) allow us to hope that a detailed study of the processes that occur in such systems will help to solve the problem of lightning protection.

4. CONCLUSIONS

It has been shown that a pulsed electric discharge produced in air over the water surface can initiate a LO, which is a one-component plasma with no neutralizing positive background. The LO can exist over a few hundred milliseconds without external energy supply. The LO has a rather complicated structure: it consists of a shell formed by negative charged particles with a high density or high mobility and the internal space filled with negative atomic and molecular ions. Between the shell and the internal space, there is a nonradiative layer free of charged particles. This layer forms due to the Coulomb repulsion between the shell and the internal region.

The self-organization of natural Coulomb systems (such as thunderclouds and lightning) and artificial ones (such as charged aerosols and LOs) can be attributed to the fact that these systems are far from ideal [9]. Studies in this field could lead to the development of new methods for protecting vulnerable objects from lightning strikes.

Among the possible methods for the laser control of lightning, the most promising is to initiate lightning by a laser spark in the region where the thundercloud field is maximum [7, 8] and then to guide the lightning by a low-intensity laser to the required point [4, 5].

ACKNOWLEDGMENTS

We are grateful to A.I. Egorov and S.I. Stepanov for their assistance in experiments; O.M. Zherebtsov, G.M. Amal'skiĭ, S.E. Emelin, and V.L. Bychkov for fruitful discussions; S. Tyagin for photographing; and A.I. Grigor'ev for his valuable remarks. We would like to thank the anonymous referee for amending the manuscript.

REFERENCES

1. G. D. Shabanov, in *Proceedings of the 3rd Intrnational Conference on Natural and Antropogenic Aerosols, St. Petersburg, 2001*, p. 368.
2. G. D. Shabanov and O. M. Zherebtsov, in *Proceedings of the 10th Russian Conference on Cold Nuclear Transmutation and Ball Lightning, Sochi, 2002* (NITs FTP Érzion, Moscow, 2003), p. 285.
3. A. I. Egorov and S. I. Stepanov, Zh. Tekh. Fiz. **72** (12), 102 (2002) [Tech. Phys. **47**, 1584 (2002)].
4. G. D. Shabanov and O. M. Zherebtsov, Opt. Zh. **71** (1), 6 (2004).
5. G. D. Shabanov and O. M. Zherebtsov, in *Proceedings of the 5th Russian Conference on Atmospheric Electricity, Vladimir, 2003*, p. 279.
6. S. I. Stepanov, A. I. Egorov, and G. D. Shabanov, in *Proceedings of the 5th Russian Conference on Atmospheric Electricity, Vladimir, 2003*, p. 117.
7. É. M. Bazelyan and Yu. P. Raizer, Usp. Fiz. Nauk **170**, 753 (2000) [Phys. Usp. **43**, 701 (2000)].
8. E. M. Bazelyan and Yu. P. Raizer, *Lightning Physics and Lightning Protection* (Nauka, Moscow, 2001; IOP, Bristol, 2000).
9. L. M. Vasilyak, I. P. Vereshchagin, V. V. Glazkov, *et al.*, Teplofiz. Vys. Temp. **41**, 200 (2003).
10. O. V. Kozlov, *Electric Probe in Plasma* (Atomizdat, Moscow, 1969).
11. G. D. Shabanov and O. M. Zherebtsov, *11th Russian Conference on Cold Nuclear Transmutation and Ball Lightning, Sochi, 2003* (NITs FTP Érzion, Moscow, 2003), Abstracts of Papers, p. 16.
12. L. Hornekar, N. Kjargaard, A. M. Thommesen, and M. Drewsen, J. Phys. Rev. L **86**, 1994 (2001).
13. A. P. Nefedov, O. F. Petrov, V. I. Molotkov, *et al.*, Pis'ma Zh. Éksp. Teor. Fiz. **72**, 313 (2000) [JETP Lett. **72**, 218 (2000)].
14. R. D. J. Hill, J. Geophys. Res. **68**, 1365 (1963).
15. L. M. Vasilyak, M. N. Vasil'ev, S. P. Vetchinin, *et al.*, Izv. Akad. Nauk, Fiz. **67**, 1333 (2003).
16. A. G. Temnikov, A. V. Orlo, and M. A. Koshelev, in *Proceedings of the 5th Russian Conference on Atmospheric Electricity, Vladimir, 2003*, p. 98.

Translated by N.F. Larionova

Plasma Physics Reports, Vol. 31, No. 6, 2005, pp. 519–523. Translated from Fizika Plazmy, Vol. 31, No. 6, 2005, pp. 567–571.

LOW-TEMPERATURE PLASMA

Numerical Simulations of the Development of an Open Discharge

A. V. Karelin* and A. R. Sorokin**

**Institute of Terrestrial Magnetism, Ionosphere, and Radio Wave Propagation, Russian Academy of Sciences, Troitsk, Moscow oblast, 142092 Russia*

***Institute of Semiconductor Physics, Siberian Division, Russian Academy of Sciences, pr. Akademika Lavrent'eva 13, Novosibirsk, 630090 Russia*

Received April 5, 2004; in final form, July 22, 2004

Abstract—Results are presented from numerical simulations of the time evolution of open discharges in helium that are excited in the presence of an anode grid and generate electron beams over a wide range of helium pressures (up to ~10^4 Pa). It is shown that electron emission from the cathode is almost entirely dominated by the bombardment of the cathode by heavy particles, while the contribution of photoemission is negligibly small. For conditions typical of open discharges (for a helium pressure of 4 kPa and voltage amplitude of 7.4 keV), the following percentages are obtained for the partial contributions of the main processes whereby the discharge develops: 96% for atom–electron emission, 2.3% for electron multiplication in the discharge gap, 1.7% for ion–electron emission, 2×10^{-3}% for electron emission under the action of metastable atoms diffusing from the discharge gap toward the cathode, and 2×10^{-4}% for photoemission from the cathode. © *2005 Pleiades Publishing, Inc.*

1. An open discharge (OD) initiated in the presence of a grid anode is an efficient source of electron beams (EBs), which, in particular, are successfully used to excite laser media [1]. In order to provide a proper choice of the OD operating mode, it is necessary to know the mechanism by which the discharge generates an EB. Because of the anomalously high efficiency of the formation of an EB in an OD, it was suggested that the OD is a new type of discharge, namely, photoelectron discharge [2] maintained by photoemission from the cathode. This is why close attention is being given to the mechanism for the development of an OD. The concept of the photoelectron nature of an OD has been criticized in a number of papers. The results presented in them were summarized and supplemented in [3], where it was shown that the basic ideas proposed by the adherents of this concept, in particular, by the authors of a review paper [2], are unjustified.

Thus, the results of numerical simulations presented in [4] show that the electron emission intensity required to explain the main properties of an OD is ensured by the bombardment of the electron-emitting cathode by fast atoms and ions; this agrees with the long-existing established views about the glow discharge. The numerical simulations reported in [4] were carried out based on the known data from measurements of the electric fields in ODs and of the coefficients of electron emission from a cathode bombarded by helium atoms and ions. In [5], simple noncontradictory estimates of the energy required for a photoelectron to escape the cathode surface in an OD were obtained. According to those estimates, the discharge cannot be maintained by photoemission and the contribution of photoelectrons to the energy efficiency of the formation of EBs should be negligibly small.

In order to gain a deeper insight into the main processes occurring in an OD and, in particular, into the controversial question about the discharge mechanism, a more careful theoretical analysis was needed. Such an analysis was performed by one of us in [6], but only for a particular and not quite typical case. In that paper, the development of an OD was simulated numerically for conditions corresponding to the experimental conditions in [7], specifically, for a helium pressure of p_{He} = 200 Pa, a discharge gap of length d = 0.65 mm, and a drift region (the region between the anode and the collector) of length L = 19.5 mm, the maximum potential difference between the electrodes being U_0 = 3.5 kV. The results obtained were found to agree well with the experimental data. The simulations yielded the following percentages for the contributions of different particular processes to the discharge dynamics: 80.6% for atom–electron emission, 16.1% for ion–electron emission, and 3.2% for electron emission under the action of metastable helium atoms diffusing from the discharge gap toward the cathode (the corresponding electron emission coefficients being $\gamma(2^3S) = 0.24$ and $\gamma(2^1S) = 0.4$). The maximum percentage for photoemission from the cathode under the action of short-wavelength (primarily resonant) radiation from the cathode–anode and anode–collector gaps (the accepted photoelectron emission coefficient being 3×10^{-2}) was found to be rather low (about 0.1%).

1063-780X/05/3106-0519$26.00

The objective of the present paper is to extend numerical simulations to the entire range of working pressures in an OD (up to ~10^4 Pa) and to reveal possible important changes in the dynamics of the development of the discharge in this pressure range.

2. For simulations, we utilized the PLASER computer software package [8–10] and used a time-dependent kinetic model of a helium plasma that was modified to describe the formation of the discharge current.

We numerically solved a two-zone problem: zone 1 was the discharge gap between the cathode and the anode grid, and zone 2 was the space between the anode grid and the collector. We used a kinetic model of a source of spontaneous emission from a He–H_2 mixture. Zone *1* was considered to contain the following plasma components: metastable atoms He*(^1S) and He*(^3S), slow atomic ions He_z^+, fast atomic ions He_f^+, slow and fast helium atoms He and He_f, slow electrons *e*, and fast beam electrons e_f. The natural background ionization frequency was assumed to be constant and was set equal to $\nu_i = 4 \times 10^{-19}$ s^{-1}. The initial densities of atomic helium ions and fast electrons could be varied over broad ranges. The initial natural density of atomic helium ions was set to be $[He_z^+]_0 = 5 \times 10^{-5}$ cm^{-3} (hereafter, the square brackets denote the particle densities). When a voltage was applied across the discharge gap, slow atomic ions were accelerated toward the cathode and fell into the group of fast ions,

$$He_z^+ \longrightarrow He_f^+, \quad k_1(t) = \frac{v(t)}{2l} = \frac{\sigma_g[He]v(t)}{2}. \quad (1)$$

Here, k_1 is the characteristic inverse time of acceleration (the ratio of one-half of the maximum speed of the accelerated ions to the ion mean free path, which in turn depends on the density of neutral atoms and the gas-kinetic cross section $\sigma_g = 1.45 \times 10^{-15}$ cm^2). The maximum velocity $v(t)$ was set equal to the ion speed corresponding to an energy acquired by an ion under the action of the applied voltage $U(t)$ divided by the number of gas-kinetic collisions in the discharge gap: $v(t) = \sqrt{\frac{2eU(t)}{Md\sigma_g \cdot [He]}}$, where *e* is the charge of an electron and *M* is the mass of a helium atom.

As an ion accelerates, it collides with neutral helium atoms to produce *n* fast atoms (the number *n* depends on the length of the discharge gap) with energies equal to 1/2*n* of the energy corresponding to the applied voltage (under conditions typical of ODs, the characteristic length of charge exchange of an ion is much less than the interelectrode distance):

$$n \cdot He + He_f^+ \longrightarrow n \cdot He_f + He_f^+, \quad k_2 = \sigma_g v(t). \quad (2)$$

For estimates, it is assumed here that the mean velocity of the electrons accelerated within a time interval between collisions is twice that in the expression for $k_1(t)$.

Fast ions and atoms then strike the cathode surface (in this case, the ions recombine on the surface and thereby leave the group of fast ions) and knock electrons out of the cathode. These electrons fall rapidly into the group of fast electrons (or equivalently become the beam electrons):

$$He_f^+ \longrightarrow e_f, \quad k_3(t) = \frac{v(t)\gamma_{He_f^+}}{\Lambda}, \quad (3)$$

$$He_f \longrightarrow e_f, \quad k_4(t) = \frac{v(t)\gamma_{He_f}}{\Lambda}, \quad (4)$$

where $1/\Lambda = \pi/d$ (here, the diffusion approximation is used for estimates because, in collisions, the ions and atoms are deflected from their paths). The coefficients γ are determined by the material of the cathode and the quality of its surface. In simulations, we used the following dependences of the coefficients γ on the energy ε (in eV):

$$\gamma_{He_f^+} = 1.7 \times 10^{-2}\varepsilon^{0.47}, \quad (5)$$

$$\gamma_{He_f} = \exp\left(-\frac{210}{\varepsilon}\right). \quad (6)$$

At this point, we should note the following: In [11], it was pointed out that, in numerical simulations, it is necessary to use the emission coefficients measured under technical-grade vacuum conditions (>10^{-7} torr). If use is made of γ values measured in an ultrahigh vacuum (<10^{-9} torr), then, in the range of voltages required for ODs, it is necessary to ignore the kinetic emission from both fast neutrals and ions and to consider only the potential emission from ionized atoms (for helium, the potential emission coefficient is equal to ≈0.2). In [12], it was shown that, under conditions in which the potential ion–electron emission serves as the only mechanism for secondary electron emission from the cathode, a discharge cannot be initiated when the applied voltage exceeds a certain critical value U_0 because of the generation of runaway electrons and the resulting decrease in the ionizing ability of the electrons. For instance, in helium, the critical voltage U_0 at *pd* = 200 Pa cm is about 1.5 kV [12]. Essentially the same result also follows from the curves for discharge initiation that were calculated in [13, 14]. In those curves, in contrast to the conventional left branch of the Paschen curve, the calculated branch again bends to the right to form a loop. It is only when the bombardment of the cathode by fast neutral atoms (which make a decisive contribution to the electron emission from the cathode) was additionally taken into account in [13] that the left branch of the calculated Paschen curve was coincident with the one measured. In our simulations, as in [6, 13], we used the γ values that were measured under technical-grade vacuum conditions in [15].

Fast electrons flying through the discharge gap ionize and excite the gas and leave the discharge plasma:

$$e_f + \mathrm{He} \longrightarrow \mathrm{He}_z^+ + e + e_f, \quad k_7 = \sigma_i v_e, \tag{7}$$

$$e_f + \mathrm{He} \longrightarrow \mathrm{He}^* + e_f, \quad k_8 = \sigma_{ex} v_e, \tag{8}$$

$$e_f \longrightarrow \text{escape of a fast electron from the plasma,}$$

$$k_9 = \kappa v_e/d. \tag{9}$$

Here, $\kappa \le 1$ is the adjusting parameter, which characterizes the cutoff of the electron current due to the accumulation of the electric charge behind the anode grid (this parameter was varied in our simulations). The main mechanism governing the κ value seems to be that associated with the ionization of helium atoms in zone 1 by the relatively slow electrons from the Debye sheath around the anode grid, separating zones 1 and 2.

The beam current density was estimated from the formula

$$j(t) = 1.6 \times 10^{-19} [e_f(t)] v_e(t), \tag{10}$$

where $[e_f(t)]$ is the density of the fast electrons and $v_e(t)$ is their velocity after they have passed through the discharge gap.

Zone 2 was considered to contain the following atoms, molecules, and ions: He*, He_2^*, He^+, He_2^+, He_3^+, H^+, $\mathrm{H}_2^+(v)$, H_3^+, $\mathrm{H}_2(v)$, H, HeH^+, $\mathrm{He}_2\mathrm{H}^+$, and HeH_2^+. The kinetics of the excited levels of a hydrogen atom was modeled with allowance for the ground state and three excited levels with n = 2–4. The kinetics of the excited levels of a molecular hydrogen ion was modeled with allowance for six excited levels with v = 0–5. The kinetics of the processes occurring in zone 2 under the action of an electron beam was simulated in the traditional manner. The energy distribution function of the plasma electrons was assumed to be Maxwellian. The photoelectron emission (with a coefficient of 3×10^{-2}) under the action of photons emitted in the deexcitation of $\mathrm{He}(^1P_1)$ atoms and the decay of He_2^* molecules within the entire volume of zone 2 was taken into account through the reaction

$$\hbar\omega \longrightarrow e_f, \quad k_{11} = 9 \times 10^8 L/d^2. \tag{11}$$

The rate of production of the secondary electrons in the discharge gap was calculated from the formula $F = [\hbar\omega] \times 3 \times 10^{-2} Lc/d^2$, where $[\hbar\omega]$ is the number density of short-wavelength photons, L is the length of zone 2, and c is the speed of light in vacuum. Note that the product $[\hbar\omega]c$ is the photon flux density and the quantity $[\hbar\omega]Lc/d$ has the meaning of the flux density of the photons collected from the entire zone 2 and operating in the discharge region. Here, we ignored the fact that a fraction of 5/6 of the total number of photons could fly away from the discharge volume toward the side walls. This was done to obtain an upper estimate for the effect of photoelectron emission. The resonant helium lines were described with allowance for reabsorption and deexcitation to metastable states; in particular, we took into account the excitation of the state $\mathrm{He}(^1P_1)$ in zone 2 under the action of a fast electron beam, the deexcitation of this state to the ground and metastable states, and the mixing of the excited states by electrons [6].

The escape coefficient θ was estimated for the Doppler contour of the 58.4-nm resonant emission line [16]:

$$\theta = \frac{1}{2\kappa_1 R_1 \sqrt{\pi \ln(\kappa_1 R_1)}} = 1.21 \times 10^{-5}, \tag{12}$$

where

$$\kappa_1 = 3\frac{\lambda^2}{4}\frac{A}{\gamma_1}[\mathrm{He}], \tag{13}$$

$$\gamma_1 = \frac{2\sqrt{\pi \ln 2}\,\omega v_m}{c}, \tag{14}$$

$A_1 = 1.355 \times 10^9\ \mathrm{s}^{-1}$ is the probability of the radiative deexcitation of the upper state, $\omega = 3.2 \times 10^{16}\ \mathrm{s}^{-1}$ is the central frequency of the resonant line, $v_m = 1.4 \times 10^5$ cm/s is the thermal velocity of helium atoms, and R_1 is the radius of zone 2.

The equations for zone 1, along with the equations for zone 2, which describe the generation of short-wavelength photons and the resonant atomic emission, constitute a closed set of equations. We numerically solved a set of 32 time-dependent ordinary differential equations involving 125 reactions. A more detailed information on the computational technique and on the elementary processes included in simulations can be found in [6].

In simulations, we established that, over the ranges of helium pressures (up to ~10^4 Pa) and discharge voltages (several kilovolts and higher) under study, the main role in the development of an OD is played by the emission resulting from the bombardment of the cathode by helium atoms and ions, whereas the role of photoemission turns out to be insignificant. At pressures higher than 100 Pa, the governing role is played by atom–electron emission. At lower pressures p (for the same value of d), due to a decrease in the charge-exchange rate, the dominant role may be played by ion–electron emission (the number of fast atoms is small). As the voltage decreases, the contribution of photoemission becomes increasingly larger; however, experiments show that, even under the conditions that are most favorable for photoemission in normal glow discharges, its contribution does not exceed 15% [17]. Note that the main properties of ODs in another gases (e.g., in air) are qualitatively the same as those of ODs in helium [18].

The properties of a typical OD (d = 0.5 mm, p_{He} = 4 kPa, and U_0 = 7.4 kV) are illustrated in Fig. 1 by the measured [19] and calculated waveforms of the voltage and currents. Let the geometrical transparency of the anode grid be characterized by the coefficient μ = 0.75,

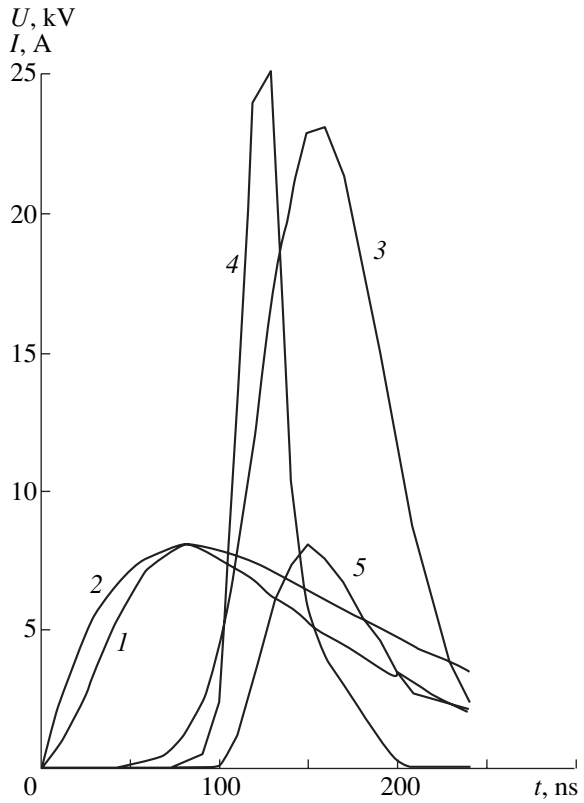

Fig. 1. Waveforms of the (*1*) measured [19] and (*2*) calculated voltages and of (*3*) the calculated total current, (*4*) the measured collector current, and (*5*) the measured anode current [19] for p_{He} = 4 kPa and d = 0.5 mm. The surface area of the cathode is 0.8 cm^2.

and let the length of the drift region be equal to L = 25 mm (since the values of these parameter were not presented in [19], we chose their typical values used in our simulations). The time dependence of the discharge voltage was approximated by the function

$$U(t) = \frac{U_0 at}{1.68 \times 10^{-5}(1 + \exp(at + 10))}, \qquad (15)$$

where $a = 1.2 \times 10^7$ s^{-1}.

It can be seen from Fig. 1 that the calculated amplitude of the total current, I_c, agrees satisfactorily with the amplitude of the measured current I ($I = I_{eB} + I_a$, where I_{eB} is the collector current and I_a is the anode current). The time at which the current I_c begins to increase depends substantially on the prepulse charge density in the discharge gap. A slower decrease in the voltage U given by formula (15) (in comparison to the measured voltage) manifests itself in that, at the trailing edge of the waveform of U, the calculated current I_c exceeds the measured current I (e.g., for an anomalous discharge, we have $I \sim U^3$ [3]). The most pronounced is the difference in the growth rates of the currents I_c and I; this, however, can be explained logically.

In simulations, the effect of the holes in the anode grid on the field distribution over the discharge gap was ignored. In the simple case of a discharge in which the electric field is only slightly distorted by the space charge, the holes in the anode grid make the field lines nonparallel, because the field penetrates partially through the holes. The ions that are most efficiently produced in such a depressed field move along the field lines and thereby are focused at the cathode along the axial lines of the grid holes. This effect is utilized in hollow-anode electron guns to produce narrow EBs [20] with a diameter one order of magnitude less than the diameter of the anode hole.

The same is observed in the initial phase of a pulsed OD even when the value of the parameter pd is large. In the case in question, the discharge current during the period of the efficient generation of an EB is carried mainly by the beam electrons; consequently, in the initial discharge stage, when the field is only slightly distorted by the space charge, the EB passes through the anode holes without coming into contact with the anode grid, so the anode current is essentially zero (as is the case in Fig. 1). As the cathode fall increases, a preanode plasma region arises and extends in which the field is depressed and ionization is enhanced. As a result, the EB begins to form over the entire cathode surface and is partially absorbed by the anode grid, giving rise to an appreciable anode current. Since, in a typical OD, the electric field is sufficiently strong over the entire discharge gap (including the preanode plasma region [3]), its partial penetration through the anode hole can also influence the high-current stage of the discharge. As a result, the discharge current density at the anode grid turns out to be lower than that in the holes; this effect always manifests itself in the cathode eroding the greatest near the axial lines of the anode holes.

Hence, the electric field partially penetrates through the holes of the anode grid and thereby becomes depressed within them, giving rise to a region behind the anode where ionization is enhanced and the ion flux from which hastens the development of the discharge. When the field penetration through the grid holes of the anode was ignored, the simulations yielded a lower growth rate of the discharge current.

With the above in mind, we can conclude that, on the whole, the calculated currents agree well with the ones measured and the discrepancies between them can be explained quite logically and do not qualitatively affect the balance of the processes occurring in an OD.

The contributions from different processes to the development of a discharge was estimated from the following formula for the time- and volume-integrated fluxes of reactions, which were calculated by the formula

$$F_{ij} = \int_0^t k_i N_j dt, \quad \text{cm}^{-3}, \qquad (16)$$

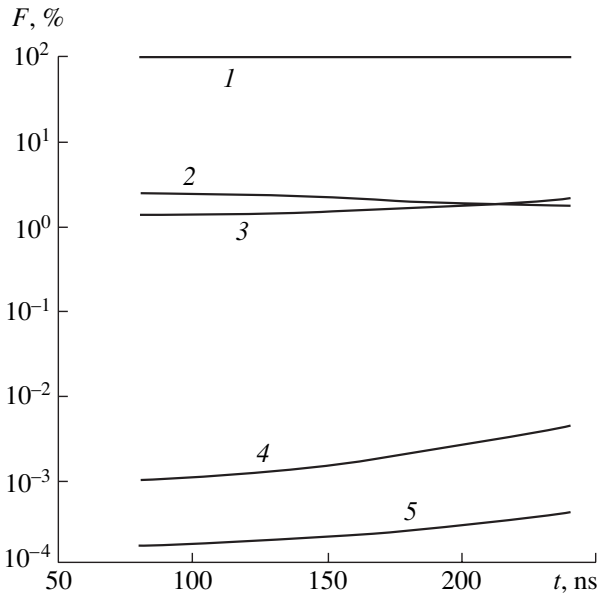

Fig. 2. Time evolution of the partial contributions of the main processes whereby the discharge develops under the experimental conditions in [19]: (*1*) atom–electron emission, (*2*) electron production in the discharge gap, (*3*) ion–electron emission, (*4*) electron emission under the action of metastable atoms diffusing from the discharge gap toward the cathode, and (*5*) photoemission from the cathode. The functions F for different processes were calculated using expression (16) for the functions F_{ij}.

where k_i is the probability (in s^{-1}) or the rate constant (in cm^3/s) of the process and N_j is the density of the corresponding plasma component or the product of the densities of the components involved in the process. For the adopted discharge conditions, the simulations yielded the following approximate percentages of the partial contributions of different processes to the discharge dynamics (see Fig. 2): 96% for atom–electron emission, 2.3% for electron production in the discharge gap, 1.7% for ion–electron emission, 2×10^{-3}% for electron emission under the action of the metastable atoms diffusing from the discharge gap toward the cathode, and 2×10^{-4}% for photoemission from the cathode. The last percentage value turned out to be three orders of magnitude less than that for a low-pressure discharge considered in [6]. This may be attributed to the enhancement of the reabsorption of radiation and the resulting decrease in the density of atoms in the resonant states due to their more efficient deexcitation to the metastable states in inelastic collisions with plasma electrons.

3. The results of our simulations agree well with the numerical results obtained earlier and are confirmed by the available data from previous experiments on ODs, including the experiments carried out by the adherents of the concept of the photoelectron nature of the OD. Our simulations have supported once again the view that the OD is a kind of glow discharge, which, as is generally accepted now, is maintained by the ionization processes and by the bombardment of the cathode by fast heavy particles. All this leads to the following conclusion, which is very important from the practical point of view: the large amount of information on ODs that is contained in more than 100 publications, with the corresponding corrections of the interpretations of experiments, applies directly to the phenomenon of glow discharges excited over the entire range of pressures, first of all, at moderate pressures (from a few torrs to atmospheric pressure [21])—a range that was previously poorly studied in experiments on the generation of electron beams in glow discharges.

REFERENCES

1. V. M. Batenin, V. V. Buchanov, M. A. Kazaryan, *et al.*, *Lasers on Self-Limited Transitions of Metal Atoms* (Nauchnaya Kniga, Moscow, 1998).
2. A. P. Bokhan and P. A. Bokhan, Opt. Atmos. Okeana **15**, 216 (2002).
3. A. R. Sorokin, Opt. Atmos. Okeana **17**, 266 (2004).
4. A. R. Sorokin, Pis'ma Zh. Tekh. Fiz. **26** (24), 89 (2000) [Tech. Phys. Lett. **26**, 1114 (2000)].
5. A. R. Sorokin, Pis'ma Zh. Tekh. Fiz. **29** (20), 1 (2003) [Tech. Phys. Lett. **29**, 836 (2003)].
6. A. V. Karelin, Laser Phys. **14** (1), 15 (2004).
7. A. R. Sorokin, Pis'ma Zh. Tekh. Fiz. **29** (10), 15 (2003) [Tech. Phys. Lett. **29**, 404 (2003)].
8. A. M. Boĭchenko, V. I. Derzhiev, A. G. Zhidkov, *et al.*, Preprint No. 282 (Inst. of General Physics, USSR Acad. Sci., Moscow, 1987).
9. V. I. Derzhiev, A. G. Zhidkov, O. V. Sereda, *et al.*, Tr. Inst. Obshch. Fiz. AN SSSR **21**, 139 (1989).
10. O. V. Sereda, Candidate's Dissertation in Mathematics and Physics (Moscow, Inst. of General Physics, USSR Acad. Sci., 1990).
11. A. R. Sorokin, Pis'ma Zh. Tekh. Fiz. **29** (17), 1 (2003) [Tech. Phys. Lett. **29**, 701 (2003)].
12. S. V. Arlantsev, B. L. Borovich, V. V. Buchanov, *et al.*, J. Russ. Laser Res. **16** (2), 99 (1995).
13. K. N. Ul'yanov and V. V. Chulkov, Zh. Tekh. Fiz. **58**, 328 (1988) [Sov. Phys. Tech. Phys. **33**, 201 (1988)].
14. A. N. Tkachev and S. I. Yakovlenko, Pis'ma Zh. Éksp. Teor. Fiz. **77**, 264 (2003) [JETP Lett. **77**, 221 (2003)].
15. H. C. Hayden and N. G. Utterback, Phys. Rev. A **135**, A1575 (1964).
16. V. I. Derzhiev, A. G. Zhidkov, and S. I. Yakovlenko, *Radiation from Ions in a Nonequlibrium Dense Plasma* (Énergoatomizdat, Moscow, 1986).
17. B. N. Klyarfel'd and B. I. Moskalev, Zh. Tekh. Fiz. **39**, 1066 (1969) [Sov. Phys. Tech. Phys. **14**, 800 (1969)].
18. G. V. Kolbychev and E. A. Samyshkin, Zh. Tekh. Fiz. **51**, 2032 (1981) [Sov. Phys. Tech. Phys. **26**, 1185 (1981)].
19. G. V. Kolbychev, Opt. Atmos. Okeana **6**, 635 (1993).
20. M. A. Zav'yalov, Yu. E. Kreĭndel', A. A. Novikov, *et al.*, *Plasma Processes in Technological Electron Guns* (Énergoatomizdat, Moscow, 1989).
21. A. R. Sorokin, Pis'ma Zh. Tekh. Fiz. **29** (9), 42 (2003) [Tech. Phys. Lett. **29**, 373 (2003)].

Translated by G.V. Shepekina

Plasma Physics Reports, Vol. 31, No. 6, 2005, pp. 524–527. Translated from Fizika Plazmy, Vol. 31, No. 6, 2005, pp. 572–576.

LOW-TEMPERATURE PLASMA

H^- Ion Density in the Plasma of a Low-Voltage Cesium–Hydrogen Discharge as a Function of the Cathode Emission Current

F. G. Baksht and V. G. Ivanov

Ioffe Physicotechnical Institute, Russian Academy of Sciences, Politekhnicheskaya ul. 26, St. Petersburg, 194021 Russia

Received July 19, 2004

Abstract—It was shown theoretically that the increase in the cathode emission current in a low-voltage cesium–hydrogen discharge to ≈10 A/cm^2 leads to an increase in the electron temperature in the anode plasma to $T_e \geq 1$ eV. In this regime, the rate constant for the production of H^- ions via dissociative electron attachment to vibrationally excited H_2 molecules is close to its maximum value and the density of H^- ions is maximal (about 10^{13} cm^{-3}) in the anode plasma. © *2005 Pleiades Publishing, Inc.*

The possibility of achieving the high density of H^- ions ($N_{H^-} \sim 10^{13}$ cm^{-3}) in the plasma of a low-voltage cesium–hydrogen discharge was theoretically predicted in [1, 2]. In such a discharge, H^- ions are produced due to the dissociative attachment of the heated plasma electrons to vibrationally excited H_2 molecules in the $X^1\Sigma_g^+(v)$ ground electronic state [3–5]. The discharge plasma is produced via the ionization of Cs atoms, whereas hydrogen (both molecular and atomic) remains almost unionized. The latter stems from the cathode potential fall φ_1 being such that $e\varphi_1 \leq E_d$, where $E_d \approx 8.8$ eV is the threshold energy for the direct electron-impact dissociation of H_2 molecules from the ground vibrational state $X^1\Sigma_g^+(v = 0)$. Since the threshold excitation energies for all the other electronic transitions from the ground state of H_2 molecules or H atoms are higher than E_d, fast electrons with energies that are high enough to induce either direct dissociation or stepwise ionization of hydrogen are almost absent in the discharge.

The theory of a low-voltage discharge was developed in a number of studies (see, e.g., review [6]). The case of a low-voltage discharge in a dense collisional cesium–hydrogen plasma was most thoroughly considered in [2]. By dense plasma we mean a plasma in which the mean free path of the particles and the energy relaxation length $L_E = (D_0\tau_E(\varepsilon_0))^{1/2}$ of the cathode beam are much shorter than the electrode gap length L. Here, D_0 is the diffusion coefficient of the cathode electrons in the discharge plasma, $\tau_E(\varepsilon_0) = \varepsilon_0^2/(2\pi e^4 v_0 n_e \Lambda)$ is the relaxation time of their energy ($\varepsilon_0 = e\varphi_1$) due to the binary collisions with thermal plasma electrons, n_e is the density of the thermal electrons trapped in the potential well, and $v_0 = (2\varepsilon_0/m_e)^{1/2}$. It was shown in [6] that, for molecular hydrogen pressures of $p_{H_2} \sim 1$ torr and an average density of Cs atoms in the gap of $N_{Cs}^{(0)} \sim 10^{14}$ cm^{-3}, an electron temperature of $T_e \approx 1$ eV (which is optimal for the dissociative attachment of electrons to vibrationally excited molecules [4, 5]) and, accordingly, the high density of negative hydrogen ions ($N_{H^-} \sim 10^{13}$ cm^{-3}) can be achieved in the plasma.[1]

In [6, 8–10], the density N_{H^-} in the plasma of a low-voltage cesium–hydrogen discharge was determined from laser absorption caused by the photodetachment of electrons from H^- ions. It was shown that the calculated H^- density satisfactorily agreed with experimental results (previously, such agreement was achieved between theoretical and experimental results on the electric potential φ, electron temperature T_e, and electron density n_e). It should be noted, however, that under conditions in which theory and experiment were compared to one another [10], the electron temperature $T_e(x)$ decreases substantially from the cathode to the anode. In this case, the relatively high electron temperature ($T_e \approx 0.7$–0.8 eV) corresponding to the large rate constants for dissociative attachment occurred only in the cathode region. It is in this region where the high H^-

[1] For parameters typical of a low-voltage discharge ($e\varphi_1 \leq E_d$ and $n_e/N_{H_2} > 10^{-3}$), the plasma electrons are heated to the required temperature in spite of the relatively low power of such a discharge because almost the entire energy of the accelerated cathode beam is spent on the heating of thermal electrons, whereas the remaining energy losses are insignificant [7].

1063-780X/05/3106-0524$26.00 © 2005 Pleiades Publishing, Inc.

density ($N_{H^-} \approx (0.4–0.6) \times 10^{13}$ cm^{-3}) was observed in both experiments and simulations. In the anode region, the electron temperature was $T_e \approx 0.3–0.5$ eV, which was appreciably lower than the temperature optimal for dissociative attachment. Accordingly, the rate constants for dissociative attachment were small within the range of the vibrational spectrum of H_2 molecules ($v \approx 4–8$; see Section 4) that is most promising for the production of H^- ions. Therefore, the effective (averaged over vibrational levels) rate constant $\langle K_{DA} \rangle = \sum_v f_v K_v(T_e)$ for the production of H^- ions was small and, accordingly, the density of H^- ions in the anode region was low: $N_{H^-} \approx (0.05–0.15) \times 10^{13}$ cm^{-3}. Here, $f_v = N_v / N_{H_2}$ is the normalized to unity vibrational distribution function (VDF) of H_2 molecules, N_{H_2} is the total density of H_2 molecules, N_v is the density of molecules excited to the vth vibrational level, and $K_v(T_e)$ is the rate constant for the dissociative attachment of electrons to molecules at the vth vibrational level.

Our purpose here is to show that an increase in the power $j_{es}U$ deposited in a low-voltage discharge (actually, an increase in the density of the cathode emission current j_{es}) leads to a discharge mode in which the electron temperature only slightly varies along the discharge gap. In this case, T_e in the anode region is fairly high and the rate constant $K_v(T_e)$ is close to its optimal value within the range of the vibrational spectrum of H_2 molecules that is most promising for the production of H^- ions. As a result, N_{H^-} in the anode region increases substantially (cf. [10]). Note that the achievement of high N_{H^-} values in the anode region is of particular interest from the standpoint of using the low-voltage cesium–hydrogen discharge as a volume source of intense narrow beams of H^- ions, extracted from the anode plasma through an opening in the anode.

We performed calculations for a high-temperature cathode with a relatively high density of the cathode emission current, $j_{es} \approx 10$ A/cm^2 (such an emission current density is characteristic of a LaB_6 cathode at a temperature of $T_1 = 2000$ K). The anode temperature T_2 was assumed to be 600 K.

When calculating the parameters of a low-voltage discharge, the voltage drop φ_1 across cathode sheath was assumed to be $\varphi_1 \approx E_d/e \approx 9$ V. The distributions of the plasma parameters along the discharge gap, as well as the discharge voltage, the decelerating (for electrons) potential barrier φ_2 in the anode sheath, and the total density of the discharge current j (under the given conditions, it is very close to the density of the cathode emission current j_{es}), were determined by solving the set of transport equations for the discharge plasma [2]. The results of calculations are shown in Figs. 1 and 2.

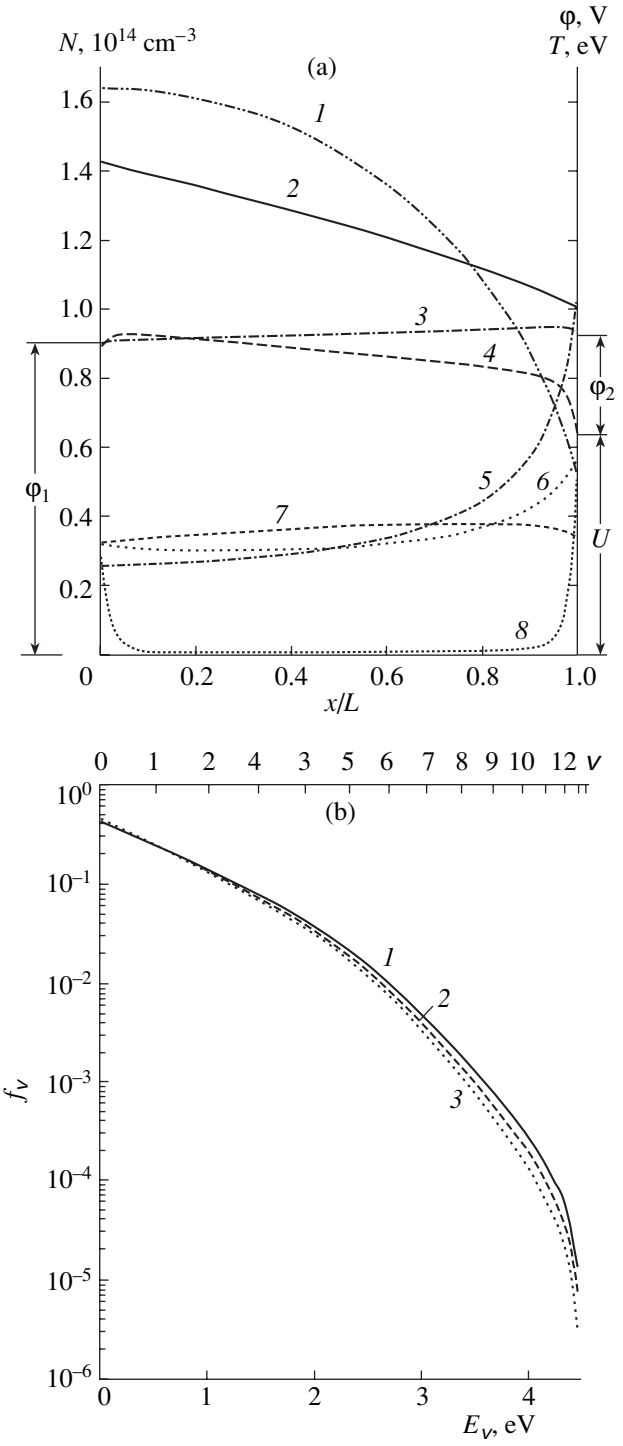

Fig. 1. (a) Longitudinal profiles of the main plasma parameters in a cesium–hydrogen discharge: (*1*) $10T_g$, (*2*) T_e, (*3*) 0.1φ, (*4*) n_e (*5*) $0.01N_{H_2}$, (*6*) $10N_{H^-}$, (*7*) $0.1N_H$, and (*8*) N_{Cs}; (b) VDFs of H_2 molecules at different distances from the cathode, x/L = (*1*) 0.1, (*2*) 0.5, and (*3*) 0.9. The electrode gap length is $L = 0.6$ cm, $T_1 = 2000$ K, $T_2 = 600$ K, $p_{H_2} = 0.75$ torr, $N_{Cs}^{(0)} = 0.92 \times 10^{14}$ cm^{-3}, $j_{es} = 10$ A/cm^2, $U = 6.42$ V, and $j = 9.43$ A/cm^2.

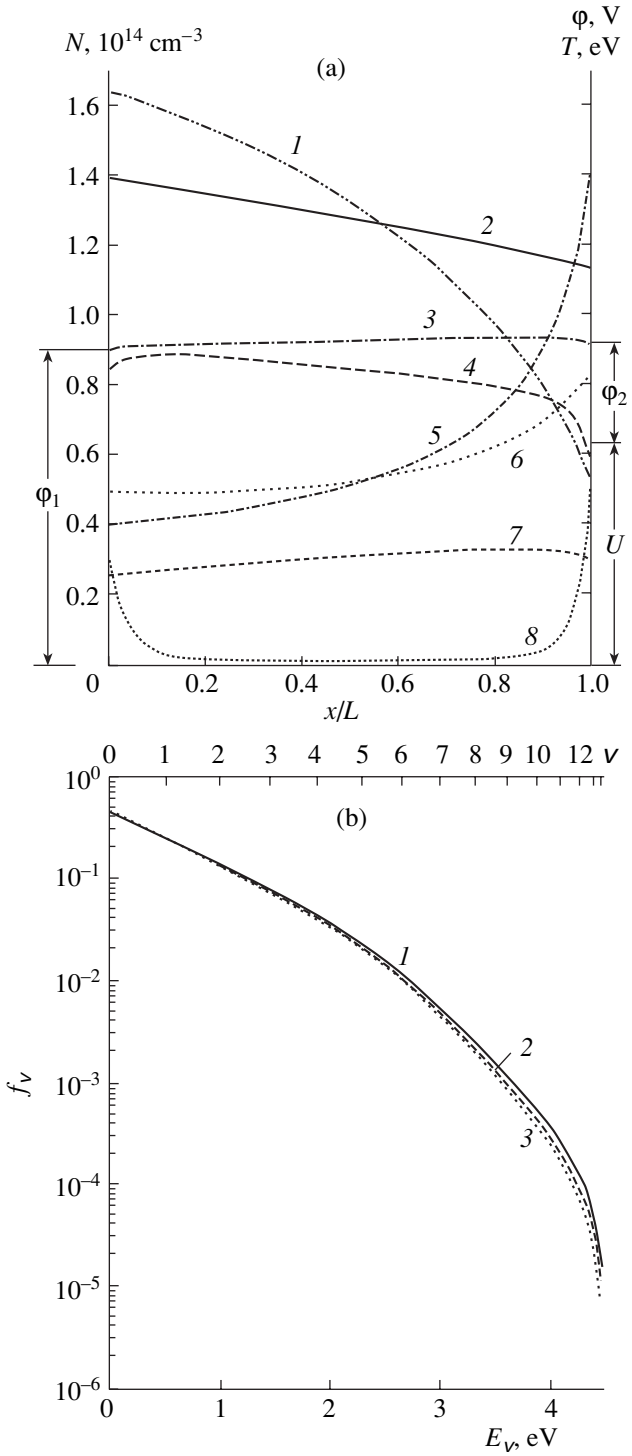

Fig. 2. The same as in Fig. 1, but for L = 0.3 cm, T_1 = 2000 K, T_2 = 600 K, p_{H_2} = 1 torr, $N_{Cs}^{(0)} = 0.93 \times 10^{14}$ cm^{-3}, j_{es} = 10 A/cm^2, U = 5.9 V, and j = 9.49 A/cm^2.

Figures 1a and 2a show the longitudinal profiles of the main parameters of the quasineutral plasma, including the densities of molecular and atomic hydrogen ($N_{H_2}(x)$ and $N_H(x)$), the density of cesium atoms $N_{Cs}(x)$, the gas temperature $T_g(x)$, and the density of H^- ions for two electrode gap length: L = 0.6 and 0.3 cm. The electrode sheaths are not shown because their lengths are small compared to the gap length L. Only the potential drops φ_1 and φ_2 across the sheaths are indicated. Note that the potential drop φ_1 in Figs. 1a and 2a is equal to $\varphi(0)$ because, in our calculations, the potential of the cathode surface is assumed to be zero.

In our calculations, along with φ_1, L, j_{es}, T_1, and T_2, we also specified the pressure p_{H_2} of molecular hydrogen and the average (over the gap) density of cesium atoms $N_{Cs}^{(0)}$. The two latter quantities were not chosen arbitrarily (as was done in [2]) but were rather determined in the course of discharge optimization in terms of maximizing the density $N_{H^-}(L)$ of negative hydrogen ions at the anode boundary of the quasineutral plasma. It can be seen from Figs. 1a and 2a that a characteristic feature of such an optimized discharge is the presence of the maximum of $N_{H^-}(x)$ at the anode boundary of the plasma.

Figures 1b and 2b show the VDF of H_2 molecules at three characteristic points: near the cathode, near the anode, and in the middle of the gap. The VDFs were calculated taking into account the following processes:

(i) Electronic–vibrational (EV) exchange was calculated by the method used in [5]. All the parameters of the one-quantum EV exchange, which greatly prevails over multiquantum transitions, were expressed via the cross section σ_{01} for the electron-impact excitation of the $v = 0 \longrightarrow v = 1$ transition. The value of σ_{01} was taken from [11].

(ii) The vibrational–vibrational (VV) and vibrational–translational (VT) exchange between H_2 molecules were calculated by the method used in [12]. The relevant rate constants Q_{10}^{01} and P_{10} were taken from [13, 14].

(iii) VT exchange between hydrogen molecules and atoms was calculated by the method proposed in [15, 16].

(iv) We also took into account the dissociative attachment of electrons, which destroys vibrationally excited H_2 molecules, and another processes with the participation of vibrationally excited molecules (see [17]).

It can be seen from Figs. 1b and 2b that the calculated VDFs f_v vary only slightly along the discharge gap. The reason for this is that, under the given conditions, the major role in the VDF formation is played by EV exchange. In this case, the electron density n_e and the rate constant for the electron-impact excitation of the $v = 0 \longrightarrow v = 1$ transition (see, e.g., [18]) vary insignificantly along the discharge gap.

Figure 3 shows the energy dependence of the quantity $\Gamma_v = f_v K_v(T_e) / \sum_v f_v K_v(T_e)$, which characterizes the relative contribution from different vibrational lev-

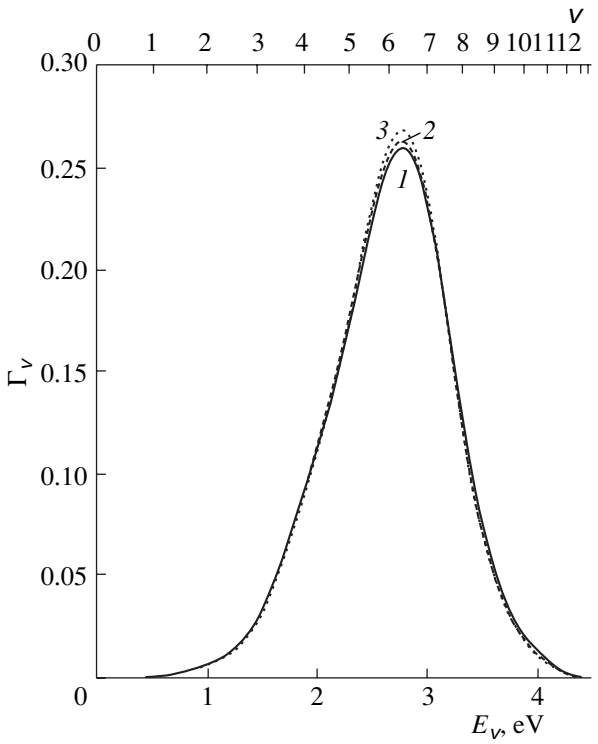

Fig. 3. Relative contribution from different vibrational levels v to the total production rate of H^- ions via the dissociative attachment of electrons to vibrationally excited H_2 molecules. The discharge parameters and the numeration of the curves are the same as in Fig. 2b.

els v to the total production rate of H^- ions via dissociative attachment. It can be seen that the levels $v \approx 4$–8 make the main contribution to dissociative association. Note that, for optimized discharge modes, the temperature T_e in the anode plasma is such that the rate constants $K_v(T_e)$ for dissociative attachment are close to their maximum values K_{vm}. For example, for curve *3* in Fig. 3, the K_v/K_{vm} ratio lies in the range $0.85 \le K_v/K_{vm} \le 1$ for $v = 4$–8.

A comparison between Figs. 1a and 2a shows that, as the gap length L decreases, the drop in T_e across the gap decreases and the electron temperature in the anode plasma increases. The temperature equalizes because of the increased role of electron heat conduction in the equation for electron energy transfer. In the electron temperature range under study (T_e in the anode plasma is close to 1 eV), the equalization of the temperature leads to an increase in the rate constant $K_v(T_e)$ in the anode plasma and the corresponding increase in the density of H^- ions.

Thus, our simulations have shown that the use of a hot cathode with an emission current density of $j_{es} \approx 10$ A/cm^2 allows one to achieve operating regimes of a low-voltage cesium–hydrogen discharge in which the density of negative hydrogen ions is maximal ($N_{H^-} \approx 10^{13}$ cm^{-3}) in the anode plasma.

ACKNOWLEDGMENTS

We are grateful to S.M. Shkol'nik for useful discussions.

REFERENCES

1. F. G. Baksht and V. G. Ivanov, Pis'ma Zh. Tekh. Fiz. **12**, 672 (1986) [Sov. Tech. Phys. Lett. **12**, 278 (1986)].
2. F. G. Baksht, L. I. Elizarov, and V. G. Ivanov, Fiz. Plazmy **16**, 854 (1990) [Sov. J. Plasma Phys. **16**, 497 (1990)].
3. M. Bacal and G. W. Hamilton, Phys. Rev. Lett. **42**, 1538 (1979).
4. J. M. Wadehra, Phys. Rev. A **29**, 106 (1984).
5. D. A. Skinner, A. M. Bruneteau, P. Berlemont, *et al.*, Phys. Rev. E **48**, 2112 (1993).
6. F. G. Baksht, V. G. Ivanov, and S. M. Shkol'nik, in *Proceedings of the International Conference on Physics of Low-Temperature Plasma, Kyiv, 2003*, Invited Paper 1.1.4-i.
7. F. G. Baksht and V. G. Ivanov, Fiz. Plazmy **12**, 286 (1986) [Sov. J. Plasma Phys. **12**, 165 (1986)].
8. F. G. Baksht, V. G. Ivanov, S. Kon'kov, *et al.*, in *Proceedings of the 30th EPS Conference on Controlled Fusion and Plasma Physics, St. Petersburg, 2003*, Papers 0-1,4D.
9. F. G. Baksht, V. G. Ivanov, S. I. Kon'kov, and S. M. Shkol'nik, Zh. Tekh. Fiz. **71** (8), 17 (2001) [Tech. Phys. **46**, 946 (2001)].
10. F. G. Baksht, L. I. Elizarov, V. G. Ivanov, *et al.*, Fiz. Plazmy **29**, 256 (2003) [Plasma Phys. Rep. **29**, 231 (2003)].
11. M. A. Morrison, R. V. Crompton, B. C. Saha, and Z. L. Petrovic, Aust. J. Phys. **40**, 239 (1987).
12. B. Gordiets and S. Zhdanok, in *Nonequilibrium Oscillatory Kinetics*, Ed. by M. Capitelli (New York, Springer-Verlag, 1986; Mir, Moscow, 1989).
13. J. H. Kiefer, J. Chem. Phys. **57**, 1938 (1972).
14. J. H. Kiefer and R. M. Lutz, J. Chem. Phys. **44**, 668 (1966).
15. E. Garcia and A. Lagana, J. Chem. Phys. **90**, 987 (1986).
16. E. Garcia and A. Lagana, Chem. Phys. Lett. **123**, 365 (1986).
17. F. G. Baksht, L. I. Elizarov, V. G. Ivanov, and V. G. Yur'ev, Fiz. Plazmy **14**, 91 (1988) [Sov. J. Plasma Phys. **14**, 56 (1988)].
18. R. K. Janev, K. Evans, W. D. Langer, and D. E. Post, *Elementary Processes in Hydrogen–Helium Plasmas* (Springer, Berlin, 1987).

Translated by N.N. Ustinovskiĭ